Surface passivation for silicon solar cells

by

Ruy Sebastian Bonilla Osorio

Thesis submitted for
the Degree of Doctor of Philosophy

May, 2015

Supervisor: Prof Peter R Wilshaw

To Vivi and Martin,
Who throughout the years have filled
my life with boundless love and happiness.

To my parents Irlanda & Rodrigo,
Who taught me to question, learn,
work hard, persevere and be free.

Abstract

Surface passivation for silicon solar cells

Ruy Sebastian Bonilla Osorio
Corpus Christi College
Department of Materials, University of Oxford

Thesis submitted for the Degree of Doctor of Philosophy
Trinity Term, 2015

Passivation of silicon surfaces remains a critical factor in achieving high conversion efficiency in solar cells, particularly in future generations of rear contact cells –the best performing cell geometry to date. In this thesis, passivation is characterised as either intrinsic or extrinsic, depending on the origin of the chemical and field effect passivation components in dielectric layers. Extrinsic passivation, obtained after film deposition or growth, has been shown to improve significantly the passivation quality of dielectric films.

Record passivation has been achieved leading to surface recombination velocities below 1.5 cm/s for 1 Ωcm n-type silicon covered with thermal oxide, and 0.15 cm/s in the same material covered with a thermal SiO_2/PECVD SiN_x double layer. Extrinsic field effect passivation, achieved by means of corona charge and/or ionic species, has been shown to decrease by 3 to 10 times the amount of carrier recombination at a silicon surface.

A new parametrisation of interface charge, and electron and hole recombination velocities in a Shockley-Read-Hall extended formalism has been used to model accurately silicon surface recombination without the need to incorporate a term relating to space-charge or surface damage recombination. Such a term is unrealistic in the case of an oxide/silicon interface.

A new method to produce extrinsic field effect passivation has been developed in which charge is introduced into dielectric films at high temperature and then permanently quenched in place by cooling to room temperature. This approach was investigated using charge due to one or more of the following species: ions produced by corona discharge, Na^+, K^+, Cs^+, Mg^{2+} and Ca^{2+}. It was implemented on both single SiO_2 and double SiO_2/SiN_x dielectric layers which were then measured for periods of up to two years. The decay of the passivation was very slow and time constants of the order of 10,000 days were inferred for two systems: 1) corona-charge-embedded into oxide grown on textured FZ-Si, and 2) potassium ions driven into an oxide on planar FZ-Si. The extrinsic field effect passivation methods developed in this work allow more flexibility in the combined optimisation of the optical properties and the chemical passivation properties of dielectric films on semiconductors.

Increases in cell Voc, Jsc and η parameters have been observed in simulations and obtained experimentally when extrinsic field effect passivation is applied to the front surface of silicon solar cells. The extrinsic passivation reported here thus represents a major advancement in controlled and stable passivation of silicon surfaces, and shows great potential as a scalable and cost effective passivation technology for solar cells.

PREFACE

This thesis is an account of the work I carried out as a postgraduate student at the Department of Materials, University of Oxford. I have not submitted any part of this thesis for a degree at this University or elsewhere. The work of other authors was duly acknowledged in the text and appropriate references are given.

Work presented in this thesis has been published in the following scientific journals or conference proceedings:

1. ***Ruy S Bonilla***, Christian Reichel, Martin Hermle, George Martins and Peter R Wilshaw (2015). “Extrinsic passivation of silicon surfaces for solar cells”. Energy Procedia. In proceedings of the 5th International Conference on Silicon Photovoltaics, SiliconPV 2015. In press.

2. George F. Martins, Phi. Macdonald, Toby. Burton, ***Ruy S. Bonilla***, Peter R. Wilshaw (2015). “Saw damage gettering for improved mc-Silicon”. Energy Procedia. In proceedings of the 5th International Conference on Silicon Photovoltaics, SiliconPV 2015. In press.

3. ***Bonilla R.S.***, Woodcock F, and Wilshaw P.R. (2014) ”Very low surface recombination velocity in n-type c-Si using extrinsic field effect passivation”. J. Appl. Phys. 116, 054102 (2014).

4. ***Bonilla, R. S.***, Wilshaw, P. R. (2014). “A technique for field effect surface passivation for silicon solar cells”. Applied Physics Letters, 104, 232903 (2014).

5. ***Bonilla, R. S.***, Reichel, C., Hermle, M., & Wilshaw, P. R. (2014). “On the location and stability of charge in SiO2/SiNx dielectric double layers used for silicon surface passivation”. J. Appl. Phys, 115(14), 144105.

6. ***Ruy S. Bonilla***, Christian Reichel, Martin Hermle and Peter Wilshaw. (2014). “Electric field effect surface passivation for silicon solar cells”. Solid State Phenomena. Vols. 205-206 pp 346-35.

7. ***Ruy S Bonilla***, Christian Reichel, Martin Hermle, Semih Senkader and Peter Wilshaw. (2014). “Controlled field effect surface passivation of crystalline n-type silicon and its application to back-contact silicon solar cells”. Proceedings of the 40th IEEE Photovoltaic Specialist Conference. Denver, CO, United States. 2014

8. ***Bonilla, R. S.***, & Wilshaw, P. R. (2013). “Stable field effect surface passivation of n-type Cz silicon”. Energy Procedia, Volume 38, 2013, Pages 816-822

ACKNOWLEDGMENTS

In January 2004 I started my path of higher education in Los Andes, Colombia. Over 10 years later, I am finishing my doctorate at Oxford and I couldn't feel happier and more grateful. I feel that by submitting this thesis I am bringing to an end this long journey as a student. And although I know very little will change now, I also know this is a day I have waited for long, and there is a myriad of people without whom I couldn't have got here. I apologise in advance for all of those who I manage to miss, but I am writing this less than 48 hours before my submission deadline, and I am sure many of you may never even get to read this. In the first place I want to acknowledge my supervisor Peter Wilshaw, for the immense and invaluable mentoring, nurturing and teaching he has dedicated to me over the past three and a half years. I thank our collaborators in Germany: Martin Hermle, Christian Reichel and Manuel Schnabel, for the provision of FZ silicon material, oxide growth, nitride deposition, scientific discussions, and hosting me for standard testing of solar cells. I am also thankful to the Clarendon Fund and Corpus Christi College for providing graduate funding. Being at Oxford and part of the Semiconductor group has been a wonderful and enriching experience, and for this I specially thank George and Abu, but also all the members of the group: Min, Shark, Manuel, Semih, Kanad, John, James and Katie, all the part II students I interacted with: Tas, Ian, Fred, Richard and Lucy, and the support staff: Radka and Laurie. In Oxford, I also have to thank the wonderful people that I have had the pleasure to meet and with whom I have shared beautiful moments, specially my awesome flat mate Jo, and my friends Divija, Thomas, Pauline, Marc, Julia, Hong Sheng, Cris, and Jessica. In Cambridge Halliki, in Colombia, Paula, Andrea and Vlady, in the US Arturo, Nancy, Tracy, Ed and Marie. For our brief, yet intense, wonderful, life changing and crazy love story, I thank Maryhen. For their tutoring and mentoring I thank my ex-supervisors Michelle Moram, Alejando Bonilla, David Barney, and specially Alba Ávila. Before you think I have forgotten about you, my sincere gratitude to my good old friend Ariel, for being such an amazing companion, starting in Bogota, all the way to Geneva, London, and now at Oxford. We've shared amazing times and you've given me so much laughter, joy and counsel over the past 10 years. I couldn't finish without thanking my parents, my brother and sister, and all of my family in Colombia, specially Diego, Francy, Eutimio, los chinos, Yanet, Leo, Jenny, Jorge, Clara, Fabis and Chava QEPD, and my gran parents, who have given me all their admiration, love and support over the years, and have (sometimes reluctantly) shared my happiness and success abroad from home. I carry you all in my heart.

LIST OF ACRONYMS

CB	Conduction band
CV	Capacitance-voltage technique
Cz	Czochralski, referring to one of the silicon casting processes.
FEP	Field-effect passivation.
FZ	Float Zone, referring to one of the silicon casting processes.
IV	Current-voltage
KP	Kelvin Probe
mc	multi-crystalline, referring to a kind of raw silicon material.
MIS	Metal-insulator-semiconductor
OI	Oxford Instruments, plasma technology manufacturer.
PECVD	Plasma enhanced chemical vapour deposition.
PSG	Phospho-silicate glass.
RIE	Reactive Ion Etching
sccm	Standard centimetre cubed per minute, flow unit.
SCR	Space charge region
SiN_x	Silicon nitride, refers to the non-stoichiometric form of this dielectric film
SiO_x	Silicon oxide, refers to the non-stoichiometric form of this dielectric film
SMU	Standard measuring unit.
SOG	Spin-on glass.
STC	Standard testing conditions
VB	Valence band
FSF	Front surface field
BSF	Back surface field
c-Si	Crystalline silicon

LIST OF SYMBOLS

S_{eff}	Effective surface recombination velocity [cm/s]
ϕ	Electric Potential in semiconductors [V]
q	Electron fundamental charge (1.6 x 10^{-19} C)
V_ρ	Potential shift due to dielectric volume charge [V]
V_t	Thermal potential [V] (0.026 V at room temperature)
V_{fb}	Flat band voltage of a MIS structure [V]
V_c	Contact potential between to metals [V]
V_b	Backing potential in Kelvin Probe [V]
V_{kp}	Kelvin Probe surface potential=$-V_b$ [V]
N_{dop}	Semiconductor dopant density (positive for p-type negative for p-type Si) [cm^{-3}]
$\mathcal{E}$	Electric field [V/cm]
$\mathcal{E}_s$	Electric field at the surface of a semiconductor [V/cm]
Φ_s	Semiconductor work function [eV]
Φ_m	Metal work function [eV]
n_i	Semiconductor intrinsic charge carrier concentration [cm^{-3}]
ε_0	Vacuum permittivity [F/cm]
K	Relative permittivity
ε_s	Semiconductor permittivity = $K_s\varepsilon_0$ [F/cm]
t_i	Insulator thickness [cm]
t_{air}	Probe-to-specimen distance in KP [cm]
$\delta(x)$	Delta-Dirac function in a single space dimension [1/cm]
V_i	Potential drop across the insulator [V]
V_s	Substrate potential, normally the semiconductor [V]
E	Energy [J or eV]
E_F	Semiconductor Fermi energy [eV]
E_i	Semiconductor intrinsic energy [eV], normally take as reference.
E_C	Semiconductor conduction energy [eV]
E_V	Semiconductor valence energy [eV]
ϕ_F	Semiconductor Fermi potential [V]
Q_{Si}	Silicon space charge density [C/cm^2]
Q_T	Total charge in the dielectric/semiconductor system[C/cm^2]
p_s	Hole density at the surface [cm^{-3}]
n_s	Electron density at the surface [cm^{-3}]
p_b	Hole density in the bulk[cm^{-3}]
n_b	Electron density in the bulk [cm^{-3}]
$p(z)$	Holes density as a function of depth in the semiconductor [cm^{-3}]
$n(z)$	Electron density as a function of depth in the semiconductor [cm^{-3}]
S_{n0}	Energy independent recombination velocity for electrons[$cms^{-1}eV^{-1}$]
S_{p0}	Energy independent recombination velocity for holes [$cms^{-1}eV^{-1}$]
J_0	Dark saturation current density ($J_0 = J_{01} + J_{02}$) [A/cm^2]
J_{sc}	Short circuit current density [mA/cm^2]
V_{oc}	Open circuit voltage [V]
η	AM1.5 Cell efficiency [%]
σ_{ion}	Ionic surface concentration [cm^{-2}]
ϕ_{scr}	Semiconductor surface potential due to the space chare region [V]
S_n	Energy dependent recombination velocity for electrons[$cms^{-1}eV^{-1}$]
S_p	Energy dependent recombination velocity for holes [$cms^{-1}eV^{-1}$]
τ_{kp}	Decay time constant of Kelvin Probe surface potential [days]

TABLE OF CONTENTS

Chapter 1 Introduction 1

1.1 Climate change 1
1.2 Renewable energy sources and silicon photovoltaics 2
1.3 Silicon solar cells and carrier recombination 5
1.3.1 Solar cell fundamentals 5
1.3.2 Carrier recombination in crystalline silicon 7
1.3.3 Bulk recombination 8
1.3.3.1 Radiative recombination 9
1.3.3.2 Auger recombination 9
1.3.3.3 Shockley-Read-Hall recombination 11
1.3.4 Surface recombination 12
1.4 Silicon surface passivation 14
1.4.1 Dielectric films 15
1.4.2 Surface doping 17
1.4.3 Controlled field effect surface passivation 18
1.5 Aim of this work 18
1.6 Background science 20
1.6.1 Corona discharge 20
1.6.2 Field assisted ion drift in solids 22
1.6.3 Charge storage and ionic conduction in the SiO_2/Si system 23
1.6.3.1 Ion injection in SiO_2 using a metal contact 23
1.6.3.2 SiO_2 corona charged films 25
1.7 Structure of this thesis 26

Chapter 2 Experimental Methods 29

2.1 Silicon substrate material 29
2.1.1 Surface finish 30
2.1.2 Sample labelling 30
2.2 Dielectrics used for surface passivation 31
2.2.1 Thermal oxides 31
2.2.2 Chemical vapour deposited dielectrics 31
2.2.3 Summary of dielectrics 32
2.3 Extrinsic chemical passivation 33
2.4 Extrinsic field-effect passivation 33
2.4.1 Corona discharge 33
2.4.1.1 Dehydration and HMDS coating 35

2.4.2 Ionic species ... 36
2.4.2.1 Deposition ... 36
2.4.2.2 Transport ... 37
2.5 Electrical characterisation ... 38
2.5.1 Minority carrier lifetime ... 38
2.5.1.1 Calculation of decay time constants for aging measurements ... 40
2.5.2 Capacitance-Voltage measurements ... 41
2.5.2.1 Mercury probe contact and charge profiling ... 44
2.5.3 Thermally stimulated ionic conductivity ... 45
2.5.4 Kelvin Probe measurement of surface potential ... 46
2.5.4.1 Calculation of decay time constants for aging measurements ... 52
2.5.5 Solar cell testing ... 52
2.5.5.1 In-house solar simulator ... 52
2.5.5.2 Standard testing conditions ... 53
Chapter 3 Effect of dielectric charge on surface recombination ... 55
3.1 Theoretical background ... 55
3.1.1 Shockley-Read-Hall surface recombination ... 55
3.1.2 The effect of surface band bending ... 58
3.1.3 Recombination in the space charge region ... 62
3.2 Development of the model for surface recombination ... 65
3.2.1 Recombination in a near-surface region ... 67
3.2.2 The effect of electron and hole recombination in effective SRV ... 68
3.2.3 Effect of interface charge concentration ... 72
3.2.4 Discussion ... 74
3.3 Case study: FEP of oxidised n-type silicon ... 75
3.3.1 The effect of corona charge on effective lifetime ... 76
3.3.2 Modelling surface recombination for Si/SiO_2 ... 78
3.3.3 Discussion ... 80
3.4 Summary ... 86
Chapter 4 Field-effect passivation using corona discharge ... 87
4.1 Corona discharge conditions ... 88
4.1.1 Corona current-voltage characteristics ... 88
4.1.2 Uniformity of charge ... 90
4.1.3 Corona charge deposition and its effect on lifetime ... 91
4.1.4 Summary ... 93
4.2 Effect and location of corona charge on SiO_2 passivated n-type c-Si ... 94
4.2.1 Surface passivation of oxidised n-type c-Si using extrinsic FEP ... 94

4.2.2 Corona charge location ... 96
4.2.3 Textured silicon ... 97
4.2.4 Forming gas annealed SiO_2 ... 97
4.1.1. Discussion ... 98
4.2.5 Summary ... 100
4.3 Stability of corona charge in SiO_2 passivated Si ... 100
4.3.1 Leakage of corona charge ... 100
4.3.2 Chemical surface modification of SiO_2 ... 102
4.3.2.1 Forming gas annealed SiO_2 ... 105
4.3.3 Discussion ... 106
4.3.4 Summary ... 107
4.4 Embedding corona charge into SiO_2 films ... 108
4.4.1 Post-corona charge anneal in HMDS treated SiO_2 ... 109
4.4.2 Textured silicon surface ... 111
4.4.3 Discussion ... 112
4.4.4 Summary ... 114
4.5 Effect, location and stability of corona charge in SiO_2/SiN_x passivated Si ... 115
4.5.1 Extrinsic corona FEP of c-Si using SiO_2/SiN_x double layers ... 115
4.5.2 Separating the chemical and field effect components of passivation in SiO_2/SiN_x double layers ... 116
4.5.3 Stability of charge and HMDS chemical treatment ... 120
4.5.3.1 Textured surfaces ... 122
4.5.4 Discussion ... 123
4.5.5 Summary ... 125
4.6 Chapter summary ... 125

Chapter 5 Field-effect passivation using ionic charge ... 129

5.1 Transport of ionic charge ... 130
5.1.1 Drift using a metal contact ... 131
5.1.2 Alkali ion diffusion ... 135
5.1.3 Ionic drift using corona charge induced electric field ... 139
5.1.4 Discussion ... 141
5.1.5 Summary ... 142
5.2 Passivation effect of migrated charged ions on oxidised FZ n-Si ... 143
5.2.1 Diffused ions ... 143
5.2.1.1 Sodium and Potassium ... 143
5.2.1.1.1 Interface defect generation ... 146
5.2.1.2 Magnesium and Calcium ... 147
5.2.1.3 Caesium ... 148

5.2.2 Drift using corona charge induced electric field 149
5.2.3 Discussion 151
5.2.4 Summary 153
5.3 Stability of ion induced passivation.. 153
5.3.1 High Temperature diffused ions.. 153
5.3.1.1 Sodium and potassium.. 153
5.3.1.2 Calcium and magnesium 155
5.3.2 Corona charge drifted ions 156
5.3.2.1 Sodium and potassium.. 156
5.3.2.1.1 Surface chemical treatments...157
5.1.1.1. Calcium and magnesium 160
5.3.3 Discussion 161
5.3.4 Summary 165
5.4 Chapter summary.. 166

Chapter 6 Influence of field effect passivation on silicon solar cells 169

6.1 Solar cell geometries 169
6.2 Modelling cell efficiency and surface recombination 172
6.2.1 FEP in a front contacted cell (PC1D simulations) 173
6.2.1.1 Simulation setup.. 173
6.2.1.2 Results 174
6.2.1.3 Discussion 178
6.2.1.4 Summary 180
6.2.2 FEP in a back contacted cell (PC2D simulations)...................................... 180
6.2.2.1 Simulation setup.. 180
6.2.2.2 Results 182
6.2.2.3 Discussion 184
6.2.2.4 Summary 186
6.3 Influence of FEP on research scale IBC cells... 186
6.3.1 In-house non-standard solar simulator 187
6.3.2 FEP cells evaluated using standard testing conditions................................ 188
6.3.3 Discussion and summary.. 192
6.4 Chapter summary.. 193

Chapter 7 Summary and further work 195

7.1 The importance of field effect passivation in solar cells 195
7.2 Modelling SRV as a function of dielectric charge and minority carrier injection.. 196
7.3 Extrinsic Field effect passivation using corona charge 197
7.4 Extrinsic Field effect passivation using ionic charge 198

7.5 Further work 199

8 References 205

9 Appendix A... 223

Insulator charge calculation.. 223
Characterisation of surface state density using high frequency CV measurements 227

10 Appendix B.. 231

Modelling ionic injection with first order kinetics 231

11 Appendix C.. 233

Summary of samples and processing 233

LIST OF FIGURES

Figure 1. Energy Resources of the World. “These constant flows of energy amount to about 3,000 times the total present day energy consumption of the whole of mankind”. After [11]. 3

Figure 2. a. Estimated renewable energy share of global final energy consumption at 2011. After [10]. b. Global electricity mix in 2011 and in 2050 in three ETP 2014 scenarios proposed by the Internagiona Energy Agency, After[12]. 4

Figure 3: Schematic of a conventional silicon solar cell illustrating electron-hole pair generation. 6

Figure 4: Electron-hole pair generation, collection and recombination in a solar cell.6

Figure 5: Calculated defect related bulk lifetime as a function of excess minority carrier concentration for a shallow ($Et - Ev = 0.1\ eV$), medium ($Et - Ev = 0.2\ eV$), and deep ($Et - Ev = 0.5\ eV$) recombination centre. Lifetime is calculated using Shockley-Read-Hall statistics on equation (1. 15). T=300 K. 12

Figure 6: Schematic diagram showing surface states in a. bare silicon b. chemically passivated silicon and c. chemically and field effect passivated silicon. 15

Figure 7: a. Record passivation quality obtained using state-of-the-art techniques, b. Specimen characteristics including references. 17

Figure 8: Scheme of electret charge storage via ionic charges and polarized molecules on a dielectric film on silicon. 20

Figure 9: Schematic of a point-to-plane corona discharge apparatus. High potential on the sharp needle cause ionization of surrounding molecules, which in turn drift towards the lesser potential electrode. 21

Figure 10: Standard for sample labelling. 30

Figure 11: a. Circuit diagram of charging apparatus, with corona distance labelled “d”, b. Results of numerical model of Warburg’s Law, showing corona current as a function of position, for corona distances of 7.5 and 15cm. Adapted from Bonilla et al [119]. 35

Figure 12. Schematic of HMDS chemical treatment 1 35

Figure 13. Schematic of HMDS chemical treatment 2 36

Figure 14: Schematic of the thermal evaporation of ionic species. 37

Figure 15: Schematic diagram of the photo-conductance decay system used to measure minority carrier lifetime. 40

Figure 16. Example calculation of decay time constant for the decrease in effective lifetime over time of samples n1_1 and n7_6. 41

Figure 17: a. Processing methodology for creating MIS capacitors, b. Equivalent circuits and typical capacitance-voltage curves for a MIS capacitor in a n-type semiconductor, red curve indicates the ideal high-frequency capacitance, the blue curve indicates the contribution of surface defect states and the green curve indicates the contribution of dielectric fixed charge to the semiconductor capacitance, c. Schematic diagram of a MIS capacitor in the flat-band condition when charge in the dielectric is compensated by charge in the metal contact, including band diagram and the charge, electric field and potential in the structure. 43

Figure 18: Schematic diagram of the sample holder and front contact connection to form a MIS capacitor using Hg. 44

Figure 19: a. Schematic diagram of the TSIC technique, b. A MIS capacitor is subjected to a bias stress while the temperature is raised and the current recorded. The typical experiment has a linear temperature rise and produces characteristic peaks depending on the trapping energy of different types of ionic species inside the insulator. Integration of the recorded current allows the total migrated charge $Qion$ to be deduced. 46

Figure 20: Kelvin Probe principles in a two metal plates system and their work functions. 47

Figure 21: Metal probe - insulator – semiconductor schematic diagram including the band structure (a) without charge in the insulator and with a small external bias applied and (b) with an external bias applied such that zero Kelvin probe current is detected for the given charge concentration in the insulator. The charge, electric field, and electric potential diagrams at the bottom omit the work function difference for simplicity. 49

Figure 22: Variation of space charge density as a function of SCR potential ϕscr. 50

Figure 23. Example calculation of decay time constant for the decay in surface potential of samples nC_8 and n9_x1. 52

Figure 24: a. Schematic of in-house solar cell testing rig, b. IV curve taken on cell BC47-25C produced by Fraunhofer ISE. 53

Figure 25: a. Photographs of the sun simulator at Fraunhofer ISE, b. IV curve taken on cell BC47-17G using standard testing conditions. The STC efficiency was 20.2%. 54

Figure 26: Calculated surface recombination velocity for a range of capture cross sections and excess minority carrier concentration. SRV is calculated using the extended Shockley-Read-Hall statistics of equation (3. 2). 58

Figure 27: Calculated surface recombination velocity as a function of excess minority carrier concentration for different doping concentrations. SRV is calculated using the extended Shockley-Read-Hall statistics on equation (3. 1). 58

Figure 28: Schematic representation of the band bending problem at the surface of silicon due to charge present near and at the interface with a dielectric film. 60

Figure 29: Computed surface recombination velocity as a function of excess minority carrier concentration for different semiconductor SCR potentials due to positive surface fixed charge. SRV is calculated using the extended Shockley-Read-Hall statistics on equation (3. 1). A constant Dit and $\boldsymbol{Sn,p}$ have been assumed throughout the band-gap, T=300 K. 62

Figure 30: Computed electric potential, field and carrier concentration for 1 Ωcm n-Si with a surface charge of $+10^{12}$ q/cm^2 photo-injected with 10^{15} cm^{-3} minority charge carriers, T=300 K. ... 63

Figure 31: Computed normalised space charge region recombination for 1 Ωcm n-Si with a surface charge of $\pm 1.2\, x\ 10^{12}$ q/cm^2 as a function of minority charge carriers concentration, T=300 K. Auger recombination is calculated using Richter's parameterisation [28]. ... 65

Figure 32. Surface recombination velocity for n-type silicon as a function of positive and negative dielectric fixed charge concentration in q/cm^{-2}, for an excess minority carrier concentration of 10^{15} cm^{-3}, and a variation in the surface recombination of holes and electrons given by the curvatures an and ap. Four combinations of an, ap have been chosen as illustrated by the legend in the figure. Inset: Holes (green) and electrons (black) surface recombination functions used to calculate surface recombination velocity. Red horizontal lines represent the value the functions take when the dependence is eliminated ($a0 = 0$). .. 71

Figure 33. Effective surface recombination velocity for n-type silicon as a function of positive and negative dielectric fixed charge concentration, for an excess minority carrier concentration of 10^{15} cm^{-3}, and a variation in the charge stored at surface states Qit, given by the dependence on Dit. The green trace illustrates SRV when $Dit(E) = Dit0$, blue trace when $Dit(E) = Dit0 + DitVemVE + E0V$, red trace when $Dit(E) = Dit0 + DitCemCE + E0C$, and black trace when $Dit(E) = Dit0 + DitCemCE + E0C + DitVemVE + E0V$..... 74

Figure 34. Lifetime measurements of n-type ⟨100⟩ FZ Silicon (1 Ωcm) passivated with a 100 nm-thick thermal oxide (Sample n6b_3), for negative (left) and positive (right) corona deposited surface charge (q/cm^2). Arrows in the left graph illustrate the sub sequential charge deposition steps.: Effective lifetime is first reduced (blue and green) when negative charge is deposited, but further deposition of negative charge then increases lifetime (red and turquoise)... 78

Figure 35. Surface recombination velocity measurements and simulations as a function of negative (left) and positive (right) corona deposited surface charge [q/cm^2], for three excess minority carrier concentrations (Sample n6b_3). ... 79

Figure 36. Surface recombination velocity measurements and simulation for n-type FZ Silicon passivated with a 100 nm thermal oxide (Sample n6b_3). Negative (left) and positive (right) surface dielectric charge concentrations are in [q/cm^2]. This data is the equivalent SRV from data shown in Figure 34. ... 80

Figure 37. Simulation of effective surface recombination velocity for 1Ωcm FZ n-type silicon passivated with SiO_2, as a function of dielectric fixed charge and excess minority carrier concentration. Simulation parameters are given in Figure 35. Notice the x-axis on this figure is not a logarithmic axis. ... 84

Figure 38. a. Schematic of deposition of corona ions including the effective area where ions land, the corona distance, the corona potential and the corona current, b. Current-voltage characteristics of the 8 cm and 15 cm rigs... 90

Figure 39. a. Surface potential map of 87.5 nm thermal oxide on n-type Cz-Si (Sample nCb3) charged on corona Rig 1 for ~90 seconds. b. Statistical analysis of the distribution of charge across sample nCb3. c. Surface potential map of 100 nm thermal oxide on n-type FZ-Si (Sample n6b_4) charged on corona Rig 2 for 70 seconds. d. Statistical

analysis of the distribution of charge across sample n6b_4. A normal probability function is fitted to the probability density functions observed. 91

Figure 40. a. KP surface potential as a function of corona discharge time on c-Si samples with 100 nm and 87.5 nm oxides, b. Effective lifetime at 10^{15} cm^{-3} carrier injection as a function of corona charging time. Void magenta markers indicate the second cycle on sample n17b_1. 93

Figure 41. Lifetime measurements of n-type ⟨100⟩ Cz-Silicon (5 Ωcm) passivated with a 87.5 nm-thick thermal oxide (Sample nCb3), for positive charge deposited using corona discharge. Surface charge concentration, calculated using Kelvin Probe surface potential, is listed in the legend for each experimental lifetime plot.................................... 95

Figure 42. Lifetime measurements of n-type FZ Silicon passivated with a 100 nm-thick thermal oxide (Sample n17b_1), when deposited with positive corona charge in two cycles (left and right) using corona charge Rig 2. Surface charge concentration measured using Kelvin Probe surface potential... 96

Figure 43. Lifetime measurements of textured n-type FZ Silicon passivated with a 100 nm-thick thermal oxide (Sample nT1_9), for positive charge deposited using corona charge Rig 1. Surface charge calculated using the Kelvin Probe surface potential. 97

Figure 44. Lifetime measurements of n-type FZ Silicon passivated with a 100 nm-thick thermal oxide and FGA, Sample n17_8. Control sample n10_5a. Both samples were deposited with positive corona charge using Rig 1 for 120 seconds.................................... 98

Figure 45. Kelvin probe (KP) surface potential of c-Si oxidised specimens (Samples nE1, nC8 and n9_x1) after corona charge deposition, b. (KP) surface potential and effective lifetime @ $\Delta p=10^{15}$ cm^{-3}, for corona charged sample n9_x1. Corona was applied using Rig 1. 102

Figure 46. Kelvin probe (KP) surface potential and effective lifetime for a corona charged 87.5 nm oxide on n-type Cz-Si licon, 5 Ωcm (Samples nC1 and nCb3), at an excess minority carrier concentration of 10^{15} cm^{-3}. The surface potential of a sample without HMDS chemical treatment is included for comparison (red triangles) 103

Figure 47. The time and spatial variation of the charge induced potential on the dielectric surface. Kelvin Probe maps of corona charged 87.5 nm thermal oxide on n-type Cz-Si licon, 5 Ωcm (Sample nCb3), with HMDS treatment, and no further heat treatment, at the beginning and at the end of the measurement period. 104

Figure 48. Kelvin probe (KP) surface potential and effective lifetime for a corona charged (Rig 1) 100 nm oxide on n-type FZ silicon, 1 Ωcm (Samples n9_x1 and n1_6), at an excess minority carrier concentration of 10^{15} cm^{-3}. a. Sample n9_x1 had no HMDS treatment. b. Sample n1_6 had HMDS treatment 1... 105

Figure 49. Kelvin probe (KP) surface potential and effective lifetime for a corona charged (Rig 1) 100 nm oxide on n-type FZ silicon, 1 Ωcm (Samples n17_5 and n17_7), at an excess minority carrier concentration of 10^{15} cm^{-3}. a. Samples n17_5 had no HMDS treatment, b. Sample n17_7had HMDS treatment 1. 106

Figure 50. Surface potential and effective lifetime for a corona charged n-type Cz Silicon (5Ωcm) passivated with a 87.5 nm (a. Sample nCb4 and b. Control sample nCb7 without PC anneal) and 21.4 nm (c. Sample nBb1 and d. Control sample nBb2 without PC

anneal). PC stands for post-corona. All samples have been chemically treated with HMDS. 110

Figure 51. KP surface potential and effective lifetime at 10^{15} cm^{-3} for FZ n-Silicon, corona charged in Rig 1, a. with and b. without HMDS treatment 1 (Samples n1_1 and n7_6). PC stands for post-corona. 111

Figure 52. KP surface potential and effective lifetime for a corona charged (Rig 1) 100 nm oxide on textured n-type FZ silicon (Samples nT1_9), at an excess minority carrier concentration of 10^{15} cm^{-3}. Sample had no-HMDS treatment but a post-corona 400 ^{o}C anneal for 1 minute. 112

Figure 53. The mechanisms of high temperature corona charge migration in thermal oxides: a. Starting state after corona charge deposition, b. charge migration into the oxide through defect states charge hopping, c. Charge migration via diffusion and drift of charged corona ions into the oxide film. 114

Figure 54. Effective lifetime as a function of injection level for single and double oxide/nitride passivation films on 1 Ωcm FZ n-Si. Samples OX1-5_6, OX1-1_5, n17_8, n19_3. 116

Figure 55. Injection-dependent effective lifetime for 1Ωcm n-type FZ-Si passivated with a thermally grown oxide and a PECVD deposited nitride (Sample n21b_5), plus the impact of FEP via external corona charge. Inset plots SRV of the SiO_2/SiN_x + Corona specimen. Control sample n17_8 without SiN_x is included. 118

Figure 56. (a) Capacitance-voltage measurements of single and double layer oxide/nitride films on 1 Ωcm c-Si. Solid lines represent the ideal theoretical curves. Inset picture a back etch experiment to determine charge location (b) Interface state density calculated for the dielectric layers of (a), using the high frequency CV Terman's method. 120

Figure 57. KP surface potential and effective lifetime for a corona charged (Rig 1) 100/80 nm oxide/nitride on n-type FZ silicon. a. Sample n6_5 had no HMDS treatment, b. Sample n6_8 had HMDS treatment 1 121

Figure 58. KP surface potential and effective lifetime for a corona charged (Rig 1) 10/60 nm oxide/nitride on n-type FZ silicon. a. Samples OX1-1_1 had no HMDS treatment, b. Sample OX1-1_4 had HMDS treatment 1 122

Figure 59. KP surface potential and effective lifetime for a corona charged (Rig 1) 10/60 nm oxide/nitride on n-type textured FZ silicon. a. Samples OX1-5_1 had no HMDS treatment, b. Sample OX1-5_5 had HMDS treatment 1 123

Figure 60: Summary of the effectiveness and stability of passivation in FZ-Si passivated with oxide and oxide/nitride layers, HMDS treated, deposited and/or embedded with corona charge. The effective lifetime quoted is that at the end of the measurement period. The decay time constant was estimated from the data between day 50 and the end of the period. 127

Figure 61. Comparison of record passivation quality obtained using state-of-the-art techniques and the passivation achieved using the techniques proposed in this work. 'Ox' suffix and blue colour are used for the samples in this work. Red colour is used for SRV reported elsewhere, for which details are included in Figure 7. 128

Figure 62. Migration mechanisms for ionic charge into silicon dioxide. X indicates an alkali ionic specie while C indicates a corona ion. 131

Figure 63. TSIC experiment on 100 nm thermal oxide grown on FZ n-Si and deposited with 10^{14} cm^{-2} NaCl. Sample n5_x2p1. a. First ionic migration from M/O to oxide/silicon interface, b. Second ionic migration from oxide/silicon to M/O interface, c. Raw current and temperature data for the two cycles in the ionic migration pictured in (a), d. CV curves before first migration (blue) and after second migration (green). Green curve includes the up-sweep and down-sweep in potential. 133

Figure 64. Ion dynamics modelling for TSIC experiment on 100 nm thermal oxide grown on FZ n-Si and deposited with 10^{14} cm^{-2} NaCl. Sample n5_x2p1. a. Positive bias experiment, b. Negative bias experiment. 134

Figure 65. a. Concentration of ionic species in the oxide as a function of oxide thickness, for an oxidised FZ n-Si sample annealed at 450 °C for 18 minutes (Sample n14_6), b. Schematic of the model proposed for ion migration from one interface to the other....... 136

Figure 66. Concentration of (a) sodium and (b) potassium ions migrated to the oxide/silicon interface as a function of anneal time for a range of temperatures and times. (Different samples taken from wafer n14). 138

Figure 67. Surface potential for oxidised n-type FZ Si when Na and K ionic charge is migrated using drift and diffusion in a. One single 6 minute step, samples n7_1 and n7_3 respectively, control sample n7_6, and b. In three consecutive steps of 2, 4 and 4 minutes, samples n7_2 and n7_4 respectively, control sample n7_5. 141

Figure 68. Effective lifetime as a function of minority carrier concentration for samples deposited with 10^{14} cm^{-2} sodium and potassium chloride and then annealed at 450 °C for different time periods. Sodium deposited samples (closed symbols) were annealed for 0, 5 and 15 minutes, while potassium deposited samples (open symbols) for 0, 5, 10, 15 and 20 minutes. (Samples n9_2 and n10_2 respectively) 144

Figure 69. Effective lifetime as a function of annealing time for samples deposited with 10^{14} cm^{-2} sodium and potassium chloride/hydroxide and then annealed at 400 °C for different time periods. (Samples n2_1, 2_5 and control n2_8) 145

Figure 70. Effective lifetime for oxidised n-type FZ Si subjected to temperature anneals when no purposefully deposited ionic charge is present on the surface (control Sample n5_3). 145

Figure 71. Effective lifetime at a minority carrier concentration of 10^{15} cm^{-3} for samples deposited with sodium and potassium and then annealed at different temperatures for up to 100 minutes. NaCl samples n9_3,2,1,5 for diffusion at 400, 450, 500 and 550 °C and KCl samples n10_3,2,1,7, for diffusion at 400, 450, 500 and 550 °C. 147

Figure 72. Effective lifetime for oxidised n-type FZ Si when MgCl and CaCl ionic charge is migrated using diffusion (Samples n5_1 and n5_2 respectively) 148

Figure 73. Effective lifetime for oxidised n-type FZ Si when CsOH ionic charge is migrated using diffusion at 400 °C (Sample n4_5) 149

Figure 74. Effective lifetime for oxidised n-type FZ Si when Na and K ionic charge is migrated using drift and diffusion (samples n7_1 and n7_3 respectively, control sample n7_6) 150

Figure 75. Effective lifetime for oxidised n-type FZ Si when Na and K ionic charge is migrated using drift and diffusion in three consecutive steps of a. 2, b. 4 and c. 4 minutes. (Samples n7_2 and n7_4 respectively, control sample n7_5) 151

Figure 76. Effective lifetime for oxidised n-type FZ Si when ionic charge is diffused into the oxide using for a. NaCl (Samples n9_3,2,1,5 for diffusions at 400, 450, 500 and 550 ^{o}C) and b. KCl (Samples n10_3,2,1,7, for diffusions at 400, 450, 500 and 550 ^{o}C). 155

Figure 77. Effective lifetime for oxidised and HMDS treated n-type FZ Si when ionic charge is diffused at 400 ^{o}C into the oxide using NaCl and KCl (Samples n2_1 and n4_1). 155

Figure 78. Effective lifetime for oxidised n-type FZ Si when ionic charge is diffused at 400 ^{o}C into the oxide using MgCl (Samples n5_1) and CaCl (Sample n5_2). . 156

Figure 79. Surface potential and effective lifetime for oxidised n-type FZ Si when NaCl, a. Sample n7_1 and d. Sample n7_2, and KCl, b. Sample n7_3 and e. Sample n7_4, ionic charge is migrated into the oxide using corona drift and three diffusion steps. Control Samples c. n7_6 and f. n7_5 went through the same processing without ionic species. The top row samples were diffused in a single step for 6 minutes. Bottom row samples were diffused in three steps for 2, 4 and 4 minutes subsequently. 157

Figure 80. Effective lifetime for oxidised n-type FZ Si when K ionic charge is migrated using drift and diffusion on a specimen treated with FGA and HMDS (Sample n16_2, control sample n16_7) 158

Figure 81. Surface potential and effective lifetime for oxidised n-type FZ Si when KCl ionic charge is migrated using drift and diffusion on a. FGA and HMDS treated oxide (Samples n16_2, control sample n16_7), b. Non-FGA treated, but HMDS treated (Sample n2_4), c. FGA treated but not HMDS treated (Sample n16_1) and d. Neither FGA or HMDS treated (Sample n2_3). 159

Figure 82. Surface potential and effective lifetime for oxidised n-type FZ Si when K ionic charge is migrated into the oxide using a. drift and diffusion (Sample n17_2, control sample n17_6). Arrows indicate the order of the process. 160

Figure 83. Surface potential and effective lifetime for oxidised n-type FZ Si when a. Mg (Sample n6_1) and b. Ca (Sample n6_2) ionic charge is migrated into the oxide using drift and diffusion. 161

Figure 84. Summary of effectiveness and stability of passivation in oxides with diffused ionic charge. Effective lifetimes at the end of the measuring period are reported. The decay time constant is estimated between day 5 and the end of the period. * indicates that effective lifetime showed a rapid decay in the first 1-50 days followed by a slow decay. .. 163

Figure 85. Summary of effectiveness and stability of passivation in oxides with drifted and diffused ionic charge. Effective lifetimes at the end of the measuring period are reported. The decay time constant estimated between day 50 and the end of the period. Time quoted for the total length of the drift and diffusion process. 164

Figure 86. Passivated emitter, rear locally-diffused (PERL) cell geometry, including a double layer of oxide and antireflection coating, and front diffused contacts.................. 170

Figure 87. Back-junction back-contact (BJBC) cell geometry and its interdigitated contacts.. 171

Figure 88. PC1D device schematic for a front contacted p-type Si solar cell with surface charge, shunt and series resistance and a textured surface. 174

Figure 89. Cell performance when FEP is altered in the front surface by changing dielectric charge in a p-type front contacted cell.. 176

Figure 90. Cell performance when FEP is altered in the rear surface by changing dielectric charge in a p-type front contacted cell.. 176

Figure 91. AM1.5 cell efficiency when FEP is applied to the front and rear surface in a p-type front contacted cell for different a. base doping concentration, b. emitter doping concentration, c. BSF doping concentration, and d. cell thickness. Simulation parameters are those given in Table 6 unless specified in the figure labels. 178

Figure 92. Simulation domain and definition of regions for the IBC cell modelled in PC2D. 181

Figure 93. a. Dark saturation current in a model diode simulated in PC1D when surface charge is changed, b-d. Cell performance simulated in PC2D when FEP is altered in the front surface by changing J_{01} in a n-type IBC cell that includes a 253 **Ω**/sq FSF for passivation... 183

Figure 94. a. Dark saturation current in a model diode simulated in PC1D when surface charge is changed, b-d. Cell performance simulated in PC2D when FEP is altered in the front surface by changing J_{01} in a n-type IBC cell that does not include a FSF.. 184

Figure 95. Normalised V_{oc}, J_{sc} and P_{out} for two identical back-junction back-contact n-type silicon solar cells. The cells were submitted to 6 corona charging steps using a single point at 9 kV potential, 8 cm from the cell, each lasting 5 seconds. Normalisation values of V_{oc}, J_{sc} and P_{out} are included for each cell.. 187

Figure 96: a. Example of surface charge concentration calculated for three different assumed charge distributions in a 100/60 nm oxide/nitride double layer dielectric film, giving a -5 V insulator voltage. b. Change of gate potential as a function of a planar charge distribution situated at different positions in an $Al/Si_3N_4/SiO_2/Si$ system. 226

Figure 97: a. Capacitance-voltage measurement of an $Al/SiO_2/Si$ MIS capacitor for the upsweep (trace) and the down-sweep (re-trace). The red trace is the theoretically calculated capacitance for this MIS capacitor including the insulator charge, b. Oxide/silicon interface state density calculated using Terman's high frequency method......................... 229

LIST OF TABLES

Table 1. Summary of the samples used in this project. 29

Table 2. Parameters of the thermal oxidations carried out for this project. DCE: Dichloroethylene. 31

Table 3. Summary of samples used in this project. (T) stands for a textured surface. (F) stands for Forming Gas Anneal. 32

Table 4. Summary of activation energies and initial ion concentration found for ion dynamics in MOS and oxide/silicon systems. * Data from reference [202]. 139

Table 5. Estimated concentration of charged ions difussed into oxide films at different temperatures. Obtained from a combination of data in Figure 66 and Figure 71.. 162

Table 6. Cell parameters for PC1D simulation 174

Table 7. Simulation parameters for back contact cell modelled in PC2D.............. 182

Table 8. Summary of performance improvements in IBC cells deposited with positive corona charge... 192

CHAPTER 1
INTRODUCTION

1.1 Climate change

The variations in climatological conditions the planet is presently undergoing are globally accepted as Climate Change [1]. Emission of greenhouse gases, primarily caused by the increasing use of fossil fuels, has caused a disruption in the climate system of our planet. Greenhouse gases reflect the infrared radiation emitted by the earth during its cooling process after having absorbed solar radiation. Effectively, greenhouse gases trap the heat released by the earth, which then makes the earth warmer. Such gases include carbon dioxide, methane, and nitrous oxide. Carbon dioxide (CO_2) is by far the most produced greenhouse gas. Its concentration has increased 40% in the last two centuries, primarily due to the use of fossil fuels since the industrial revolution [2]. The concentration of all greenhouse gases, however, has reached unprecedented levels since, at least, the past 800,000 years [2].

Global warming is a frequently used term that describes the consequences of climate change. The accumulation of greenhouse gases in the atmosphere has provoked an average combined land and ocean temperature rise of 0.85 °C over the period 1880 to 2012 [2]. This warming has produced severe weather and climate events such as increased heat waves, abnormal and heavy precipitation, droughts, decrease in snow cover, and the rise of sea level due to the increased loss of mass from glaciers and ice sheets [2]. These events endanger the

survival of the human race, and are already starting to show their harmful effects [3], with billions of pounds already spent on damage repair [4].

Currently, the world's annual energy demand is 152 PWh [5]. This number is expected to grow by 56% between 2010 and 2040 [6], therefore setting a real challenge to the generation and use of energy over the next decades. Strong and long-term economic growth will be the main driver of this increasing energy demand [6]. It will be localized in countries outside Europe and North America, particularly those today known as the BRICS countries [7], thus shifting the attention in policy making and empowerment to the East. Despite this, several western countries have grouped under the Organisation for Economic Co-operation and Development, and are actively engaged in plans for climate change mitigation [8], [9].

The vast majority of the world's CO_2 emissions result from the production and use of energy [1]. The landscape for the reduction of fossil fuels in energy generation is demoralising [7]. Greenhouse gases will therefore continue to be emitted and this will cause further warming and more devastating consequences to the already disrupted climate system. Limiting climate change requires a drastic change in energy sources. Renewable energy sources hold real promise for future carbon free energy generation as explored below.

1.2 Renewable energy sources and silicon photovoltaics

The world's energy supply is currently undergoing one of the most dramatic changes seen since the industrial revolution. The exhaustion of fossil fuels and the alarming consequences of climate change have set the challenge of shifting to reliable and sustainable sources of energy. Major 'clean' energy sources include solar, wind, water and biomass. They have immense potential thanks to their vast availability, see Figure 1. This potential is already

being exploited, with over 19% of global energy demand being supplied by renewables in 2011 [10]. The total power capacity from renewable sources exceeded 1470 GW in 2012, which accounts for an increase of about 8.5% from 2011 [10]. Hydro, biomass, geo and solar thermal energy are the main sources used at present, as pictured in Figure 2.a. The main deployment however, has been on wind, hydro and solar PV energy, which from 2011 to 2012 accounted for 39%, 26% and 26% of the renewable added power capacity [10].

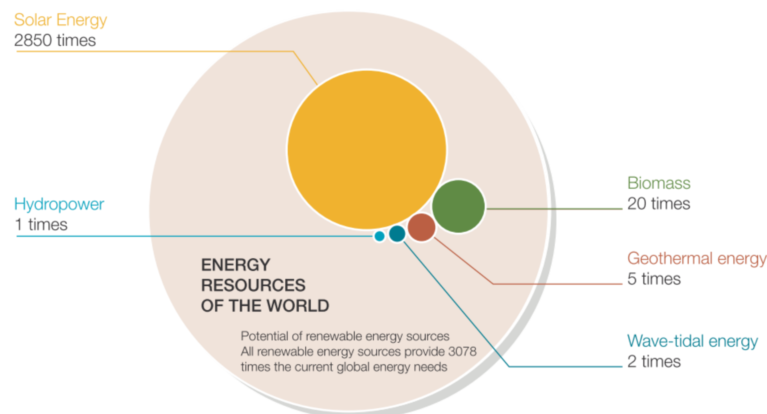

Figure 1. Energy Resources of the World. “These constant flows of energy amount to about 3,000 times the total present day energy consumption of the whole of mankind”. After [11].

The European Renewable Energy Council has set out a vision for a 100% renewable energy system in Europe by 2050 [11]. For this to happen, an increase of more than 80% will be necessary in the deployment of renewable energy sources in the next 40 years [11]. The International Energy Agency has set out a similar vision, where 79% of the global electricity demand is supplied by renewables by 2050 [12]. They have outlined this pathway by suggesting the potential technological mix required for global sustainable energy consumption. By 2050, a strong contribution of wind, hydro, and solar photovoltaic (PV) is expected, with PV providing 16% of global electricity –i.e. ~6400 TWh/yr, see Figure 2.b. Several of these clean energy technologies are already available but some are still undergoing strong development. Solar PV and onshore wind power, for example, have experienced strong price reductions in the last 10 years due to technological advances, economies of scale and surplus production, especially coming from manufacturing in China

[10]. These technologies are expected to play a key role in the energy scenario of the world over the next century.

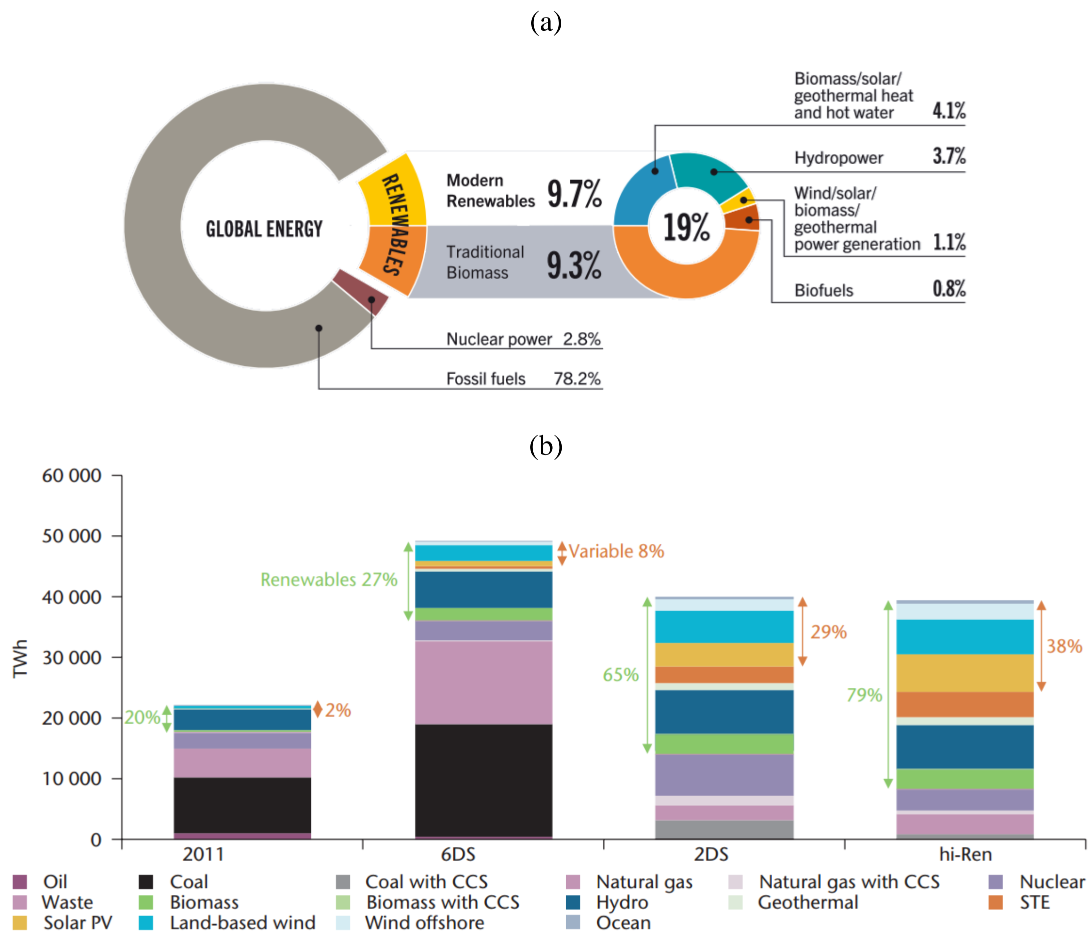

Figure 2. a. Estimated renewable energy share of global final energy consumption at 2011. After [10]. b. Global electricity mix in 2011 and in 2050 in three ETP 2014 scenarios proposed by the International Energy Agency, after[12].

Amongst this varied mix of renewable energies, solar power is one of the most abundant and environmentally favourable sources (Figure 1). Solar energy is now being exploited thanks to the advances in photovoltaic (PV) research and industry in the last two decades. The PV industry is now one of the fastest growing, with over 140 GW of installed capacity at 2015, and a five-year average growth rate exceeding 40% [10]. Europe has established a strong position in the advancement and deployment of renewable energy sources. At 2012, for the second year running, the EU installed more PV energy than any other electricity-generating technology [10]. Even more, Solar PV is expected to supply up to 12% of the electricity demand in Europe by 2020 [9]. It has enormous benefits including a

direct reduction of CO_2 emissions from power generation, long-term energy security , technology leadership and job creation, possibility for decentralised electrification, and reduced energy payback time [9]. Solar PV is therefore a key technology to provide the world with renewable, inexpensive and reliable energy.

The solar energy market is strongly dominated by **silicon** based PV. This technology today accounts for over 80% of the PV market [13], and it has shown enormous technological advancements in the last decade with 24% efficient crystalline silicon (c-Si) solar cells now available in the market [14]. Current developments in silicon PV aim to obtain cleaner and better feedstock material, reduced material use per cell, enhanced module performance and reliability, smarter interconnections, inverters and grids, and better cell performance with lower-cost processing. These developments will guarantee that Silicon PV continues to be a remarkably successful technology. The outlook of Silicon PV as potential and substantial source of renewable energy is extremely promising.

1.3 Silicon solar cells and carrier recombination

1.3.1 Solar cell fundamentals

A solar cell is a device that converts light energy into usable electric energy. Charles Fritts constructed the first intentionally made solar cell in 1883 [15]. However, research on photovoltaic devices only started to grow when, in 1954, Pearson, Fuller and Chapin created a 6% efficient silicon solar using the concept of a semiconductor pn junction [16].

Typical silicon solar cells normally consist of a p-n+ junction, a metal rear contact, a front contact, and an anti-reflection front layer. This is illustrated in Figure 3, along with a representation of how photo-excited carriers can be collected at the metal contacts and hence be used to supply electrical energy.

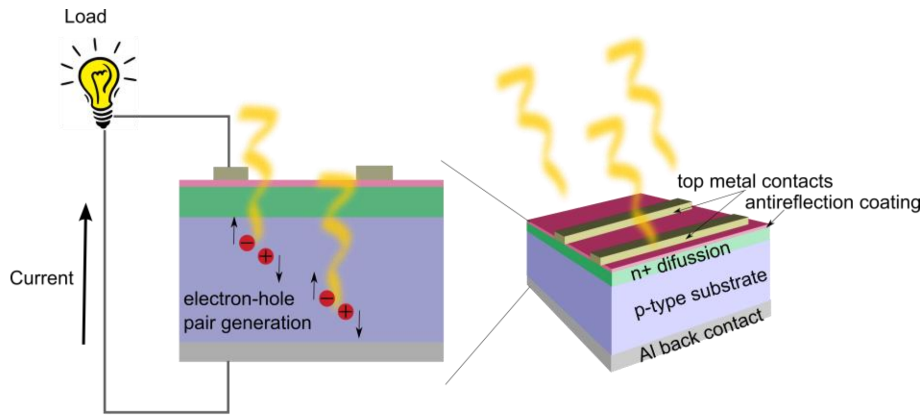

Figure 3: Schematic of a conventional silicon solar cell illustrating electron-hole pair generation.

Silicon solar cell operation is described by the pn junction theory, originally developed by Shockley [17], but later modified to account for additional semiconductor phenomena [18], [19]. Absorbed photons can create electron-hole pairs (EHP) in all regions of a cell, but they will only create a photocurrent in the external circuit if the minority carriers cross the junction. For this to happen, the minority carriers must diffuse from where they are created to the junction without recombining with majority carriers. One way in which EHP can recombine is via intermediate band-gap energy levels or defect centres, produced by crystallographic defects and impurities [20]. Interfaces in a solar cell often produce band gap energy levels that act as centres for recombination. Figure 4 illustrates how photo-excited minority carriers are collected, and how a band-gap state in the p-type region can mediate EHP recombination. The different mechanisms by which this process can take place are explored next. It is emphasised here that a key requirement in achieving high energy conversion efficiency is to minimize the loss of charge carriers due to recombination.

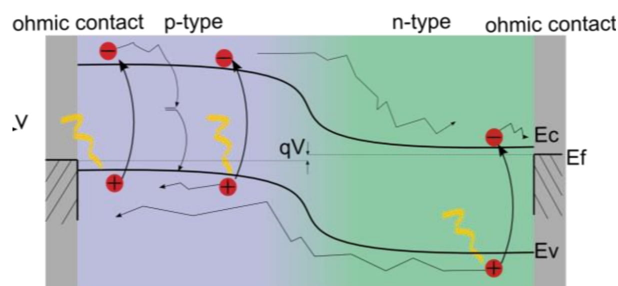

Figure 4: Electron-hole pair generation, collection and recombination in a solar cell.

1.3.2 Carrier recombination in crystalline silicon

The term recombination indicates all the mechanisms by which an electron can make a transition from the conduction band (CB) to the valence band (VB), thus eliminating a previously created electron-hole pair. In thermal equilibrium, there are no net transitions of carriers in the band gap since the thermal generation rate of EHP equals the recombination rate, and the electron(hole) carrier concentration $n_0(p_0)$ of n-type and p-type silicon can be defined as:

$$n_o = N_D, \;\; p_0 = \frac{n_i^2}{n_0}$$
$$p_0 = N_A, \;\; n_0 = \frac{n_i^2}{p_0} \qquad (1.\ 1)$$

assuming full ionization of dopants. N_D represents the donor concentration while N_a represents the acceptor concentration. The present work is focused on n-type silicon hence only equations relevant to n-type material will be presented.

When additional carriers are injected from the VB to the CB, for instance by incident light of sufficient energy, recombination mechanisms provide the means by which the excess carriers $\Delta n = n_b - n_o$ and $\Delta p = p_b - p_0$ are reduced, and the equilibrium restored. Here n_b and p_b represent the bulk carrier concentrations in steady state.

The semiconductor continuity equations describe the carrier dynamics in a semiconductor. For the one-dimensional case, in the absence of electric fields and carrier concentration gradients, the temporal change in minority carrier concentration is given by [20]:

$$\frac{\partial p}{\partial t} = G_p - R_p \qquad (1.\ 2)$$

or equivalently, using the recombination only caused by excess carriers, or net recombination:

$$\frac{\partial \Delta p}{\partial t} = -U_p(\Delta p, n_0, p_0). \tag{1. 3}$$

It is common to assume low level injection in semiconductors such that U is not a function of Δp. In such cases the solution to equation (1. 3) is a mono-exponential decay with time constant τ defined as:

$$\tau \equiv \frac{\Delta p}{U} \tag{1. 4}$$

τ is termed the minority carrier lifetime. In physical terms, τ is the average time a minority carrier exists before recombination, and it is related to the distance it travels, L, according to:

$$L = \sqrt{D\tau} \tag{1. 5}$$

where D is the minority carrier diffusion coefficient and L the minority carrier diffusion length.

Although the low level injection assumption is not normally the case in silicon solar cells, this definition of minority carrier lifetime (τ) is widely used since it holds for multi-exponential decays, and it helps interpret the contribution of different mechanisms towards carrier recombination. The total net recombination rate is a sum of individual and independent mechanisms. They arise from bulk and surface physical processes explored in the following subsections.

1.3.3 Bulk recombination

Bulk recombination comprises the contribution of intrinsic and extrinsic processes. Intrinsic recombination is present in all semiconductors, while extrinsic recombination is related to the impurities and defects in the crystal. Electrons can transfer energy, and decay back into the valence band by two intrinsic physical processes: energy can be released as a photon in a radiative process, or it can be transferred to another carrier by a thermalisation process.

These processes are known as radiative recombination and Auger recombination. Radiative recombination has very small influence on silicon since it is an indirect semiconductor [21].

Extrinsic recombination happens via energy states in the band-gap, which are the product of crystallographic defects and impurities. Such recombination is best characterised using Shockley-Read-Hall statistics, and hence it is known as Shockley-Read-Hall recombination [22].

Since total recombination is the sum of independent recombination rates, the total lifetime is the reciprocal sum of independent lifetimes:

$$\frac{1}{\tau_B} = \frac{1}{\tau_{Rad}} + \frac{1}{\tau_{Aug}} + \frac{1}{\tau_{SRH}}. \quad (1.6)$$

1.3.3.1 Radiative recombination

Recombination mediated by photon emission is of minor importance for indirect semiconductors like silicon. The process involves the additional participation of a phonon since an electron has to make a change in both energy and momentum when transferring from the conduction to the valence band. The net radiative recombination rate depends on the concentration of both electrons and holes:

$$U_{Rad} = B\left(n_b p_b - n_i^2\right). \quad (1.7)$$

The resulting radiative carrier lifetime is:

$$\tau_{rad} = \frac{1}{B(n_0 + p_0 + \Delta p)} \quad (1.8)$$

where B is the band-to-band recombination coefficient found by Gerlach et al to be 1 x 10^{-14} cm^3s^{-1} [23].

1.3.3.2 Auger recombination

Auger recombination is a three-particle process in which the energy released by the transition of an electron from the conduction to the valence band is transferred either to a neighbouring

electron in the CB, or a neighbouring hole in the VB [24]. The first process is characterized by the presence of two electrons and one hole (eeh) so that recombination is proportional to n^2p, while the second process requires one electron and two holes (ehh) and the recombination is proportional to p^2n. The net Auger recombination is then given by the sum of both processes:

$$U_A = C_n\left(n_b^2 p_b - n_0^2 p_0\right) + C_p\left(n_b p_b^2 - n_0 p_0^2\right) \tag{1. 9}$$

where C_n and C_p are the Auger coefficients for eeh and ehh processes, respectively. They were first suggested to be constant values by Dziewior and Schmidt [24]. However, subsequent experimental observations discovered an enhancement of Auger recombination at low carrier densities (10^{13}-10^{16} cm^{-3}). Today, Hangleiter and Häcker's theory of Coulomb-enhanced (CE) Auger recombination is widely accepted [25]. They suggest that under low injection conditions (LLI), the Auger coefficients are scaled by enhancement factors:

$$U_{A,LLI} = g_{eeh} C_n\left(n_b^2 p_b - n_0^2 p_0\right) + g_{ehh} C_p\left(n_b p_b^2 - n_0 p_0^2\right) \tag{1. 10}$$

A complete model including high level injection was suggested by Glunz et al [26], in which new Auger coefficients are defined as a function of $g_{eeh}, C_n, g_{ehh}, C_p, n_0, p_0$ and Δp, using Altermatt's parameterisation of the enhancement factors for LLI [27]. However, the most recent and accepted parameterisation of Coulomb enhanced Auger recombination has been proposed by Richter et al [28], where by fitting data collected using different passivation methods and differently doped silicon wafers, they suggested a dopant and injection level dependent Auger lifetime:

$$\tau_{ceA} = \frac{\Delta p}{(n_b p_b - n_{ieff}^2)(2.5\,x10^{-31} * g_{eeh}\, n_0 + 8.5\,x10^{-32} g_{ehh} p_0 + 3\,x10^{-29} \Delta p^{0.92})} \tag{1. 11}$$

with

$$g_{eeh} = 1 + 13\left\{1 - \tanh\left(\left(\frac{n_0}{N_{0,eeh}}\right)^{0.66}\right)\right\}$$

$$g_{ehh} = 1 + 7.5\left\{1 - \tanh\left(\left(\frac{p_0}{N_{0,ehh}}, eeh\right)^{0.63}\right)\right\} \quad (1.\ 12)$$

$$N_{0,eeh} = 3.3\ x10^{17} cm^{-3}, N_{0,ehh} = 7\ x10^{17} cm^{-3}$$

1.3.3.3 Shockley-Read-Hall recombination

Crystallographic defects, such as impurities, vacancies and dislocations, place energy levels in the otherwise forbidden band-gap in silicon. Such energy levels act as effective mediators by which electrons can transit from the conduction to the valence band, and are therefore referred to as recombination centres. The recombination rate of such processes was first described by Shockley and Read [22] and later complemented by Hall [29]. They developed a statistical model to describe the defect associated recombination rate as a function of the recombination centre density N_t, its capture cross section for holes and electrons $\sigma_{n,p}$, i.e. the area around a trap in which a carrier has a high probability of being captured, and the energy level of the recombination centre E_t:

$$U_{SRH} = \frac{n_b p_b - n_i^2}{\frac{p_b + p_1}{N_t \sigma_n v_{th}} + \frac{n_b + n_1}{N_t \sigma_p v_{th}}} \quad (1.\ 13)$$

where v_{th} is the thermal velocity such that carriers sweep a volume $\sigma_{n,p} v_{th}$, and p_1, n_1 are the carrier concentrations in the traps:

$$p_1 = n_i e^{\frac{E_i - E_t}{kT}}$$

$$n_1 = n_i e^{\frac{E_t - E_i}{kT}} \quad (1.\ 14)$$

Using equations (1. 4) and (1. 13), the Shockley-Read-Hall lifetime can be defined as:

$$\tau_{SRH} = \frac{\tau_{p0}(n_0 + n_1 + \Delta p) + \tau_{n0}(p_0 + p_1 + \Delta p)}{p_0 + n_0 + \Delta p} \quad (1.\ 15)$$

where $\tau_{n0} = (N_t \sigma_n v_{th})^{-1}$ and $\tau_{p0} = \left(N_t \sigma_p v_{th}\right)^{-1}$ are termed the capture time constants for electrons and holes, and are a measure of the “intrinsic” strength of a particular type of trap state to capture electrons or holes. Note that the *actual* capture of carriers will depend not only on this “intrinsic” strength but also the occupation of traps, the material doping level, injection conditions and other experimental variables. Figure 5 illustrates the calculated Shockley-Read-Hall lifetime for 1 Ωcm n-type silicon and three different trap energies. Here, lifetime has been normalised by the capture time constant of the minority (holes) carrier. The strength of a recombination deep centre is evident when $E_t - E_V$ =0.5 eV. At low injection levels the majority carrier capture time constant is of little importance. Recombination is dominated by the minority (hole) carrier capture strength as illustrated by the dotted curves in Figure 5.

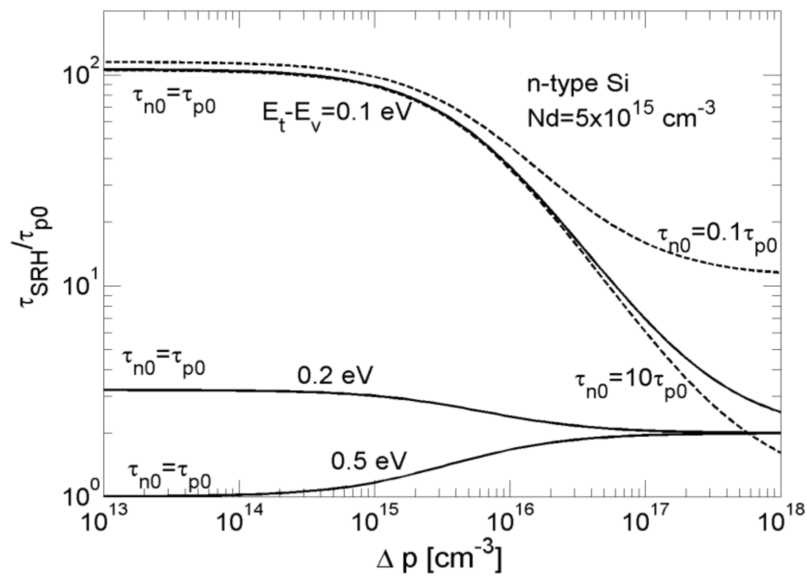

Figure 5: Calculated defect related bulk lifetime as a function of excess minority carrier concentration for a shallow ($E_t - E_v = 0.1\ eV$), medium ($E_t - E_v = 0.2\ eV$), and deep ($E_t - E_v = 0.5\ eV$) recombination centre. Lifetime is calculated using Shockley-Read-Hall statistics on equation (1. 15). T=300 K.

1.3.4 Surface recombination

The surface in a semiconductor is an abrupt crystal discontinuity. In a bare silicon surface, many atoms may be partially bonded and hence they leave dangling bonds that create intermediate band-gap energy levels, also known as surface energy traps or surface states

[20]. In general usage, the term 'surface' refers to a solid-air interface. However, in practical solar cells, bare silicon surfaces are not present and recombination actually takes place at interfaces between the semiconductor and other materials. Even so, it is standard practice to refer to this as surface recombination and the concept of "surface" states is still applicable.

The effectiveness of a surface as a site for recombination can be characterised by the parameter

$$S_0 \equiv \frac{U_s}{\Delta p} \tag{1. 16}$$

normally expressed in units of centimetre per second, and thus referred to as the surface recombination velocity (SRV). U_s indicates the surface recombination rate in $cm^{-2}s^{-1}$. The lower its value the less recombination happens, and the better a surface is from the point of view of solar cell efficiency. SRV depends on doping concentration, injection level and doping type as will be expanded in Chapter 3. An important distinction needs to be made between surface and bulk recombination. In thermal equilibrium, the energy bands are flat throughout the semiconductor (for uniform doping and defect density). However, in practical semiconductors, a space charge region (SCR) is normally present at the surface, thus creating a small region where the conduction and valence bands bend due to charge near or trapped at the interface. In general, recombination happening in the SCR originates from surface induced defects and is included in the surface recombination velocity parameter. For this purpose, recombination that takes place within the band-bent region is considered a component of surface recombination, and recombination in a flat-band region is considered bulk recombination. A more general definition of SRV is then:

$$S_{eff} \equiv \frac{U_{z<d_{scr}}}{\Delta p_{d_{scr}}} = S_0 + S_{d_{scr}} \tag{1. 17}$$

where the z axis is perpendicular to the semiconductor surface and increases towards the bulk, with d_{scr} being the edge of the space charge region. $S_{d_{scr}}$ represents the

recombination taking place in the SCR while S_0 only includes recombination at the true surface.

1.4 Silicon surface passivation

The term "surface passivation" covers all the physical and chemical processes carried out to a semiconductor's surface in order to reduce the surface recombination rate. There are two independent approaches to passivate silicon surfaces [21]:

1. An optimisation of the "chemical" interface properties by forming bonds between silicon and a different material. This reduces the number of defect states at the surface.
2. Reduction of the available carrier concentration. Recombination requires the presence of both electrons and holes. It then follows that a reduction in the surface carrier concentration of either carrier type results in a reduction of SRV. This method is normally known as field effect passivation (FEP) since it uses an electric field to repel one type of carrier from the surface.

The SRV of a silicon surface can often be reduced by using a dielectric or semiconducting coating. This results in a portion of the dangling bonds at the coating-silicon interface being eliminated by the formation of covalent bonds with oxygen, nitrogen, or silicon atoms in the coating layer. Hydrogen atoms in the coating can further reduce SRV by bonding with many of the dangling bonds that may remain at the coating-silicon interface. Both these effects can be considered chemical effects.

Since charge carriers are susceptible to electric fields, two independent techniques can be used to repel either type of carriers from the surface. Firstly, the implementation of a doping profile within the silicon, at the surface, builds in an electric field due to the gradient of the doping concentration. Secondly, field effect passivation can be implemented by

installing an electric field in the dielectric coating using fixed charges associated with the dielectric. Such a field penetrates into the semiconductor, repels like charges and so depletes the semiconductor surface of one kind of carriers [21]. The latter is shown schematically in Figure 6.

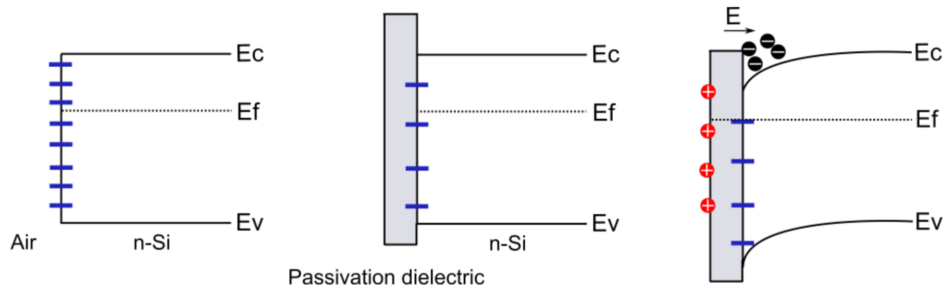

Figure 6: Schematic diagram showing surface states in a. bare silicon b. chemically passivated silicon and c. chemically and field effect passivated silicon.

1.4.1 Dielectric films

Thermal oxidation of silicon is a basic method, originally developed by the microelectronics industry, to passivate silicon surfaces. Thermally grown silicon dioxide (SiO_2) provides very low surface state densities of the order of 10^9 $cm^{-2}eV^{-1}$ [30]. However, this technique requires temperatures above 900 ^oC, making it undesirable in terms of solar cell production cost and throughput [30]. The lowest SRV reported for thermal oxide (before this work) is 2.5 cm/s at an injection level of $10^{15}cm^{-3}$, on float zone 1.5 Ωcm n-type silicon [26], [31].

For the last decade, the industry standard for cell passivation has been a layer of plasma enhanced chemical vapour deposition (PECVD) silicon nitride (SiN_x) [32]–[34]. The excellent surface passivation of SiN_x is due not only to a chemical reduction in the density of interface states and their capture cross section, but also its high concentration of fixed positive charges. Thus, the passivation effect of these films is both chemical and field effect in origin. The lowest SRV reported using remote PECVD SiN_x is 1.26 cm/s at an injection level of 10^{15} cm^{-3}, on float zone 1 Ωcm n-type silicon [28].

In practice, many dielectric coatings already have built-in electrostatic charges, so that field effect passivation is already exploited in a variety of films [17], yet in a non-

optimised way. SiN_x has two technologically important advantages over other films: its refractive index makes it an excellent anti-reflective coating; and the high hydrogen content of PECVD SiN_x deposited layers provides additional chemical passivation of the interface with the silicon, and even provides some passivation of bulk defects as the hydrogen diffuses into the silicon cell [17].

Some of the best and most researched passivation techniques reported to date include:

- The so called 'Alneal' [35]: A layer of 100 nm of aluminium is deposited on top of thermal SiO_2 and annealed in forming gas for a period of 30 minutes. It is hypothesised that atomic hydrogen from residual water at the Al-SiO_2 interface diffuses and binds to silicon surface atoms at the Si-SiO_2 interface, thus passivating the semiconductor surface to levels as low as 2.4 cm/s on 2.5 Ωcm n-type Cz-Si [35]. This process is time and resource consuming therefore it has never been used by industry.
- A double layer of thermally grown or CVD deposited SiO_2, and PECVD SiN_x [36]–[38]. It combines the good chemical passivation of silicon dioxide with the field effect passivation of silicon nitride. It has been shown to produce a SRV as low as 3.2 cm/s on 2.5 Ωcm n-type Cz-Si [39]. This approach, when industrially implemented, is the workhorse of solar cell passivation to date.
- Atomic layer deposition (ALD) of aluminium oxide (Al_2O_3) has proved to have a high interface fixed negative charge density capable of reducing SRV in 1 Ωcm n-type silicon to 1-10 cm/s [40]–[42]. ALD is an expensive and slow process and only recently a modification of the ALD process, namely spatial ALD, has been used at industrial level [43], [44].
- Double layers of hydrogenated PECVD amorphous silicon and silicon dioxide have shown SRV below 1 cm/s on 3 Ωcm n-type Si [45]–[48].

As a reference benchmark for the results obtained in this thesis, Figure 7 illustrates some of the best passivation technologies available at research level. It evident here that SRV below 10 cm/s are reasonably good, and those < 1 cm/s are outstanding.

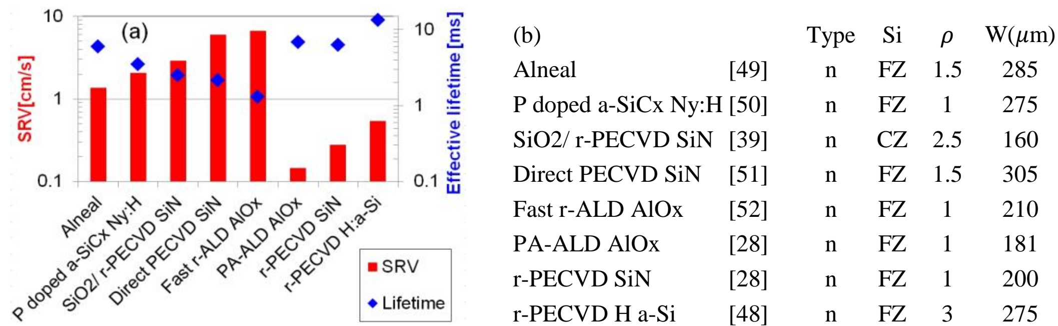

(b)

		Type	Si	ρ	W(μm)
Alneal	[49]	n	FZ	1.5	285
P doped a-SiCx Ny:H	[50]	n	FZ	1	275
SiO2/ r-PECVD SiN	[39]	n	CZ	2.5	160
Direct PECVD SiN	[51]	n	FZ	1.5	305
Fast r-ALD AlOx	[52]	n	FZ	1	210
PA-ALD AlOx	[28]	n	FZ	1	181
r-PECVD SiN	[28]	n	FZ	1	200
r-PECVD H a-Si	[48]	n	FZ	3	275

Figure 7: a. Record passivation quality obtained using state-of-the-art techniques, b. Specimen characteristics including references.

1.4.2 Surface doping

A doping profile is one of the methods by which the concentration of one type of carriers at the surface can be reduced. When it is used on the cell's rear side passivation, this scheme is known as back surface field (BSF). When it is used on the cell's front side, it is called a front surface field (FSF) or floating junction.

The BSF adopted its name from the process of firing aluminium into p-type silicon. This technique was proposed by Mandelkorn in 1972 [53], [54], and it comprised an aluminium deposition on p-silicon, followed by a 800-900 ^{o}C heating step that melted the aluminium and drove it into the silicon creating a p+p junction on the rear surface of the solar cell. This junction provided low values of contact resistance and reduced recombination since an electric field was formed at the surface so that electrons were repelled while holes were collected.

Floating junctions are n+p or p+n diffusions formed on the front of the cell, where the outer most material is not electrically connected to the cell, and is therefore floating. This concept has just recently begun to be exploited in research and for industrial solar cells that have all their electrical contacts on the back [55], [56]. If the active region of the junction is

created sufficiently close to the surface, the minority carriers of the outer most layer will be depleted and the surface recombination rate will be reduced [21].

One important consequence of using BSF or floating junctions, is the fact that an increase in the doping concentration produces an increase in the amount of bulk Auger recombination. A trade-off is normally achieved between the two components by using doping concentrations of 10^{17}-10^{19} cm^{-3}, and always $<10^{20} cm^{-3}$ [33].

1.4.3 Controlled field effect surface passivation

A drawback of CVD SiNx passivation is the trade-off between fixed charge for field effect passivation and refractive index for antireflection. CVD SiNx deposition has to be very well controlled to achieve the best of both, and it yet does not work as well on n-type silicon as it does on p-type, yet the former is the main candidate for future solar cells designs [57].

It is well known that SRV values as low as 30-70 cm/s can be achieved on n and p Si wafers with resistivity ≥ 1 Ωcm, by transferring charge in negative CO^{-}_{3} and positive $(H_2O)H^+$ ions to a dielectric film, using a corona charging apparatus [58]–[61]. Previous research has demonstrated the improvement of SRV with charge concentration [26], [62], mainly due to net electronic charge deposited on the film [63]–[65]. However, very little research has gone into the charge storage mechanism, its stability and alternative mechanisms [64], [66], [67]. Consequently, controlled field effect passivation has never been commercially used since the effect of the charges only lasts from a few hours to a few days, and their stability with respect to UV irradiation is rather poor [17].

1.5 Aim of this work

Previous sections have shown how unwanted recombination of photo-excited carriers at the interfaces present in solar cells is a major limiting factor in overall efficiency [2], [3]. Currently, industrial solar cells are passivated with a single or double layered dielectric

coating that provides both chemical and field-effect passivation simultaneously. In addition, when used on the cell's front surface, the film thickness and chemistry is adjusted to tune its optical properties, but industrially deposited films rarely optimise all three. This is because it is very difficult to control the deposition parameters finely enough to maintain good chemical and field effect passivation while also achieving the optimum refractive index and low parasitic absorption to obtain ideal optical properties. ***Intrinsic*** passivation by both chemical and FEP mechanisms – i.e. that obtained during dielectric film growth, is therefore somewhat limited. ***Extrinsic*** passivation, obtained *after* film deposition, uses atomic species and externally added charge to provide enhanced chemical and FEP. The use of extrinsic passivation thus allows more flexibility in the combined optimisation of the optical properties and the chemical and field effect passivation properties of dielectric films on semiconductors.

Extrinsic passivation has been previously demonstrated but its lack of stability has been the overriding issue preventing it from being adopted in real device manufacturing. The overall aim of this project is to stabilise the improvements given by extrinsic FEP of dielectrics to the 30 year timescale – the life cycle of commercial solar cells. A new approach to controlled and stable extrinsic FEP is proposed in the context of this project. This involves the introduction of permanent charge by "quenched in" ions in the dielectric film. The science developed in this work aims to further the understanding of charge carrier dynamics at semiconductor interfaces, and overall, it can translate into an improvement in the conversion efficiency and cost of silicon solar cells. In particular, solar cells where the contacts are at the rear side, and that perform 20% (relative) more efficiently than front contact cells [70], will benefit from this further improvement in passivation efficacy and cost. An additional goal is to generate a dielectric coating which will not only give enhanced field-effect passivation of the solar cells surface for periods of decades, but also allow an independent selection of the best refractive index film for antireflection, and the best charged film for field effect passivation.

Charged dielectric films are known as electrets since they exhibit a quasi-permanent electrical charge. The charge may consist of a net absence or excess of electrons on the dielectric constituent atoms, a net polarization of the film, or the presence of ionic species within the film matrix [71]. This concept is illustrated in Figure 8.

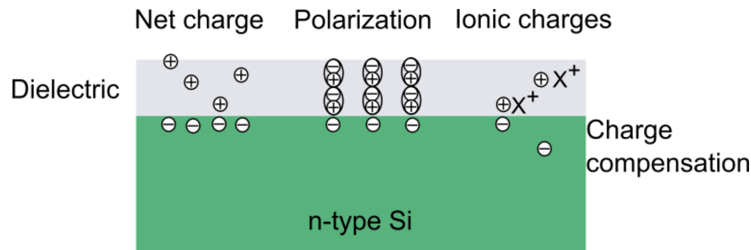

Figure 8: Scheme of electret charge storage via ionic charges and polarized molecules on a dielectric film on silicon.

Charge in electrets may occur inherently in some polymers and biological materials. However, electrets are often formed by the external injection of charge using discharges, particle beams, contact electrification, or injection from a deposited metal at high fields [71]. Internal injection of carriers is also possible via heat, or photo injection, but such techniques can physically degrade the dielectric. Film polarization has previously been found to be unstable [72]–[74] and it is hence of no interest for this work. In the following section the current understanding on charge deposition and migration in insulating films is detailed. Especial attention is given to silicon dioxide, as it is the model dielectric system used in this project.

1.6 Background science

1.6.1 Corona discharge

The term corona discharge refers to the electrical conduction path formed between two electrodes due to the ionization of molecules in the dielectric media surrounding one of them. Such discharge requires a very high electric field near one of the electrodes [75]. This is normally achieved using a sharp point at a high potential (5-10 kV). Corona discharge differs from dielectric breakdown, or sparking, in the nature of the conducting path. When a

dielectric breaks down, a series of ionized atoms creates low resistance conduction path for electrons to flow instantly between the two electrodes. In a corona discharge, molecules near the electrode ionize upon contact with the electrode. They create a local conduction region that reduces the magnitude of the electric field near the electrode. Atoms then slowly scatter and drift towards the second electrode; in their path, they scatter and transfer charge to other molecules until they are neutralized at the opposite electrode [75], thus creating a high resistance conduction path between the two [76]. Figure 9 shows its typical configuration. A sharp metal needle, often tungsten or stainless steel, is set to a 5-10 kV potential at a distance (typically ~ 5-10 cm) from the sample.

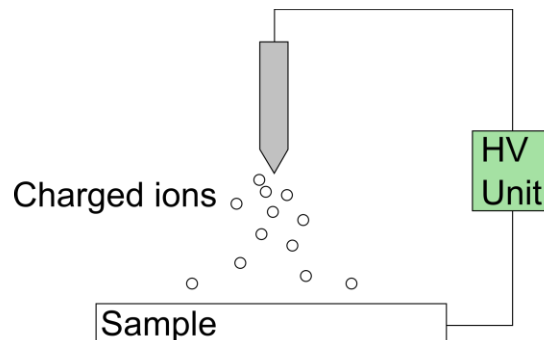

Figure 9: Schematic of a point-to-plane corona discharge apparatus. High potential on the sharp needle cause ionization of surrounding molecules, which in turn drift towards the lower potential electrode.

The dielectric media or fluid is normally air, oxygen or an inert gas. The ionization formed near the electrode forms a plasma with a corona-like shape, hence the technique's name. Corona charge is widely used in applications from ozonizers, air filters and surface treatment for adhesion and coating [76], [77], to electrochemical reactors and semiconductor characterization [78], [79]. Corona discharges of both polarities are possible, yet their physics are very different. On a positive corona, the reaction is maintained by the generation of secondary electrons between ionized and non-ionized molecules at the edge of the local plasma region. The electrons travel inwards to the high potential electrode, and hydrated $(H_2O)H^+$ molecules mainly compose the outwards charge flow [75], [80]. On a negative corona, the generation of secondary electrons is achieved by photoelectric escape of

electrons from the electrode itself. Such electrons run outwards from the high potential point and create CO^{-}_{n} ions, which compose most of the negative charge flow [80].

1.6.2 Field assisted ion drift in solids

Ion drift producing conduction in solids has been known since 1838, when Faraday discovered conduction of electricity in PbF_2 and Ag_2S [81], and later Warburg proved the mobility of Na^+ ions in glass [82]. Ever since, ionic conductors have been used as solid electrolytes in applications from batteries and fuel cells to gas sensors [83].

One of the first occurrences in which ionic drift/conduction in glass was used to purposely establish an internal electric field on a material was electrostatic or anodic bonding, also known as Mallory bonding thanks to its inventor [84]. Anodic bonding is a technique used to join glass to a metal or semiconductor substrate, and is relevant to the present project since it uses a quasi-stable electric field in a dielectric material. It has had great success due to its use at temperatures well below the softening point of the glass. Applications include package sealing, encapsulation, device mounting, pressure transducer manufacture and heat sink manufacture [85].

In electrostatic bonding, the two material surfaces are smoothed to micrometre level roughness. They are brought in contact in a metal-glass-substrate sandwich structure, and an electric field is applied across the glass, with the substrate (a metal or semiconductor) at a higher potential. The structure is then heated to a temperature at which ionic conduction starts to take place. At this point, ions in the glass (mostly H^+ and Na^+ [86]) start to drift towards the metal electrode (lower potential). A depletion of positive ions is formed at the glass-substrate interface region due to the ionic conduction. The changes in the glass composition in this region produce a region of O^- ions, which then drift and form covalent bonds with the substrate atoms, and the materials are joined together. This process leads to a permanent chemical bond at the glass/substrate interface using an intermediary oxide layer [87]–[90].

Electrostatic forces in this process are only mediating the ionic drift process. They allow the depletion region to be formed so that oxygen ions can be pulled to the interface, and creates compression of the two surfaces while the bonds are formed [87]. The stability of such electrical fields has never been the subject of study since the bond is chemical in essence and therefore very stable. However, various studies have confirmed the movement of ions in an amorphous silicon dioxide matrix at temperatures below 400 ^{o}C [86]–[90].

In a similar process, Cattaruzza et al [91] demonstrated doping of silicon dioxide using a solid-state field-assisted technique. They doped silica glass with Ag and Au ions by subjecting a metal/ion-supplier/silica/metal structure to 400 ^{o}C, while biasing with an electric field of 50 V/cm. Their results indicate that field assisted drifting of ions in dielectric films is a potential technique for ionic doping. The following subsection will explore the reported literature on both corona discharge and ion drift techniques applied to silicon dioxide electrets, thermally grown on silicon.

1.6.3 Charge storage and ionic conduction in the SiO_2/Si system

Thermally grown silicon dioxide is not only a suitable material for surface passivation but also an excellent electret. There are three main methods by which an electric field can be established at the SiO_2-Si interface: 1. Injection of charge into the dielectric as net charges or ionic species using a metal contact, 2. polarizing the film so that dipoles are aligned with a selected field direction, and 3. depositing charged molecules on the dielectric surface using a corona discharge apparatus:

1.6.3.1 Ion injection in SiO_2 using a metal contact

During the mid and late 1960's Bell Labs, Fairchild Semiconductor and IBM published the first reports on the charge storage capability of thermal SiO_2. Their work concentrated on eliminating instabilities due to mobile ionic species present in silicon dioxide, which

degraded the electrical characteristics of metal-oxide-semiconductor (MOS) field effect transistors (FET).

In early works, Yamin [92]–[94] and Kerr et al [95], [96] observed ionic conductivity in SiO_2 at temperatures ranging from 100 °C to 400 °C. In a metal-SiO_2-Si system, Yamin [93] found that charge could be injected at high temperature due to the ionic conductivity of the oxide. A build-up of space charge near the oxide/silicon interface created an additional potential between the silicon and the metal, which led to the device failure. He also reported that such charge was permanent when the system was brought to room temperature after the combined temperature/bias stress, thus indicating that the charged ionic species remained in the oxide quasi-permanently, yet no long term measurements were reported. Kerr et al [95] and Balk et al [97] investigated the effect of phosphorous pentoxide (P_20_5) doped SiO_2, or phosphosilicate glass (PSG). They found that it stabilised the electrical properties of the oxide/silicon interface by inhibiting charge accumulation. Very soon after, Snow et al [98] reported a study on the nature of such charged species using the MOS capacitance-voltage (CV) technique, and concluded that the reliability problems were related to alkali ion contamination, most notably sodium (Na^+), but also potassium (K^+). P_20_5 doped SiO_2 was seen to lock such ions and therefore stabilize the MOS structure, yet its use was later discontinued since the PSG layer itself could cause instability due to self-polarization [97], [99]. Nowadays, the instability problem has been solved by eliminating all sources of contamination.

Other complementary studies followed by Yon, Ko, and Kuper [100], who used neutron activation to determine the sodium profiles before and after SiO_2 films were bias-temperature stressed. They reported distributions of “immobile” sodium that indicated a pile-up near the oxide-silicon interface which agreed with CV measurements of the same structures. Their results indicate that most ionic contamination is stored very close to the Si-SiO_2 interface once it has been drifted. Lastly, a very recent report by Krivec et al [101]

confirmed the accumulation of sodium at the interfaces using TISC and time-of-flight-secondary ion mass spectrometry (ToF-SIMS). They proved that the inclusion of nitrogen in SiO_2, for example to produce silicon oxinitride or silicon nitride, did not exhibit such permeability for Na^+ at temperatures up to 150 ^oC. The use of nitrides had been suggested to block the displacement of ionic contaminants; however, it has never been thoroughly analysed. Due to such poor ionic conduction and charge storage in nitrides (e.g. see [63], [102]), SiO_2 films have been mainly studied in this project.

1.6.3.2 SiO_2 corona charged films

Another method to create SiO_2 electret films is the use of corona discharge as explained in section 1.6.1. SiO_2 electrets, and inorganic electrets in general, became popular when they were postulated as a replacement of polymeric electrets. They could be used for the construction of electrostatic micro machined devices, including microphones, dosimeters and pressure sensors [59].

Storage of corona deposited charge in SiO_2 has been postulated since the late 1970-1990's by different researchers in the field of micro machined transducers [103]–[107]. In the early 1990's, it was suggested that poor stability of SiO_2 films could be overcome by reducing their large lateral surface conduction due to water absorption [59], [108]. A chemical surface modification has since been used to reduce surface conductivity and provide sufficient charge stability. The corona charge dynamics have also been analysed by Gunther and Xia [108] in wet thermal oxides. They found negative charges to migrate on a detrapping – retrapping mechanism from the surface to the Si-SiO_2 interface, when subjected to high temperature. Positive charges on the other hand, are only trapped at the surface and continuously drift to the silicon when sufficient energy is provided [108]. Other factors that contribute to stability are silicon type and crystal orientation, dehydration, chemical surface treatment, constant voltage or current corona charging, and the charging temperature [109], [110].

Improvements in stability and chargeability have also been proposed by using double layers of thermal SiO_2, and atmospheric pressure (AP) or plasma enhanced (PE) chemical vapour deposited (CVD) silicon nitride (SiN) [102], [111]. Measured charge stability of up to three years has been reported for thermal SiO_2 – APCVD SiN_x systems under high humidity (95%) or high temperature (300 ^oC) environments [112]. The charge was found to drift towards the film interface at temperatures exceeding 300 ^oC with a maximum at approximately 400 ^oC, thus revealing an increase in the activation energy necessary to discharge the double layer electrets in comparison to a single layer [112]. In a different report, Leonov et al [113] found a thermal SiO_2 – PECVD SiN_x double layer electret stable for time periods of 2.5 years, and estimated lifetimes of 50-200 years for such structures. They also established that the maximum charge the electret can retain is governed by the dielectric breakdown potential, and that such charge is immobile on chemically treated films at room temperature.

PECVD oxides have also been studied and proved to have similar charge retention characteristics when used in double layers [106], [114], [115]. These reports indicate a chargeability and stability as good as the one previously published on thermal oxide electrets. SiN_x layers between 50 and 500 nm were reported to give increased charge stability to the electrets. Thicker oxide layers would only increase the chargeability but not contribute to stability. Similar to single layers, maximum stability is achieved by dehydrating and chemically treating the samples prior to charge deposition.

1.7 Structure of this thesis

The work presented here will cover four major advances relating to the passivation of silicon surfaces using extrinsic charge. The experimental methodology followed is firstly described in Chapter 2. Chapter 3 demonstrates how extrinsic passivation plays a major role in silicon surface passivation and for the first time describes a theoretical formalism that accurately

models the physical phenomena at the surface of silicon. Chapter 4 shows how corona discharge can be optimised to produce remarkable passivation that can last for years given the adequate processing of the dielectrics. Chapter 5 explores a new concept of passivation using extrinsic ionic species and it shows that good passivation quality can be achieved in combination with high stability. Chapter 6 explores how improved surface passivation, in particular that achieved using extrinsic field effect, can impact the performance of solar cells. Chapter 7 summarises the major findings of this thesis and provides a context for further research and development of this science.

CHAPTER 2
EXPERIMENTAL METHODS

This chapter describes the origin, fabrication and processing of specimens used in this project, along with the characterisation methods used to study the optical and electrical properties of the dielectric films, including their ability to store charge.

2.1 Silicon substrate material

Current industrial solar cells are mainly made of single-crystalline Czochralski (Cz) or multi-crystalline (mc) silicon. Since recombination in mc-silicon is limited by its high defect density and low purity, it is not of interest for this project. Here, high quality silicon is required so that the minority carrier effective lifetime is mainly limited by surface recombination. Cz-Si is remarkably pure, yet the purest silicon produced to date is Float Zone (FZ). The base material for silicon solar cells has been predominantly boron doped p-type silicon. However, phosphorous doped n-type silicon substrates are gaining acceptance in industry thanks to their higher lifetime and better stability [57]. For this project I have used a range of n-type Cz-Si and FZ-Si substrates obtained from project collaborators. Table 1 describes the different substrates used during this project.

Kind	**Resistivity [Ωcm]**	**Thickness**	**Source**
n-type Cz-Si	5	675 μm	SunEdison
n-type Cz-Si	30-60	675 μm	SunEdison
n-type FZ-Si	1	200 μm	Fraunhofer ISE

Table 1. Summary of silicon substrates used in this project.

2.1.1 Surface finish

A common practice used to maximise light absorption in silicon solar cells is to texture the surface. On a rough surface, light reflected has the chance of bouncing back onto an adjacent surface. This increases the probability of a given photon being absorbed and generating an electron hole pair. Surface texturing was accomplished here by subjecting bare silicon wafers to an anisotropic etch in a solution of IPA and KOH. This solution preferentially etches {100} planes resulting in a surface made up of pyramids. This is known in industry as a random pyramid texture. For the purpose of this work such a process was performed on some of the material by collaborators at the Fraunhofer ISE.

2.1.2 Sample labelling

All specimens were labelled according to the wafer from which they were cut. Each wafer was given a short label and each sample cut from that wafer was numbered sequentially with the wafer's name as prefix. The labels were scribed on the corner of all samples to allow easy and consistent identification. Some samples without labels were measured using the characterisation methods described in this chapter and no effect was inferred due to a scribed label. All wafers were labelled starting with the doping type, followed by a combination of letters and numbers to reference the source wafer, and an additional number for the sample. When the wafer ended in a number, an underscore character was added before the sample number. Examples of this standard are given in Figure 5. Appendix C includes a list of all samples and processing steps for samples reported in this thesis.

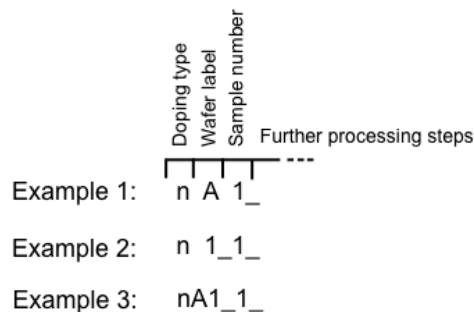

Figure 10: Standard for sample labelling.

2.2 Dielectrics used for surface passivation

2.2.1 Thermal oxides

Silicon was thermally oxidised to grow pure SiO_2 directly on top of Si. In this process the silicon specimen is subjected to elevated temperatures (> 800 ^oC) in an oxygen rich atmosphere. High temperature processing must be conducted in remarkably clean conditions since any impurities present in the environment can diffuse into the silicon and create defects that decrease its minority carrier lifetime. It was found that oxidation at Oxford sometimes reduced carrier lifetimes to the order of 1ms or below due to the lack of process cleanliness. Thus wafer oxidation was performed elsewhere. Oxidation was conducted at three different laboratories with the parameters described in Table 2.

Thickness	Environment	Temperature	Furnace	Laboratory
21.5 nm	O_2 and N_2	900 ^oC	N/A	SunEdison
87.5 nm	Wet O_2, N_2 and H_2	1000 ^oC	N/A	SunEdison
67 nm	O_2 and N_2	1000 ^oC	Tempress	Southampton U.
100 nm	O_2 and DCE	1050 ^oC	Centrotherm	Fraunhofer ISE
10 nm	O_2 and DCE	850 ^oC	Centrotherm	Fraunhofer ISE

Table 2. Parameters of the thermal oxidations carried out for this project. DCE: Dichloroethylene.

2.2.2 Chemical vapour deposited dielectrics

Silicon nitride (SiN_x) and silicon oxide (SiO_x) layers were deposited in the Begbroke clean room at Oxford using plasma enhanced chemical vapour deposition (PECVD) in an Oxford Instruments (OI) PlasmaLab 80+ PECVD system. Standard recipes suggested by OI were used and they were not optimised for overall passivation quality since the focus of this work was on charge stability in dielectrics. The standard SiN_x deposition used was a 70$\pm$5 nm layer deposited using a gas mixture of silane/nitrogen (5%SiH_4/95%N_2 – 400 sccm),

ammonia (NH_3 – 20 sccm) and nitrogen (N_2 – 600 sccm) as precursor gas. Specimens were placed on the reactor bottom plate, which was held at 350 ^oC during deposition. The chamber pressure was 650 mTorr. A 20 W RF source at 13.56 MHz was used to maintain the plasma. The thickness and refractive index of SiN_x films were measured using reflectance spectrometry using a Filmetrics 205 instrument. The refractive index of SiN_x was 2.20$\pm$0.1.

Additional SiN_x films were produced at Fraunhofer ISE. Wafers previously oxidised were deposited with ~60 nm of SiN_x using an industrial-type, in-line PECVD system (Roth&Rau SiNA XS). SiH_4 and NH_3 were used as precursor gases, and the gas flux ratio was optimised to achieve optimal passivation, with a resulting refractive index of n~2.15, as described in Ref. [116].

2.2.3 Summary of dielectrics

Wafer label	Silicon type	Resistivity [Ωcm]	Dielectric	Deposition Technique	Thickness [nm]
nC	Cz	5	SiO_2	Thermal oxidation	87.5
nB, nE	Cz	5	SiO_2	Thermal oxidation	21.5
nC	Cz	5	SiO_2/SiN_x	Thermal oxidation / Direct PECVD	87.5/80
nB	Cz	5	SiO_2/SiN_x	Thermal oxidation / Direct PECVD	21.5/80
n1-n15 **n1b-n17b** **n16-n22 (F)** **nA1-nA5(F)** **nT1 (T)**	FZ	1	SiO_2	Thermal oxidation	100
Ox1_1 - Ox1_4(F)	FZ	1	SiO_2/SiN_x	Thermal oxidation / Direct PECVD	10/60
Ox1_5 - Ox1_8 (T, F)	FZ	1	SiO_2/SiN_x	Thermal oxidation / Direct PECVD	10/60
Ox1_9 - Ox1_12 (F)	FZ	1	SiO_2/SiN_x	Thermal oxidation / Direct PECVD	100/60

Table 3. Summary of samples used in this project. (T) stands for a textured surface. (F) stands for Forming Gas Anneal. Additional details of all samples are provided in Appendix C.

2.3 Extrinsic chemical passivation

Extrinsic passivation of silicon dangling bonds at the silicon surface was also used. When hydrogen atoms are added to the dielectric coating they can further reduce surface recombination by bonding with many of the dangling bonds that may remain at the dielectric/silicon interface. This reduces the electrical activity of interface defects and hence limits surface recombination. Hydrogen passivation has been commonly applied to the surface of semiconductors using a forming gas (~5% H_2 / 95% N_2) anneal (FGA) at ~425 ^oC. For this project, such a process was conducted on a set of wafers in a Centrotherm tube furnace for 25 minutes. This was carried out at Fraunhofer ISE. Table 1 includes the wafers that underwent this process and are marked as (F).

In addition, chemical passivation can be obtained from hydrogen liberation that occurs during a PECVD SiNx deposition process, or from hydrogen that remains in the dielectric and is migrated to the interface using a post dielectric deposition anneal [117]. Both of these methods have been used here.

2.4 Extrinsic field-effect passivation

2.4.1 Corona discharge

Chapter 1 described the fundamentals of corona discharge. For this project, a point to plane corona discharge apparatus was designed and built – which will be referred to as Rig 1. The high voltage power supply, Ultravolt HVRack, had dual polarity output of up to $\pm$ 20 kV and 1.5 mA configurable maximum current, with independent control and monitoring of each channel and remote and interlocked control for safety. Figure 11.a shows a schematic of Rig 1 and its connection to the power supply. This rig was used to conduct cold and hot corona discharge, on a single side of the sample. The total deposited charge depended on the charging conditions including point electrode potential, time, distance and temperature. The

standard charging conditions for Rig 1 were a positive potential of 9kV applied to a stainless steel pin 8 cm from the sample, such that a corona current of ~1 uA was produced.

During the third year of the project, a second improved corona discharge rig (Rig 2), was designed and constructed in collaboration with a Part II student, Fred Woodcock. This new corona discharge apparatus was a similar point-to-plane configuration equivalent to that shown in Figure 11.a. In contrast, this rig was optimised to provide uniform field effect passivation to the specimens. This rig was used for single-side charging, performed at room temperature in laboratory conditions. For the purpose of charge optimisation, the non-uniformity was defined as the coefficient of variation of the charge concentration measured across the whole tested area of the sample. This is equal to the ratio of the standard deviation to the mean of charge surface concentration. The corona current was modelled as described by Warburg's Law [118], [119]:

$$J = J_0 cos^5(\theta) \tag{2. 1}$$

where θ is the angle to the plane normal defined by the direction between the electrode tip and the position on the sample. Increasing the distance from the specimen at which the corona is struck reduces the variation in θ across the sample, and increases the uniformity of current. This is shown in Figure 11.b. On the other hand the distance between the point electrode and the sample plane must be smaller than the distance between the electrode and the grounded case. This ensures that the electric field is not significantly altered by the case, and that the field lines point evenly towards the sample. This simple model indicated that a distance of 15 cm would give a corona current with a coefficient of variation of 1% across a 3 x 3 cm^2 sample - the standard size used throughout this project. Experimentally, a variation of less than 5% was measured using corona Rig 2. Similar to Rig 1, a corona current of ~1 uA was established by applying a potential of 15 kV to the point electrode. More details of the design, construction and comparison between the two corona discharge apparatuses can be found in Mr Woodcock's thesis [120].

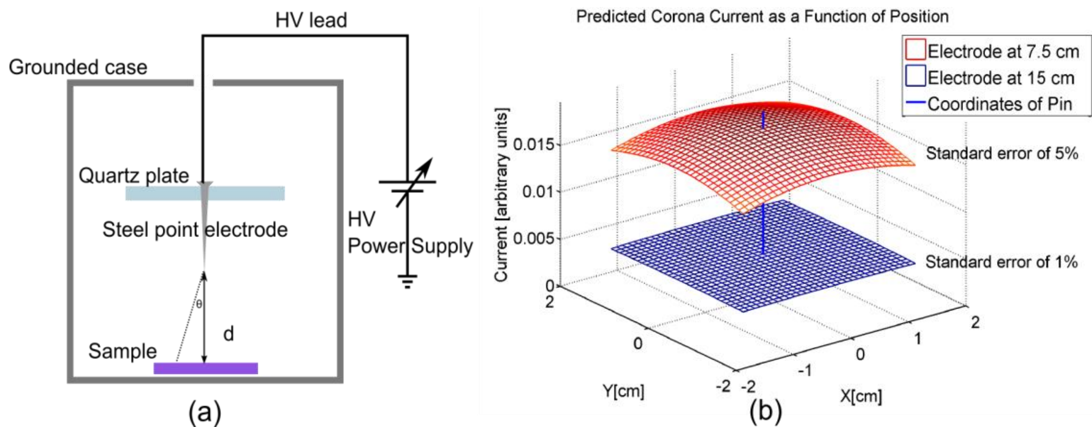

Figure 11: a. Circuit diagram of charging apparatus, with corona distance labelled "d", b. Results of numerical model of Warburg's Law, showing corona current as a function of position for corona distances of 7.5 and 15cm. Adapted from Bonilla et al [121].

2.4.1.1 Dehydration and HMDS coating

Absorption of water in dielectric films has previously been reported to induce lateral conductive paths through which the film's charge can leak away [59], [122], [123]. To avoid this a hexamethyldisilazane (HMDS) chemical treatment, known to provide a highly hydrophobic monolayer coating [108], was applied to some specimens using one of two different methods:

Method 1

Samples were dehydrated in a box furnace at 400 ^{o}C for 30 minutes, immediately followed by exposure to hexamethyldisilazane (HMDS) vapour at a temperature of 140-160 ^{o}C for 20 minutes, see Figure 12.

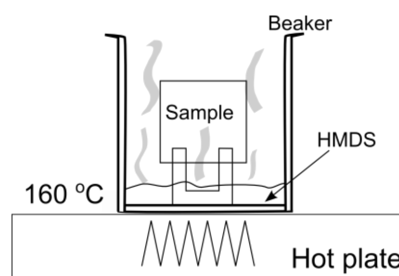

Figure 12. Schematic of HMDS chemical treatment 1.

Method 2

Samples were placed in a tube furnace with an argon through-flow and dehydrated at 200°C for 30 minutes. The temperature was then reduced to 120°C over a period of 30-50

minutes, and the argon flow was then bubbled through HDMS to coat the surface, over a period of further 30 minutes. Figure 13 illustrates this process.

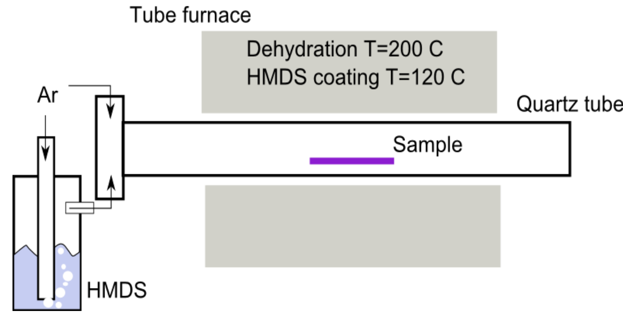

Figure 13. Schematic of HMDS chemical treatment 2.

2.4.2 Ionic species

2.4.2.1 Deposition

A new technique to provide field-effect passivation was proposed in this project. Here ionic species are deposited on top of a dielectric film and subsequently transported into the film at high temperature, to be quenched into the dielectric during cooling. To achieve this, a controlled concentration of an ionic precursor was first deposited on top of the dielectric. Chloride or hydroxide salts, used as precursors for a variety of ionic species, were deposited using thermal evaporation. The surface concentration required was below that of a monolayer (< 10^{18} cm^{-2}) so that a special technique, previously reported by Snow [98], was used. An ionic solution of ultrapure cleanroom water and a weight (W_{ion}) of the ion chloride salt was mixed. A micrometric pipette was then used to extract a 50 μL droplet of the ionic solution and deposit it on a tungsten boat where it was dried at 100 ^{o}C. The boat was then used as an evaporation source in a laboratory scale thermal evaporator. The amount of chloride salt (W_{ion}) mixed in the solution was approximated as follows: Given a nominal ion surface concentration of σ_{ion} =10^{14} cm^{-2}, the number of XCl molecules that must be evaporated is that which will cover a hemisphere at the plane of the sample, Figure 14:

$$Molecules = \sigma_{ion}(2\pi r^2) \quad (2.\ 2)$$

where r is the distance between the sample and the tungsten boat. The amount of the chloride salt is therefore given by:

$$W_{ion} = \frac{W_{sol}}{W_{drop}} \frac{\rho_{XCl}}{N_{AVG}} Molecules \tag{2. 3}$$

where ρ_{XCl} is the density of the chloride salt, W_{sol} is the weight of the solution, W_{drop} is the weight of the droplet here taken as 50μL, and N_{AVG} is Avogadro's constant. This calculation indicates that, for a nominal surface concentration of 10^{14} cm^{-2} of, for example, sodium chloride, 120 mg of NaCl should be mixed in the 500 mL solution from which the 50 μL drop is taken. That this method produced the required concentration on the specimen surface was corroborated using thermally stimulated ionic conductivity (TSIC)[124] in a metal-oxide-semiconductor (MOS) capacitor, as described later in this chapter.

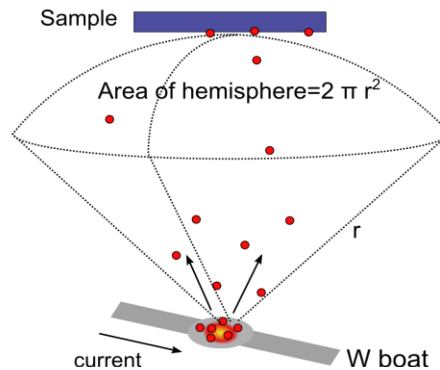

Figure 14: Schematic of the thermal evaporation of ionic species.

2.4.2.2 *Transport*

Migration of ionic species into the body of the dielectric films was achieved using two mechanisms: diffusion and drift. Samples were submitted to high temperature anneals using a box furnace in laboratory conditions –i.e. no clean room cleanliness, at temperatures between 300-600 ^{o}C to in-diffuse the ions. A drift component could be added to their movement by depositing corona charge immediately before the anneal. Additionally, MOS capacitors were fabricated on top of some films that were previously deposited with a known

concentration of ionic species. In such specimens the drift component was added using a direct bias potential on the metal electrode of the capacitor.

2.5 Electrical characterisation

2.5.1 Minority carrier lifetime

The effective minority carrier lifetime as a function of the excess minority carrier concentration (Δp) was measured using a Sinton WCT-120 photo-conductance instrument [125], using both quasi-steady state and transient modes [126], [127]. The measurement of carrier recombination in silicon normally results in an effective carrier lifetime τ_{eff} that contains the contributions of all the different mechanisms mentioned in Chapter 1. The effective minority carrier lifetime for a silicon wafer as a whole can be expressed as the reciprocal sum of the bulk and the surface components:

$$\frac{1}{\tau_{eff}} = \frac{1}{\tau_B} + \frac{1}{\tau_s} \qquad (2.\ 4)$$

Increasing both these lifetimes is the key in improving cell efficiency. However, this work is only concerned with the surface component. The bulk component, including Auger and radiative recombination, will be assumed to be described by Richter's parameterisation [28], with the radiative recombination term found by Gerlach et al [23].

The surface lifetime component has a more elaborate dependence on SRV. The amount of recombination at the surface depends on the spatial variation of the injected carriers. Carriers generated far from the surface may only recombine when they diffuse to the surface. Similarly, carriers generated at the surface may recombine instantaneously or diffuse to the bulk. To account for this dependence, Luke and Cheng [128] developed a formalism and found a solution that indicates that the effective SRV is a function of an infinite sum of

decaying exponential terms of effective lifetime. The first mode is dominant and it is written as:

$$S_{eff} = \sqrt{D_p\left(\frac{1}{\tau_{eff}} - \frac{1}{\tau_b}\right)}\tan\left(\frac{W}{2}\sqrt{\frac{1}{D_p}\left(\frac{1}{\tau_{eff}} - \frac{1}{\tau_b}\right)}\right) \quad (2.\ 5)$$

For sufficiently low SRV, $\tan(x) \approx x$, and the complete expression for effective lifetime can be written as:

$$\frac{1}{\tau_{eff}} = \frac{1}{\tau_{Rad}} + \frac{1}{\tau_{Aug}} + \frac{1}{\tau_{SRH}} + \frac{2S_{eff}}{W} \quad (2.\ 6)$$

This expression has been proved accurate to better than 4% when recombination is the same at both surfaces and $\frac{S_{eff}W}{D_p} < \frac{1}{4}$ [129]. For the specimen thickness and dopant density used in this project this criterion is fulfilled when S_{eff} <150 cm/s which was the case for all the passivated specimens used in this project. The SRH limited bulk lifetime in FZ single crystal material is often assumed to be infinite. However, this is not true and thus this approximation results in an upper limit to the value of effective surface recombination velocity:

$$S_{UL} = \frac{W}{2\left(\tau_{eff}^{-1} - \tau_{Aug}^{-1} - \tau_{Rad}^{-1}\right)^{-1}} \quad (2.\ 7)$$

In the Sinton instrument sample conductivity is measured using a RF bridge circuit including a coil placed very near the sample. The coil's impedance varies with the conductivity of the sample which varies due to photo-injected carriers, Figure 15. In a semiconductor the conductivity is directly related to carrier concentration as:

$$\Delta p = \frac{\Delta\sigma}{q(\mu_n + \mu_p)} \quad (2.\ 8)$$

Since the continuity equation states that:

$$\frac{\partial \Delta p(t)}{\partial t} = G - R = G - \frac{\Delta p(t)}{\tau_{eff}} \quad (2.9)$$

The effective lifetime can be directly estimated from the measurement of conductivity as a function of time:

$$\tau_{eff}(\Delta p) = \frac{\Delta p(t)}{G(t) - d\Delta p(t)/dt} \quad (2.10)$$

Where $G(t)$ is the photo generation normally estimated using a calibrated sensor near the sample for the quasi-steady state mode [126]. In transient mode $G(t) = 0$ for the time duration during which conductivity measurements are made. In this thesis effective lifetime is generally reported for an excess carrier concentration of $\Delta p = 10^{15}$ cm^{-3}. This Δp was chosen since 1 Ωcm c-Si at 1-Sun AM1.5 illumination conditions (see Section 2.5.5) has $\Delta p \sim 10^{15}$ cm^{-3}. Additionally, this is the value commonly reported in the literature.

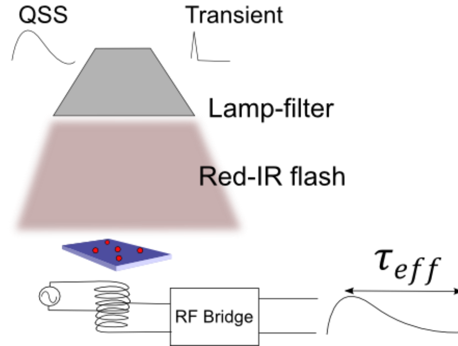

Figure 15: Schematic diagram of the photo-conductance decay system used to measure minority carrier lifetime.

2.5.1.1 *Calculation of decay time constants for aging measurements*

The stability of the passivation techniques used in this work was a major topic of study. To characterise how stable a passivation method is, measurements of effective lifetime were taken over period of ~ 2 years. Stability was evaluated by fitting a single decay exponential term to the effective lifetime measurements as $\tau_{eff}(t) = (\tau_{eff,FEP} - \tau_{eff,0})e^{-\frac{t}{\tau_{FEP}}} + \tau_{eff,0}$, using the Non Linear Least Squares method [130]. $\tau_{eff,0}$ is the intrinsic effective lifetime prior extrinsic FEP, and $\tau_{eff,FEP}$ the lifetime achieved once the passivation method is applied. It was generally observed that the decrease in effective lifetime showed a

combination of two decay terms -a fast and a slow exponential decay. In this work the fast exponential decay has been discarded as it occurs in the first 50 days and as such is not relevant for the high stability required in solar cells. The lifetime decay time constants were calculated between day 50 and the end of the measurement period. Figure 16 illustrates an example fitting of both a fast and a slow single exponential decay terms, together with the estimated decay time constants τ_{FEP} for two data scenarios. The decay constants include 95% confidence intervals.

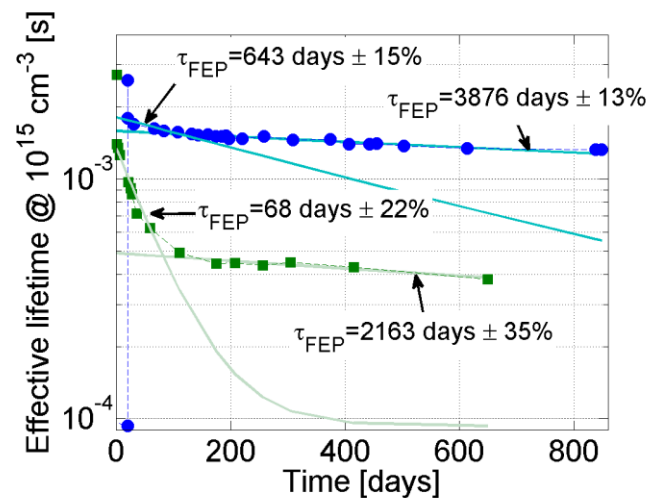

Figure 16. Example calculation of decay time constant for the decrease in effective lifetime over time of samples n1_1 and n7_6.

2.5.2 Capacitance-Voltage measurements

Capacitance-voltage (CV) measurements are widely used in semiconductor science to characterise metal-insulator-semiconductor (MIS) structures. In CV measurements a MIS capacitance is recorded as a function of an external bias potential $C_{exp} = f(V_{bias})$. The bias potential is used to change the charge carrier conditions at the surface of the semiconductor. Accumulation and inversion regimes are induced when biasing the metal strongly positive and negative with respect to an n-type semiconductor. This allows investigation of the semiconductor properties when the insulator and metal are well characterised. For this project however, the semiconductor was well characterised and CV measurements were mainly used to study the insulator properties, in particular its charge concentration. Figure 17.a illustrates the processing methodology used to fabricate MIS capacitors. Insulator film

deposition or growth was described in section 2.2. Insulator removal via reactive ion etch (RIE) was conducted in an Oxford Instruments PlasmaLab 80+ reactor using a gas mixture of 50% CHF_3/50% Ar at 30 mTorr, held at 20 ^oC, and a 200W RF source at 13.56 MHz. Alternatively rear oxide removal was possible by rubbing an HF dipped cotton bud on the specimen until the film was removed. Aluminium evaporation was carried out using a EuroCoater thermal evaporator with a tungsten filament wrapped with 99.999% pure Al. Front surface Al contacts where evaporated through a shadow contact mask to produce either 1 mm or 2 mm diameter dots. The thickness deposited was recorded using an acoustic impedance monitor calibrated for Al.

Figure 17.b illustrates the a simplified equivalent circuit of a MIS capacitor as proposed by Nicollian and Goetzberger [131]. Capacitance is defined as the rate of change in charge with electric potential, $C = dQ/dV$. The total measured capacitance is therefore given by the series equivalent of the insulator capacitance and the semiconductor capacitance:

$$C_{meas} = \frac{C_S C_i}{C_s + C_i} \tag{2. 11}$$

Where C_s is the capacitance of the semiconductor and C_i is the capacitance of the insulator. When interface traps are considered, additional charge is stored on the trap states and it too depends on the semiconductor potential. The capacitance of the semiconductor hence becomes the sum of the depletion region capacitance C_D and the interface states' capacitance C_{it}, $C_S = C_D + C_{it}$. The additional charge stored in interface states induces a stronger dependence of capacitance on voltage in the depletion and inversion regimes, while insulator charge offsets the potential at which the semiconductor in the MIS capacitor switches from an accumulation to a depletion regime (ΔV). This is illustrated in the bottom graph in Figure 17.b.

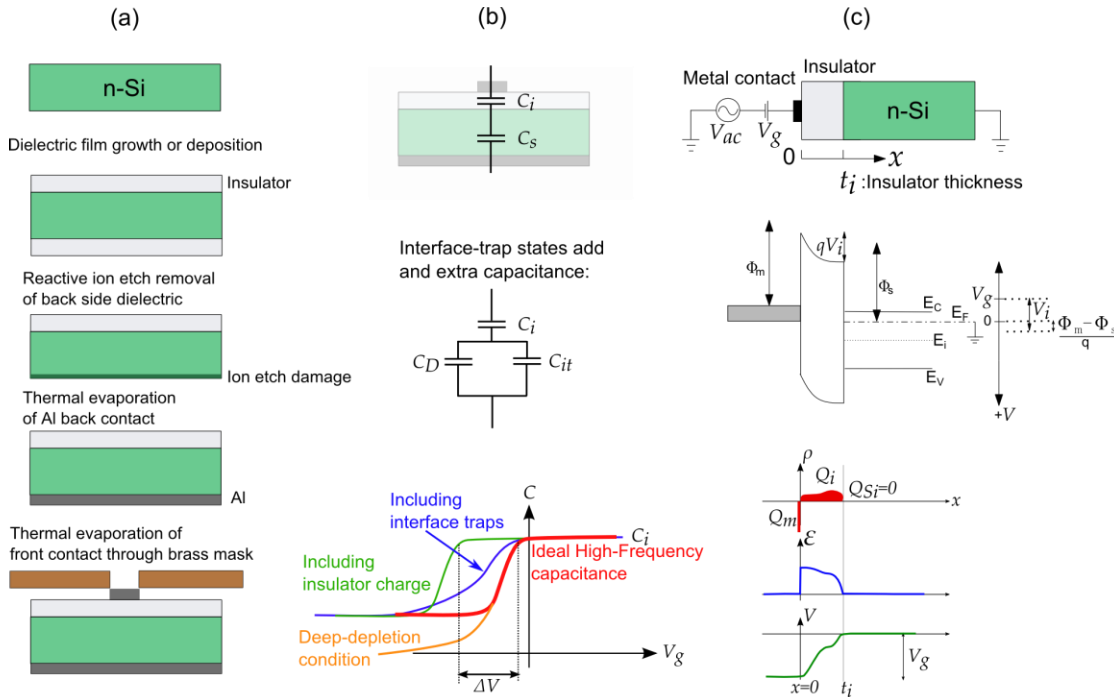

Figure 17: a. Processing methodology for creating MIS capacitors, b. Equivalent circuits and typical capacitance-voltage curves for a MIS capacitor in a n-type semiconductor, red curve indicates the ideal high-frequency capacitance, the blue curve indicates the contribution of surface defect states and the green curve indicates the contribution of dielectric fixed charge to the semiconductor capacitance, c. Schematic diagram of a MIS capacitor in the flat-band condition when charge in the dielectric is compensated by charge in the metal contact, including band diagram and the charge, electric field and potential in the structure.

Figure 17.c illustrates a schematic of a CV measurement conducted using a MIS capacitor. Capacitance was measured using a Boonton 7200 meter using a 1 MHz AC signal $V_{ac} = 50$ mVpp and a gate bias V_g ranging from -50 to 50 V. Figure 17.c also includes a band diagram, and the charge concentration, electric field and electric potential traces. In this case the semiconductor bands near the surface are flat. This is the flat-band condition and occurs as the semiconductor surface switches between the accumulation and depletion regimes. In this condition the electric field in the Si is zero, and therefore the Si space charge concentration is zero.

In this CV measurement scheme, the metal contact voltage V_g (commonly referred to as the gate voltage) falls across the insulator and the semiconductor as:

$$V_g = \frac{\Phi_{\text{ms}}}{q} + \phi_{scr} + V_i \qquad (2.\ 12)$$

Where Φ_{ms} is the metal to semiconductor work-function difference, ϕ_{scr} the potential difference between the bulk and the surface of the semiconductor due to the SCR, and V_i is the potential drop in the insulator including both of its interfaces to the metal and the semiconductor, Figure 17.c. CV measurements were used specifically to find the insulator charge and insulator/semiconductor interface state density as described in Appendix A.

2.5.2.1 Mercury probe contact and charge profiling

Deposition of a front Al contact to form MIS capacitors has the disadvantage of preventing further processing from being performed on the same dielectric. Once the metal contact is deposited, the dielectric/metal interface affects the physical processes that may take place inside the dielectric itself. To overcome this problem a temporary metal contact for MIS capacitors was devised using a mercury probe (Hg-p). A sample holder was built and attached to a pipe containing Hg as shown in Figure 18. This rig allowed a Hg contact to be formed directly on the front dielectric without the need for the second Al thermal evaporation in Figure 17.a.

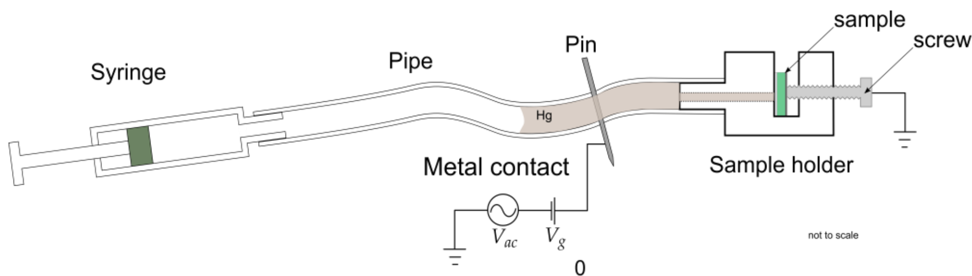

Figure 18: Schematic diagram of the sample holder and front contact connection to form a MIS capacitor using Hg.

A key advantage of this method is that it allowed the formation and measurement of several MIS capacitors at different times and in different positions on the sample. This allowed measurement of the same MIS capacitor after different processing steps and allowed the same insulator to be measured multiple times as the insulator was back-etched to reduce its thickness. The latter measurements allowed a profile of the charge distribution through a dielectric to be obtained. To do this, insulator/semiconductor structures where back-etched in

an electronic grade 10% concentration solution of hydrofluoric (HF) acid (for SiO_2), or 85% phosphoric acid (H_3PO_4) at 160-190 ^oC (for SiN), for different subsequent periods of up to 10 minutes, each followed by Hg-p CV measurements to assess charge concentration in the dielectric. Since charge calculations depend on the insulator capacitance, either the thickness or the area of the capacitor has to be measured using an independent technique. In the Hg-probe rig used here, the area of the contact varied depending on the pressure applied with the syringe. This made it impossible to maintain a constant area of the contact. The insulator thickness was therefore measured using reflectance spectrometry.

Charge profiling was also conducted using Al gate contacts. This was performed by using a set of specimens from the same sample and etching each of them for a different length of time. In this case the film thickness after subsequent etching steps could be calculated from area of the capacitor. CV measurements were used to calibrate the capacitor area on a film of known thickness, and such area was in turn used for calculation of film thicknesses using similar area capacitors on different insulators.

2.5.3 Thermally stimulated ionic conductivity

Thermally stimulated ionic conductivity (TSIC) is an electrical technique used to investigate the transport of charge via ion displacement inside MIS structures. This technique involves subjecting a MIS capacitor to a constant bias stress, while the temperature of the capacitor is raised and the current recorded. In the absence of other conduction mechanisms –e.g. thermionic or Frenkel-Poole [132], the current measured is only caused by conduction of ionic species through the insulator layer. To minimise inaccuracies a two-sweep process has been carried out, with the second sweep subtracted from the first to eliminate additional conduction mechanisms, which are not related to ionic migration. This is adopted after the works of Hickmott [124]. Figure 19 outlines this technique together with typical voltage, current and temperature traces. A Keithley 2611A source measure unit (SMU) was used to monitor current and voltage (V_g, I) while the sample was heated up using a 5 mm x 30 mm x

0.8 mm, 0.01 Ωcm piece of silicon as heater. This heater was powered using a Thurlby-Thandar TSX3510P bench-top power supply, controlled via a GPIB port using a Labview programmed PID. The PID controller was used to set the temperature to follow the profile in Figure 19.b. A National Instruments USB-6009 acquisition card was used to read the sample temperature from a K-type thermocouple. The heater and sample were enclosed in a 10 x 10 x 5 cm^3 calcium silicate thermally insulating box. This technique was used to study the kinetics of ionic species when diffused into an insulator matrix. Appendix B explains the theory used to analyse these experiments.

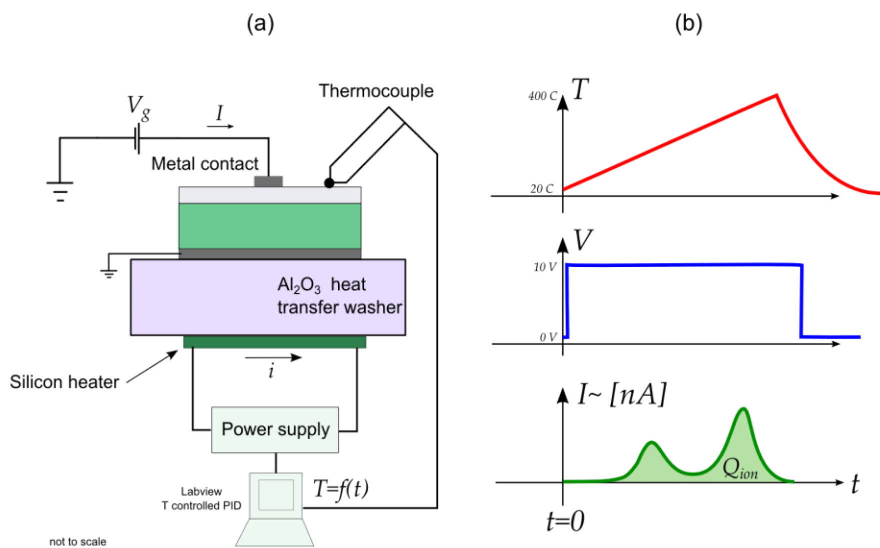

Figure 19: a. Schematic diagram of the TSIC technique, b. A MIS capacitor is subjected to a bias stress while the temperature is raised and the current recorded. The typical experiment has a linear temperature rise and produces characteristic peaks depending on the trapping energy of different types of ionic species inside the insulator. Integration of the recorded current allows the total migrated charge Q_{ion} to be deduced.

2.5.4 Kelvin Probe measurement of surface potential

Kelvin probe (KP) characterisation allows non-contact measurements of work function differences between metals, or surface potential differences for non-metals. The technique was used here to measure the surface potentials of dielectrics on silicon which are strongly dependent on surface charge. KP measurements of surface potential were conducted using a modified version of the Scanning Kelvin Probe (KP) 3.1 by KP Technology Ltd [133]. The modifications allowed biassing of the sample rather than the tip and measurement of surface potentials using Baikie's method [134]. In the KP technique a probe (Metal 1) is brought

near the sample (Metal 2) to capacitively couple them, Figure 20. The probe is then oscillated such that the distance between them, and thus the capacitance, is modulated by the oscillations (δd). In the absence of any other electric potential, the modulation in capacitance due to the change in separation of the metals produces a modulation in the charge in the capacitor, and therefore a current $I_b = \frac{dQ}{dt} = \frac{dC}{dt}V$. It is possible to find the contact potential, if an external potential (termed the backing potential V_b) is added to Metal 2, such that the total contact potential is cancelled, and thus the measured current I_b is zero. In Baikie's method [134] the null point is found by taking a range of V_b values, generally between a positive and a negative voltage rail (-8 to 8 V), and finding the peak to peak amplitude of the current I_b for each backing potential. A linear fitting is then applied to the I_b vs V_b data to find the interpolated potential at which the current amplitude goes to zero. Such a value is the negative of the contact potential between the probe and the specimen $V_{kp} = -V_b$.

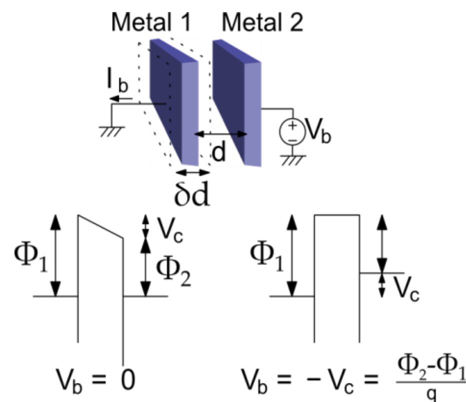

Figure 20: Kelvin Probe principles in a two metal plates system and their work functions.

A KP system using this method was set up at the beginning of the project. The theory of contact potentials and work functions of metals has long been described thanks to the developments by William Thomson (Lord Kelvin) [135] and his successors [136]. The influence of charge on the surface potential of semiconductors has been described in less detail, for example in Schroder's textbook [137]. In the following these concepts are developed focusing on the dielectric - n-type silicon system. Figure 21 is a schematic of the system, including an energy diagram and the charge, electric field and electric potential functions in a one-dimensional representation, excluding the potential associated with work

function differences. When a metal-insulator-semiconductor structure is brought together without any charge in the insulator (Figure 21.a), the backing potential necessary to null the current measured by the metal probe is analogous to the flat-band voltage of a MIS structure discussed in Section 2.5.2, with the small difference that here the controlled potential is being set to the semiconductor instead of the gate. In Figure 21.a an external potential has been added across the structure to illustrate an off-flatband condition. The voltage difference between the Kelvin probe V_g and the substrate V_s can be calculated as:

$$V_g - V_s = \frac{\Phi_{ms}}{q} + \phi_{scr} + V_i \tag{2. 13}$$

It therefore follows that the backing potential found in KP measurements is given by

$$V_b = V_s = \frac{\Phi_{sm}}{q} - \phi_{scr} - V_i \tag{2. 14}$$

In the absence of insulator charge and the external potential, the potential across the insulator and semiconductor vanishes, and the KP voltage is the difference between the materials' work functions, Figure 21.a. If charge is present in the insulator, Figure 21.b, the KP backing potential includes the potential drop across the insulator and semiconductor.

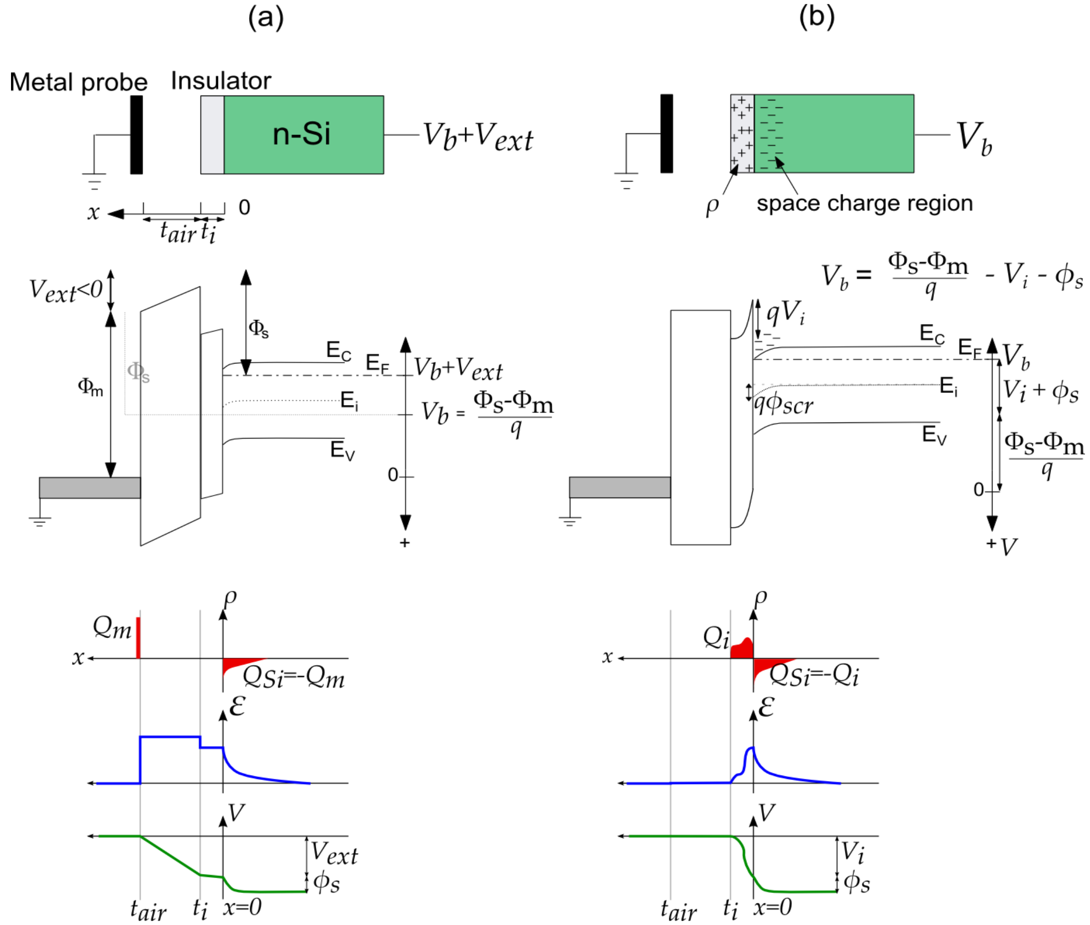

Figure 21: Metal probe - insulator – semiconductor schematic diagram including the band structure (a) without charge in the insulator and with a small external bias applied and (b) with an external bias applied such that zero Kelvin probe current is detected for the given charge concentration in the insulator. The charge, electric field, and electric potential diagrams at the bottom omit the work function difference for simplicity.

The work function of metals has been well researched in the past [20]. The semiconductor work function is defined in terms of the doping concentration and type since the Fermi energy is a function of these parameters:

$$\Phi_s = \chi + \frac{E_g}{2q} + \frac{|N_{dop}|}{N_{dop}} V_t \ln\left(\frac{|N_{dop}|}{n_i}\right) \tag{2. 15}$$

When charge is present in the metal probe (Figure 21.a) or the insulator (Figure 21.b), part of the potential is dropped inside the semiconductor. This is characterised by the semiconductor SCR potential ϕ_{scr}. To determine this quantity it is necessary to follow an iterative process that finds the charge neutrality condition given the metal, insulator, interface and semiconductor charge concentrations. This was reported by Girisch et al [138] and will be used in modelling surface recombination in Chapter 3 . At this stage it is only useful to

draw the relation between semiconductor charge and SCR potential and analyse its contribution to KP surface potential. The space charge density in silicon is given in equation (A. 15) and is shown in Figure 22. When only positive charge is present in the insulator, as is the case for most of the work in this project, the relative contribution of potential from the semiconductor ϕ_{scr} is less than 0.25 V when the silicon surface charge density is kept below 10^{13} q/cm^2. The semiconductor SCR potential can then be disregarded in equation (2. 14). For a positive space charge region (SCR) the contribution could be as high as 1 V when large band bending is produced and thus ϕ_{scr} should be included in the calculation of insulator charge as a function of KP surface potential.

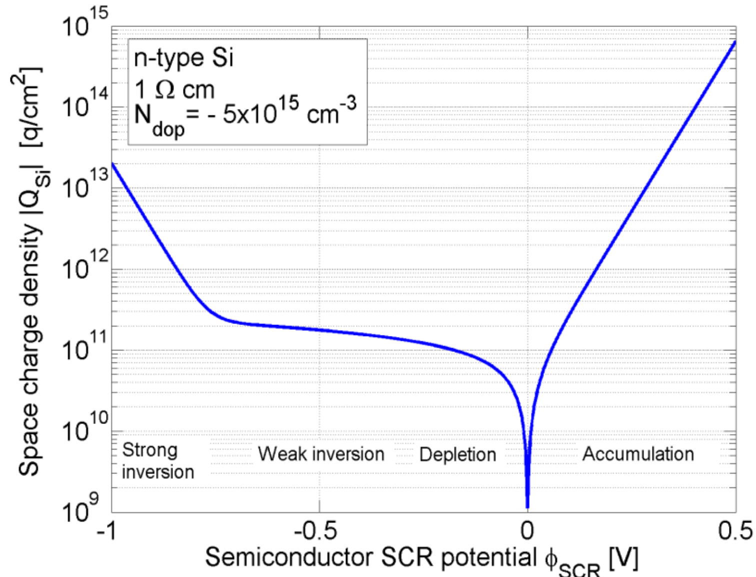

Figure 22: Variation of space charge density as a function of SCR potential ϕ_{scr}.

The insulator voltage V_i is calculated in a similar way to the flat-band shift in a MIS structure, except the bias is applied to the semiconductor rather than the metal, thus the depth axis x is inverted, as depicted in Figure 21 [139]:

$$V_i = \frac{1}{K_i \varepsilon_0} \int_0^{t_i} x \rho_i(x) dx + \frac{1}{\varepsilon_0} \int_{t_i}^{t_i + t_{air}} \left(\frac{t_i}{K_i} + (x - t_i) \right) \rho_{air}(x) dx \qquad (2.\ 16)$$

where K_i is the relative permittivity of the insulator. Since no charge concentration is allowed in the air, the insulator potential reduces to:

$$V_i = +\frac{1}{K_i \varepsilon_0} \int_0^{t_i} x \rho_i(x) dx \tag{2. 17}$$

And the KP surface potential is therefore given by:

$$V_b = \frac{\Phi_{sm}}{\mathrm{q}} - \frac{1}{K_i \varepsilon_0} \int_0^{t_i} x \rho_i(x) dx \tag{2. 18}$$

It is now convenient to study the case where all the charge is concentrated in a plane at a distance t_σ from the insulator-silicon interface, for which case the charge distribution is a delta Dirac function centred at t_σ: $\rho = \sigma\, \delta(x - t_\sigma)$, the backing potential is then:

$$V_b = \frac{\Phi_{sm}}{\mathrm{q}} - \frac{t_\sigma \sigma}{\varepsilon_i} \tag{2. 19}$$

Thus the surface charge concentration can be found as:

$$\sigma = \frac{\varepsilon_i}{t_\sigma}\left(\frac{\Phi_{sm}}{\mathrm{q}} - V_b\right) \tag{2. 20}$$

This calculation indicates that the KP surface potential is equivalent to flat-band voltage in the capacitance voltage method of a MIS structure, except the semiconductor is here biased instead and so charge at the insulator-air interface is more easily discerned. Additional advantages of KP measurements are its speed and the lack of sample preparation. CV and KP measurements are therefore complementary however both of them assume a location of the charge in order to obtain the charge density. A combination of both techniques has been suggested by previous authors to estimate the charge location [140] however this report is believed to contain errors. As an example of KP charge measurements, consider a gold ($\Phi = 5.1$ eV [132]) plated probe that measures a -10 V backing potential on a 100 nm oxidised 1 Ωcm silicon specimen. Assuming the charge resides at the surface of the insulator $t_\sigma = 100$ nm, the total charge density is calculated to be 2.336 x 10^{12} q/cm^2. All subsequent Chapters will report KP surface potential instead of backing potential. This is preferred since the surface potential relates directly to the polarity of the surface charge.

2.5.4.1 *Calculation of decay time constants for aging measurements*

The stability of corona charge was characterised using KP surface potential measurements over period of ~ 60 days. Stability was evaluated by fitting a single decay exponential term as $V_{kp} = V_{kp0}e^{-t/\tau_{kp}}$, using the Non Linear Least Squares method [130], where $V_{KP,0}$ is the surface potential immediately after corona charge deposition and τ_{KP} the decay time constant. Figure 23 illustrates an example fitting of a single exponential decay term for surface potential including the estimated decay time constant and its 95% confidence interval.

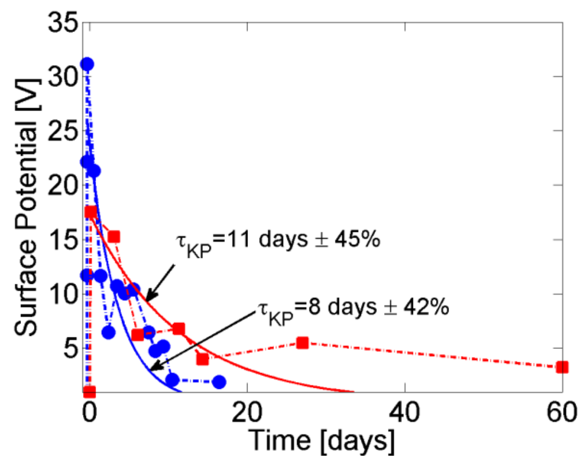

Figure 23. Example calculation of decay time constant for the decay in surface potential of samples nC_8 and n9_x1.

2.5.5 Solar cell testing

The contribution of field-effect surface passivation to the overall performance of solar cells was studied in this project. For this purpose, controlled extrinsic FEP via corona discharge was applied to back-contact silicon solar cells and improvements were measured by acquiring the current-voltage (IV) characteristics of the cells, under controlled illumination.

2.5.5.1 *In-house solar simulator*

An in-house solar cell test rig was built with the purpose of characterising cell parameters as the passivation was modified via the extrinsic field-effect. Figure 24.a illustrates the set-up. A BS472X xenon halogen lamp (H4, 12V, 60/55W) was encased in an Al-foil-wrapped

beaker and placed 7 cm above a base, where a cell holder was fitted with < 0.1 mm precision. The xenon lamp was chosen as it reproduced closely the sun light spectrum [141]. The light intensity of the lamp was measured by a silicon sensor placed in the stand. A current-controlled PID was programmed in Labview to maintain the light intensity constant for the time of the measurement, and was reproducible across measurements to better than 1%. An Agilent 34401A digital multimeter was used to measure the sensor short-circuit current while the lamp power was operated on a Thurlby-Thandar TSX3510P bench-top power supply. Once the light was set constant, the IV curve was traced using a Keithley 2611A source measure unit (SMU). Figure 24.b illustrates a typical IV curve obtained with such set-up. This set up under-illuminates the cell, as the power generated by a 2 x2 cm^2 cell is only a few tenths of milliwatts, while a same size 10% efficient cell would generate 72 mW under AM1.5 illumination. However, these measurements were useful to assess the changes in cell performance when the front surface passivation was modified in IBC cells.

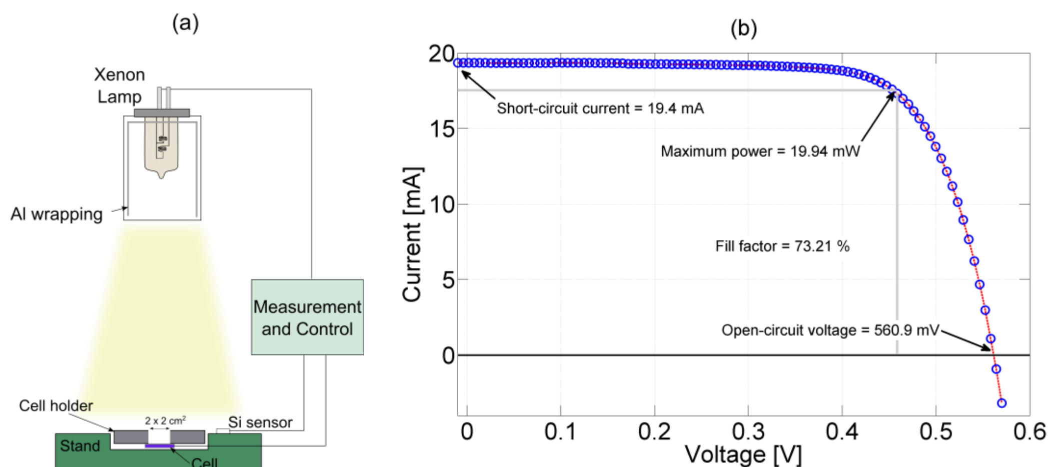

Figure 24: a. Schematic of in-house solar cell testing rig, b. IV curve taken on cell BC47-25C produced by Fraunhofer ISE.

2.5.5.2 *Standard testing conditions*

Testing of solar cells needs to be conducted under standardised conditions of illumination. For this purpose the American Society for Testing and Materials (ASTM) has produced a reference spectrum for photovoltaic performance evaluation in their ASTM G-173-03 standard. This spectrum is considered the standard testing condition (STC) for evaluating

solar cells and is the spectrum of sunlight that reaches the earth's surface, with 37 degrees south facing tilt and an absolute air mass of 1.5 [142]. A sun simulator that could produce such conditions was provided at Fraunhofer ISE in Freiburg, Germany. Their set up consisted of a Wacom high grade xenon lamp type AB-451, temperature controlled and calibrated according to ASTM G173, see Figure 25.a. A cell holder with a 2 x 2 cm^2 aperture was also provided to mount their IBC cells, together with a H&H voltmeter and an Agilent ammeter. Figure 25.b illustrates a standard tested IBC solar cell showing an efficiency of 20.2%. Standard testing conditions were used at Fraunhofer ISE to measure the effect of FEP on IBC cells.

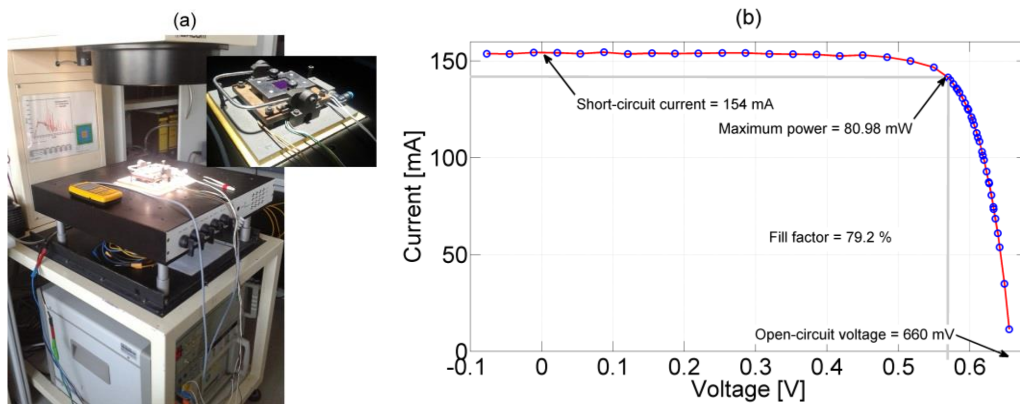

Figure 25: a. Photographs of the sun simulator at Fraunhofer ISE, b. IV curve taken on cell BC47-17G using standard testing conditions. The STC efficiency was 20.2%.

CHAPTER 3
EFFECT OF DIELECTRIC CHARGE ON SURFACE RECOMBINATION

Chapter 1 described the main mechanisms of recombination in silicon, including a brief account of surface recombination. A complete description of surface recombination will be developed in this chapter, with particular emphasis on the reduction of recombination via the electric field effect. For this, a theoretical model of surface recombination based on Shockley-Read-Hall statistics is revised, and a new parametrisation of density of interface traps and their capture cross section is proposed. This extension to existing theory allows the most accurate description to date of surface recombination for a range of dielectric charge and minority carrier concentrations in practical specimens. This new approach is applied to the thermal oxide / silicon system used throughout this project and, using the electron and hole recombination velocities and the density of interface traps as the only fitting parameters, it successfully describes the dependence of effective surface recombination with dielectric charge and carrier injection level over the whole range of experimental conditions used in this work.

3.1 Theoretical background

3.1.1 Shockley-Read-Hall surface recombination

In 1952, Shockley and Read, and later Hall, reported the first comprehensive study of injection dependent recombination of carriers via defects [19], [22], [29]. They proposed a

recombination rate as a result of detailed balance of emission and capture rates of both electrons and holes via a single defect located at an energy E_t. When the same recombination model is applied to the semiconductor surface, two important modifications need to be applied. Firstly, the semiconductor surface is a large crystal discontinuity and as such it produces a continuum of defect states in the band-gap that have to be considered. Secondly, the physical concept of carrier lifetime becomes ambiguous since it is expressed for carriers traveling to the surface rather than in the bulk, hence the need to define the surface recombination velocity. Surface recombination (U_s) is described by extending the Shockley-Read-Hall formalism to an arbitrary trap level density function [138]:

$$U_s = \int_{Ev}^{Ec} \frac{\left(n_s p_s - n_i^2\right)}{\frac{[n_s + n_1(E)]}{v_{th} D_{it}(E)\sigma_p} + \frac{[p_s + p_1(E)]}{v_{th} D_{it}(E)\sigma_n}} dE \tag{3. 1}$$

where D_{it} is the energy dependent density of interface traps, n_s and p_s are the carrier concentrations at the surface, v_{th} is the thermal velocity of carriers, σ_n/σ_p are the capture cross sections for electrons/holes and n_1/p_1 are the carrier concentrations at the trap states, as previously indicated in equation (1. 13). The surface recombination velocity disregarding recombination in the band-bent region is then obtained by combining equations (1. 16) and (3. 1):

$$S_0 = \frac{1}{\Delta p} \int_{Ev}^{Ec} \frac{\left(n_s p_s - n_i^2\right)}{\frac{[n_s + n_1(E)]}{S_p} + \frac{[p_s + p_1(E)]}{S_n}} dE \tag{3. 2}$$

Where Δp is the excess minority carrier concentration in n-Si, $S_p(E) = v_{th} D_{it}(E)\sigma_p(E)$ is the energy dependent recombination velocity for holes, and $S_n(E) = v_{th} D_{it}(E)\sigma_n(E)$ is the energy dependent recombination velocity for electrons. Physically, S_p and S_n represent the rate at which holes and electrons are captured independently. S_0, on the other hand, comprises the total recombination occurring at the surface as a result of capture of both types of carriers. An example calculation of S_0 using equation (3. 2) will now be

discussed for the case of negligible surface charge -i.e. no band bending. In this case the concentration of carriers in the bulk and at the surface is the same: $n_s = n_b$, $p_s = p_b$ where n_b and p_b are the bulk carrier concentrations.

Figure 26 illustrates the normalised surface recombination velocity (S_0/S_{p0}) as a function of excess minority carrier concentration for 1 Ωcm n-type silicon and different values of electron surface recombination velocities. Both S_n and S_p are considered energy independent, and will be referred to as S_{n0} and S_{p0}. Similar to the case of SRH lifetime at a single defect in the bulk, surface recombination velocity at low injection levels is dominated by the capture of minority carriers, hence the normalisation by $1/S_{p0}$. This plot is useful to determine the effects that electron and hole capture rates have on total SRV, and the form SRV takes when the capture rate of electrons is different to that of holes. This is referred to as the asymmetry between hole and electron recombination velocities. Despite a wide variation in S_{n0}, the SRV at low injection levels is approximately constant. For high injection levels however, both types of carriers contribute to recombination and thus the minimum S_0 (better from the point of view of passivation) is controlled by whichever of S_{p0} and S_{n0} is smaller. Figure 26 also shows the injection level dependence of SRV as the recombination velocity of holes becomes increasingly asymmetrical to that of electrons. This is an important characteristic since, as will be shown later, most silicon interfaces present such asymmetry. Figure 27 shows a plot of normalised SRV for various doping concentrations. Surface recombination increases with doping level. This makes highly doped silicon surfaces difficult to passivate, in particular for the injection levels solar cells normally operate at, $\Delta p \sim 10^{15}$ cm^{-3}. In this region S_0 is seen to increase by an order of magnitude when the surface dopant density increases by three orders of magnitude.

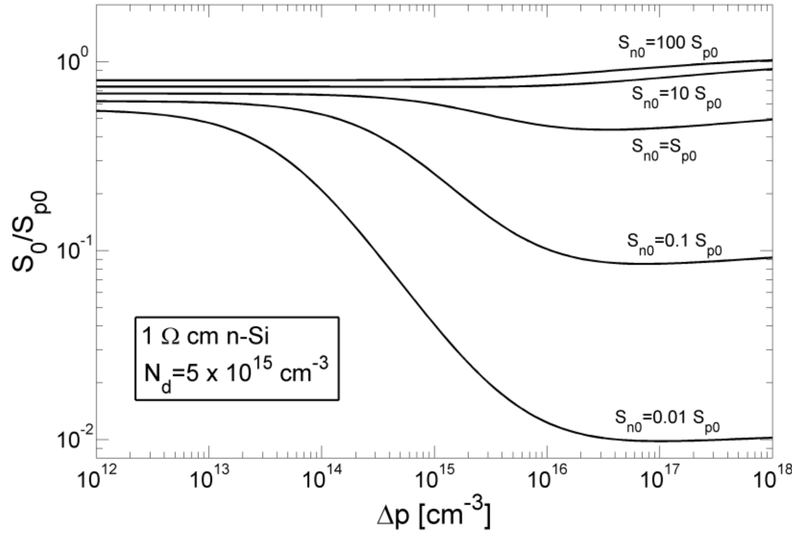

Figure 26: Calculated surface recombination velocity for a range of capture cross sections and excess minority carrier concentration. SRV is calculated using the extended Shockley-Read-Hall statistics of equation (3. 2).

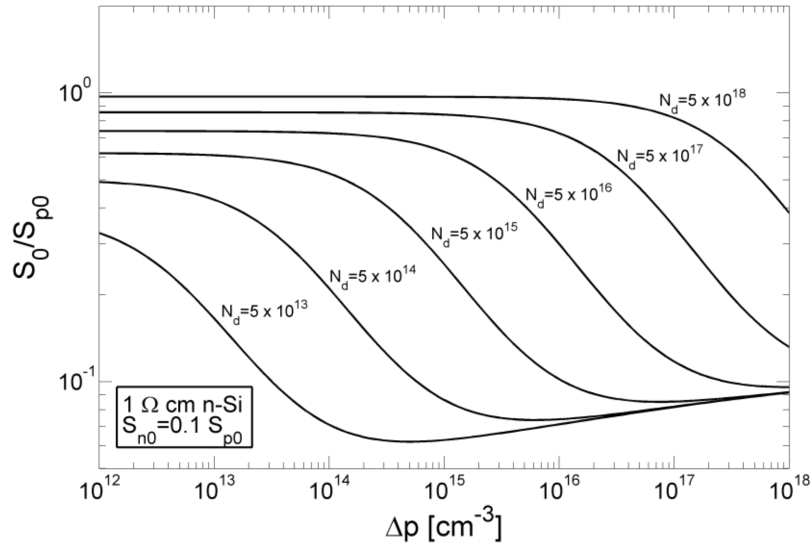

Figure 27: Calculated surface recombination velocity as a function of excess minority carrier concentration for different doping concentrations. SRV is calculated using the extended Shockley-Read-Hall statistics of equation (3. 1).

3.1.2 The effect of surface band bending

As mentioned in Chapter 1, a SCR normally forms near the semiconductor surface due to the presence of one or more of the following; external charge near the semiconductor surface, a metal gate with different work function or potential difference, a doping profile, or interface-trapped charge. The previously computed S_0 is an idealised case for surface recombination when no band bending occurs. In practical semiconductors surface band bending is always present, even in the absence of dielectric charge or gate electrodes. Intrinsic band bending

arises from charged states at the semiconductor surface, which are in turn balanced by near-surface semiconductor charge. Such surface trap states may be donor type (become positively charged when they donate an electron) or acceptor type (become negatively charged when they accept an electron). The total charge in surface defect states is therefore given by the sum of ionized donor and acceptor states:

$$Q_{it} = q\int_{E_v}^{E_c} D_{it,d}(E) f_d(E) dE - \int_{E_v}^{E_c} D_{it,a}(E)(1 - f_d(E))\, dE \qquad (3.3)$$

where the subscripts d and a in D_{it} indicate donor-like states, and acceptor-like states. f_d is the trap occupation probability for holes in donor states given by the SRH recombination model as [143]:

$$f_d = \frac{n_1 + S_r p_s}{(n_s + n_1) + S_r(p_s + p_1)} \qquad (3.4)$$

Where $S_r = S_{p0}/S_{n0}$ is the ratio between the hole and electron surface capture rate.

Regardless of the origin of semiconductor surface charge, the end result is a net change in the concentration of carriers at the surface. These depend both on the minority carrier injection level (Δp) and the band bending, that is the semiconductor potential as a function of depth $\phi(z)$. Figure 28 illustrates the band diagram and charge concentration of a semiconductor/dielectric interface when charge in the semiconductor balances fixed charge in the dielectric layer Q_f. Q_f is compensated by charge in the semiconductor both as filled interface defects, and as a near-surface space charge region (SCR). Computing $\phi(z)$ requires the simultaneous use of Poisson's equation and the continuity equations describing carrier dynamics. Such a solution can only be found using finite element simulation packages such as Sentaurus [144] and PC1D [145]. However, a numerical solution can be obtained by assuming that the quasi-Fermi energy levels are constant throughout the SCR. This assumption has been previously proven reasonable [146]. Such a calculation is achieved by

following an iterative procedure outlined by Girisch et al [138], and extended by Aberle et al [143] to include the steady-state generation of minority carriers by illumination.

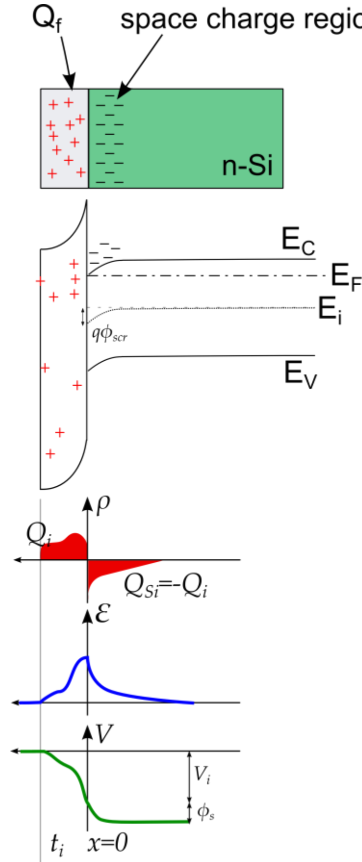

Figure 28: Schematic representation of the band bending problem at the surface of silicon due to charge present near and at the interface with a dielectric film.

Girisch and Aberle's algorithm goes as follows: Given a minority carrier concentration $n_b = n_0 + \Delta n$ and $p_b = p_0 + \Delta p$, quasi-Fermi levels are computed and assumed to be constant through the space charge region:

$$\phi_n = -\frac{E_i}{q} - \frac{kT}{q}\log\left(\frac{n_b}{n_i}\right)$$
$$\phi_p = -\frac{E_i}{q} + \frac{kT}{q}\log\left(\frac{p_b}{n_i}\right) \quad (3.5)$$

The assumption is made that when carriers are injected, sufficient time has passed and the system has achieved steady state such that generation and recombination is balanced and the steady state minority carrier concentration can be used to calculate band bending and

recombination rate. Quasi Fermi levels are used to find the semiconductor SCR potential ($\phi_{scr} = \phi(z = 0)$) that produces charge neutrality –i.e. minimises the system's total charge Q_T, by iterating:

$$Q_T = Q_f + Q_{Si} + Q_{it} \tag{3. 6}$$

for different values of ϕ_{scr} until $Q_T \to 0$. Q_f is the fixed external charge density, and Q_{Si} is the silicon charge concentration per unit area as shown in Equation (A. 15). The iterative procedure is necessary since both Q_f and Q_{it} depend on band bending and recombination at the silicon/dielectric interface. Each iteration produces a solution to the balanced system where all processes are considered to take place and be in steady state. When the solution that provides charge neutrality is found, the surface concentration of carriers is calculated as:

$$n_s = n_b e^{+\frac{\phi_{scr}}{kT/q}}$$
$$p_s = p_b e^{-\frac{\phi_{scr}}{kT/q}} \tag{3. 7}$$

which serves as the input parameters to equation (3. 1).

Using Aberle's algorithm it is possible to plot SRV as a function of excess minority carrier concentration for different concentrations of fixed dielectric charge, which in turn produce different levels of band bending. This normalised S_0/S_{p0} relation is illustrated in Figure 29. The density of interface states D_{it} used for this calculation is a typical value reported for the Si/SiO_2 interface [143], [147]. When the bands are bent, the concentration of one type of carrier is lowered while the other increases. For this example, the bands have been bent downwards due to a net positive dielectric charge. An increase in electron concentration occurs near the semiconductor surface, together with a depletion of holes. This is an accumulation regime for n-type Si. A substantial reduction in the concentration of one kind of carriers therefore produces a noticeable decrease in the amount of recombination that

can take place at the interface. This is because for SRH recombination to take place, both types of carriers need to be present within the capture cross section of the defect. Hence, once again, a depletion of the less available carrier (holes) limits the amount of recombination. This reduction in recombination is the basis of field effect passivation (FEP).

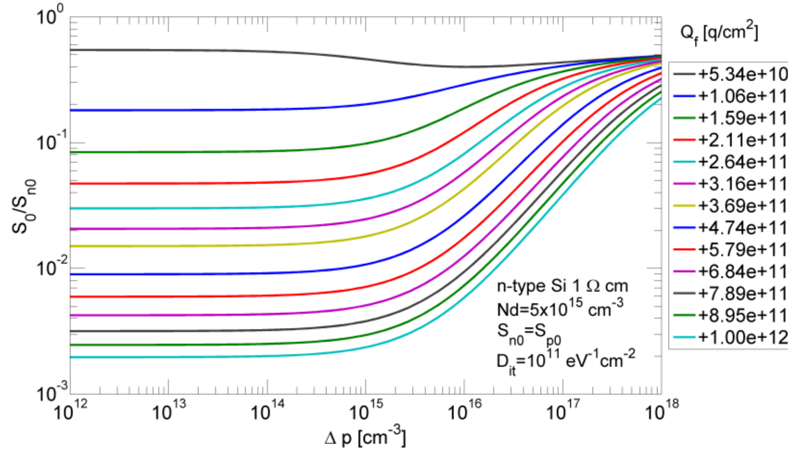

Figure 29: Computed surface recombination velocity as a function of excess minority carrier concentration for different semiconductor SCR potentials due to positive surface fixed charge. SRV is calculated using the extended Shockley-Read-Hall statistics on equation (3. 1). A constant D_{it} and $\boldsymbol{S_{n,p}}$ have been assumed throughout the band-gap, T=300 K.

3.1.3 Recombination in the space charge region

Recombination that takes place within a bent-band region (by distinction to that occurring at the interface states) also contributes to surface recombination as previously shown in equation (1. 17). It is found by integrating the volumetric SCR recombination rate U_{sc} over its depth:

$$S_{scr} = \frac{1}{\Delta \mathrm{p}} \int_0^{d_{scr}} U_{scr}(z) dz \quad (3.\ 8)$$

where the z axis is perpendicular to the semiconductor surface and increases towards the bulk, with d_{sc} being the edge of the space charge region, and Δp is the excess carrier concentration at the edge of the SCR. The integration in (3. 8) requires the knowledge of carrier density as a function of distance from the surface $n(z), p(z)$, and the surface band bending $\phi(z)$. Such calculation can only be done numerically. Example solutions can be found in detail in Mönch's book [148]. Here, a numerical solution to Poisson's equation was

found using a finite difference method that implements a Lobatto IIIa formula in Matlab [149]. For 1 Ωcm n-Si, for example, a surface charge of $+10^{12}$ q/cm^2 produces an SCR potential (band bending) of 0.1564 V when the excess minority carrier concentration is 10^{15} cm^{-3} (data from Figure 29). Figure 30 illustrates the $n(z)$ and $p(z)$ values calculated from a numerical solution to Poisson's equation for this scenario. The electric field and potential have also been included as they are the result of solving Poisson's equation.

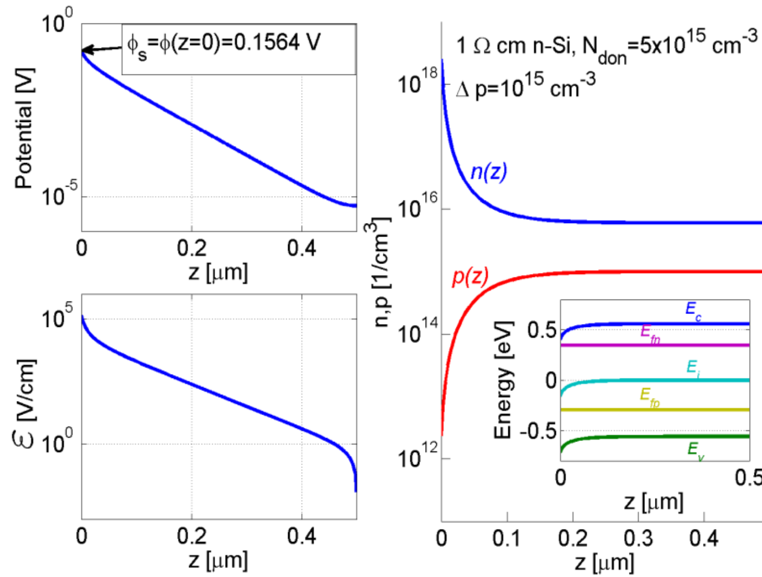

Figure 30: Computed electric potential, field and carrier concentration for 1 Ωcm n-Si with a surface charge of $+10^{12}$ q/cm^2 photo-injected with 10^{15} cm^{-3} minority charge carriers, T=300 K.

Recombination in the SCR can be Auger, radiative and SRH type. SCR surface recombination can then be calculated as:

$$S_{sc} = \frac{1}{\Delta \mathrm{p}} \int_0^{d_{sc}} (U_{Aug}(z) + U_{rad}(z) + U_{SRH}(z))dz$$

$$S_{sc} = \frac{1}{\Delta \mathrm{p}} \int_0^{d_{sc}} C_n(n^2p - n_0^2p_0) + C_p(np^2 - n_0p_0^2) + B(np - n_i^2) + \frac{np - n_i^2}{\tau_n(p + p_1) + \tau_p(n + n_1)})dz \quad (3.9)$$

where $n = n(z)$ is the semiconductor electron concentration as a function of depth and $p = p(z)$ is the hole concentration as a function of depth. All other parameters are

equivalent to those defined in Chapter 1 for Auger, radiative and SRH recombination. The edge of the space charge region is defined as [150]:

$$d_{sc} = \sqrt{\frac{2\epsilon_s |\phi_s|}{qN_{don}}} \quad (3.10)$$

Figure 31 illustrates the contribution of SCR recombination towards the overall surface recombination velocity for both polarities of charge –i.e. upward and downward band-bending. The Auger and radiative components, and the SRH component of SCR recombination have been plotted independently. In Figure 31 SRV is normalised as $S_{SCAug+Rad}/S_{p0}$ for the Auger and radiative terms, and $S_{SC,SRH} * \tau_{p0}$ for the SRH term. This allows a percentage comparison to Figure 29 . A typical density of interface states D_{it} for Si/SiO_2 was used here [143], [147]. Auger and radiative SCR recombination contribute negligibly to the total SRV. For a negative dielectric charge an inversion region is formed near the n-type silicon surface and thus, at a characteristic depth from the surface, the concentration of both types of carrier equalizes. For these conditions higher recombination is observed yet it contributes to less than 0.1% of the total recombination. For the SRH recombination term, a deep state with symmetrical lifetime has been assumed. Similarly, only when the surface is inverted (Q_f<0) this term substantially contributes to surface recombination. This contribution is more prominent for SRH type recombination than for intrinsic Auger and radiative. Overall, SCR recombination is a negligible source of surface recombination. Significant SCR recombination only occurs when the defects present in the SCR are active recombination centres and thus the carrier lifetime associated with the SRH term is small, for example $\tau_{p0} <$ 1ms.

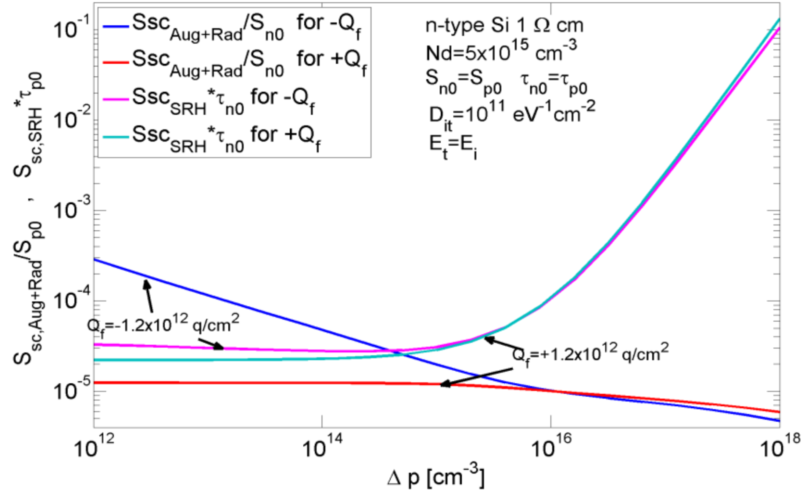

Figure 31: Computed normalised space charge region recombination for 1 Ωcm n-Si with a surface charge of $\pm$ 1.2 x 10^{12} q/cm^2 as a function of minority charge carriers concentration, T=300 K. Auger recombination is calculated using Richter's parameterisation [28].

Literature reports normally account for such SCR recombination using a recombination current J_2 [26]:

$$J_2 = J_{02}\left(e^{\frac{V_{oc}}{mkT}} - 1\right) = J_{02}\left[\left(\frac{\Delta\text{p}}{p_0} + 1\right)^{\frac{1}{m}} - 1\right] \tag{3. 11}$$

where m is the ideality factor, normally set to 2, hence the 'J_{02}' name, and J_{02} is the saturation current density. Previously reported values for J_{02} have been arbitrarily chosen for theory to match experiments [26], [151]–[153], and the injection dependence of J_2 does not compare to that shown in Figure 31. The need for an SCR recombination term will be discussed in the next section. Here it is noted that the SCR recombination due to the intrinsic Auger and radiative mechanisms is negligible and hence will not be considered hereafter.

3.2 Development of the model for surface recombination

The previous section explored a solution to SRH surface recombination using Aberle et al's [143], [154] algorithm. In Aberle's report, however, experimental evidence for S_{eff} =

$f(\Delta p, Q_f)$ was limited to a single value of dielectric charge. Their study entailed fitting values of the model parameters so that theory matched the experiments for the one value of dielectric charge that had been present in the specimens studied. Hence, the dependence of recombination on varying dielectric charge predicted by the model could not be verified. Indeed the model predicted values of SRV well below 1 cm/s when enough charge was present in the dielectric –e.g. Figure 29, yet such values have so far been rarely achieved experimentally. Additionally, an increase in SRV has been experimentally observed at low minority carrier injection levels, which is not accounted for in the aforementioned model. Several reports have addressed this discrepancy by proposing an enhanced recombination region near the surface yet this hypothesis remains unsupported by direct experimental evidence. Field effect passivation of silicon has been known for decades [33], yet no report of a modelling formalism exists in the literature where a wide range of both variables, minority excess carrier density and fixed dielectric charge, is considered, and the increase in SRV is addressed and supported with direct evidence. Studies such as those of Dauwe et al [155] and Weber et al [156] used a single minority carrier injection level and varied the dielectric charge concentration, while Kho et al [62] reported a more complete model, yet the experiments did not support the proposed model parameters. In general, when the reported data has been fitted to only one of the two independent variables, the same modelling parameters do not provide a correct dependence on the remaining variable. In the following a new parametrisation is suggested, such that the surface recombination velocity is accurately modelled over a range of both independent variables; dielectric fixed charge and excess minority carrier concentration. This modelling describes interface recombination without the need to introduce a term for enhanced near-surface recombination, and it separates the contribution of interface trap states and field effect with regard to total surface recombination. It also allows the estimation of the value of holes' and electrons' surface recombination velocities, interface trap density and their capture cross sections directly from surface recombination experiments.

3.2.1 Recombination in a near-surface region

Early reports on the theory of surface recombination predicted values of SRV well below 1 cm/s with moderate concentrations of dielectric charge. Experimentally, these were never observed, and even more an increase in SRV was seen at low minority carrier injection levels, contrary to what the theory predicted. Glunz et al [26] were first to address these discrepancies by suggesting three extensions to the SRH formalism; in-homogeneities in charge distribution, carrier recombination in the space charge region (SCR) due to tunnelling, and carrier recombination at highly active surface bad spots. Using these additions, Glunz et al modelled the SRV dependence on both dielectric charge and minority carrier concentration, but fitting of theory to experimental data was only carried out using a single independent variable; either one minority carrier injection level or one dielectric charge concentration, neither did they present additional experimental evidence supporting the extensions. Non-uniformity of charge can be verified using Kelvin probe and capacitance-voltage (CV) maps of dielectric charge [157] and can be largely minimized as shown in [121]. SCR recombination on the other hand, was argued to arise from carrier tunnelling towards surfaces states and carriers recombining at an enhanced recombination region near the surface [26], [155], yet experimental evidence of neither has been reported, in particular for the Si/SiO_2 system. Thermally grown silicon dioxide has been the basis for MOSFET technology and no evidence of such near surface recombination has been found.

Currently, the presence of a region of enhanced recombination near the surface is suggested to be the most likely cause of high SRV at low injection levels [152]. This has been defined as a surface-damaged region (SDR). Enhanced SRH recombination in the SDR would explain the observed SRV dependence, yet its origin remains unclear [158]. Section 3.1.3 showed that SCR recombination is only significant when SRH-type defects are present in the near surface region, and have strong recombination activity. Using this, various models have been proposed to introduce near surface or SDR recombination in the modelling

formalism – e.g. ref [151], [152], [158], but these lack a reasonable physical basis as there is no experimental evidence that such a defect region exists. Further, a recent report indicates that high SRV at low injection levels is an artefact in the measurement due to the sample size and the lack of uniform passivation, particularly on the specimen edge [159]. Other reports, however, still support the surface damage region extension, in particular in CVD deposited dielectrics such as SiN_x and AlO_x [153], [160]. Glunz's extensions remain the most appealing for surface recombination modelling. However, the development of the model in sections 3.2.2 to 3.2.3 will show that SRV can be described without introducing a term for near-surface recombination and is thus able to account for recombination at the interface between Si and thermally grown SiO_2 and other dielectrics without the introduction of an "unphysical" surface defect region.

3.2.2 The effect of electron and hole recombination in effective SRV

Previously reported calculations of SRV have used direct measurements of the density of interface traps (D_{it}) and the hole and electron capture cross sections ($\sigma_{p,n}$). These have been measured using the DLTS technique and have been input directly into the formalism. The accuracy of DLTS characterisation of D_{it} and $\sigma_{n,p}$ depends strongly on the signal-to-noise ratio of the measured transients, the level of accuracy of the temperature measurement, the extent of the temperature range, and method of evaluation used [161]–[164]. Moreover, this method relies on simulations [165] and only provides values of D_{it} and $\sigma_{n,p}$ for half of the band-gap [166]. Lastly, the Si/SiO_2 interface characteristics depend on the growth conditions and post-growth physical and chemical treatments [167]. Although these studies provided a remarkable insight into the Si/SiO_2 interface, in particular for the development of MOSFET technology, their lack of accuracy, precision, completeness and agreement has translated into an imprecise theoretical formulation of SRV. This has been overcome in this project by extending the SRV formalism to include a parametrisation of the product $D_{it} \times \sigma_{n,p}$. An energy dependent surface recombination velocity for holes and electrons is used for this

purpose. $S_{p/n}(E)$ lumps these two fundamental interface properties together in the same way that carrier lifetime is used in the single defect SRH model, yet $S_{p/n}$ is taken as an energy dependent parameter. An additional advantage of using $S_{p/n}(E)$ is that it relates directly to the ability of surface defects to capture carriers, and thus seeking the value of $S_{n/p}(E)$ that accurately describes the total surface recombination is easier. This will become clear in the next section where this formulation is applied. In this section, the effect $S_{p/n}$ has on total SRV is studied, and particular emphasis is put on its energy dependence.

D_{it} and $\sigma_{p,n}$ are energy dependent quantities commonly parametrised as Gaussian functions [26]. Measurements of D_{it} using Terman's [168], Berglund's [169], Castagne and Vapaille's [170], or Nicollian and Goetzperger's [131] methods demonstrate that an inverse Gaussian function best describes the dependence of D_{it} with energy. Similarly, $\sigma_{p,n}$ measured via DLTS [143], [167] has been best described by a Gaussian function. The product between a Gaussian function and an inverse Gaussian function is Gaussian too. Previous models have shown that the energy dependence of $\sigma_{p,n}$ is larger than that of D_{it}. This means that in their product, the dependence of $\sigma_{p,n}$ would prevail over that of D_{it}. The resulting function is therefore an inverse Gaussian:

$$S_{p,n} = S_{0p,n} e^{-a_{n,p}\left(E-E_{0p,n}\right)^2} \qquad (3.\ 12)$$

where $S_{0n/p}$ is the mid-value of the function, which characterises the maximum surface recombination rate for each carrier type at an energy E_0 (the centre of the function). a is the curvature of the function, which represents how strongly $S_{n,p}$ depends on the energy where the trap states are located.

An assessment of the influence of equation (3. 12) on equation (3. 1) shows that S_{eff} increases whenever the mid-value ($S_{0n/p}$) increases for either holes or electrons. However, if the dependence of S_{eff} on dielectric charge Q_f is considered, it is clear that surface recombination is governed by S_{0n} when negative charge is present in the dielectric, or by S_{0p}

when positive charge is present in the dielectric. This can be inferred from the carrier concentrations at the surface. When positive charge exists in the dielectric, holes in the semiconductor are repelled from the surface, while electrons are attracted. Recombination is dependent on the concentration of both types of electrical carriers, and it is limited by the less available carrier, in this case the holes. Consequently, for a given positive and negative dielectric charge concentration, the minimum value of S_{eff} is given by S_{0p} and S_{0n} respectively. The maximum value of S_{eff}, on the other hand, depends on both S_{0p} and S_{0n}, and occurs when the concentration of electrons and holes at the surface is balanced so that $S_n n_s = S_p p_s$. This occurs at a moderate (~ 10^{10} q/cm^2) negative dielectric charge concentration for n-type Si, or positive charge for p-type Si.

The dependence of $S_{n,p}$ on energy is given by the function curvature $a_{p,n}$, which can only take positive values. When the curvature of either function increases, $S_{n,p}$ decreases around its maximum, $S_{0n/p}$ at E_0, and a smaller tail of states is observed towards the centre. Smaller values of $S_{p,n}$ mean poorer capture of carriers, so that the larger the curvature, the smaller the effect on the total S_{eff}. This is illustrated in Figure 32 where S_{eff} is plotted as a function of dielectric charge for a single carrier injection level. The $S_{p,n}$ functions are included and the effect of a higher curvature/dependence with energy is signalled by the arrows. SRV functions have been centred at the mid-point of the upper and lower half of the band-gap, following capacitance-voltage and deep level transient spectroscopy data reported in the literature [26].

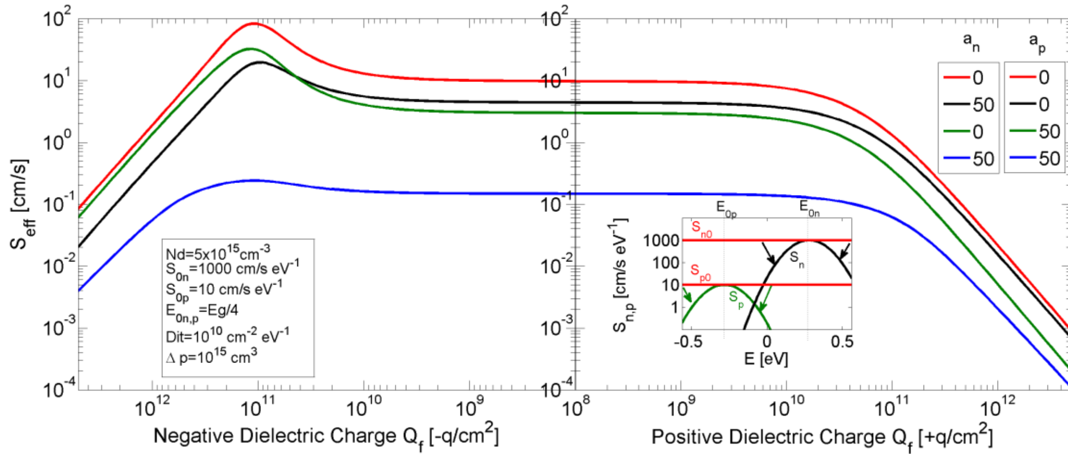

Figure 32. Surface recombination velocity for n-type silicon as a function of positive and negative dielectric fixed charge concentration in q/cm^{-2}, for an excess minority carrier concentration of 10^{15} cm^{-3}, and a variation in the surface recombination of holes and electrons given by the curvatures a_n and a_p. Four combinations of a_n, a_p have been chosen as illustrated by the legend in the figure. Inset: Holes (green) and electrons (black) surface recombination functions used to calculate surface recombination velocity. Red horizontal lines represent the value the functions take when the dependence is eliminated ($a_0 = 0$).

From Figure 32 it is clear that $S_{0p} < S_{0n}$ produces a smaller S_{eff} for a given positive charge, versus that S_{eff} of the same negative charge. Similarly, increasing the curvature of S_p reduces surface recombination for positive dielectric charge and increasing the curvature of S_n reduces it for negative dielectric charge. If both hole and electron SRV functions have a high curvature parameter, then the overall recombination is reduced as illustrated by the blue trace in Figure 32. It is also evident that the negative dielectric charge, at which the kink is produced in Figure 32, is directly dependent on the ratio of hole surface recombination to electron surface recombination $S_r = S_p/S_n$.

The centre or axis of the SRV Gaussian functions determines the position in the band-gap where recombination is most likely to happen. For the case in Figure 32 the functions are centred at one quarter of the band-gap energy above the valence band for holes, and below the conduction band for electrons. Similar to the standard SRH theory, deep level impurities are stronger recombination centres than shallow level impurities. Moving the function axis (E_0) is equivalent to shifting the energy level of the maximum recombination rate. Hence, when the maximum is moved towards the centre of the band-gap –i.e. deeper, the probability of recombination is promoted and the surface recombination velocity

increases. On the contrary, when both function centres are shifted away from the mid-gap, trapping is less efficient and the surface recombination velocity decreases.

3.2.3 Effect of interface charge concentration

In the previous section, a new parametrisation was proposed where D_{it} and $\sigma_{p,n}$ were integrated into the surface recombination velocities for holes and electrons. In order to calculate the concentration of charge at the interface, Q_{it} in equation (3. 3), a separate D_{it} parameter is required. The calculation of Q_{it} is the subject of this section.

Semiconductor interface charge strongly influences the value of SRV. When dielectric charge is compensated in the semiconductor, some of this compensating charge can be found occupying interface states rather than modifying the near surface carrier concentration. The higher the concentration of states at the surface, the fewer the carriers needed in the semiconductor to compensate the dielectric charge, and therefore a smaller change in surface carrier concentration occurs and recombination is not as effectively reduced. Although D_{it} has been best described by an inverse Gaussian function, additional extensions have been proposed by adding exponential tail functions to model the high density of states near the band edges [26], [171]. However, the high density of states near the band edges contributes negligibly to the recombination activity at the surface. This is a consequence of the extended SRH algorithm as described in section 3.2.2. D_{it} has been experimentally observed to depend weakly on energy near the mid-gap, but depend strongly near the band edges [171]. In this study it is proposed that a three term exponential function best models D_{it}. The first term represents the mid-gap density of interface states D_{it0}, the second density of states near the conduction band-edge, and the third the density of states near the valence band-edge:

$$D_{it}(E) = D_{it0} + D_{itC}e^{m_C E + E_{0C}} + D_{itV}e^{m_V E + E_{0V}} \tag{3. 13}$$

where $E_{oC,V}$ represent the energy at which the tail of states near the edges equals that of the middle of the gap. As suggested by Sze, it is useful to define a neutral energy level E_0 that separates acceptor-like and donor-like traps in the band-gap [20]. The total charge in surface defect states is therefore given by a modified form of equation (3. 3):

$$Q_{it} = q \int_{E_D}^{E_0} D_{it,d}(E) f_d(E) dE - \int_{E_0}^{E_C} D_{it,a}(E)(1 - f_d(E))\, dE \tag{3. 14}$$

The value E_0 takes has been previously suggested to be near the mid-gap [171], [172]. Simulations conducted in this thesis corroborated that a value of neutral energy E_0 in the range $-E_g/4 < E_0 < +E_g/4$ had a negligible effect on SRV, thus a value of $E_g/2$ is assumed and this is not considered further.

The effect of D_{it0} on S_{eff} is first explored in Figure 33 (black and green curves), by assuming $D_{itC} = D_{itV} = 0$. Values of $S_{p/n}$ and D_{it0} commonly reported in the literature were used and S_p, S_n were kept constant so that variations in D_{it} only affected the interface charge concentration and not the carrier dynamics. An increase in the mid-gap trap density D_{it0} is seen to increase S_{eff} for small values of dielectric charge $|Q_f| < 10^{11} q/cm^2$. This is a direct consequence of having more charge stored in surface traps, rather than compensated in the near-surface region. As more states become available at the interface, less charge is compensated and the field effect is lost, allowing for more recombination at the surface. This is an important fact, as it indicates that if better chemical passivation is provided (smaller D_{it}), the effectiveness of dielectric charge to produce FEP is increased and hence less charge is necessary in the dielectric. Note that this effect is in addition to that normally associated with chemical passivation namely that a reduction in surface states directly reduces the number of sites available for recombination. Conversely, if not enough chemical passivation is provided, then effective passivation can only be achieved using substantial concentrations of dielectric charge.

The increase in D_{it} near the band-edges is represented by the second and third terms in equation (3. 13). When D_{it} increases near the conduction band –i.e. higher D_{itC}, S_{eff} is seen to decrease its dependence on charge for positive dielectric charge (red curve in Figure 33), but no change is observed for negative dielectric charge (green curve in Figure 33). This change of dependence (slope) is due to the increased compensating charge present at interface states rather than in the near surface SCR. In the absence of such defect state charge concentration, the number of electrons in the conduction band would be higher and S_{eff} would be further reduced. Similarly, when D_{it} increases near the valence band (D_{itV}), S_{eff} dependence with negative dielectric charge decreases, since a bigger portion of the compensating positive charge is now present at interface states rather than in the SCR (blue trace in Figure 33). The dependence of S_{eff} on interface compensated charge has been found to be a very important parameter involved in modelling S_{eff}, as will become clear in the section 3.3 when analysing experimental data.

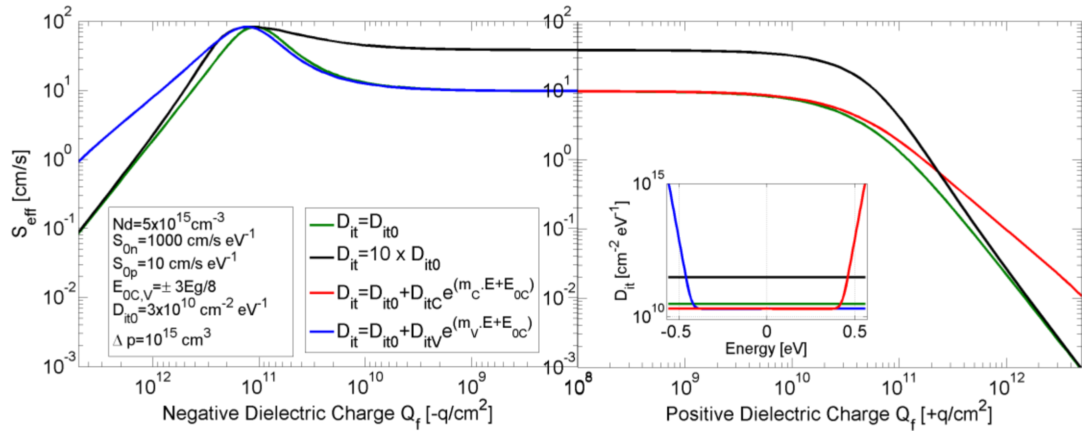

Figure 33. Effective surface recombination velocity for n-type silicon as a function of positive and negative dielectric fixed charge concentration, for an excess minority carrier concentration of 10^{15} cm^{-3}, and a variation in the charge stored at surface states Q_{it}, given by the dependence on D_{it}. The green trace illustrates SRV when $D_{it}(E) = D_{it0}$, blue trace when $D_{it}(E) = D_{it0} + D_{itV}e^{m_V E + E_{0V}}$, red trace when $D_{it}(E) = D_{it0} + D_{itC}e^{m_C E + E_{0C}}$, and black trace when $D_{it}(E) = D_{it0} + D_{itC}e^{m_C E + E_{0C}} + D_{itV}e^{m_V E + E_{0V}}$.

3.2.4 Discussion

This section has set out the theoretical formalism required to describe carrier recombination at the silicon surface. The extended Shockley-Read-Hall model was used, and carrier

dynamics parameters (σ, D_{it}) were lumped together into a parameter that relates directly to the velocity with which holes and electrons are independently captured at the surface. The direct physical interpretation of this parameter helps estimate their values. Charge concentration at the interface Q_{it} was also parametrised, and it was seen to greatly influence the dependence of S_{eff} with Q_f. The new parametrisation approach has proven to be advantageous in understanding recombination at the oxide/silicon interface, particularly when considering the effect of capture of electrons and holes, and the influence of interfacial charge. The model development has also provided an overview of the effect that excess minority carrier density and dielectric charge concentration have in effective SRV. Overall, this theoretical model provides a valuable insight into the dynamics of carriers at the surface of semiconductors. This will be used in the next section to infer the characteristics of the interface between silicon and silicon dioxide.

3.3 Case study: FEP of oxidised n-type silicon

This section presents a case of study of the expanded modelling approach proposed, and serves to demonstrate the effectiveness of extrinsic field effect passivation. Previous research has mainly focused on the effect of the surface charge on the effective lifetime of silicon for one excess minority carrier concentration or one surface charge density [63]–[65]. Here, the dependence of surface recombination velocity on both independent variables is explored. An investigation of excess minority carrier concentration from 10^{13} to 10^{16} cm^{-3} and dielectric charge concentration from -2 x 10^{12} to 2 x 10^{12} q/cm^2 is performed. By exploring both variables simultaneously, it is possible to suggest the interface properties that provide the best model for the experimental data obtained. The methodology to study the effect of charge on FEP of silicon is first described. Experimental lifetime data is then converted to SRV and the modelling formalism is applied to find the theoretical parameters that describe this Si/SiO_2 interface.

3.3.1 The effect of corona charge on effective lifetime

Field effect passivation has been applied to n-type FZ silicon using corona discharge. Improvements in surface passivation have been extracted from measurements of effective lifetime for 200 μm thick wafers with resistivity 1 Ωcm, dry oxidised to 100 nm. These were first cut into 3 x 3 cm^2 specimens and subsequently deposited with charge using corona discharge rig 2. Chapter 4 will describe the conditions of the charging process. Charge deposition was immediately followed by a photo-conductance decay lifetime measurement and a KP measurement of charge concentration. This three-step measurement methodology (corona charge – lifetime – KP) was repeated until the change in lifetime with increasing surface charge was minimal.

Kelvin Probe mapping was used to assess the uniformity of the charge deposited. Chapter 2 described the experimental set up that provided charge deposition uniformity better than 5%. The modelling formalism set out in section 3.1 and Appendix A also provides the relation between semiconductor SCR potential ϕ_{scr} and dielectric charge Q_f. If computed using previously reported parameters [26], the variation in SCR potential for a 5% variation in dielectric charge is ~ 5 mV, when $Q_f \sim 10^{12}$ q/cm^2. This is less than 3% variation in semiconductor SCR potential for the range of dielectric charge studied, and thus in-homogeneities in charge distribution are not considered in this work.

One additional measurement is necessary since oxide films normally exhibit an intrinsic charge concentration, which generally resides very close to the oxide-semiconductor interface [173] and therefore is not detected by KP measurements, see section 2.5.4. The intrinsic oxide charge concentration must be measured by different means in order to have a correct relation between SRV and the total dielectric charge Q_f. In this work, high frequency capacitance-voltage measurements were made on specially fabricated metal-oxide-semiconductor (MOS) capacitors from the same wafer. The flat-band voltages obtained using CV measurements (see Appendix A) implied that for the specimens used in this experiment

an intrinsic charge concentration of ~ +3 x 10^{11} q/cm^2 resided at the oxide/silicon interface. The charge concentration obtained via KP measurement was corrected to account for the intrinsic charge concentration in the oxide films. This correction was performed for every set of specimens investigated, since intrinsic dielectric charge is very sensitive to deposition or growth parameters.

The measured effective lifetime as a function of total dielectric charge is illustrated in Figure 34. For this sample (n6b_3), positive polarity charge was first deposited and an increase in effective lifetime was recorded, right plot in Figure 34. This increase in lifetime is directly related to improved surface passivation via FEP as expected from the theory. Charge deposition was conducted in 5 second intervals until the increase in lifetime was minimal (less than 5% between steps). In this way the dielectric charge was taken from 2 x 10^{10} q/cm^2 to over 2 x 10^{12} q/cm^2. Afterwards the sample was rinsed with IPA to remove all charge [174] and negative polarity charge was deposited in similar steps, left plot in Figure 34. As predicted from theory, an initial decrease in effective lifetime (higher SRV) is observed when small concentrations of negative charge are present on the dielectric. This is indicated by the arrows in Figure 34. The starting charge concentration is represented by the black trace, Q_f =1.2 x 10^{10} q/cm^2 . Negative charge is then deposited to take the total dielectric concentration to -9 x 10^{10} q/cm^2, blue trace. Maximum recombination (minimum lifetime) is observed when negative charge is deposited and Q_f =-3.7 x 10^{11} q/cm^2, green trace. Further deposition of negative charge then reduces surface recombination (increases lifetime) as shown by the red curve onwards. The scatter seen at low injection levels, below 10^{14} cm^{-3}, is a measurement artefact given by trapping and releasing of carriers [175]. Curves where the effective lifetime is below 200 μs were measured using quasi steady state PCD instead of transient PCD as suggested by Sinton [126].

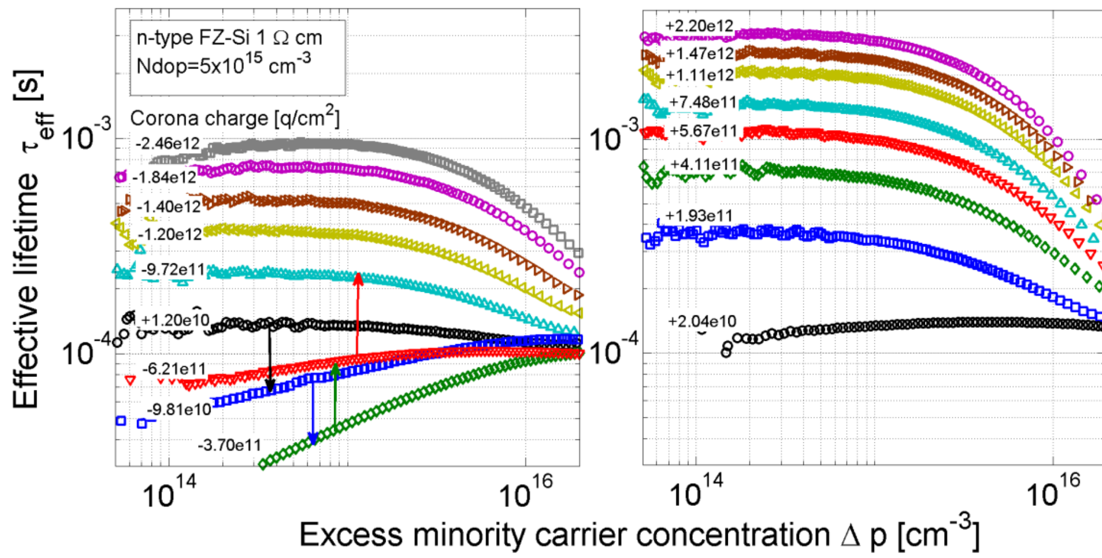

Figure 34. Lifetime measurements of n-type ⟨100⟩ FZ Silicon (1 Ωcm) passivated with a 100 nm-thick thermal oxide (Sample n6b_3), for negative (left) and positive (right) corona deposited surface charge (q/cm^2). Arrows in the left graph illustrate the sub sequential charge deposition steps: Effective lifetime is first reduced (blue and green) when negative charge is deposited, but further deposition of negative charge then increases lifetime (red and turquoise).

3.3.2 Modelling surface recombination for Si/SiO_2

Field effect passivation provided by dielectric charge has been demonstrated to reduce surface recombination and thus increase the effective lifetime of oxide passivated silicon. In order to apply the modelling formalism in sections 3.1 and 3.2, experimental lifetimes must be translated to values for SRV at the Si/SiO_2 interface. Chapter 2 described the relation between effective lifetime and SRV. Figure 35 illustrates SRV as a function of positive and negative dielectric charge concentration Q_f for three different minority carrier injection levels Δp. Data points in Figure 35 indicate the measured values of S_{UL} for the three different Δp, while the solid lines represent the theoretically calculated S_{eff}. These values of Δp were chosen as the most representative in the domain of interest, 10^{13}-10^{16} cm^{-3}. Using the theory set out in sections 3.1 and 3.2, values for D_{it}, S_n and S_p were selected so that the model best fitted the experiments. The search for parameters started from known previously reported values [26], [143], [171], and those calculated from results of CV measurements [121], [171]. The value of each parameter was kept within a range where they were

physically meaningful, while still providing a good agreement between theory and experiments. The observations made in section 3.2 provided the frame of reference to empirically find an accurate parametrisation of SRV. Figure 35 however, only illustrates three minority injection levels. Injection dependent plots of SRV for different values of dielectric charge are illustrated in Figure 36 for the same set of measurements as in Figure 34. Here experimental SRV has been calculated using equation (2. 7), and modelled S_{eff} has been calculated for each dielectric charge. The concentrations of dielectric charge used in the simulated curves, however, differ from the ones measured via KP, previously quoted in Figure 34. For $Q_f < 5 \times 10^{11}$ q/cm^2 this discrepancy is due to the non-uniformity of the oxide intrinsic charge, which can only be controlled during film growth. For high charge concentrations $Q_f > 5 \times 10^{11}$, the accuracy of charge measurements using KP is reduced due to the high values of KP surface potential measured. When the KP potential measured is outside the bias range of the instrument, extrapolation is required as described by the Baikie's method [134], and the accuracy is reduced. However, the difference between modelled and measured Q_f taken here is acceptable considering that the uniformity of the measured dielectric charge concentration was ~ 5%, as reported previously for this set of specimens.

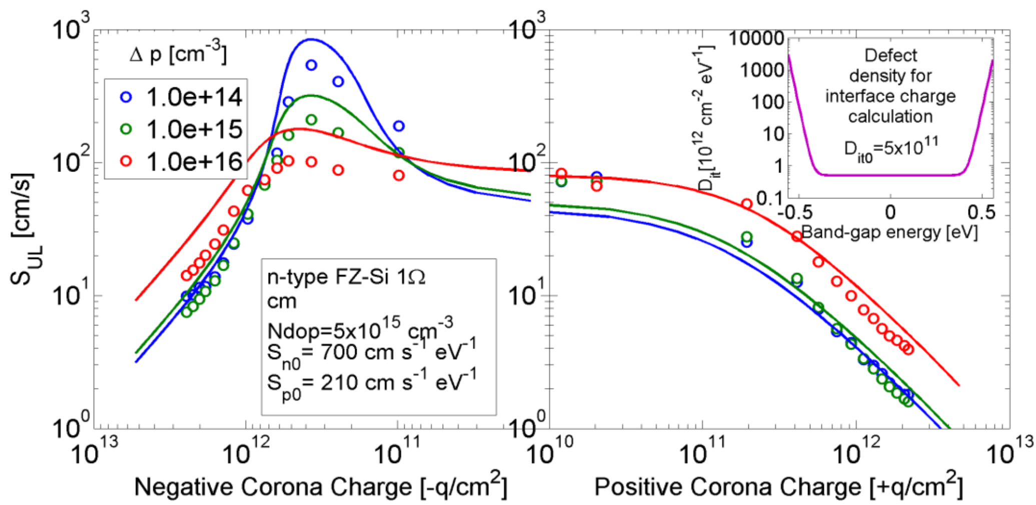

Figure 35. Surface recombination velocity measurements and simulations as a function of negative (left) and positive (right) corona deposited surface charge [q/cm^2], for three excess minority carrier concentrations (Sample n6b_3).

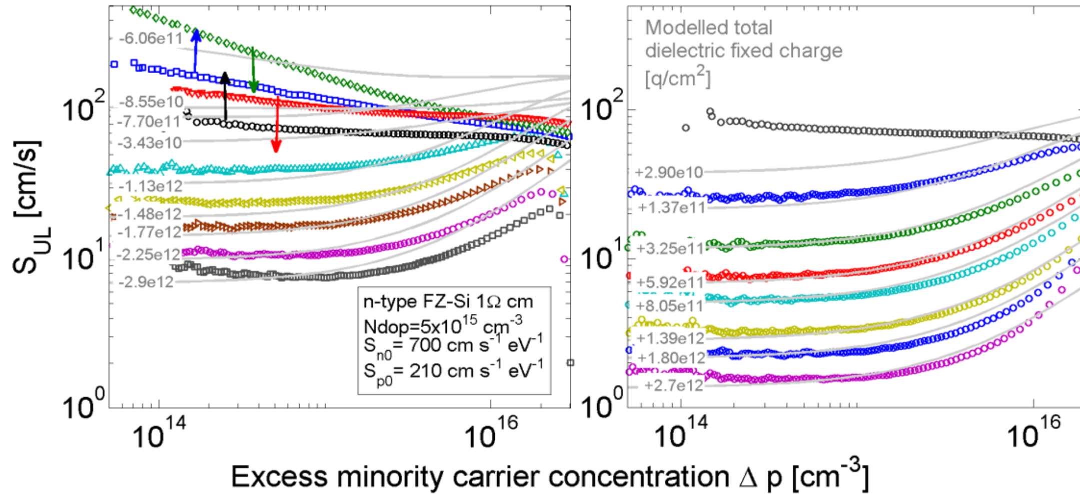

Figure 36. Surface recombination velocity measurements and simulation for n-type FZ Silicon passivated with a 100 nm thermal oxide (Sample n6b_3). Negative (left) and positive (right) surface dielectric charge concentrations are in [q/cm^2]. This data is the equivalent SRV from data shown in Figure 34.

3.3.3 Discussion

This section has presented experimental evidence of the reduction in surface recombination achieved via FEP. For this, an experimental methodology has been set up to extrinsically modify and measure the concentration of charge on a SiO_2 film. A characterisation of the uniformity of charge was conducted with a lateral resolution of 1 mm, and the methods used produced surface charge uniformity to better than 5%. This demonstrates that, given controlled deposition of surface charge, the first extension proposed by Glunz et al [26] to account for surface potential variations is unnecessary given the large scale (~mm) of lifetime and surface potential measurements. Effective lifetime was recorded as a function of minority carrier concentration and total dielectric charge concentration, as presented in Figure 34. This data shows the potential of field effect passivation in reducing surface recombination. An increase in effective lifetime of over 18-fold was demonstrated for the studied range of excess minority carrier concentrations, surpassing any other reported data on the potential of field effect passivation [62], [147], [156]. The influence of such low recombination on solar cell efficiency is difficult to assess due to the other factors in the cell fabrication process. Nonetheless, modelled solar cells have been reported to obtain up to 2% absolute increase in efficiency due to reduced surface recombination [117], [176]. Chapter 6

of this thesis explores this in more detail. The possibility of such an increase in efficiency confirms that controlled and extrinsic FEP is a potential method for providing surface passivation to industrial scale solar cells, particularly when the techniques, as used here, are fast and inexpensive. Figure 34 also reveals the difference in passivation provided by positive versus negative charges. This asymmetry is a characteristic feature of the interfacial physical properties. It can be quantified by computing the ratio $S_{eff}(-Q_f)/S_{eff}(+Q_f)$. It was empirically found that such a value was proportional to the ratio of surface recombination of holes to that of electrons $S_r = S_{p0}/S_{n0}$, and hence it provides an indication of the values $S_{n,p}$ should take in the theoretical model. For example, at a charge concentration of $\pm 5\ x\ 10^{11}$ q/cm^2, the ratio of SRV for positive to negative charge is ~0.1, for the range of injection levels here studied. Therefore, it is expected that the chosen values of S_{p0} and S_{n0} that best match the experimental observations is in the range [0.1-0.4]. Here this value was determined to be $S_r \sim 0.3$. This experimental rule contributes to the understanding of the Si/SiO_2 interface, and it reduces to one variable the search for parameters that best describes the $S_{eff} = f(Q_f, \Delta p)$ relation, which includes $S_n, S_p,\ D_{it0}, D_{itV}$ and D_{itC}.

This is the first time such a complete set of lifetime and charge measurements is reported for FZ silicon. Kho et al [62] reported the effect of positive charge on effective lifetime of oxide passivated n-type FZ silicon. Their measurements differed greatly from those shown here in several aspects: First, in their work the minority concentration at which the lifetime is at a maximum is 10^{15} cm^{-3}, with a prominent peak. Kho et al attributed this peak to surface recombination, in particular when the peak reduced its prominence with increasing dielectric charge. Secondly, in their work a decrease in lifetime for low injections is observed. Here, effective lifetime increases equally for all carrier injections. Additionally, the intrinsic passivation of the Si/SiO_2 interface for the specimens used here was of poorer quality, as evidenced from the lower effective lifetimes prior any extrinsic FEP. However, when deposited with charge, the effective lifetime measured in this work exceeded by over

3-fold that of Kho et al. Finally, an increase in SRV for $\Delta p > 10^{15}$ cm^{-3}, which is mainly attributed to Auger recombination is observed in both studies.

The theoretical formalism outlined in previous sections was used here to find the best modelling parameters that described the Si/SiO_2 interface. The search for parameters was conducted by plotting the experimental S_{eff} as a function of Q_f for three indicative minority carrier injection levels, and then performing a parameter sweep using the frame of reference set by the new parametrisation proposed. Figure 35 illustrates this plot including the set of parameters that best described the experimental data. The values of S_n and S_p reflect the asymmetry kink observed for negative dielectric charge, the value of D_{it0} reflects the independence of SRV on dielectric charge for low concentrations ($Q_f < 10^{11}$ q/cm^2), and D_{itC} and D_{itV} reflect the degree of dependence that SRV exhibits with charge for large concentrations of both positive and negative dielectric charge. These parameters are comparable to those previously inferred using other techniques as reported in references [143], [147], [171]. They show a moderate chemical passivation component and a low FEP component in the oxide. However, two key aspects are highlighted here: First, the asymmetry between the capture of electrons and holes is much smaller than previously reported. Here $S_r \sim 0.3$, while most other studies report $S_r \sim 0.001 - 0.01$. Second, although literature reports D_{it} and $\sigma_{n,p}$ highly dependent on energy in the band gap, their product $S_{n,p} \sim D_{it} \times \sigma_{n,p}$ seems highly independent of energy. This indicates that capture cross sections for states near the band edges tend to be negligibly small, while those for states near the mid gap are in the order of 10^{-16} cm^2.

The accuracy of the theoretical model was further tested by producing injection dependent curves of SRV and fitting them to the experimentally measured ones. Figure 36, in contrast to Figure 34, depicts the surface recombination velocity reduction for all carrier injections studied here. This data demonstrates that S_{eff} < 2 cm/s can be achieved using controlled FEP. To the author's knowledge such a low recombination velocity is among the

best passivation schemes reported in the literature [35], see section 1.4.1 for more details, and is the lowest SRV reported on oxide passivated FZ-Si [39] . Disagreement between experimental and modelled curves, for the regime of $Q_f < \pm 10^{11}$ q/cm^2, may arise from the lack of uniformity of the intrinsic charge in the oxide whose uniformity was not assessed in the present work. The fits observed for low negative charge are particularly poor. These can also arise from the quasi-steady-state nature of the lifetime measuring technique and the calculation of SRV, Section 1.3.4. This is also observed in the black curve on the right of Figure 36. These variations are not important since the low charge range is not relevant to FEP for solar cell applications where dielectric films present much higher charge concentrations.

The solid grey lines in Figure 36 show the best theoretical fits of S_{eff}. Here the total dielectric charge concentration has been used as the fitting parameter while $S_n, S_p,\ D_{it0}, D_{itV}$ and D_{itC} remain constant. The values of charge used for these fits corresponded well to those measured using KP, thus indicating that the SRH model used represents well surface recombination at the Si/SiO_2 interface. The modelled $S_{UL} = f(Q_f, \Delta p)$ can also be plotted for the entire domain of both independent variables studied here. Figure 37 illustrates such a plot, where dielectric charge is swept from -3 x 10^{12} to +3 x 10^{12} q/cm^2 and carrier injection from 10^{13}-10^{16} cm^{-3}. The influence of positive and negative charge on S_{UL} is well illustrated here. At low carrier injection levels, S_{UL} is strongly dependent on the concentration of charge present on the dielectric. As the minority carrier concentration becomes comparable with the majority carrier concentration, the dependence reduces and dielectric charge does not reduce recombination as effectively. Maximum recombination occurs at a small negative charge for all levels of injection. This depends on the doping type and concentration of the material and occurs when both electrons and holes are captured with the same probability ($S_n n_s = S_p p_s$). A moderate depletion of electrons from the n-type silicon surface is therefore required to achieve such maximum recombination. This depletion occurs for a negative charge

concentration ~10^{11} q/cm^2, which results in the kink in Figure 32. The asymmetry of S_{UL} with dielectric charge polarity is also clear in Figure 37. Positive charge is seen to better passivate the surface down to S_{eff} < 10 cm/s levels. The reason for this asymmetry is the difference between the hole and electron recombination velocities, as discussed in section 3.2.2. This is an important effect and shows that for the Si/SiO_2 interface better passivation can be achieved using positive rather than negative charge. However this is not necessarily true for all dielectric semiconductor combinations and if, for a particular materials system, $S_p > S_n$ then the best passivation would be achieved with negative charge.

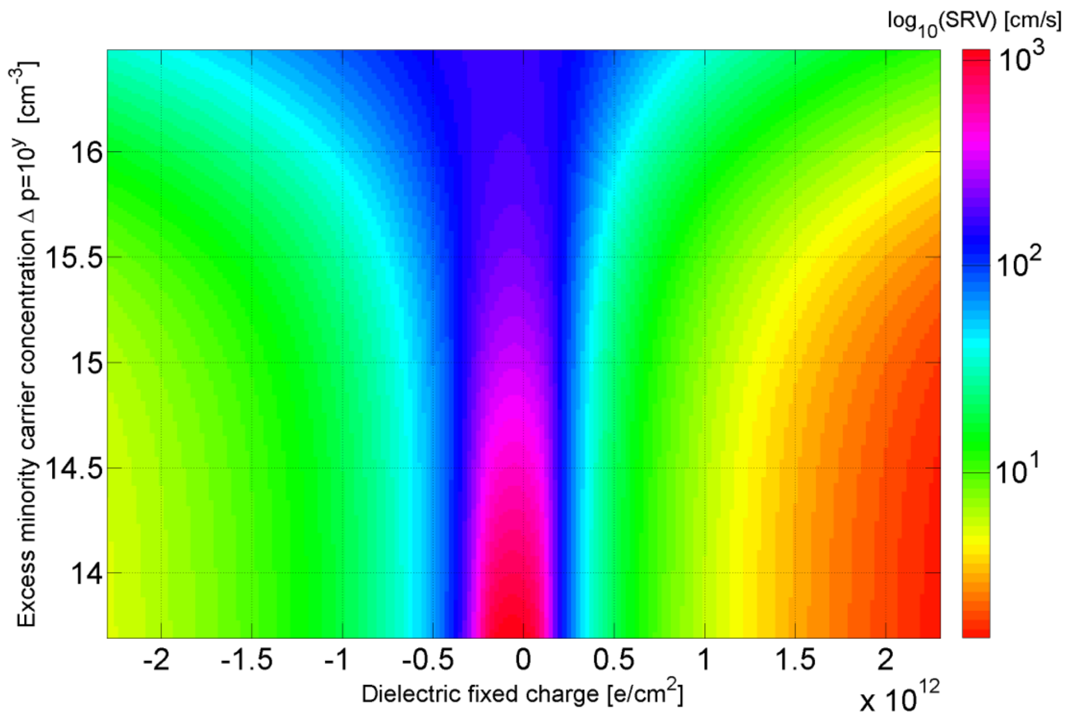

Figure 37. Simulation of effective surface recombination velocity for 1Ωcm FZ n-type silicon passivated with SiO_2, as a function of dielectric fixed charge and excess minority carrier concentration. Simulation parameters are given in Figure 35. Notice the x-axis on this figure is not a logarithmic axis.

It has been observed that an essentially ideal fit can be obtained for a range of experimental fit parameters but that all of these different combinations will have the same energy dependence of D_{it}, that is a large density of states towards the band edges and a low density in the mid gap. An algorithm that minimises the error between modelled and measured values could possibly render a more accurate parameter set, yet such implementation was not carried out in this work. Additionally, it is important to notice that

none of the extensions suggested by Glunz et al [26] have been considered significant in obtaining an accurate model of SRV for the materials system considered here. Previous research on p-type silicon suggests an increase in surface recombination for low carrier injection levels and high positive dielectric charge concentration similar to that found here for n-type material. Such an increase in recombination, which also gives rise to a clear peak in the injection-dependent lifetime curves, was accounted for by introducing an extra recombination term. This term was then postulated to be due to i) space charge region recombination [152], ii) shunt currents [26] or iii) a surface damage region (SDR) [151], yet the present study reveals that such a term is not necessary to describe recombination at a Si/SiO_2 interface. Furthermore, since there is no direct experimental evidence supporting the existence of such additional recombination mechanisms it is postulated that the analysis developed here will also provide an accurate description of surface recombination in many other systems. In addition, it has been reported recently that the decreasing lifetime at low injection levels is a measurement artefact due the lack of uniform passivation on specimen edges [159], [177].

The present work has demonstrated that a complete analysis of the $S_{eff} = f(Q_f, \Delta p)$ relation using the extended SRH formalism is sufficient to model recombination at certain semiconductor surfaces, given a correct parametrisation of the interface phenomena. It is believed that the analysis will be generally applicable to many other passivating dielectrics in addition to the Si/SiO_2 combination experimentally investigated here. However, it should be noted, that the present work does not rule out the need to account for the presence of a SDR if dielectrics have been deposited by plasma techniques in such a way that a damaged region of silicon is produced at the interface with the dielectric.

3.4 Summary

This chapter has reviewed the theoretical description of surface recombination at the surface of a semiconductor and has provided a powerful methodology to infer interface parameters. The experimental data presented here demonstrates a potential lifetime improvement in n-type FZ-Si, by using corona discharge to provide FEP. The lifetime increase can be controlled, but the question still remains to what degree such controlled field effect passivation can be used for practical solar cells when the high degree of passivation must be stable over a period of decades. This is the subject of the next chapters.

Calculations of SRV showed that the Shockley-Read-Hall extended formalism, without any extensions, is a suitable mathematical description of the FZ-Si/SiO_2 interface. Specifically, effective surface recombination velocity has been calculated for a wide range of excess minority carrier and dielectric charge concentrations. The experimental and measurement methodology proved to be a strong tool to characterise the properties of the FZ-Si/SiO_2 interface. They provided the values for interface trap density, and surface recombination for holes and electrons without the need for DLTS or multi-frequency Capacitance/Conductance-Voltage measurements. For the FZ-Si/SiO_2 interface, it is concluded that the electron SRV, and hence the capture cross section, is higher than for holes, but to a lesser extent than previously suggested in the literature [138]. Additionally, the interface defect concentration is notably higher than reported before, such that a significant concentration of charge is trapped at the interface rather than compensated in the near-surface region. Finally, the importance of the uniformity of charge deposited via corona discharge is noted. This could affect the accuracy of the modelling formalism.

CHAPTER 4
FIELD-EFFECT PASSIVATION USING CORONA DISCHARGE

In this work field effect passivation has been shown to be a potential method to extrinsically enhance the passivation properties of a dielectric film while preserving its optical and chemical characteristics. Such extrinsic FEP can be achieved by depositing ions, for example via a corona discharge apparatus, as has previously been reported [58], [59]. Previous research has mainly concentrated on the effect of charge on the effective lifetime of minority carriers [26], [62], yet very little has been reported about its long term stability and potential as a controlled method for surface passivation. The question remains whether extrinsic charge can be rendered stable such that it becomes of practical relevance for solar cell manufacture. This work aims to address this question. For this, the optimal conditions for deposition of charge using corona have been determined and will be presented. The dynamics of corona charge on a silicon dioxide film are then studied, with emphasis on its effectiveness for silicon surface passivation. The stability of passivation is analysed and different approaches are proposed to modify the dynamic behaviour of corona deposited charge on SiO_2. The study of corona charge dynamics is then extended to a double layered passivation film of SiO_2 and SiN_x. Lastly a discussion of the prospects of extrinsic FEP using corona discharge is provided.

4.1 Corona discharge conditions

4.1.1 Corona current-voltage characteristics

Figure 38 illustrates the main parameters to consider in a corona discharge rig including the measured current-voltage (IV) relation for this set up. Given a point-to-plane distance d_c and a positive corona, a threshold potential V_{Cth} is required before the corona current is produced, Figure 38.b. This was in the order of 7-8 kV for the positive corona. After the corona is started, the current to voltage characteristic follows a linear regime before electric breakdown and sparking at sufficiently high fields. The breakdown regime was not achieved in this rig at 20 kV as illustrated in Figure 38.b for a distance d_c of 8 or 15 cm. In the case of a negative corona, the IV characteristic does not present a threshold voltage for a corona to start. Corona current is detected at corona potentials as low as 1 kV. Moreover the IV relation for negative corona charge is exponential rather than linear. Chapter 1 includes a brief description of the nature of positive and negative coronas explaining how these differences arise.

A distance of 8 cm was first used in this project following previous work [61], [76], [178]. This distance was then increased to 15 cm to improve uniformity, as previously described in Chapter 2. For a set corona distance, the total deposited charge can be estimated by integrating the charge per unit time per unit area landing on the sample. For a constant corona current I_c and an effective area for ions to land A_c as pictured in Figure 38.a, the total concentration of ions at the surface of the specimen is given by:

$$Q_{Ctot} = \frac{1}{A_c}\int_0^{t1} I_c dt = \frac{1}{A_c} I_c t1 \quad (4.\ 1)$$

The corona potential and current adequate for extrinsic FEP was selected as follows: FEP in dielectric films has been reported to be produced by a surface concentration of charge in the range 10^{11} -10^{13} q/cm^2 with a typical value of 10^{12} q/cm^2. When extrinsically adding

charge to the dielectric it is desired to produce small incremental improvements in passivation such that 20 to 30 measurements can be performed sequentially, before the charge deposited on the film exceeds the film's breakdown strength. For SiO_2 the electric field strength is 5-10 MV/cm. In a 100 nm SiO_2 film, a field of 5 MV/cm is achieved when a concentration of charge of ~10^{13} q/cm^2 is present at the surface of the dielectric. If a 5 seconds corona discharge is applied on an effective area of 100 cm^2, the solution to equation (4. 1) shows that a charge concentration of ~ 3 x 10^{11} q/cm^2 is deposited on the sample when the corona current is 1 μA. This allows 30 5-second charge steps before reaching the film's breakdown strength. Following the IV characteristics in Figure 38.b, the default setting for positive corona in charge Rig 1 was chosen to be a corona potential $V_c = 9$ kV while in corona charge Rig 2 $V_c = 15$ kV. These corona potentials produced a corona current $I_c = 1$ μA. For negative corona charge $V_c = -8$ kV in Rig 1 and $V_c = -10$ kV in Rig 2 were chosen, such that $I_c = -1$ μA. Other factors affecting the corona include the point electrode (needle) sharpness, deposition temperature and humidity. Although these were not studied systematically some qualitative remarks can be drawn. Sharper electrodes produce higher local electric fields such that the corona sparks at lower potentials and the corona current increases rapidly. Elevating temperatures also reduces the potential at which the corona sparks. Humidity was found to change the nature of the corona ions deposited on the surface yet the IV characteristic was minimally changed [179].

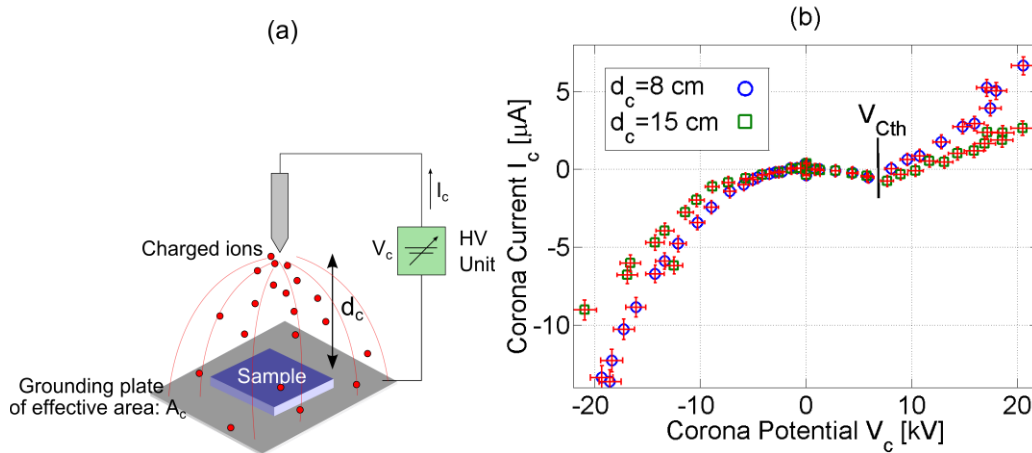

Figure 38. a. Schematic of deposition of corona ions including the effective area where ions land, the corona distance, the corona potential and the corona current, b. Current-voltage characteristics of the 8 cm and 15 cm rigs.

4.1.2 Uniformity of charge

In Chapter 2 two configurations of corona discharge rig were described. A point-to-plane distance of 8 cm was initially used to deposit charge and improve FEP. As the resulting passivation became increasingly better using the 8 cm configuration, it was found that the uniformity of charge was a key parameter to improve. Charge uniformity was assessed by mapping KP surface potential across the area of the sample. Typical maps of KP surface potential are illustrated in Figure 39 for both corona rigs. In corona Rig 1, Figure 39.a, charge uniformity was assessed using a Cz-Si specimen wet oxidised to 87.5 nm. In corona Rig 2, Figure 39.c, it was done on a FZ-Si sample dry oxidised to 100 nm. The uniformity of corona charge deposition using Rig 2 is superior to that observed with Rig 1. For sample nCb3 in Figure 39.a the coefficient of variance for the surface potential was ~ 50%. For sample n6b_4, on the other hand, the coefficient of variance for the deposited charge was < 5%, hence confirming that very uniform charge deposition was possible with an optimal set-up. Additional details on charge uniformity were published in reference [121] and can be found in Mr Fred Woodcock's thesis [120].

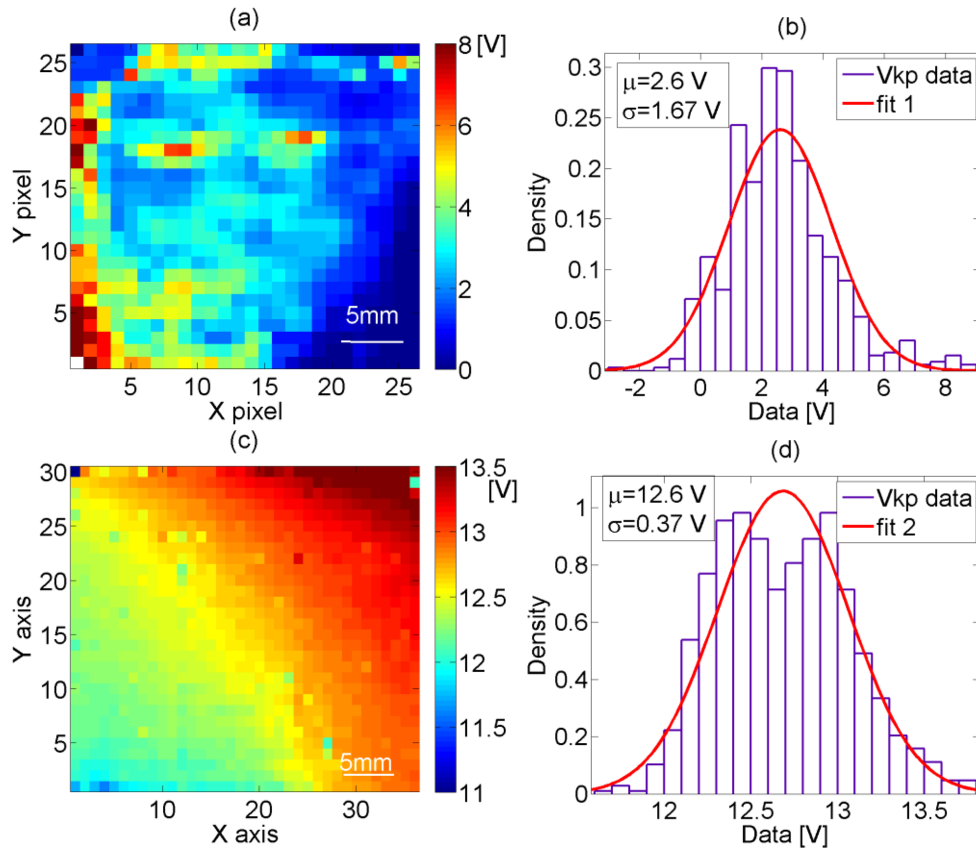

Figure 39. a. Surface potential map of 87.5 nm thermal oxide on n-type Cz-Si (Sample nCb3) charged on corona Rig 1 for ~90 seconds. b. Statistical analysis of the distribution of charge across sample nCb3. c. Surface potential map of 100 nm thermal oxide on n-type FZ-Si (Sample n6b_4) charged on corona Rig 2 for 70 seconds. d. Statistical analysis of the distribution of charge across sample n6b_4. A normal probability function is fitted to the probability density functions observed.

4.1.3 Corona charge deposition and its effect on lifetime

In Chapter 3 the effect of corona charge on effective lifetime was reported for oxide passivated silicon. It was shown that adding positive charge increased effective lifetime thanks to a direct reduction in surface recombination. The conditions for corona charge deposition were not reported then. This section presents experimental evidence to support the selection of corona discharge potential, current, and time, such that the highest extrinsic FEP is achieved.

Section 4.1.1 described the selection of the corona current $I_c = 1\ \mu$A to produce a stable and repeatable charging of dielectrics. The corona charging process was studied on 3 x 3 cm^2 samples from Cz wafers with a 87.5 nm thick wet oxide (Wafer nC), and FZ wafers with a 100 nm thick dry oxide (Wafer n1, n7 and n17b). The effect of FEP was firstly

evaluated by depositing charge in ~ 5 second time steps and recording the KP surface potential and effective carrier lifetime after each step. The KP surface potential measurements reported here after are taken in the centre of the sample. Figure 40.a illustrates the surface potential measured via KP for a given time under the corona discharge rigs 1 and 2. The equivalent charge concentration is calculated using equation (2. 20) assuming all charge resides at the surface of the oxides, and is plotted in the right y-axis. A second y-axis has been included (red) for the charge concentration in the 87.5 nm oxide, since the relation between KP voltage and charge is different, according to equation (2. 20). It is clear that the cumulative concentration of charge at the surface of the oxides depends linearly on time. For those specimens charged with corona Rig 1, KP potential is seen to scatter due to the lack of uniformity in the deposition process. The deposition rate varied between 2 - 5 x 10^{10} q/(cm^{2}s), which compares well to the previous estimation. The effect that these charge concentrations have in surface passivation is shown in Figure 40.b. Here, the effective lifetime at an injection level of 10^{15} cm^{-3} is shown as a function of corona discharge time. As presented in Chapter 3, surface recombination (U_s) can be described as proportional to the product of the chemical component which is dependent on the density of interface traps at the silicon surface (D_{it}), and the field-effect component which determines the concentration of minority carriers at the surface (p_s in n-type and n_s in p-type):

$$U_s \propto D_{it} \times p_s \tag{4. 2}$$

When positive corona charge is deposited on top of a passivating oxide, holes are repelled from the surface thus reducing recombination and increasing effective lifetime. As the dielectric charge concentration approaches 3-5 x 10^{12} q/cm^2 the effective lifetime plateaus at a maximum value. Excessive charge has been seen to deteriorate the passivation quality of these films. This can be seen in the marginal decrease in lifetime in samples n7_8 and n17b_1 after charging for 110 s, Figure 40.b. Another indication of damage of the interface is evidenced when performing a second, subsequent charging cycle. This is illustrated in the empty purple markers trace in Figure 40.b where a lower effective lifetime is achieved after

the same concentration of corona charge has been deposited. This is believed to be due to bond-breaking from breakdown of the oxide at 'hot' spots where excessive charge has accumulated, yet this is occurring at fields of 2 - 3 MV/cm. This is lower than the breakdown strength of SiO_2 typically reported [180], yet the work of Nakamura[181], Schuegraf [182], [183] and Verweij [184] showed that other conduction mechanisms are activated at lower field strengths, and these may produce damage of the Si/SiO_2 interface. These will be collectively referred to as breakdown channels. In addition, Black [141] proposed that some deterioration of the chemical passivation at the Si/SiO_2 interface could be caused by electron photoemission from the silicon which may then promote hydrogen release from the interface. For this work it is assumed that chemical de-passivation takes place by a combination of these two models. The exact mechanism was not studied in this work.

Despite the damage at the interface, Figure 40.b also illustrates that corona charge Rig 2 provides uniform FEP such that 1 ms higher lifetimes are achieved in 1 Ωcm FZ-Si. This is seen by comparting the green or turquoise traces to the purple one in Figure 40.b.

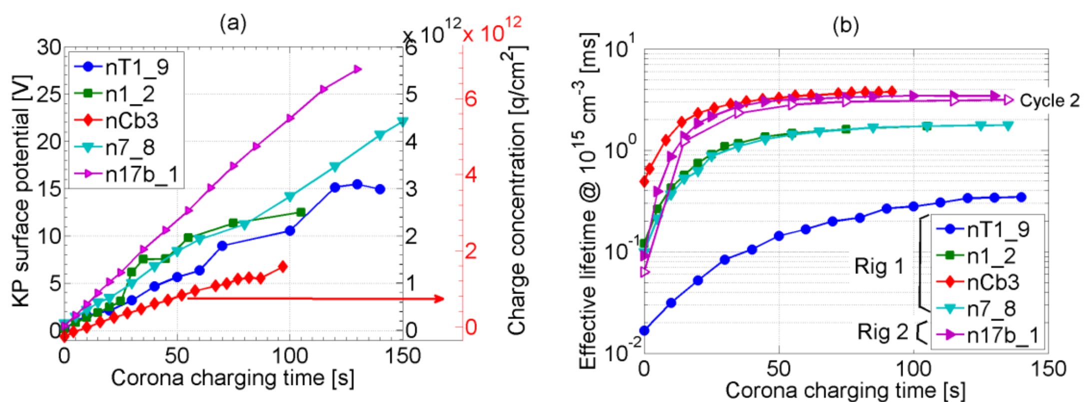

Figure 40. a. KP surface potential as a function of corona discharge time on c-Si samples with 100 nm and 87.5 nm oxides, b. Effective lifetime at 10^{15} cm^{-3} carrier injection as a function of corona charging time. Empty magenta markers indicate the second cycle on sample n17b_1.

4.1.4 Summary

The best corona extrinsic passivation was achieved by using Rig 2 with uniformities better than 5%. Optimal extrinsic FEP is applied by charging in 5-10 second intervals with $I_c = 1\mu A$, and stopping once the lifetime was seen not to increase by more than ~5% after a

further 5 s of charge deposition. On average this occurred when a surface charge density of 2 - 4 x 10^{12} q/cm^2 had been deposited, which for a 100 nm thick oxide produced a surface potential of 10 - 20 V.

4.2 Effect and location of corona charge on SiO_2 passivated n-type c-Si

4.2.1 Surface passivation of oxidised n-type c-Si using extrinsic FEP

Previous sections described the conditions to deposit charge onto dielectric films and improve their passivation quality. The model system used in this work is a silicon dioxide film thermally grown on c-Si. Deposition of corona charge has been seen to reduce surface recombination by means of FEP, thus improving the effective lifetime of minority carriers. This section will illustrate how much improvement is possible for silicon of different resistivity and different oxides, and estimates for SRV will be provided in order to compare to the state-of-the-art passivation techniques.

Effective lifetime as a function of carrier injection is illustrated in Figure 41 for 3 x 3 cm^2 samples from 5 Ωcm n-type Cz-Si oxidised to 87.5 nm. Here, effective lifetime was observed to increase from 0.5 to 3.5 milliseconds at a minority carrier concentration $\Delta p=10^{15}$ cm^{-3} when a concentration of dielectric charge of 1.37 x 10^{12} q/cm^2 was deposited on the oxide. This was conducted using corona Rig 1. The highest lifetime corresponds to an upper limit of surface recombination velocity (SRV_{UL}) of 9 cm/s @ $\Delta p=10^{15}$ cm^{-3}, when subtracting the Auger and radiative components of the bulk lifetime, as indicated in Chapter 2. For this type of silicon, the lifetime component given by defect mediated SRH recombination is of the order of ~35 ms [49]. This only contributes significantly when effective lifetimes over 5 ms are achieved. Measurements in Figure 41 show that, for low carrier injections, this condition is satisfied and thus the actual SRV can be substantially lower than the upper limit

inferred. During the course of this work it became evident that sufficiently good passivation could be achieved and thus SRH recombination would influence the SRV limits calculated. A higher quality material was used to minimize the effect of SRH bulk recombination. For this reason a large part of the work carried out here has conducted on FZ-Si.

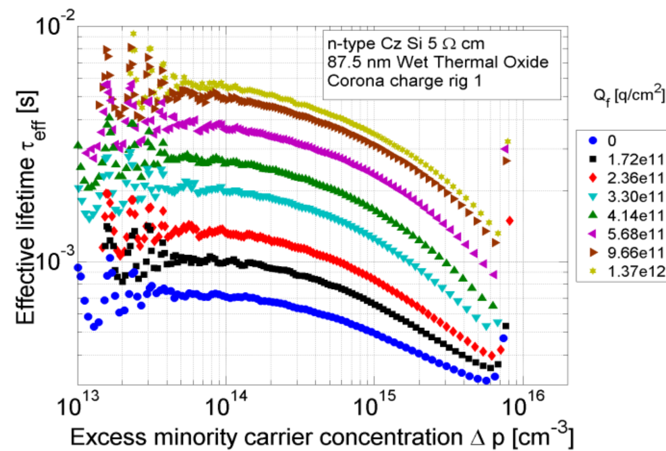

Figure 41. Lifetime measurements of n-type ⟨100⟩ Cz-Silicon (5 Ωcm) passivated with a 87.5 nm-thick thermal oxide (Sample nCb3) for positive charge deposited using corona discharge. Surface charge concentration, calculated using Kelvin Probe surface potential, is listed in the legend for each experimental lifetime plot.

A 3 x 3 cm^2 sample of 1 Ωcm n-type FZ-Si, dry oxidised to 100 nm, was deposited with corona charge using corona Rig 2. Figure 42.a illustrates lifetime measurements for this sample, and their corresponding KP measurements of charge concentration. This specimen was subjected to two cycles of positive corona charge deposition, Figure 42.a and Figure 42.b, the second preceded by an IPA rinse to remove the deposited charge. The effective lifetime was observed to increase from 0.1 to 3.4 milliseconds at $\Delta p=10^{15}$ cm^{-3}, during the first charging cycle. 3.4 ms lifetime corresponds to an effective surface recombination velocity of 1.6 cm/s when subtracting the Auger and radiative components of the bulk lifetime. As was observed for Cz-Si , the oxide/Si interface deteriorates when excessive charge is deposited. This can lead to micro breakdown of the oxide at ‘hot’ charge spots. This was also the case for sample n17b_1, which went through a second charging cycle, during which a similar concentration of charge was deposited, but the effective lifetime only reached 3 ms, compared to 3.4 ms in the previous cycle, Figure 42.b.

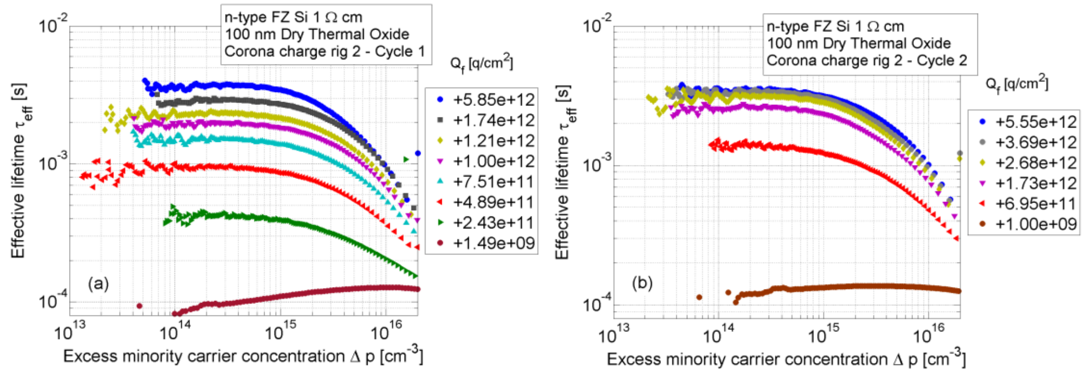

Figure 42. Lifetime measurements of n-type FZ Silicon passivated with a 100 nm-thick thermal oxide (Sample n17b_1), when deposited with positive corona charge in two cycles (left and right) using corona charge Rig 2. Surface charge concentration measured using Kelvin Probe surface potential is listed.

4.2.2 Corona charge location

The calculations of charge concentration previously presented have assumed that all corona charge resides at the surface of the film. This section addresses the veracity of this assumption. Chapter 2 presented the theory of KP and CV measurements. There, it was shown that both of these techniques could infer dielectric charge concentrations yet their accuracy relied on previous knowledge of the location of the charge. Additionally, it was shown that the maximum sensitivity of KP measurements occurred when the charge was at the surface of the film; while for CV measurements it occurred when the charge was at the dielectric/silicon interface. Conversely, CV measurements do not detect any charge when it is located at the surface of the film, at the interface between the gate metal and the dielectric, and KP measurements do not detect charge when it lies near the dielectric/silicon interface. CV measurements showed that no shift in flat-band was registered for samples deposited with corona charge versus those without corona charge, thus indicating that all deposited charge was located at the surface of the dielectric or very near the metal/dielectric interface after gate formation. Moreover, samples deposited with corona charge were dipped in a diluted solution of HF for 5 seconds. After this KP measurements of surface potential indicated that all charge had been removed. A decrease in the film thickness of 3-8 nm was recorded using reflectance spectrometry, thus confirming that the surface region, where the charge was located, had been etched by the acid.

4.2.3 Textured silicon

Chapter 2 described the texturing of silicon surfaces as commonly used to increase the light absorption probability. In this work, textured Si wafers were dry oxidised to 100 nm and cut into 3 x 3 cm^2 samples. Extrinsic FEP was evaluated by depositing corona charge and measuring effective lifetime. The resulting effective lifetime is illustrated in Figure 43 including the inferred charge concentrations from KP measurements. In textured Si the effective lifetime was observed to increase from 0.015 to 0.2 milliseconds at $\Delta p = 10^{15}$ cm^{-3}. This is an increase of over 10 fold with a charge concentration of ~ 3 x 10^{12} q/cm^2. This compares well with the lifetime increase achieved on planar surfaces. The highest lifetime achieved corresponds to an effective surface recombination velocity of ~ 40 cm/s when subtracting the Auger and radiative components of the bulk lifetime.

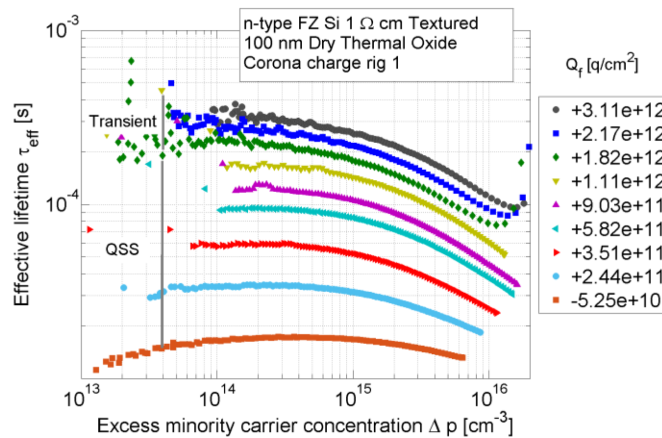

Figure 43. Lifetime measurements of textured n-type FZ Silicon passivated with a 100 nm-thick thermal oxide (Sample nT1_9), for positive charge deposited using corona charge Rig 1. Surface charge calculated using the Kelvin Probe surface potential is listed.

4.2.4 Forming gas annealed SiO_2

Surface passivation is achieved using two mechanisms: chemical and field effect. The quality of chemical passivation in a dielectric film is determined by the number of interface defect states that remain at the dielectric/silicon interface (D_{it}) after film deposition. A standard process to reduce the interface defect density *after* film deposition, extrinsically, was previously devised by the IC industry and applied to the fabrication of MOSFET devices [185]. It involves submitting the dielectric/silicon system to a <5% H/N anneal at 400-450

°C. This process is commonly known as a forming gas anneal (FGA). A subset of 100 nm oxidised FZ-Si wafers were subjected to a FGA to achieve a better chemical passivation. The improvement in effective lifetime due to extrinsic chemical passivation is illustrated in Figure 44, along with the effective lifetime of a comparison sample in the same batch that did not undergo FGA treatment. An increase of 4 fold in effective lifetime is achieved only by chemically hydrogenating a number of dangling bonds at the oxide/silicon interface. This increase in chemical passivation resulted in a lifetime improvement from 0.07 to 0.3 ms. The improvement in lifetime after deposition of positive charge is comparable for the sample that underwent FGA treatment as for that which did not. This is illustrated by the solid markers in Figure 44.

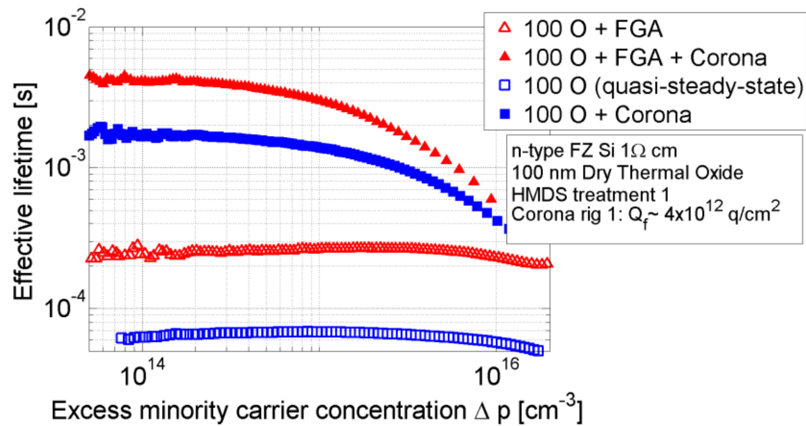

Figure 44. Lifetime measurements of n-type FZ Silicon passivated with a 100 nm-thick thermal oxide and FGA, Sample n17_8. Control sample n10_5a. Both samples were deposited with positive corona charge using Rig 1 for 120 seconds.

4.1.1. Discussion

Oxide films thermally grown on Cz-Si have been shown to provide a good level of passivation due to a good intrinsic chemical component combined with a moderate extrinsic field effect component. Such passivation was improved by means of extrinsic FEP and outstanding quality was demonstrated with SRV < 9 cm/s. It is additionally noticed that effective lifetime increases proportionally for all injection levels as charge is deposited. This indicates that overall carrier lifetime is only limited by surface recombination processes rather than bulk ones. Additionally, the actual value of SRV is likely to be much lower than

that reported since SRH bulk recombination and charge non-uniformity limited the effectiveness of the method. The former limitation was addressed by moving from Cz-Si to FZ-Si specimens. The latter was addressed by performing uniformity characterisation and modelling of the corona discharge to find adequate deposition conditions.

Work carried out in FZ-Si confirmed the strong reduction of surface recombination provided by extrinsic FEP. When corona charge is deposited on top of thermally grown oxides, SRV < 2 cm/s are readily achieved. The quality of extrinsic FEP was achieved by improving the uniformity of corona charge deposition to ensure that all areas of the surface have a charge density close to the optimum for FEP. When used in combination with a FGA process, corona charge deposition improved effective lifetime from 0.25 to 3-4 ms. This is equivalent to a SRV as low as 1.5 cm/s at a minority carrier injection of 10^{15} cm^{-3}. This is the lowest surface recombination velocity achieved on ~1 Ωcm n-type crystalline silicon passivated with a thermal oxide. A detailed comparison between this passivation quality and that achieved using state-of-the-art methods is included at the end of this chapter, section 4.6. Given the simplicity of this method, it is important to note that remarkable surface passivation is available by simply by providing extrinsic and uniform FEP. Such a level of passivation, achieved primarily by external field-effect, had not been reported before. Samples produced using corona Rig 1 lacked charge uniformity and maximum lifetimes of ~2 ms were achieved. When applied to a textured surface, extrinsic FEP produces a proportional reduction in surface recombination velocity yet effective lifetimes achieved are substantially lower (one order of magnitude) than for planar surfaces. This is not surprising since, in textured Si, the passivated surface is a <111> face of the pyramidal structure, rather than the <100> face of a planar one, and <111> faces have ~1 order of magnitude more available bonds/cm^2 than <100> faces [20]. SRV has rarely been studied on textured surfaces, yet these are the ones used in practical Si solar cells. It is important to note that although textured <111> surfaces present less chemical passivation, the effectiveness of FEP in increasing lifetime is comparable to that achieved using a <100> surface.

4.2.5 Summary

The results in this section demonstrate that the field effect component of passivation is of greater importance than has been reported before. In thermal oxide films, SRVs < 9 cm/s were obtained for 5 Ωcm Cz-Si, 2 cm/s for 1 Ωcm FZ-Si, and 1.5 cm/s for FGA 1 Ωcm FZ-Si. Textured surfaces benefited equally from extrinsic FEP and a SRV < 40 cm/s was obtained for 1 Ωcm FZ-Si. Extrinsic FEP allows more flexibility in the combined optimisation of the optical properties, and the chemical and field effect passivation properties of dielectric films. Finally, the versatility and low cost of this method make it a very promising passivation approach to be used at industrial scale and is hence of relevance to solar cell manufacture. The next key requirement is therefore to demonstrate that these methods can be integrated into manufacturing processes and that they can last for the same life span as a solar cell. This is the subject of next section.

4.3 Stability of corona charge in SiO_2 passivated Si

It has been shown that corona discharge can produce controlled and effective extrinsic passivation of silicon surfaces. Before this passivation technique is used at a practical level, it must be shown to be stable for a lifetime comparable to that of a solar cell (~25-30 years). This section explores the dynamic behaviour of corona charge. The stability of charge and the passivation it provides is studied using effective lifetime and KP measurements. A general overview of the dynamic behaviour of corona charge on SiO_2 is first provided. Then the mechanisms for charge movement or compensation are explored, and the methods to avoid charge leakage and achieve stable FEP are illustrated and discussed.

4.3.1 Leakage of corona charge

The stability of corona charge was evaluated by recording the KP surface potential and effective lifetime for a period of time after charge deposition. Corona charge was deposited to optimal passivation levels as described in section 4.1.3. KP and lifetime measurements

thereafter are illustrated in Figure 45, for 3 x 3 cm^2 samples from Cz wafers with a thermal 87.5 and 21.5 nm oxide (samples nC8 and nE1), and FZ wafers with a thermal 100 nm oxide (sample n9_x1). These specimens did not undergo FGA prior to charge deposition. Regardless of the silicon type, the dopant concentration and the thickness of the oxide, the surface potential in all samples decayed to pre-corona levels within 20 to 60 days, Figure 45.a. A decay time constant τ_{kp} of ~ 8-11 $\pm$45% days is estimated for the potential decay. The description of KP measurements in Chapter 2 showed that a decrease in KP surface potential was caused either by a decrease in charge concentration, or a decrease in the distance of the charge to the dielectric/silicon interface. In the latter case, the net concentration of charge would remain unchanged and FEP would be maintained. Figure 45.b illustrates the effective lifetime of sample n9_x1 as a function of time. Here it is evident that the decay in surface potential relates well to the decay in surface passivation quality. Additionally, when the charge is at the surface, an IPA rinse readily removes it and eliminates the FEP component, as illustrated in the last measurement in Figure 45.b.

The decay mechanism of corona charge in silicon dioxide has previously been reported to be the loss of charge due to surface conduction across the film [59]. Studies by Olthuis and Bergveld [59], [186] demonstrated that SiO_2 stored corona charge poorly due to its large lateral surface conductivity rather than its bulk conductivity. They concluded that conduction was due to silanol (SiOH) groups created at or near the surface of the oxide by chemisorption of water. Specifically, conduction took place via mobile protons in SiOH groups, or via hydrogen hopping in water molecules physisorbed to the SiOH groups. Additionally they showed that these phenomena could happen through the first 40 nm of SiO_2 thin films. No report has been found on the compensation of corona charge due to dust, air molecules or stray ions present in the environment attaching to the film and screening charge. Results in section 4.3.2 corroborate that no external compensation mechanism is observed. Despite the presence of SiOH groups, Olthuis and other authors [59], [111], [187], [188] have reported that SiO_2 could store corona charge when the surface conductivity is

reduced using a chemical surface modification. This modification is the subject of the next section.

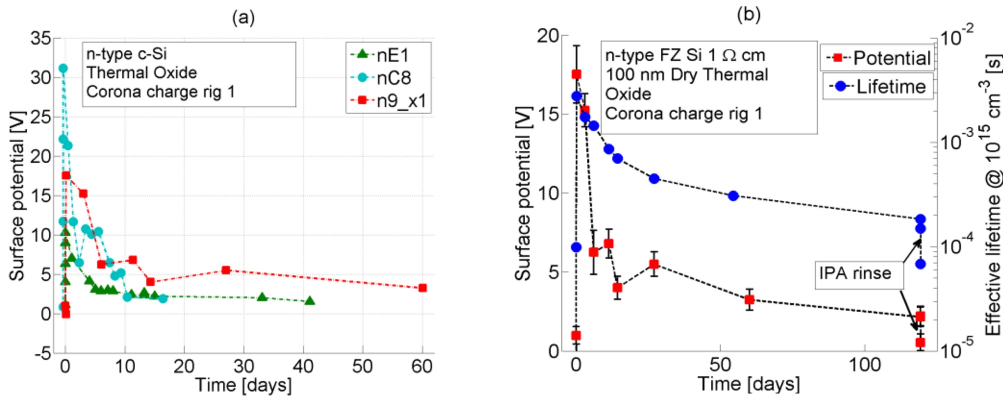

Figure 45. Kelvin probe (KP) surface potential of c-Si oxidised specimens (Samples nE1, nC8 and n9_x1) after corona charge deposition, b. (KP) surface potential and effective lifetime @ $\Delta p=10^{15}$ cm^{-3}, for corona charged sample n9_x1. Corona was applied using Rig 1.

4.3.2 Chemical surface modification of SiO_2

Olthuis et al [59], [186] demonstrated that the surface of SiO_2 films could be chemically modified to prevent water absorption, and hence surface conductivity. They proposed that a hydrophilic to hydrophobic conversion of the oxide surface was possible using a hexamethyldisilasane (HMDS) protective coating. HMDS effectively substitutes SiOH groups with polar trimethyl silyl groups that prevent proton conduction or water physisorbtion [112], [157]. This chemical modification of the surface was applied to the oxide passivating films in this project as described below.

A Cz-Si sample (nCb3) with a 87.5 nm thermal oxide was treated with HMDS prior to corona charge deposition, using treatment 1 described in Chapter 2. After charging to an optimal surface potential of 7.5 V (~10^{12} q/cm^2), the specimen lifetime and surface potential were measured over a period of 350 days. All samples reported in this chapter were stored in plastic bags in laboratory conditions without temperature, humidity or atmospheric control. The evolution of lifetime and surface potential is illustrated in Figure 46. Here, charge induced surface potential and lifetime are seen to be approximately stable for the whole measurement period. Such high stability is attributed to the effect of HMDS in preventing

adsorption of water molecules [157]. Control samples that did not undergo HMDS chemical treatment are included for comparison. In samples with HDMS treatment the effective lifetime at an injection level of 10^{15} cm^{-3} remained above 2 ms for the entire measurement period. This corresponds to an increase in lifetime of more than 5 times compared to the uncharged material. Moreover, the material, which displayed a lifetime of 0.35 ms before charging, reached a maximum of 3 ms at an injection level of 10^{15} cm^{-3} at the beginning of the measurement period. This is equivalent to a SRV_{UL} of ≤9 cm/s. A SRV_{UL} of 16 cm/s was observed by the end of the measurement period. A decay time constant τ_{FEP}~ 730 ±10% days was estimated for the loss in passivation quality.

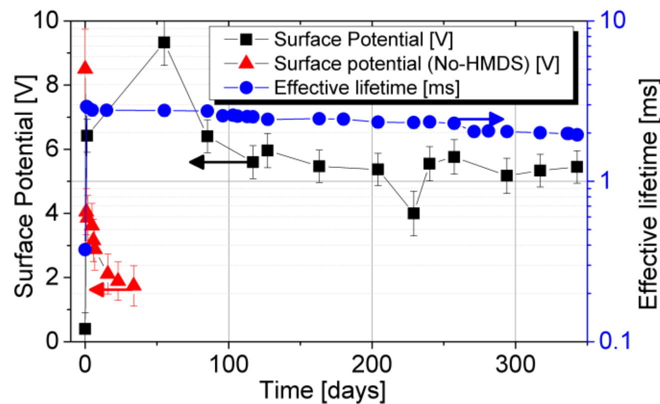

Figure 46. Kelvin probe (KP) surface potential and effective lifetime for a corona charged 87.5 nm oxide on n-type Cz-Si licon, 5 Ωcm (Samples nC1 and nCb3) at an excess minority carrier concentration of 10^{15} cm^{-3}. The surface potential of a sample without HMDS chemical treatment is included for comparison (red triangles)

Lateral charge migration was assessed by mapping the surface potential of this specimen using Kelvin Probe measurements straight after corona deposition, Figure 47.a, and a year later, Figure 47.b. It was confirmed that the uniformity of corona charge deposition using Rig 1 was rather poor. Further improvements in surface recombination would be possible when the entire surface is uniformly taken to the optimal potential. Despite this, the work presented here is a reasonable indication of what stability can be achieved. Charge mapping of the same specimen a year later revealed the presence of many small regions with substantially lower surface potential than the neighbouring regions. The average surface

potential after a year, however, was only reduced by 0.5 V. This indicates a decay time constant for KP surface potential of ~ 6,000 days. Such long decay and the variability in charge uniformity explain why there is a small apparent decay in charge when only taking a single measurement of charge in the centre of the sample. Lateral charge migration after one year was not observed to occur, at least on the scale of 1 mm. The observed horizontal lines distinguished in Figure 47.b are a measurement artefact given by a different probe to sample distance in the Kelvin Probe instrument. In scanning mode the Kelvin Probe measurements are more susceptible to this kind of error and thus a high variance is expected. Despite this the measurements falls within a ± 1 V error. This mapping experiment demonstrates that lateral migration is eliminated when HMDS removes the surface conduction on the oxide, such that corona charged molecules will not neutralise thanks to water induced conduction.

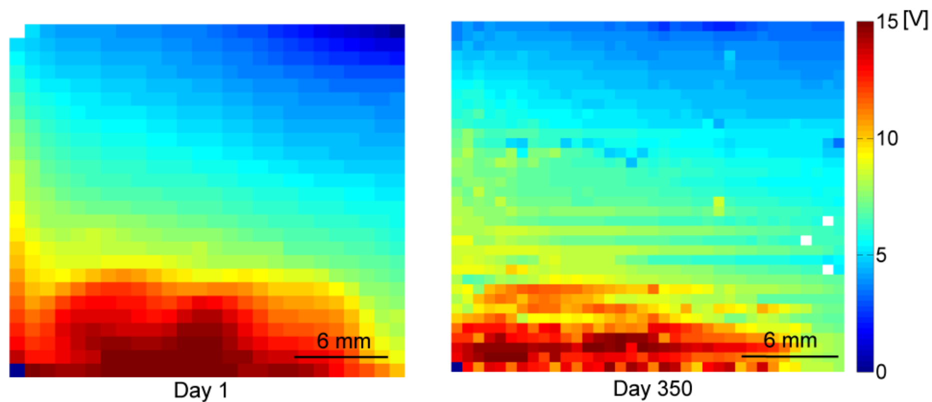

Figure 47. The time and spatial variation of the charge induced potential on the dielectric surface. Kelvin Probe maps of corona charged 87.5 nm thermal oxide on n-type Cz-Si licon, 5 Ωcm (Sample nCb3), with HMDS treatment, and no further heat treatment, at the beginning and at the end of the measurement period.

Similar to the case for Cz-Si, corona charge in oxidised FZ-Si samples was only stable when the oxide films had been chemical treated with HMDS. This illustrated in KP and τ_{eff} measurements in Figure 48. An exponential decay constant τ_{FEP} ~20 $\pm$40% days is estimated for the non-treated oxide, Figure 48.a. At the end of the measurement period this specimen was IPA rinsed to remove remaining charge and evaluate residual passivation. A decrease in the passivation quality is observed after fully removing charge. This could be due to an excessive concentration of charge in 'hot' spots. Figure 48.b shows that the HMDS

treated material, again, maintains good charge stability with no apparent decrease in surface potential in over 600 days. The effect this charge has on surface passivation is evident from effective lifetime measurements. Although charge does not notably decrease, lifetime is seen to slowly decay over the whole period. A decay time constant τ_{FEP} is estimated to ~ 600 $\pm$17% days, 30 times longer than in the absence of HMDS. The effective lifetime initially increases to 2 ms after corona charging, producing a SRV upper limit of 3.7 cm/s at an injection level of 10^{15} cm^{-3}. After 600 days passivation quality has decayed and the effective lifetime is 1 ms. SRV_{UL} is 8.7 cm/s.

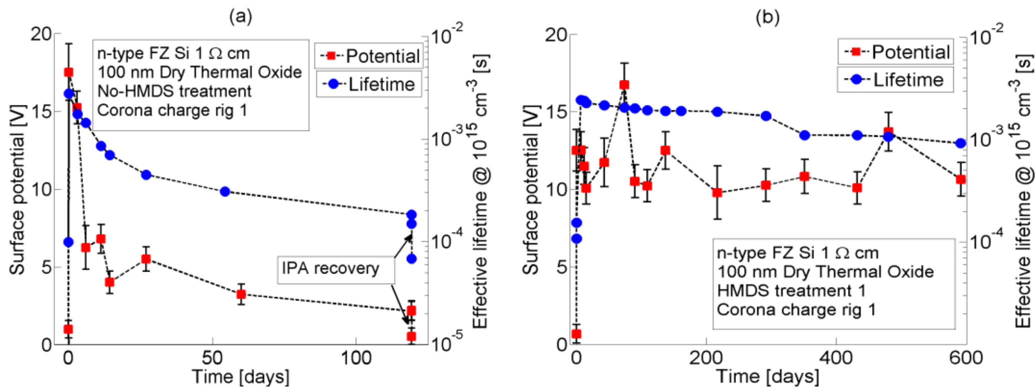

Figure 48. Kelvin probe (KP) surface potential and effective lifetime for a corona charged (Rig 1) 100 nm oxide on n-type FZ silicon, 1 Ωcm (Samples n9_x1 and n1_6) at an excess minority carrier concentration of 10^{15} cm^{-3}. a. Sample n9_x1 had no HMDS treatment. b. Sample n1_6 had HMDS treatment 1.

4.3.2.1 Forming gas annealed SiO_2

HMDS surface treatment was also applied to a specimen that underwent a FGA. This was a FZ Si specimen HMDS treated using procedure 1 in Chapter 2, and corona charged to optimal passivation. The specimen was stored in laboratory conditions and measured occasionally over a period of 600 days. Figure 49 illustrates the surface potential and effective lifetime of this specimen, and a control specimen lacking HMDS treatment. The effective lifetime before corona charge deposition is seen to increase from ~0.1 ms for as-deposited oxides, to ~ 0.2-0.4 ms for FGA oxides, as previously illustrated in section 4.2.4. After corona charge deposition the lifetime was seen to increase to ~ 2ms in these samples. Corona charge was seen to be unstable in the absence of HMDS chemical treatment, Figure 49.a. HMDS chemically treated samples, on the other hand, showed remarkable charge

stability, Figure 49.b. In FGA oxide samples the lifetime decay time constant increased to 3,000 ±32% days, while surface potential was seen to be constant throughout the measurement period.

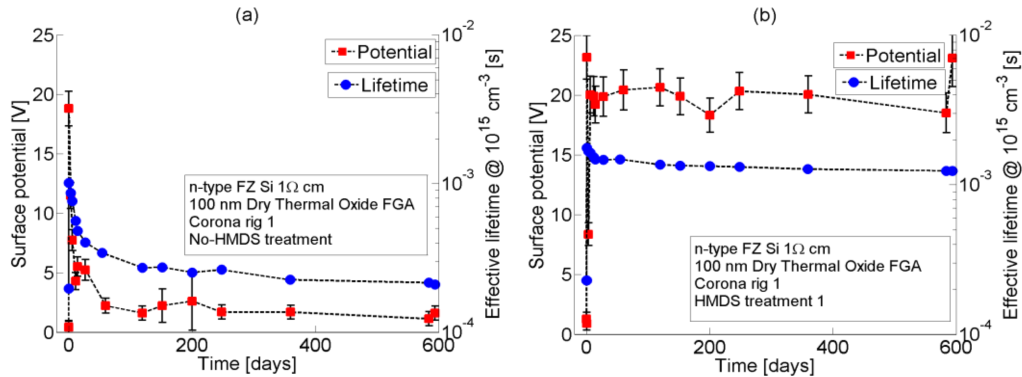

Figure 49. Kelvin probe (KP) surface potential and effective lifetime for a corona charged (Rig 1) 100 nm oxide on n-type FZ silicon, 1 Ωcm (Samples n17_5 and n17_7) at an excess minority carrier concentration of 10^{15} cm^{-3}. a. Samples n17_5 had no HMDS treatment, b. Sample n17_7had HMDS treatment 1.

4.3.3 Discussion

A promising step towards solving the stability issue was taken with the stabilisation of corona charge by eliminating surface conduction due to silanol groups and water absorption in oxide passivating layers. HMDS was used for this purpose and it proved very effective. For oxides grown in Cz-Si, HMDS extended the FEP decay time constant from 10 to 800 days, and KP surface potential presented no apparent decay. Similarly, HMDS chemically treated oxides on FZ-Si were seen to retain charge. Lifetime, however, decreased with a decay time constant of 600 ±17% days. Untreated oxide on FZ-Si showed a ~20 ±40% days decay time constant. Corona charge was also seen to be remarkably stable in specimens that underwent a FGA. Their lifetime decayed at a much slower rate than that of bare oxides. A time constant of 3,000 ±32% days was estimated for decay in effective lifetime in this specimen. This is a substantial improvement in the stability of surface passivation.

KP surface potential mapping was used to assess charge leakage and lateral migration. For an HMDS treated oxide it was shown that, after a year, a number of small ~ 1-3 mm^2 regions had partially lost their charge yet no lateral migration could be evidenced

within the lateral resolution of the technique. This indicates that HMDS is effectively eliminating lateral conduction mechanisms in the oxide, yet there seems to be a number small ‘bad’ spots on the oxide. These small, low surface potential regions suggest that a component of bulk conduction in the oxide is present at those regions, presumably caused by small break down channels. This leads to leakage of the corona charge through the oxide, and it is more commonly observed at high surface potential regions. It is also possible that this may be due to sample manipulation and storage, or imperfections in the wet oxide growth process, yet in such a case the bad spots would be observed to be randomly distributed. Despite this leakage component, the average surface potential for the measured specimen only reduced by 0.5 V (~ 5 x 10^{10} q/cm^2). This indicates a minimal loss of charge. The effective lifetime of all samples was seen to reduce over time while surface potential was virtually stable within the experimental accuracy of the technique. It is possible that a reduction in lifetime occurs without loss of charge if chemical de-passivation takes place over time.

4.3.4 Summary

The results in this section have demonstrated that HMDS is a suitable hydrophobic layer to prevent water absorption, lateral conduction, and improve the stability of corona extrinsic FEP. Decay time constants of effective lifetime τ_{FEP} of 600 $\pm$17% and 3,000 $\pm$32% days were estimated for bare and FGA oxides. The high stability shown here therefore indicates that controlled FEP is a promising method to provide enhanced passivation for silicon surfaces. However, there is still some decay in passivation quality and the surface potential, and this small effect is still greater than that required for a commercial solar cell[1]. In

[1] The standard loss in cell energy output in industry is about 80% in year 25. In the best case scenario this loss originates purely from loss in passivation and a time constant of ~ 40,000 days is required. Realistically other factors also contribute to loss in the cell power output and the time constant for passivation decay should be ~ 80,000 days.

addition, HMDS is an organosilicon compound and no report of its long term stability in harsh environmental conditions has been published to date. It is thus believed that HMDS is not a practical solution for silicon solar cells that must endure ultraviolet radiation, humidity, and thermal bonding to ethylene-vinyl acetate (EVA) for cell encapsulation. It is hence required to have a more uniform and stable charge concentration at or near the silicon surface that could last for the lifetime of a solar cell. The next section describes a new approach developed in this work.

4.4 Embedding corona charge into SiO_2 films

Corona charge on oxide films has been proven to provide FEP to the silicon surface. The stability of corona extrinsic FEP has been assessed and a chemical modification of the oxide surface has, to a large extent, eliminated the charge leakage mechanisms in the oxide. However, this is not sufficient stability for the practical application of these methods. In the context of this project a new method of charge stabilisation in dielectrics has been proposed. In this method an electric field is established in the dielectric film at high temperatures. Once there the film is cooled down to room temperature and the field is effectively 'frozen-in'. This novel method will be called hot corona passivation. The origin of the field could be: a) polarisation of the dielectric due to movement of ions already present in the film bulk, or b) migration of ions into the dielectric due to diffusion or drift mechanisms. In the latter the driving field could be due to corona charge pre-deposited at room temperature, or a field produced at high temperature by, for example, corona or by applying a potential to a surface electrode. In this work the migration of ions into the dielectric has been investigated by submitting corona charged specimens to a post-corona anneal. This process was well controlled and repeatable, and was thought to provide the corona ions with enough energy to migrate laterally or across the film, to a stable location in the film's bulk. This section describes new findings in the charge dynamics and passivation quality when corona charged

ions are migrated into oxide films at high temperatures using a post-corona anneal. Their effect on the stability of FEP is also studied using lifetime measurements.

4.4.1 Post-corona charge anneal in HMDS treated SiO_2

HMDS treated 87.5 and 21.5 nm oxide Cz-Si samples were charged to an optimal ~ 9 V and ~ 3 V surface potential, respectively, by depositing ~ 10^{12} q/cm^2 using corona charge Rig 1. Figure 50 illustrates the effective lifetime and surface potential of these samples (nCb4 and nBb1) after a 10 minute anneal at 400 ^{o}C. Samples nCb7 and nBb2 were included for control purposes. After a post-corona anneal the surface potential is seen to drop to nearly zero. KP measurements are sensitive to the surface potential of the dielectric films, thus if the KP measurements are found to decrease this can be due either to loss of charge from the material or migration of charge away from the surface into the bulk of the film. These results indicate that both phenomena have occurred since effective lifetime only decreases by ~30% for both thick and thin oxides, and approximately zero surface potential was measured by KP after the anneal. The charge which remains in the dielectric is seen to be remarkably stable, as indicated by the constant lifetime for sample nCb4 with a 87.5 nm oxide. For sample nBb1 with a 21.5 nm oxide, however, the lifetime was seen to decay back to its original value in about 500 days. A decay time constant of ~ 3,000 $\pm$50% days is estimated for the lifetime decay in sample nCb4 and ~ 125 $\pm$35% days in sample nBb1. Control samples of corona charged oxides without a post-corona anneal are shown in Figure 50.b,d over the same time-span. Here it is evident that HMDS has stabilised corona charge at the surface of the oxide by preventing water absorption. Effective lifetime in control samples is seen to exponentially decay with a time constant of ~1200 $\pm$20% days for thick 87.5 nm oxides and ~645 days $\pm$21% for thin 21.5 nm oxides. This is double that reported in section 4.3.2 suggesting that the HMDS coating process was better in these samples. Note that the variation in charge stability cannot be unambiguously linked to the different thickness of the oxide since layers since they were grown under different conditions. Also no conclusion is made regarding the

effect of HMDS treatment on the stability of charge in post-corona annealed samples since controls lacking HMDS were omitted due to a lack of material.

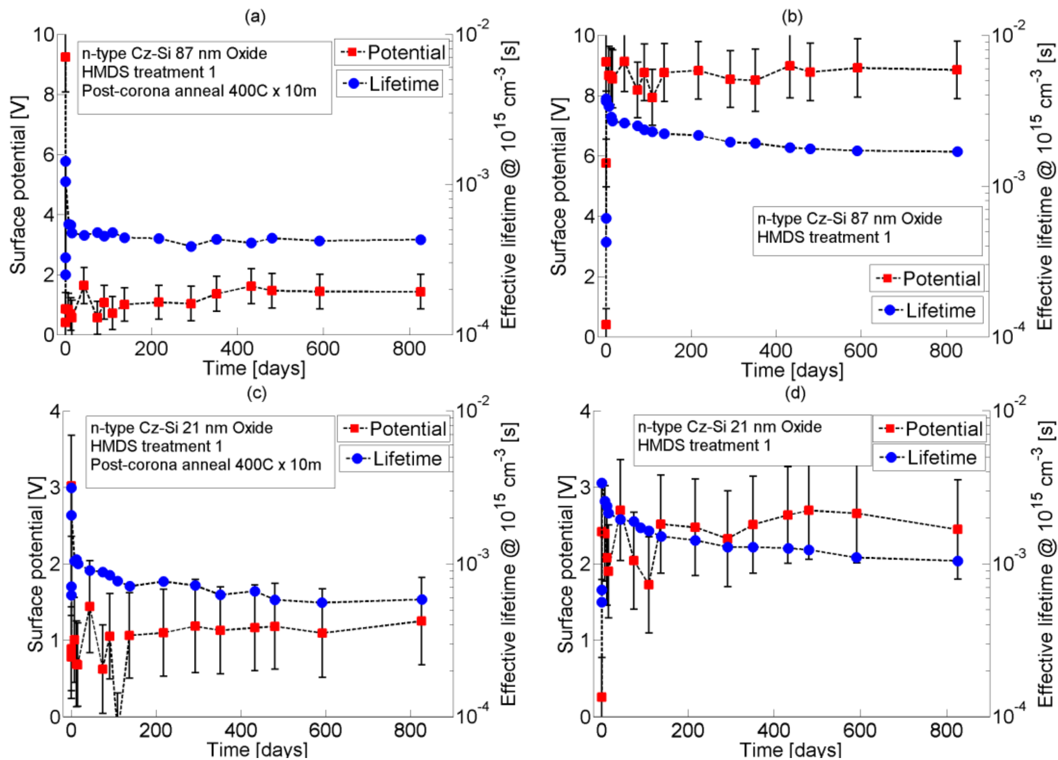

Figure 50. Surface potential and effective lifetime for a corona charged n-type Cz Silicon (5Ωcm) passivated with a 87.5 nm (a. Sample nCb4 and b. Control sample nCb7 without PC anneal) and 21.4 nm (c. Sample nBb1 and d. Control sample nBb2 without PC anneal). PC stands for post-corona. All samples have been chemically treated with HMDS.

Oxides grown on high quality FZ-Si were also subjected to a post-corona anneal with the objective of studying charge migration from the surface towards the dielectric bulk. Corona charged samples were annealed at 400 ^{o}C for 5 min. Figure 51 illustrates surface potential and effective lifetime for post-corona annealed samples with and without HMDS treatment. It is important to note that the specimen in Figure 51.a had the HMDS treatment applied after the post charge anneal step. Prior to the anneal both samples reached an effective lifetime of 2.6 ms with a charge concentration of ~10^{12} q/cm^2. During the anneal, Figure 51.a, charge quickly (< 5 min) migrates from the air/oxide interface towards the oxide/silicon interface, as indicated by the KP surface potential reducing to nearly zero while the effective lifetime only reduced by ~ 25%, from ~2.6 to ~1.5 ms. The characterisation performed on this oxide/silicon system in Chapter 3 can be used to estimate the concentration

of charge remaining in the film after the anneal; a concentration of ~ 5-8 x 10^{11} q/cm^2 charge migrates into the film and is not lost at the interface. Since the initial concentration of charge is ~10^{12} q/cm^2, it is estimated that in 5-6 minutes at 400 ^{o}C a charge concentration of ~4 x 10^{11} q/cm^2 is lost when it reaches the oxide/silicon interface, possibly due to electrons injected into the film from surface states in the Si. A direct characterisation of the stability of charge cannot be analysed since the KP surface potential measured was within the systematic error of the instrument. However, it is believed that the charge which remains in the film is stable for a period of up to 800 days as observed from the effective lifetime. A decay time constant of ~3300 ±12% days is estimated for lifetime deterioration in the HMDS treated sample versus ~ 1100 ±45% days for the untreated sample, Figure 51.b.

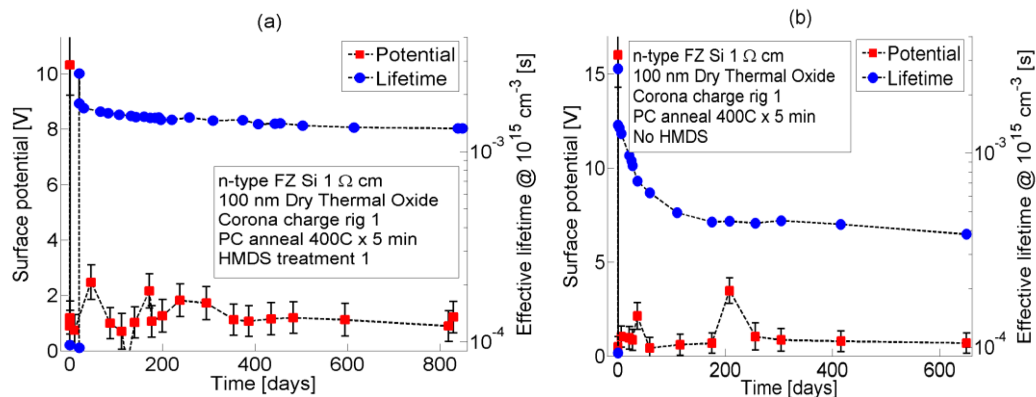

Figure 51. KP surface potential and effective lifetime at 10^{15} cm^{-3} for FZ n-Silicon, corona charged in Rig 1, a. with and b. without HMDS treatment 1 (Samples n1_1 and n7_6). PC stands for post-corona.

4.4.2 Textured silicon surface

Long term stability was also studied on textured surfaces by storing the sample after corona charge and periodically measuring its lifetime and KP surface potential. For this sample, however, HMDS treatment was not applied. The sample was post-corona annealed at 400 ^{o}C for 1 minute to drive the charge into the dielectric and stabilise it. After the anneal, charge was seen to fully migrate to the oxide/silicon interface as observed by the KP surface potential reducing to ~ 0 V and lifetime only reducing by 20%. Using data reported in Section 4.2.3 it is inferred that a charge concentration of 2 x 10^{12} q/cm^2 was compensated by charge annihilation at the interface, while the remaining 1 x 10^{12} q/cm^2 remained charged in

the oxide and provided FEP, as indicated by a lifetime of 0.13 ms, Figure 52. Regardless of the lack of chemical protection, this charge was seen to be remarkably stable for a period of up to 700 days and a time decay constant of ~ 10,000 ±21% days was estimated for lifetime deterioration.

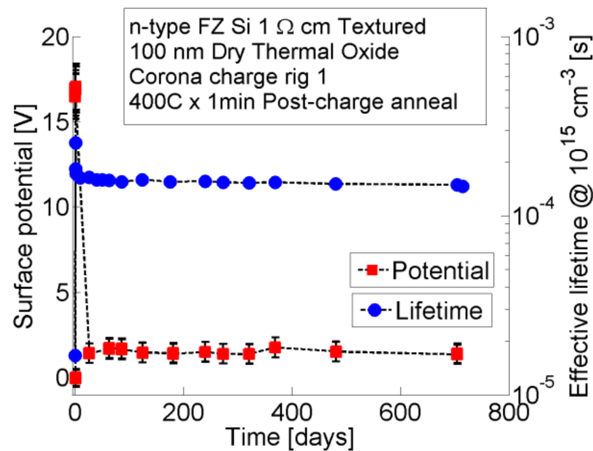

Figure 52. KP surface potential and effective lifetime for a corona charged (Rig 1) 100 nm oxide on textured n-type FZ silicon (Samples nT1_9) at an excess minority carrier concentration of 10^{15} cm^{-3}. Sample had no-HMDS treatment but a post-corona 400 ^{o}C anneal for 1 minute.

4.4.3 Discussion

A new method of charge stabilisation has been proposed and tested in this work. This involves a high temperature migration of charged corona ions into the bulk of the film. This section has shown that a 400 ^{o}C anneal after corona charge deposition can drive the charge into a SiO_2 film thermally grown on c-Si. During this anneal, however, a large portion of the charge is lost, as indicated by a reduction in lifetime combined with a drop in surface potential to nearly zero. It is thought that this portion of the corona charge migrated sufficiently close to the oxide/ silicon interface such that direct charge annihilation took place via electron injection from the Si. Although reduced, effective lifetime thereafter was seen to decay slower for samples that underwent a post corona anneal than for those which did not. This was the case for 87.5 nm oxide grown on Cz-Si, and for 100 nm oxide grown on FZ-Si, but not for for the 21.5 nm Cz-Si oxide. No conclusion is made with regards to the effect of the oxide thickness, since the oxides were grown using different conditions. Despite the highly stable charge for 87.5 nm and 100 nm oxides, the passivation quality measured in

the effective lifetime was seen to deteriorate over time. It is believed that chemical de-passivation might take place due to the high surface electric field at the so called bad spots in the oxide/silicon interface. It is also possible that a loss in charge over time is taking place since the accuracy of the KP measurements is poor when charge lies at the dielectric/silicon interface. Further studies of this phenomenon were not performed here, yet it is noted that this is a key issue for the application of this technology at a commercial level. Non-HMDS treated samples showed a faster decay in lifetime τ_{FEP}~ 1100 days. These results indicate that although corona charge has been moved deep into the film, it may still be susceptible to surface conduction provided by water absorption at the surface of the film, or that the HMDS step applied after post charge anneal allowed charge within the film to move to a more stable location. It was additionally found that the film surface conduction depended on surface texture. Oxidised textured FZ-Si samples, without HMDS treatment, corona charged and post charge annealed, showed a τ_{FEP}~ 10,000 days. No further conclusion can be made on the decay of charge since KP measurements are not sufficiently sensitive when charge is at the oxide/silicon interface.

The exact mechanism by which charge migrates into the oxide has not been studied in this work. However, a few observations can be made on what phenomena may be occurring. It was concluded that the location of charge shifted from the air/oxide to the oxide/silicon interface at high temperature. It was also concluded that a portion of charge was lost. Two distinctive mechanisms by which this may happen are proposed here. These are illustrated in Figure 53. First, an electronic charge hopping mechanism can excite charge in ambipolar trap states throughout the oxide film, such that the positive charge in corona ions is transferred in subsequent hops from the surface to the oxide/silicon interface (or equivalently by electrons moving in the opposite direction) as illustrated in Figure 53.b. Second, corona ions are sufficiently small and have sufficiently high diffusivity such that the concentration gradient and the electric field provide the diffusion and drift forces for ions to move from the surface to the oxide/silicon interface as illustrated in Figure 53.b. The

likelihood of either of these mechanisms is not conclusive from this work, yet further studies could enlighten the nature of charge migration in this system.

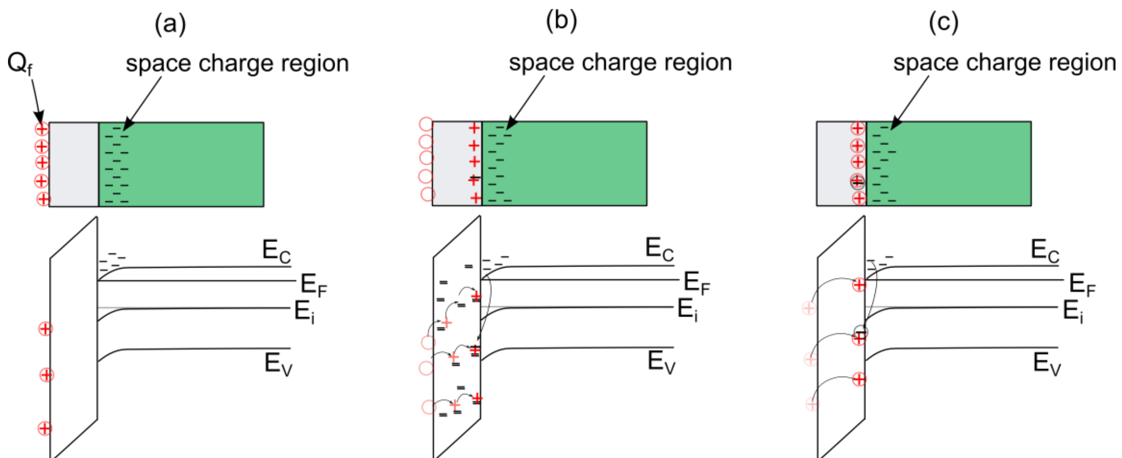

Figure 53. The mechanisms of high temperature corona charge migration in thermal oxides: a. Starting state after corona charge deposition, b. charge migration into the oxide through defect states charge hopping, c. Charge migration via diffusion and drift of charged corona ions into the oxide film.

4.4.4 Summary

This section has provided evidence of charge migration into thermally grown oxides as a result of high temperature annealing. After the migration process, charge is stable when the surface has been correctly protected with HMDS improving the stability of FEP by two to three times. Effective lifetime decay time constants of 3,300 days were achieved for HMDS treated oxides post-corona annealed. A small decay in the passivation quality is still observed and it is thought to be related to a long term loss of charge and/or chemical passivation, in planar silicon surfaces. For textured surfaces, significant stability is observed with a decay time constant of 10,000 days, despite the lack of HMDS treatment. Despite the large improvement in charge stability the decrease observed is still greater than that required for a practical solar cell, and thus this methodology is only a step towards fully stable and effective FEP. Chapter 5 will introduce the second new approach developed in this work to produce extrinsic FEP.

4.5 Effect, location and stability of corona charge in SiO_2/SiN_x passivated Si

Double layers of SiO_2/SiN_x have been widely reported in the literature as one of the best passivation systems [189]. It combines the excellent chemical passivation given by silicon dioxide [168] with the FEP provided by the intrinsic charge of the nitride. Work performed during this project demonstrated that such charge resides at the oxide/nitride interface after nitride deposition. This is thoroughly described in reference [190] and is not included here because of space limitations. In addition to chemical and FEP, double layers benefit from the extra chemical passivation component given by hydrogenation during CVD nitride deposition [191] or during a high temperature hydrogen liberation step, normally executed after film deposition [192]. Overall the oxide/nitride system is of high relevance for the manufacture of high efficiency silicon solar cells. This section expands the current understanding of surface passivation provided by the double layer oxide/nitride system. The intrinsic and extrinsic FEP of this double layer film is studied and important observations are made on the components of surface passivation, the maximum surface passivation possible, the dynamics of corona charge, and the effect of surface texturing.

4.5.1 Extrinsic corona FEP of c-Si using SiO_2/SiN_x double layers

The contribution of FEP towards the total surface passivation of double oxide/nitride layers was evaluated via the corona – Kelvin probe – lifetime experiment. Figure 54 illustrates the injection dependent lifetime of samples before and after corona charge deposition. It shows that, except for a high quality 10/60 nm oxide/nitride layer produced at Fraunhofer ISE, passivation in oxide/nitride films improved with corona charge. The film deposition conditions for 10/60 oxide/nitride films have been optimised such that the highest quality nitride passivation is produced. Such films (green circles in Figure 54) exhibited no significant change in lifetime upon charge deposition indicating that the field effect

contribution to passivation was near maximum. Textured films (blue squares), however, showed a 2-fold improvement in lifetime upon charge deposition thus indicating that, although optimised for a polished <100> surface, passivation on a textured surface using this silicon nitride would still benefit from additional charge. Figure 54 also includes a comparison with a 'non-optimal' silicon nitride film deposited using a different PECVD reactor at Oxford. This nitride was deposited on an FGA 100 nm oxide passivated sample. The FGA step increases lifetime up to 0.2 ms (red crosses in Figure 54), nitride deposition to 3.5 ms (unfilled red triangles in Figure 54), and corona charge to 5 ms (solid red triangles). This is over 40% improvement obtained as a result of extrinsic FEP. This is equivalent to an effective SRV of 0.65 cm/s. This illustrates that extrinsic FEP can substantially contribute to the overall passivation properties of a film, particularly when film deposition conditions are not optimum. Figure 54 shows some of the highest lifetimes achieved on an FGA 100/80 nm oxide/nitride passivated specimen. Average specimens with the same processing steps showed maximum lifetimes between 2-4 ms (SRV between 1-3 cm/s) after corona FEP. This wide variation was due to the nitride deposition conditions in the plasma reactor at Oxford.

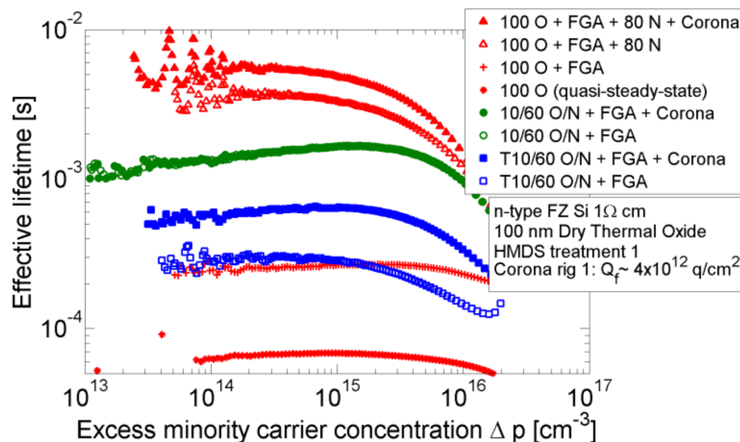

Figure 54. Effective lifetime as a function of injection level for single and double oxide/nitride passivation films on 1 Ωcm FZ n-Si. Samples n19_3, n17_8, OX1-1_5, OX1-9_1.

4.5.2 Separating the chemical and field effect components of passivation in SiO_2/SiN_x double layers

The use of extrinsic FEP makes it possible to optimise independently the chemical and field effect components of passivation in a dielectric film. For maximum passivation to be

achieved, it is important to assess the intrinsic passivation components first, such that well-tailored processes to enhance the extrinsic chemical or field effect passivation in a film can be selected. Part of this optimisation is achieved via nitride deposition in SiO_2/SiN_x double layers, yet no report of the independent components of passivation exists to date. In this section a separation of chemical and FEP is explored by means of effective lifetime, CV and KP measurements.

Figure 55 illustrates injection-dependent effective lifetime for 1 Ωcm n-type c-Si passivated with an outstanding oxide/nitride film and FGA. Passivation achieved using only the FGA oxide film is also included. When subjected to corona charge deposition in Rig 2, an improvement in effective lifetime from 0.25 to 3 ms is obtained on the FGA oxide layer. This is equivalent to a SRV as low as 2 cm/s at a minority carrier injection of 10^{15} cm^{-3}. Chemical passivation can be additionally improved if a PECVD silicon nitride is deposited on top of the oxide. SiN_x improves chemical passivation by releasing hydrogen during the deposition process such that many of the interface defect states are effectively eliminated. Annealing at 400 ^oC after nitride deposition has been suggested to increase chemical passivation due to release of hydrogen from the nitride film [193]. A 10 min anneal was performed here but no improvement in lifetime was obtained. This indicates that hydrogen passivation at the Si interface was already saturated, or that no hydrogen was released from the Oxford grown nitride film during the anneal. SiN_x also contains a moderate intrinsic concentration of charge. When deposited on the base oxide film its total effect was to reduce the SRV to ~ 3.5 cm/s. Chemical deposition processes are not perfectly uniform as reported by Veith et al [159] and consequently charge contained in as-deposited films does not provide uniform FEP across the full area of a sample. This was also observed by Herasimenka [194] who was able to achieve SRV< 1cm/s by providing extra FEP by means of corona charge. In this work a minimum surface recombination velocity has been obtained by optimizing FEP using extrinsic and uniform corona charge from Rig 2, as shown by the black solid circle trace in Figure 55. The optimum corona charge concentration was

characterized using KP surface potential and was found to be ~5 x 10^{12} q/cm^2. A remarkable effective lifetime of 6.7 ms has been achieved at a minority carrier concentration of 10^{15} cm^{-3} by such an oxide/nitride layer with extrinsic and uniform FEP[2]. The SRV for this sample is plotted in the inset of Figure 55, from which it is evident that SRV can be reduced to 0.15 cm/s when the chemical and field effect components, both intrinsic and extrinsic, of passivation are jointly and uniformly exploited.

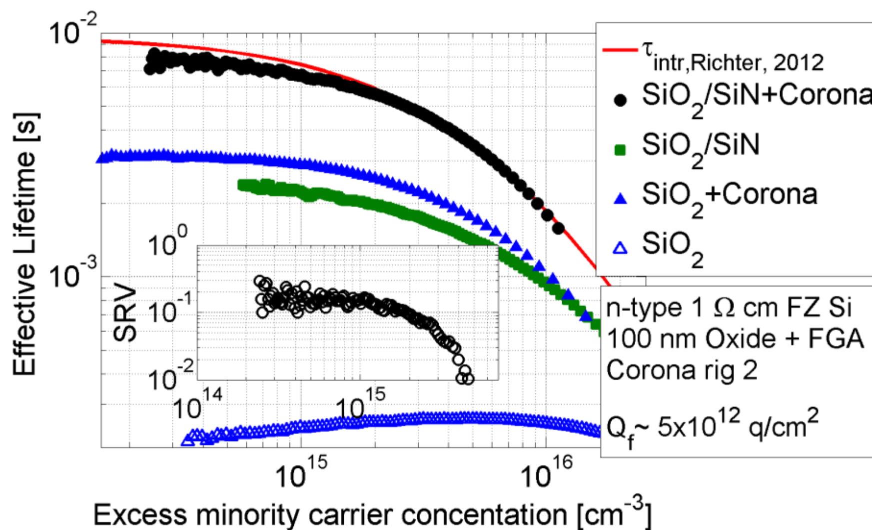

Figure 55. Injection-dependent effective lifetime for 1Ωcm n-type FZ-Si passivated with a thermally grown oxide and a PECVD deposited nitride (Sample n21b_5), plus the impact of FEP via external corona charge. Inset plots SRV of the SiO_2/SiN_x + Corona specimen. Control sample n17_8 without SiN_x is included.

The specific contribution of each of the chemical and field effect to overall passivation has been studied using a combination of Kelvin probe and CV measurements. Figure 56.a shows typical CV curves measured on oxide and double oxide/nitride layers. Figure 56.b shows the density of interface states obtained using Terman's high frequency CV method [168] on oxide and double oxide/nitride layer dielectric films. Prior to nitride

[2] This specimen produced the highest lifetime of any studied in this work. It is to note that the nitride was deposited after the 3 x 3 cm^2 specimen was cleaved. Thus the cleaved edges in this specimen received a partial passivation process. Work in this thesis (not included for reasons of limited space) shows that recombination at edges has a significant effect on the effective lifetime when lifetimes over 5 ms are observed. It is thus likely that some other specimens would also have shown longer effective lifetimes (implying lower values of SRV) if the edges of the cleaved specimens had been passivated.

deposition the mid-gap value of interface state density (D_{it}) is ~5 x 10^{10} cm^{-2} eV^{-1}. Terman's method normally under-estimates defect density in comparison to more accurate methods such as those of Berglund [169] and Castagne [170]. When the nitride is deposited, the density of states is reduced by an order of magnitude to ~5 x 10^{9} cm^{-2} eV^{-1}. This demonstrates the typical chemical passivation effect silicon nitride deposition has on an oxide/silicon interface. The same specimen in Figure 56.a was deposited with corona charge and measured again using Hg-probe CV and Kelvin probe. Kelvin probe measurements revealed that the surface charge concentration on this sample was ~5 x 10^{12} q/cm^2, similar to that for specimens in Figure 55. When measured via CV, a small shift in the flat band voltage indicated that most of the corona-deposited charge is located directly at the nitride-air interface. This superficial corona charge was subsequently removed from the sample using an IPA rinse followed by KP and CV measurements. No change in the density of states was observed following this process. Finally, an etch-back experiment was conducted to profile the charge intrinsic to the nitride. Here the nitride was removed in steps using a phosphoric acid solution and measured using Hg-p CV (Figure 56.a inset). Film thickness was monitored using reflectance spectrometry as described in Section 2.5.2.1. Hg-p CV and film thickness measurements were conducted on several different places of the same sample. In average 30% of the measurements were failed due to high leakage in the MOS device. Measurements reported in the inset in Figure 56.a are averages of at least 5 successful measurements. The inset in Figure 56.a indicates that the charge in an as-deposited oxide/nitride film –i.e. that which provides intrinsic FEP, is located within 20 nm of the interface between the two dielectrics and that all the deposited corona charge was located on top of the nitride, such that it was completely removed with the IPA rinse or the first etching step in phosphoric acid.

The combination of data presented in Figure 55 and Figure 56 makes it possible to separate the components of surface passivation at different stages in the processing. PECVD nitride deposition (and the associated H passivation) reduces D_{it} from ~5 x 10^{10} to ~5 x 10^{9}

cm^{-2} eV^{-1} and provides ~5-8 x 10^{11} q/cm^2 charge concentration, thus reducing SRV from ~40 cm/s to ~3.5 cm/s. In order to separate the chemical and field-effect components of PECVD silicon nitride passivation the modelling formalism explored in Chapter 3 is used here. Using this model the field effect component in the nitride was seen to provide a reduction from ~40 cm/s to ~10 cm/s. The enhancement of the chemical component by nitride deposition therefore provides the remaining reduction in SRV, from ~10 cm/s to 3.5 cm/s. The final optimization of the passivation scheme used here is that given by extrinsic FEP, which further contributes a reduction in SRV by more than a factor of three, from ~3.5 cm/s to ~ 0.15 cm/s. In summary, when PECVD nitride is deposited onto base oxide films surface recombination is reduced by a factor of 10, with the intrinsic FEP accounting for a factor of 4 and the intrinsic chemical a factor of 2.5. Subsequent application of extrinsic FEP further reduces SRV by a further factor of $\gtrsim 3$.

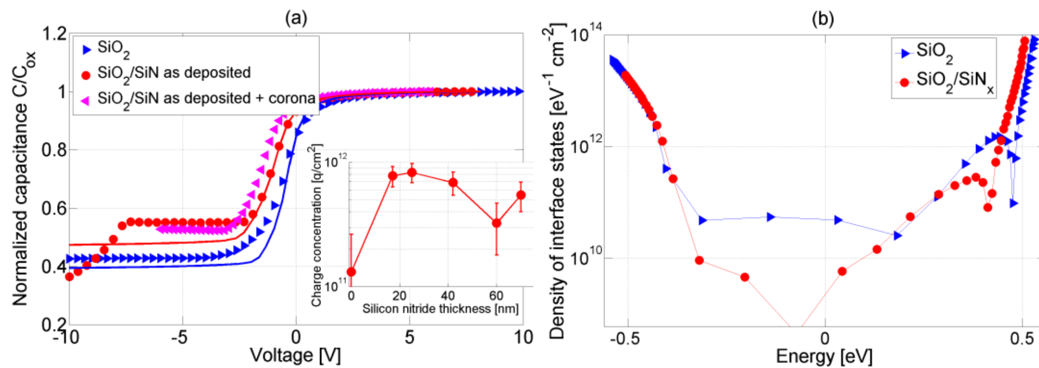

Figure 56. (a) Capacitance-voltage measurements of single and double layer oxide/nitride films on 1 Ωcm c-Si. Solid lines represent the ideal theoretical curves. Inset picture a back etch experiment to determine charge location (b) Interface state density calculated for the dielectric layers of (a), using the high frequency CV Terman’s method.

4.5.3 Stability of charge and HMDS chemical treatment

The stability of extrinsic FEP has been tested over a period of 650 days in oxide/nitride double layers. 100/80 nm and 10/60 nm oxide/nitride layers were treated with HMDS, corona charged, and their surface potential and effective lifetime monitored over this period. Samples without HMDS treatment were included for control purposes. As it has been demonstrated in single oxide layers, in the absence of HMDS treatment or post-corona anneal, the corona surface charge, and hence effective lifetime, fully decay in a time period

of < 100 days, Figure 57.a and Figure 58.a. In 10/60 oxide/nitride layers the effective lifetime was unchanged with charge deposition, indicating optimal intrinsic FEP. For the 100/80 nm oxide/nitride sample in Figure 57.b, however, the lifetime is improved by 1 ms after corona charge deposition and it is seen to be stable with a decay time constant of ~ 1,200 ±38% days. A small decay is observed over the measurement period, possibly as a result of chemical de-passivation, yet effective lifetimes >1.4 ms are observed during the two years of measurements. This is equivalent to a SRV < 6 cm/s. The surface potential in HMDS treated layers was seen to quickly (~50 days) decrease and plateau at about 50% of its value after corona charge deposition. This decay is believed to be due to charge slowly migrating from the nitride/air interface to the oxide/nitride one, instead of due to charge loss. This is indicated by the minimal decay observed in lifetime in the 100/80 nm double layer. No correlation could be drawn for the 10/60 nm double layer.

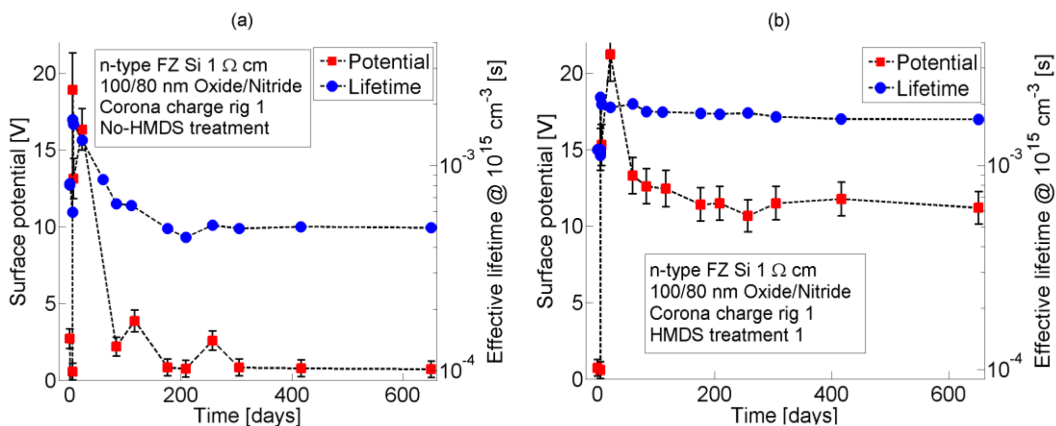

Figure 57. KP surface potential and effective lifetime for a corona charged (Rig 1) 100/80 nm oxide/nitride on n-type FZ silicon. a. Sample n6_5 had no HMDS treatment, b. Sample n6_8 had HMDS treatment 1.

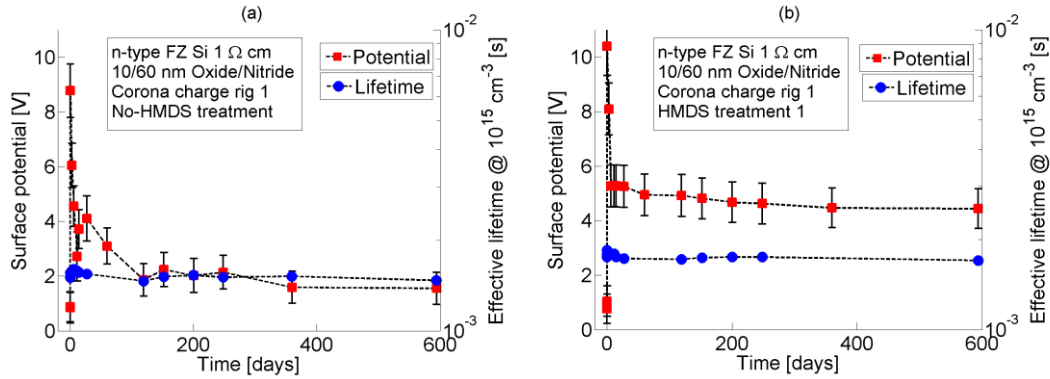

Figure 58. KP surface potential and effective lifetime for a corona charged (Rig 1) 10/60 nm oxide/nitride on n-type FZ silicon. a. Samples OX1-1_1 had no HMDS treatment, b. Sample OX1-1_4 had HMDS treatment 1.

4.5.3.1 Textured surfaces

The long term stability of corona charge on oxide/nitride double layers on textured Si is explored here. Samples were HMDS treated and corona charged in corona Rig 1. HMDS un-treated specimens were included for control. Figure 59 illustrates the surface potential and effective lifetime of HDMS treated and un-treated specimens. Similarly to the results observed for planar surfaces, surface potential and effective lifetime in un-treated samples are seen to decay. However, in addition, the decay in lifetime below its pre-charge deposition value indicates de-passivation product of corona charge deposition and/or decay. This is illustrated by the effective lifetime at the end of the measurement period in Figure 59.a. HMDS treated samples exhibit better stability, but the lifetime decay was still noticed, with a decay time constant of ~520 $\pm$10% days, possibly as a product of chemical de-passivation. Dielectric charge in treated samples, Figure 59.b, was seen to decay over the first 100 days and then to remain stable. This, together with the small decay in lifetime, indicates that charge is moving from the surface of the film to the interface between the oxide and the nitride.

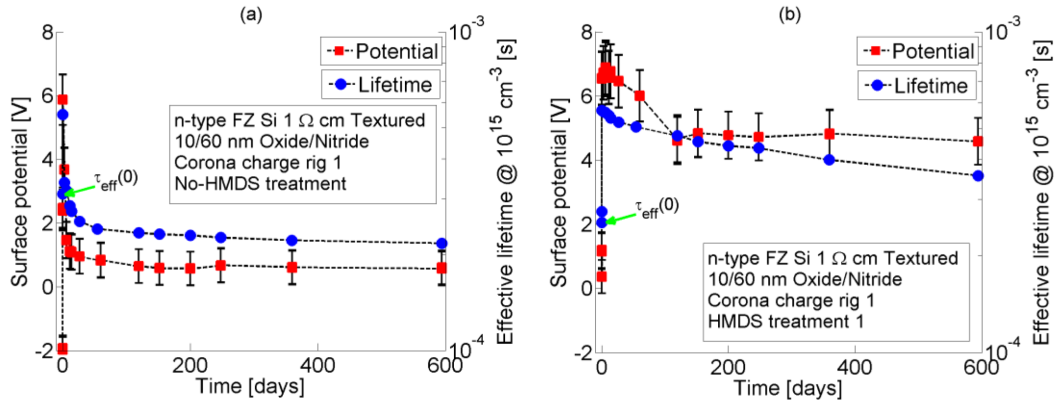

Figure 59. KP surface potential and effective lifetime for a corona charged (Rig 1) 10/60 nm oxide/nitride on n-type textured FZ silicon. a. Samples OX1-5_1 had no HMDS treatment, b. Sample OX1-5_5 had HMDS treatment 1

4.5.4 Discussion

Oxide/nitride double layers on FZ-Si were studied in this project with two aims. First, to provide an extra level of chemical passivation attained by hydrogenation during nitride deposition and FEP attained by SiN_x charge, and second, to provide a nitride/oxide interface where charge could migrate to and where it might stay for long time periods. These possibilities were studied using FZ-Si by depositing a SiN_x layer on top of 10 or 100 nm oxide layers. External deposition of charge was seen to greatly enhance surface passivation when nitride deposition conditions are not optimised. An oxide/nitride layer with optimal chemical and FEP produced at Fraunhofer ISE did not benefit from extrinsic FEP. When a nitride film only provides chemical passivation, extrinsic FEP can be used to produce outstanding passivation. For example, SRV <0.15 cm/s can be obtained when the chemical and field effect components, both intrinsic and extrinsic, of passivation are jointly and uniformly exploited. A very important chemical component is therefore observed in the passivation quality of double layers, given by a combination of the already low-defect density interface between silicon and FGA silicon dioxide, and the hydrogenation that occurs during the PECVD process. This is a remarkably low surface recombination considering the non-optimum conditions of the PECVD deposition. In fact, such surface recombination velocity is the lowest seen to date for single oxide or double oxide/nitride passivation stacks on moderately doped ~ 1 Ωcm silicon, and has only ever been outperformed by that reported

by Herasimenka using an a-Si/SiO_2/SiN_x triple layer stack which was subsequently exposed to corona charge deposition [194]. The very simple technique used here also outperforms the outstanding 'alneal' passivation achieved by Kerr and Cuevas [35], which was used to infer the intrinsic lifetime parameterisation most cited over the last decade [49], [195].

The separate effects of the chemical and field-effect components of double layer passivation have been quantified. Deposition of nitride layers is seen to chemically reduce the oxide/silicon interface state density by an order of magnitude and provide intrinsic FEP with ~5 x 10^{11} q/cm^2. This combination reduces surface recombination by an order of magnitude. Extrinsic FEP is then seen to provide an extra degree of passivation reducing recombination by a factor of ~3. In the absence of the chemical passivation provided by the nitride, extrinsic FEP can reduce surface recombination by a factor of 10-30. This indicates that, when extrinsic FEP is available, chemical passivation is of lesser importance.

Corona charge deposited on oxide/nitride films was seen to remain at the surface immediately after deposition. During 40-100 days after deposition, corona charge migrates from the air/nitride to the nitride/oxide interface, provided that the layers have undergone HMDS treatment, and once there charge is seen to be virtually stable within the experimental accuracy of the technique, for up to 650 days. This is in contrast to the report by Sharma et al [196] where samples are claimed stable for a year regardless of the chemical treatment applied to their surfaces and charge is seen to penetrate the nitride immediately after deposition, spreading throughout its thickness. The decay in surface potential observed in HMDS un-treated specimens was comparable in double and single layers, indicating that the nitride alone did not enhance stability - it required HMDS treatment. Extrinsic FEP was monitored over the 650 day period. The effective lifetime is observed to decay slowly with a time constant of 1,200 days, while surface potential is apparently constant, indicating that chemical de-passivation is taking place. For oxide/nitride double layers it has been suggested that such de-passivation can be recovered if the samples undergo a forming gas anneal as

demonstrated by Granek and Reichel [197]. This suggests the mechanism is hydrogen related. Textured silicon with double layers, on the other hand, showed much faster decay with a time constant of 520 days. This aspect of textured surfaces has not been studied further, yet it may become relevant when applying the processing techniques outlined here to practical textured solar cells.

4.5.5 Summary

This section has provided evidence that remarkable and highly stable passivation is possible in oxide/nitride double layers by combining intrinsic chemical passivation, obtained from nitride deposition, and extrinsic FEP obtained using corona discharge; given that HMDS chemical protection is applied to the layers. An impressive SRV< 0.15 cm/s was reported and a lifetime decay time constant of 1,200 days achieved. Despite these results it is evident that the rate of decrease in passivation quality still exceeds that required for a practical solar cell. Chapter 5 will describe a new method that aims to overcome this decay.

4.6 Chapter summary

In the present chapter it has been demonstrated that FEP can be applied extrinsically to dielectric films to improve their passivation quality. This improvement can be stabilised for periods of up to two years on both single SiO_2 and double SiO_2/ SiN_x dielectric layers. SRVs below 10 and 2 cm/s were routinely demonstrated in moderately doped n-type Cz and FZ Si, respectively. Chemical processing of dielectrics was observed to be a requirement for long term stability on both single SiO_2 and double SiO_2/ SiN_x dielectric layers. Post-charge heat treatment at 400 ^oC rapidly drove charge into the dielectric layers. A portion of this charge was compensated by charge exchange at the dielectric/semiconductor interface, but that which remained in the film was seen to be stable for periods of over two years. Extrinsic chemical passivation was achieved by means of FGA. This improved the interface electrical features but it did not change the charge storage characteristics of the dielectric.

Optimally processed oxide/nitride films were seen to barely benefit from extra corona charge deposition. Non-optimally deposited nitrides, textured silicon surfaces, and oxide layers, on the other hand, showed a decrease in surface recombination of 2-10 times when charged using corona discharge. These results show that very large improvements in the passivation properties of non-optimised films can be achieved by modifying the charge density associated with them. In situations where the production of optimised films is difficult, for example due to the constraints of commercial manufacturing, more attention should be paid to the engineering of the charge density associated with the films so that better passivation is achieved. Moreover, as charge in as-deposited films is located at the interface between deposited oxide and nitride layers it is suggested that more attention be paid to the interface between native (or thermally grown) oxide and nitride layers when considering how charge engineering may be achieved. The chemical and temperature treatment applied represents a potential method to produce controlled and stable field effect passivation for solar cells, yet the stability needs to be brought to the same lifespan of a practical solar cell. Figure 60 summarises the stability of passivation obtained using these techniques. It is noted that best stability is achieved in a textured FZ-Si sample oxidised to 100 nm, lacking HMDS treatment but with the charge embedded in the bulk of the film, most likely at the oxide/silicon interface. A decay time constant of 10,000 days was inferred for the effective lifetime of this specimen. The second most stable FEP was achieved in a an oxide in planar Si, HMDS treated and positively charged in corona Rig 1, followed by a post-charge anneal to embed the charge. In this case a decay time constant of 3,300 days was inferred.

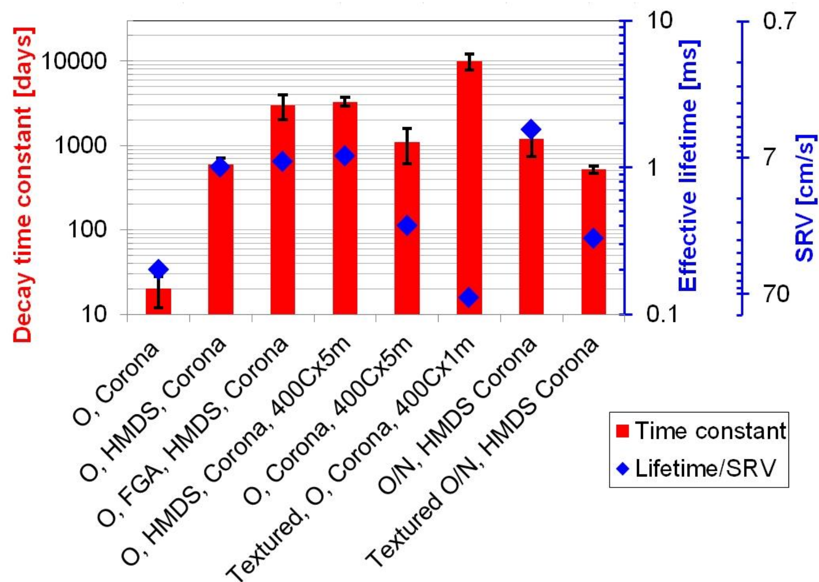

Figure 60: Summary of the effectiveness and stability of passivation in FZ-Si passivated with oxide and oxide/nitride layers, HMDS treated, deposited and/or embedded with corona charge. The effective lifetime quoted is that at the end of the measurement period. The decay time constant was estimated from the data between day 50 and the end of the period.

Extremely low surface recombination has been shown to be possible by independently combining the best chemical and field effect passivation components of dielectric films produced on silicon. Corona passivation uniformity has been optimized and it has proven to be a key factor in achieving very low surface recombination velocities. For the first time, a SRV of 0.15 cm/s has been demonstrated on 1 Ωcm n-Si using an oxide/nitride passivation layer. The strong influence of hydrogenation on the silicon surface defect density was assessed and it was found that a one order of magnitude reduction was produced by nitride deposition. The overall contribution of the different components of passivation produced by PECVD deposition of a nitride layer on thermally grown oxide were inferred as follows; the intrinsic FEP due to grown-in charge in the nitride layer accounts for a reduction in recombination by a factor of 4, the improved chemical passivation (due to hydrogen produced during deposition) accounts for a factor of 2.5, and the subsequent addition of extrinsic FEP results in a further factor of 3. Overall, an extraordinary passivation quality has been achieved via extrinsic FEP in this work, regardless of the dielectric layers used. The lowest ever surface recombination velocity achieved on oxide, and oxide/PECVD nitride stacks on ~1 Ωcm n-type silicon has been reported here. This level of passivation

outperforms the several state-of-the-art processes including the 'alneal' process proposed by Kerr and Cuevas [35], the oxide/PECVD nitride layers used by Larionova [39], the remote PECVD nitride used by Richter [28] and fast ALD AlO_x reported by Werner [52]. This comparison is outlined in Figure 7. It makes evident that the controlled and uniform FEP methods used here are as effective and, in some cases, better than state-of-the-art and expensive technologies. Extrinsic FEP is therefore a key technology to further improve passivation in high efficiency silicon solar cells. Furthermore, the versatility, low cost and now proven stability of extrinsic FEP makes it an extremely promising passivation approach to be used at the industrial scale.

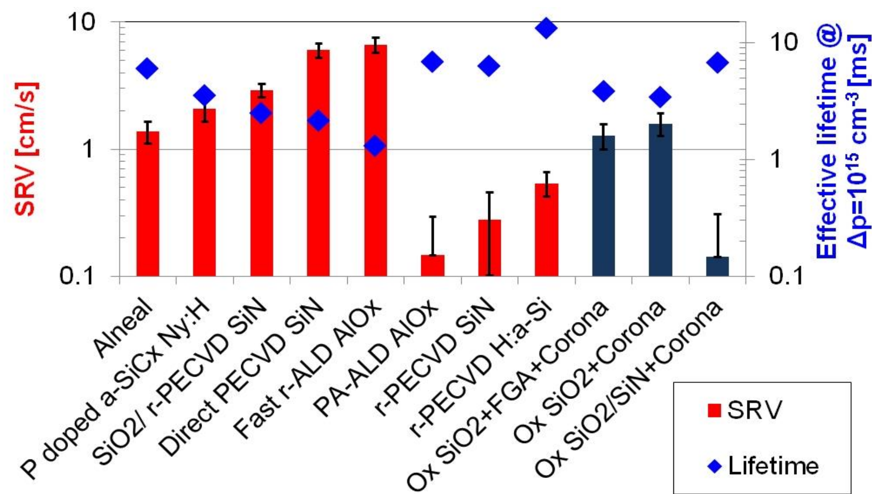

Figure 61. Comparison of record passivation quality obtained using state-of-the-art techniques and the passivation achieved using the techniques proposed in this work. 'Ox' suffix and blue colour are used for the samples in this work. Red colour is used for SRV reported elsewhere, for which details are included in Figure 7.

CHAPTER 5
FIELD-EFFECT PASSIVATION USING IONIC CHARGE

The previous chapter presented a methodology to reduce surface conduction in oxide and nitride films, and improve the stability of corona charge both deposited on and driven into the film. This methodology showed the potential of enhanced and controlled field effect passivation using corona discharge, yet the application of these methods continues to be limited by charge stability. This chapter presents a new method of independently exploiting field effect passivation by using positively charged alkali ions. Alkali ions are embedded in an oxide and provide effective and stable FEP to the silicon surface. This has been termed ionic extrinsic FEP. The study of charged ions present in an oxide is not new. For example, the unwanted presence of ionic charge has been extensively researched in the context of field effect transistors with the aim of eliminating instabilities caused by ions mobile at room temperature. Intentional incorporation of alkali ions into dielectric films has also been previously used to produce inversion layer solar cells [198], [199]. However, in this work, ionic charge purposely driven into a dielectric at raised temperature is exploited for passivation of silicon surfaces. The principal advantages of this technique are that the charge present can be controlled separately from that introduced during dielectric growth and also, since the charge is produced by ions (sessile at room temperatures) located within the dielectric, it has the potential to produce very stable results. In what follows, the experimental details and the main characteristics of the physical system are studied, and the

resulting passivation obtained is presented together with a discussion of its potential for long term passivation of silicon surfaces.

5.1 Transport of ionic charge

A new method to embed ionic charged species into a dielectric film has been proposed here to provide extrinsic FEP to silicon surfaces. To achieve this, it is important to understand the dynamic behaviour of alkali ions in the dielectric/semiconductor system. This section explores the different mechanisms of transport of ionic charge into a test system comprising an oxide film thermally grown on crystalline silicon. Ionic transport was studied on a 100 nm thermal oxide on 1 Ωcm n-type FZ-Si (wafers n1-n22). A controlled concentration of alkali species was deposited on the specimens using thermal evaporation as described in Chapter 2. Chloride and hydroxide salts were used throughout this project as precursors. No apparent difference was found between ionic dynamics with either kind of precursor. A nominal surface concentration after deposition was calculated to be ~10^{14} cm^{-2}. After deposition of ionic species these samples were submitted to three different processes in order for migration of ions to occur. These are depicted in Figure 62. In the first case, the dielectric film is subjected to high temperature while an electric field is applied to a previously deposited metallic contact on top of the dielectric. This process drifts the ions into the oxide due to the applied field. In the second case, no metal contact is deposited and the species are only subjected to a high temperature step, in which case only diffusion is active. And lastly, a concentration of corona charge is deposited on the surface of the film prior to high temperature annealing. The ionic species drift and diffuse during the high temperature step with the aid of the electric field established by the corona. The following subsections will explore each of these methods.

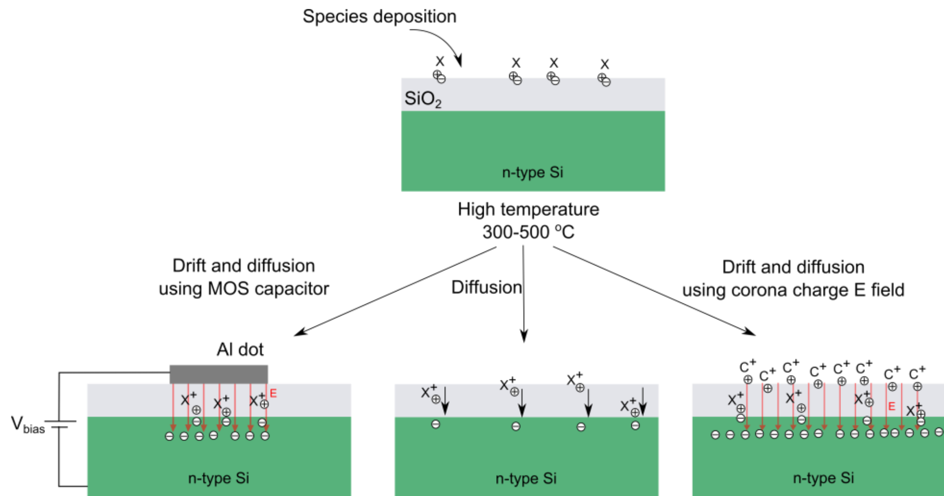

Figure 62. Migration mechanisms for ionic charge into silicon dioxide. X indicates an alkali ionic specie while C indicates a corona ion.

5.1.1 Drift using a metal contact

In Chapter 1, an overview of different studies of ionic drift in oxide gate electrodes were covered. In the following the Thermally Stimulated Ionic Conductivity (TSIC) technique is used to migrate ionic species into an oxide, quantify the concentration of species deposited, and to provide a foundation for understanding ion dynamics in a dielectric/semiconductor system. Thermally grown SiO_2 was deposited with sodium chloride. This was followed by a deposition of a 100 nm thick, 1 mm diameter Al dot as shown in Figure 62. TSIC and CV measurements were conducted to determine the total concentration of ionic species and their dynamics in a MOS structure. Figure 63 illustrates the resulting data from a TSIC experiment on this specimen. First, all ions are forced to migrate from the metal/oxide (M/O) to the oxide/silicon (oxide/silicon) interface by applying a positive bias on the Al dot with respect to the Si, and recording current as temperature is raised. The system is then let to cool to room temperature and a second bias-temperature process is applied to quantify the conduction caused by mechanisms other than ionic migration. This second recorded current is then subtracted from the first experiment to obtain the data shown in Figure 63.a. Figure 63.c illustrates the raw data obtained for the two cycles. As temperature rises, a clear peak is observed as a result of Na ion injection into the oxide and migration to the oxide/silicon interface. A very small peak, normally attributed to K ions [124], is also observed at

temperatures exceeding 250 ^{o}C. This is due to unwanted contamination resulting from lack of cleanliness in the process. The total number of injected ions is calculated by integrating the measured current density and is found to be ~ 3 x 10^{14} q/cm^2 for Na ions. The area of the capacitor is estimated using a CV measurement before the bias-temperature stress takes place as pictured in the blue trace in Figure 63.d. After the two positively biased processes, two consecutive negatively biased TSIC experiments were conducted to evaluate the dynamics of ion movement from the oxide/silicon interface to the M/O one. The resulting data is pictured in Figure 63.b. The Na peak is here seen to occur at a higher temperature (180 ^{o}C) than in the first positive bias experiment (125 ^{o}C). This indicates that ions are trapped at deeper energies at the oxide/silicon interface. A CV measurement was taken after the ions have migrated back to the M/O interface, green trace in Figure 63.d. The smaller oxide capacitance shows that part of the aluminium has oxidised thus reducing the area of the MOS capacitor. A number of interface defect states have also been created as shown by the shallower gradient of the curve. Lastly, the hysteresis observed shows that a number of ionic species have been de-trapped and not re-trapped at either interface such that they are mobile at room temperature in the oxide. The flat-band voltage calculated after the negative bias experiment indicates that a concentration of 10^{13} q/cm^2 remains near the oxide/silicon interface. This is within the range of the remaining ionic concentration calculated from the current integral, which was found to be ~ 0.2 x 10^{14} q/cm^2, since ~ 2.8 x 10^{14} q/cm^2 migrated back to the M/O interface.

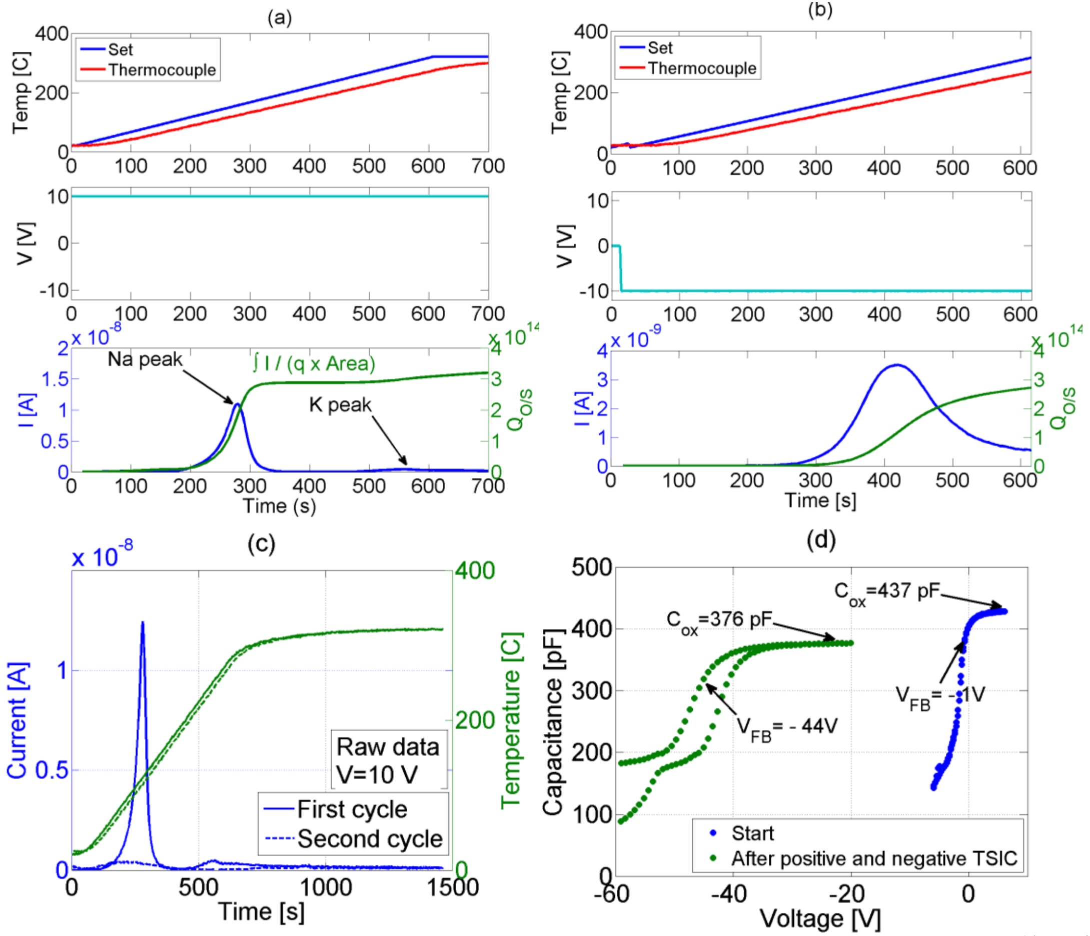

Figure 63. TSIC experiment on 100 nm thermal oxide grown on FZ n-Si and deposited with 10^{14} cm^{-2} NaCl. Sample n5_x2p1. a. First ionic migration from M/O to oxide/silicon interface, b. Second ionic migration from oxide/silicon to M/O interface, c. Raw current and temperature data for the two cycles in the ionic migration pictured in (a), d. CV curves before first migration (blue) and after second migration (green). Green curve includes the up-sweep and down-sweep in potential.

The concentration of ions being injected from the M/O interface is best modelled using first order kinetics as mentioned in Chapter 2. The concentration $n(E,t)$ is given by Equation (A. 19). Assuming perfect trapping probability, fast transport across the dielectric layer and no de-trapping from the oxide/silicon interface, the concentration of ions at the oxide/silicon interface is given by $n_{O/S}(E,t) = n(E,0)$- $n(E,t)$. The measured current is therefore given by $I(t) = -qA\int_0^\infty \frac{dn(E,t)}{dt}dE$. Figure 64 illustrates a plot of $I(t)$ vs $T(t)$ for the experiments shown in Figure 63. A proportionality factor β has been used to describe the dependency of attempt frequency with energy ($s(E) = \beta\sqrt{E}$), as described in Chapter 2. β was chosen to be 10^{10} $s^{-1}eV^{-1/2}$ based on previous works [200]. The initial distribution of ions $n(E,0)$ has been assumed to be Gaussian as suggested in [201], [202], and found empirically

to best fit the experimental data. These are illustrated on the top graphs of Figure 64. The initial ionic distribution at the M/O interface in Figure 64.a indicates that most ions are initially trapped at an activation energy of 0.9 eV, when an electric field of 1 MV/cm is present to provide a drift movement mechanism. When the ions are drifted back to the M/O interface, the trapping distribution is found to be somewhat different, Figure 64.b. Ions at the oxide/silicon interface are trapped at deeper and more broadly distributed energies. The peak concentration of traps is seen at an energy of 1.05 eV , yet the distribution broadly varies from 0.9 eV up to 1.2 eV. It is important to note that a drift component is present here and thus the activation energy of de-trapping strongly depends on this component. Additionally it is noted that assuming $n(E,0)$ to be a Gaussian only provides a good fit for the reverse sweep.

This subsection has confirmed the estimated concentration of ionic species thermally evaporated onto the oxides. The ion dynamics have also been explored and the previous findings of injection governed dynamics shown to hold true for the system studied here. This system is not practical for the introduction of ions into passivation dielectrics since a top metal contact cannot be part of cell manufacture. However these results provide the basis for the ionic migration studies in this thesis.

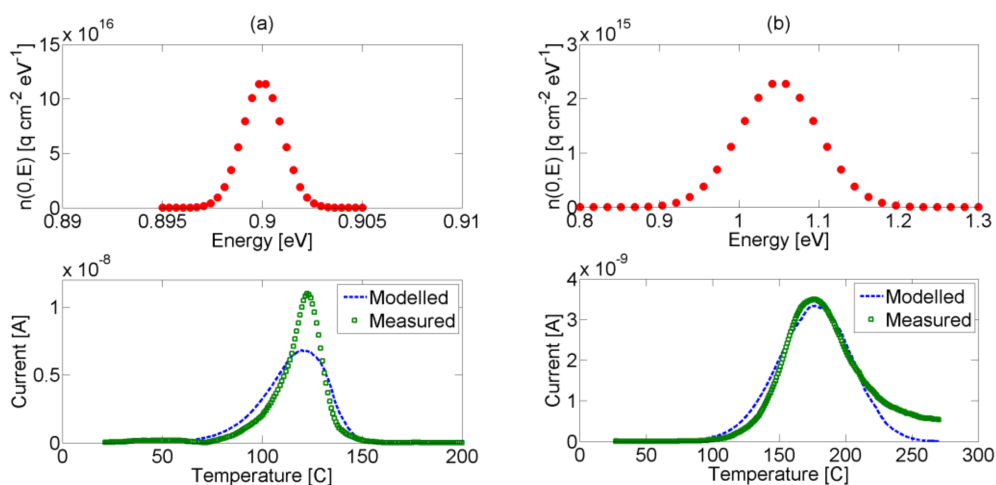

Figure 64. Ion dynamics modelling for TSIC experiment on 100 nm thermal oxide grown on FZ n-Si and deposited with 10^{14} cm^{-2} NaCl. Sample n5_x2p1. a. Positive bias experiment, b. Negative bias experiment.

5.1.2 Alkali ion diffusion

Solar cells lack a front metal contact through which an electric field component can induce migration of ionic charge into the underlying dielectrics. The dynamics of the alkali species in SiO_2, in the absence of a permanent metal contact, are the subject of this subsection. In this work the dynamic behaviour of ions was evaluated by subjecting specimens to different high temperature anneal processes and evaluating their charge concentration using mercury probe (Hg-p) high-frequency capacitance-voltage (CV) measurements. 3 x 10 mm^2 1 Ωcm n-type FZ-Si samples with 100 nm thermal oxide, and deposited with an ionic precursor, were measured after subsequent high temperature steps on the same heating stage as that used for TSIC as described in Chapter 2. This stage allowed rapid heating and cooling of specimens.

The resulting charge profile (concentration as a function of oxide thickness) after the anneal was assessed by Hg-p CV measurements after repeated etching of the initially 100 nm thick oxide layers in a 10% hydrofluoric acid (HF) solution at room temperature. The thickness of the layers was measured using reflectance spectrometry. This allowed the location of alkali ion species after high temperature diffusion to be determined. Figure 65.a illustrates the charge profile for a sample deposited with KCl and annealed at 450 ^{o}C for 18 min. If the contribution of diffusion in the dielectric bulk was significant for the overall transport process, ionic species would be distributed throughout the oxide bulk with a peak towards the interfaces –air/oxide and oxide/silicon.[100] In this work, it was found that the ionic species are instead largely concentrated at the oxide/silicon interface; hence bulk diffusion must be rapid compared to the rate at which ions are de-trapped from the air/oxide interface and re-trapped at the oxide/silicon one. After the cations have diffused to the oxide/silicon interface, it is evident that they remain there, and that, according to the present measurements, the concentration of ionic species is, for the most part, located within 10 nm (the resolution of the technique) of the oxide/silicon interface after the in-diffusion step. The effect of alkali ion diffusion in the dielectric bulk was also evaluated by submitting KCl

deposited specimens, of 100, 70 and 45 nm thick oxides, to an anneal at 500 °C. The time dependence of the ion concentration at the oxide/silicon interface was found comparable for all three thicknesses, thus indicating that bulk diffusion of these cations is rapid and interface trap-mediated ion release describes well the transport of ions from the air/oxide interface to the oxide/silicon interface, as previously reported by several authors [98], [201], [203]. Figure 65.b shows an energy trap schematic of such a process. It is assumed here that alkali chloride species on the surface dissociate at high temperature, and charged cations at the air/oxide interface, possibly trapped at different activation energies, are excited beyond the trap barrier and rapidly diffuse to the oxide/silicon interface. Once there, they are re-trapped at different activation energy wells, with the net space charge they produce providing FEP.

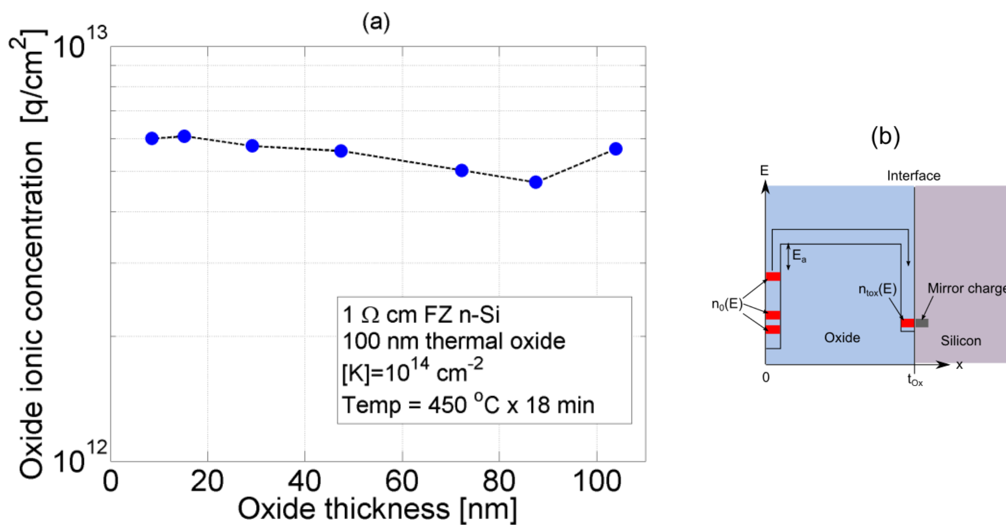

Figure 65. a. Concentration of ionic species in the oxide as a function of oxide thickness for an oxidised FZ n-Si sample annealed at 450 °C for 18 minutes (Sample n14_6), b. Schematic of the model proposed for ion migration from one interface to the other.

The transport dynamics of ions from the air/oxide to the oxide/silicon interface was studied by submitting ion-deposited specimens to subsequent high temperature steps while recording the concentration of ions located at the oxide/silicon interface. Figure 66 illustrates the concentration of ions that migrated to the oxide/silicon interface after a high temperature anneal step, for various temperatures. As mentioned in Chapter 2 and section 5.1.1, Boudry and Stagg [200] reported fitting the ion dynamics in MOS capacitors using first order kinetics [124]. However, they used an energy dependent initial distribution of ionic species at

the metal/oxide interface. In this case, a single activation energy is assumed to simplify the analysis in the case of an air/oxide interface as shown in Figure 65.b. Given a constant temperature diffusion of ions T, a β value of 10^{10} $s^{-1}eV^{-1/2}$ based on previous work [200], an initial ion concentration $n(0)$ in a trap of energy E_a at the air/oxide interface, and a pre-exponential factor $s(E_a) = \beta\sqrt{E_a}$, the concentration of ions at the oxide/silicon interface is:

$$n_{os}(t) = n(0)\left(1 - exp\left[-\beta\sqrt{E}\,exp\left(-\frac{E_a}{kT}\right)t\right]\right) \quad (5.\ 1)$$

assuming that slow de-trapping occurs at the oxide/semiconductor interface, which is the case for the early stages of the migration process. A Levenberg-Marquardt [204] algorithm has been used here to fit the experimental data in Figure 66 to this function. The activation energy E_a and initial ionic concentration $n(0)$ have been obtained from the fit. An average activation energy of 1.88 $\pm$0.02 eV has been calculated for the de-trapping of sodium from the air/oxide interface, and 1.91 $\pm$0.04 eV for potassium. The values of activation energy found for potassium de-trapping in 70 and 45 nm oxides subjected to 500 ^{o}C anneals were 1.96 eV and 1.90 eV, respectively. These are in the range of results obtained for experiments on 100 nm oxides thus indicating that bulk diffusion of ionic species can be disregarded and that the transport is modelled well by first order de-trapping kinetics from the air/oxide interface. Initial ion concentrations calculated using this fitting procedure were somewhat different to those calculated via TSIC (~5$\pm$0.5 x 10^{14} q/cm^2) on a MOS capacitor deposited with the same concentration of ionic species, Section 5.1.1. The $n(0)$ that produced the best fit for Na and K were 8.97 $\pm$2 x 10^{12} q/cm^2 and 9.96 $\pm$0.02 x 10^{12} q/cm^2 respectively. The discrepancies might be explained by de-trapping from the oxide/silicon interface, which can strongly influence $n(0)$, and has not been considered in the model. These results indicate that the majority of surface deposited cations remain at the air/oxide interface, presumably still bonded to their corresponding anion.

A qualitative observation of the data in Figure 66 shows that higher a concentration of Na ions is migrated for all temperatures. Migration of K ions saturates at about 3-5 x 10^{12} q/cm^2. Additionally, higher temperatures seem to allow a higher maximum concentration of migrated ions. This trend is particularly clear for K ions in Figure 66.b.

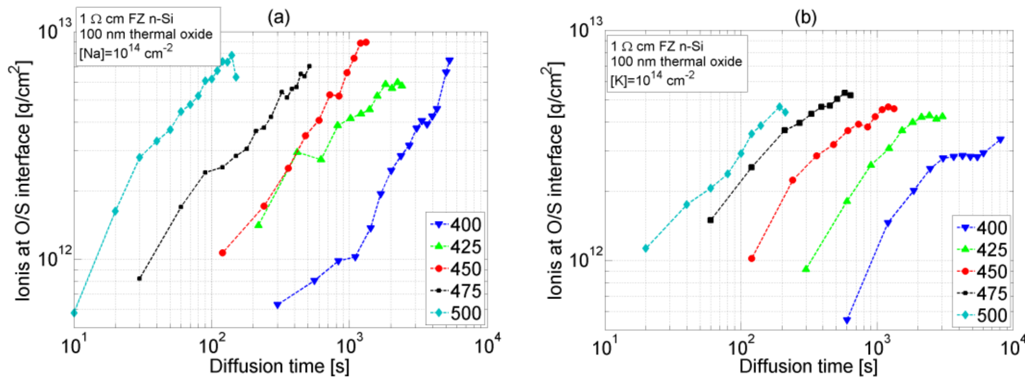

Figure 66. Concentration of (a) sodium and (b) potassium ions migrated to the oxide/silicon interface as a function of anneal time for a range of temperatures and times. (Different samples taken from wafer n14).

In summary, it has been demonstrated that ionic species can be migrated into an oxide film without the need for a metal contact. Similar to the MOS system, ion transport was seen to be governed by injection from the air/oxide interface rather than diffusion in the film bulk. A comparison of the activation energies measured on a MOS system versus those of an oxide/silicon system is included in Table 4. In the presence of a metal contact, and an applied bias, de-trapping of ion at the oxide surface has an activation energy ~0.8 eV smaller for Na and ~0.4 eV smaller for K. For this oxide/silicon system, ionic injection is therefore a slower process for the range of temperatures studied. A new mechanism by which such process can be accelerated is studied in the next subsection by adding a drift component without the need for a metal top contact.

System	Process	Activation energy [eV]	Initial ion concentration [q cm^{-2}]
Na in MOS	TSIC	0.9	3 x 10^{14} q/cm^2
K in MOS*	TSIC	~1.65	~1 x 10^{13} q/cm^2
Na in oxide/silicon	Diffusion	1.88 ±0.02	8.97 ±2 x 10^{12}
K in oxide/silicon	Diffusion	1.91 ±0.04	9.96 ±0.02 x 10^{12}

Table 4. Summary of activation energies and initial ion concentration found for ion dynamics in MOS and oxide/silicon systems. * Data from reference [205].

5.1.3 Ionic drift using corona charge induced electric field

In the last section it was shown that in the absence of a front metal contact migration of ionic charge into surface dielectrics relied purely on injection and diffusion processes. Substantial ion injection required time periods between 2-90 minutes. This scale of times is unlikely to be commercial since for in-line manufacture of solar cells the passivation processing step should, ideally, be executed in less than a minute. In this section an additional mechanism of ion migration is explored by including a drift component using corona charge deposited prior to the high temperature anneal, as shown in Figure 62. The focus of these experiments was the speed and effectiveness of passivation. All experiments in this section were hence conducted on 3 x 3 cm^2 samples and only lifetime and KP measurements were performed. No CV measurements were conducted since they required removal of the back oxide which would prevent further lifetime measurements from being taken.

The drift and diffusion dynamics of alkali species in SiO_2 were evaluated by measuring KP surface potential after one or several subsequent high temperature steps in a box furnace. 100 nm oxides were deposited with 10^{14} cm^{-2} concentrations of NaCl and KCl following deposition of corona charge and high temperature migration. Figure 67.a illustrates the surface potential after ionic deposition, corona charge deposition and a 400 ^oC anneal for 6 minutes. No substantial difference has been observed for Na, K and control samples when

submitted to this processing. After deposition of alkali ionic species the surface potential is comparable in all samples, indicating that the ionic species are neutral. Corona charge deposition increases surface potential and it is comparable to results observed in previous chapters. Corona charge and alkali ions then migrate into the oxide film at high temperature using both diffusion and drift mechanisms. After 6 minutes all ions have migrated to the oxide/silicon interface since KP potential, after annealing, reduces back to near its starting value. As demonstrated in Chapter 2, KP measurements are sensitive to the concentration of charge and its location. No surface potential is detected if the charge lies at the oxide/silicon interface, while maximum surface potential is seen when the charge lies at the surface of the oxide. If ion transport is carried out for shorter time intervals, Figure 67.b, the surface potential is seen to decrease quickly only for samples previously deposited with alkali ions. No difference is seen between Na and K deposited samples, yet the control sample shows a slower migration/compensation of charge when subjected to a high temperature step. It is suggested here that, in alkali ion deposited samples, anions are available at the surface of oxide and hence they quickly compensate any remaining corona charge. Charge that is injected into the film migrates quickly to the oxide/silicon interface and it is therefore not observed in KP measurements. A disadvantage of the corona deposition and ion migration process is that some of the driving force for drift is eliminated at the same time as both the alkali ions and the corona charge are moved to the oxide/silicon interface. If the migration of corona charge is faster than that of alkali ions then a concentration of alkali ions may remain at the surface after high temperature migration. After the cations have diffused to the oxide/silicon interface, it was not possible to assess their stability using KP measurements as the KP value fell to near zero quickly due to a major part of the charge migrating to the oxide/silicon interface. A key issue with this methodology is that KP measurements do not differentiate between corona charge and ionic charge and therefore no further conclusions can be made in terms of the dynamics of alkali ions alone.

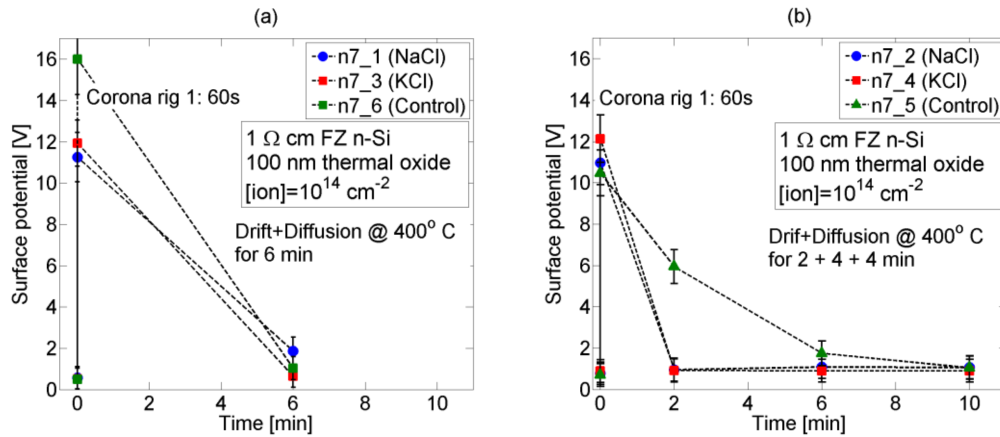

Figure 67. Surface potential for oxidised n-type FZ Si when Na and K ionic charge is migrated using drift and diffusion in a. One single 6 minute step, samples n7_1 and n7_3 respectively, control sample n7_6, and b. In three consecutive steps of 2, 4 and 4 minutes, samples n7_2 and n7_4 respectively, control sample n7_5.

5.1.4 Discussion

The rate limiting step for ion transport in both MOS and oxide/silicon systems was found to be the injection from the oxide surface into the bulk of the film. It was demonstrated that in the absence of a metal contact the ion dynamics are also trap mediated. The main parameter describing the de-trapping kinetics of ions was the release activation energy. In comparison to reported values of activation energies with the metal contact (~1 eV), the ones found here without the metal contact (~2 eV) are substantially larger. For example, in Derbenwick's [206] work, as well as that of succeeding authors [200], [205], [207], [208], activation energies for de-trapping ionic contaminants in SiO_2 were in the 0.6-1.3 eV range, similar to the TSIC results reported here. Their experiments, however, studied sodium and potassium de-trapped from the metal/oxide interface of MOS capacitors. In this work de-trapping from the air/oxide interface suggests that a metal/oxide/silicon system produces different ion dynamics. The differences between a metal contact and an open oxide surface could be for various reasons. Firstly, the metal contact will establish a contact potential with respect to the silicon so that an inherent electric field component is present, thus modifying the energy barrier for ion de-trapping. Secondly, the metal/oxide interface formed in MOS devices effectively seals the ionic species in the interface. In the absence of a metal contact, the ionic species can interact with different gases present during the diffusion process, for example to

remove the remaining chlorine present at the surface. Lastly, the interface of the oxide and metal is expected to be different to that with air such that the nature of the interfacial traps is modified, or new trap structures are created. The main result in the absence of a metal contact is the increase in the activation energies for ion injection. This translates into a lengthy migration process of species and a requirement for the drift component to be achieved via a different methodology. An alternative to using a front metal contact to produce an electric field across the sample was to deposit corona charge prior to charge migration at high temperature. Kelvin probe measurements were conducted after annealing yet they did not differentiate the nature of the charge (corona or ionic) nor the charge location, and thus provided incomplete information regarding the behaviour of ionic species. A better understanding is possible by examining the effect of the charge on the passivation quality of this system. This is explored in the next section.

This section has made reference to the two standard driving forces for transport of species: diffusion due to concentration gradients and drift due to the electric field force on charged ions. It has been made clear that transport through the dielectric is limited by de-trapping of ions at the interfaces, rather than their diffusion through the film's bulk. It is expected that adding a drift component enhances the de-trapping of ions. Thus the effect of the corona charge is to lower the activation energy for the de-trapping process. In this chapter this electric field enhanced de-trapping of ions will be referred to as the 'Drift' component, while the 'Diffusion' component remains that provided purely by the driving force due to the concentration gradient.

5.1.5 Summary

This section has presented the results on the release, migration and trapping of ionic charge in an oxide/silicon system. Ion dynamics were studied and found to be comparable to that in a MOS structure. The studies conducted here confirm that ionic charge is de-trapped from the surface of the dielectric and quickly migrates through the oxide before being re-trapped at

the oxide/silicon interface. TSIC experiments in a MOS structure provided a methodology to examine the kinetics and quantify the total concentration of ionic species that migrate from the surface of the oxide to the oxide/silicon interface. A new method was proposed by which a drift mechanism is activated using corona discharge prior to high temperature migration.

5.2 Passivation effect of migrated charged ions on oxidised FZ n-Si

The previous section demonstrated that ionic charge can be introduced into oxide passivation films to lie very close to or at the S/O interface. The effect of these alkali ions on surface recombination is the subject of this section. This was evaluated by submitting 3 x 3 cm^2 oxidised FZ n-Si samples, previously deposited with a known concentration of ionic species, to different high temperature and high electric field steps. Surface recombination was evaluated by measuring effective lifetime using transient photo-conductance decay. The following subsections present the results of extrinsic FEP obtained using a variety of ionic species and migration mechanisms.

5.2.1 Diffused ions

5.2.1.1 Sodium and Potassium

The reduction in surface recombination velocity was assessed on 3 x 3 cm^2 samples deposited with 10^{14} cm^{-2} sodium or potassium ion precursors, submitted to high temperature diffusions in a box furnace under standard laboratory conditions. Figure 68 shows the injection dependent effective lifetime (τ_{eff}) for samples subsequently annealed at 450 ^{o}C for 5 minute intervals. A maximum effective lifetime of 1 ms was obtained for a sample deposited with sodium chloride and annealed for 15 minutes. Similarly, a 1.27 ms effective lifetime was achieved for a sample deposited with potassium chloride and annealed for 20 minutes. This is equivalent to a S_{eff} of 8.6 and 6.5 cm/s respectively. These results confirm

the assumption that, at high temperatures, some of the cations dissociate from their corresponding chlorine anions, diffuse across the oxide towards the oxide/silicon interface, and provide FEP.

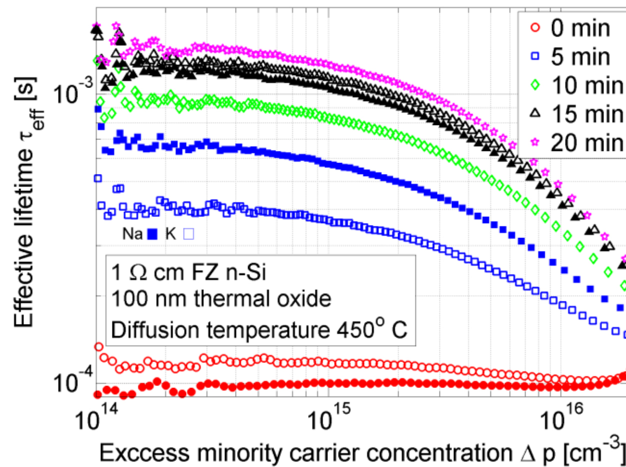

Figure 68. Effective lifetime as a function of minority carrier concentration for samples deposited with 10^{14} cm^{-2} sodium and potassium chloride and then annealed at 450 °C for different time periods. Sodium deposited samples (closed symbols) were annealed for 0, 5 and 15 minutes, while potassium deposited samples (open symbols) for 0, 5, 10, 15 and 20 minutes. (Samples n9_2 and n10_2 respectively)

Performing these diffusions at lower temperatures increases substantially the time for sufficient ionic injection to take place and produce FEP. This is evident in Figure 69 where samples deposited with NaCl and KOH were submitted to 400 °C for up to 60 and 90 minutes, respectively, before lifetime plateaued. Here it is also evident that the de-trapping rate of alkali species from the air/oxide to the oxide/silicon interface is faster for sodium than for potassium, as to be expected from the difference in cation size and also consistent with the ion dynamics in MOS structures as presented in section 5.1.1. Figure 69 also includes a control specimen that was kept free of sodium and potassium contamination. It is clear that, in the absence of ionic concentration, a 90 minute anneal at 400 °C only increases its lifetime up to ~ 200 μs at $\Delta p = 10^{15}$ cm^{-3}. This indicates that the majority of the surface passivation after annealing with Na and K ions present is due to the ions themselves and not from modification of the oxide/silicon interface by the anneal.

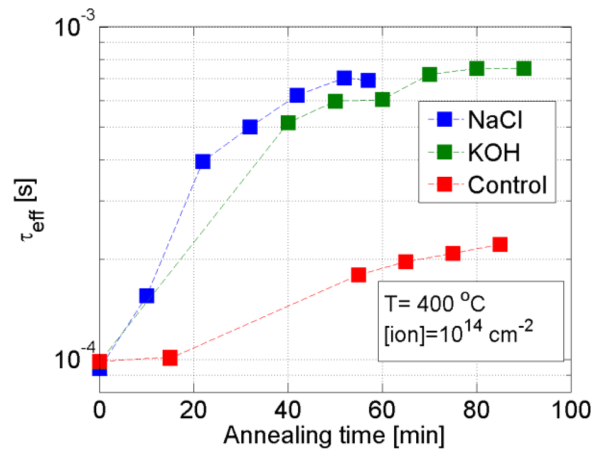

Figure 69. Effective lifetime as a function of annealing time for samples deposited with 10^{14} cm^{-2} sodium and potassium chloride/hydroxide and then annealed at 400 ^{o}C for different time periods. (Samples n2_1, n2_5 and control n2_8)

When a control sample was annealed for longer, however, the effective lifetime continued to increase up to ~ 350 μs at $\Delta p = 10^{15}$ cm^{-3}, Figure 70. Although the control sample in Figure 70 was not processed jointly with those in Figure 69, the diffusion time was much longer, allowing for any passivation mechanisms to reach a steady state. Additionally, since these experiments were carried out in a box furnace in laboratory conditions, it is believed that a small (< 10^{11} cm^{-2}) concentration of alkali ionic contamination may be present in control samples. This was corroborated by CV measurements of lifetime control samples that showed an average fixed charge of 5 x 10^{11} q/cm^{2}. The dip and increase in lifetime for high injection levels in Figure 70 is due to an artefact of the photo-conductance technique.

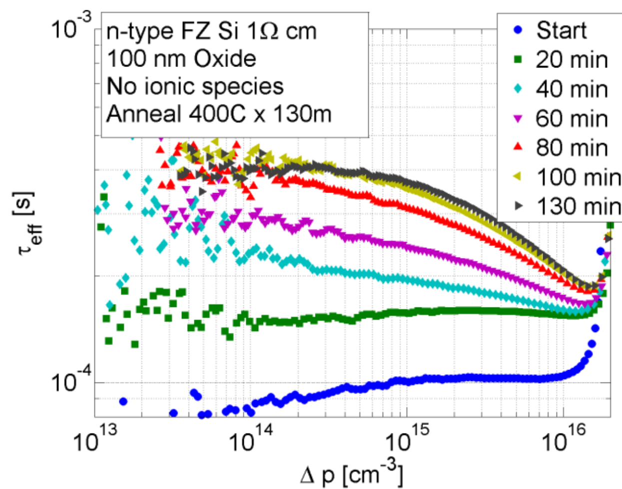

Figure 70. Effective lifetime for oxidised n-type FZ Si subjected to temperature anneals when no deliberately deposited ionic charge is present on the surface (control Sample n5_3).

5.2.1.1.1 Interface defect generation

The diffusion of alkali cations across the oxide was also carried out at different temperatures, Figure 71. This shows that initially the FEP increases with increasing anneal time and that the rate of change increases with increasing temperature but, because the relation between surface recombination and charge in the dielectric is highly non-linear, see Chapter 3, it is difficult to infer the details of the transport processes from these results. It is also noted that the data obtained for anneals performed at 450 ^oC and 500 ^oC is similar but that this may be due to the $\pm$ 20 ^oC uncertainty in temperature measurements. In Figure 71 it is seen that the effective lifetime reaches a maximum value and, for samples annealed at 450 ^oC and above, there is a subsequent lowering at the final stage of the transport process. This can be explained by changes in the oxide/silicon interface produced as a result of ion migration. When an excessive concentration of ions accumulates at the interface, it appears to increase the density of interface states. This density of interface states (D_{it}) has been quantified using Terman's method [168] involving high frequency Hg-p CV measurements. D_{it} was calculated for every CV measurement as ions were progressively migrated into the oxides of all the samples studied. As the concentration of charged ions at the oxide/silicon interface increases from ~10^{11} to 10^{13} (data from Figure 66), the mid-gap value of the density of trap states is seen to increase from 2 $\pm$0.2 x 10^{10} $cm^{-2}eV^{-1}$ to 4 $\pm$0.2 x 10^{11} $cm^{-2}eV^{-1}$, regardless of the kind of ion. This indicates that after an excessive concentration of ions has migrated to the oxide/silicon interface, the FEP they provide can no longer compensate for the loss in chemical passivation, hence the lifetime is reduced.

One additional effect noticeable from Figure 71 is that higher effective lifetimes are observed as the diffusion temperature is increased, up to 500 ^oC. However, beyond 500 ^oC this effect is not seen which may be due to unwanted impurities present in the box furnace that diffuse into the film and contaminate both the surface and the bulk of the specimens.

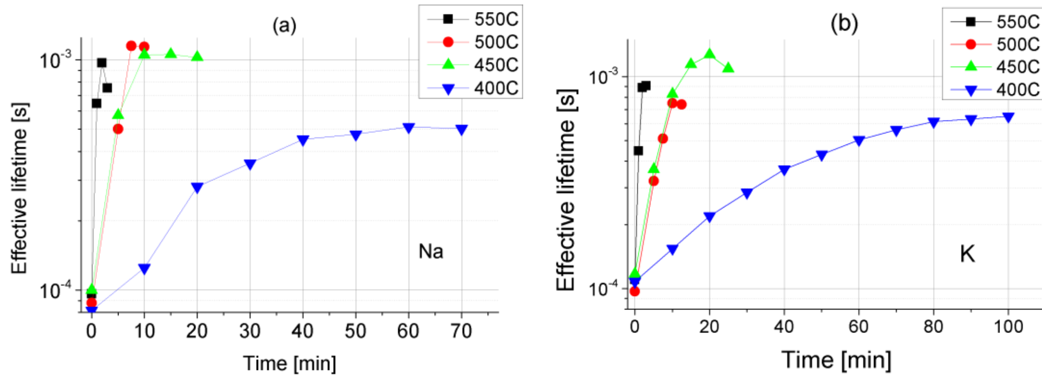

Figure 71. Effective lifetime at a minority carrier concentration of 10^{15} cm^{-3} for samples deposited with sodium and potassium and then annealed at different temperatures for up to 100 minutes. NaCl samples n9_3,2,1,5 for diffusion at 400, 450, 500 and 550 ^{o}C and KCl samples n10_3,2,1,7, for diffusion at 400, 450, 500 and 550 ^{o}C.

5.2.1.2 Magnesium and Calcium

The study of ionic extrinsic FEP was extended to ions not previously observed to be a source of instability in MOS capacitors. Samples deposited with 10^{14} cm^{-2} magnesium and calcium chloride were submitted to high temperature diffusion in a box furnace. Figure 72 shows the injection dependent effective lifetime (τ_{eff}) for samples subsequently annealed at 400 ^{o}C for 10 minute intervals. Maximum effective lifetimes of 0.5 and 0.45 ms were obtained after 10 minutes for samples deposited with magnesium and calcium respectively. This is equivalent to S_{eff} of 18 and 20 cm/s. Further annealing did not increase lifetime, suggesting that either no more charged ions were being injected into the oxide or that injected ions were reducing the chemical passivation by creating interface defects at the oxide/silicon interface. The lifetime dependence on carrier concentration observed in Figure 72 is noticeably different to that observed in Figure 68.

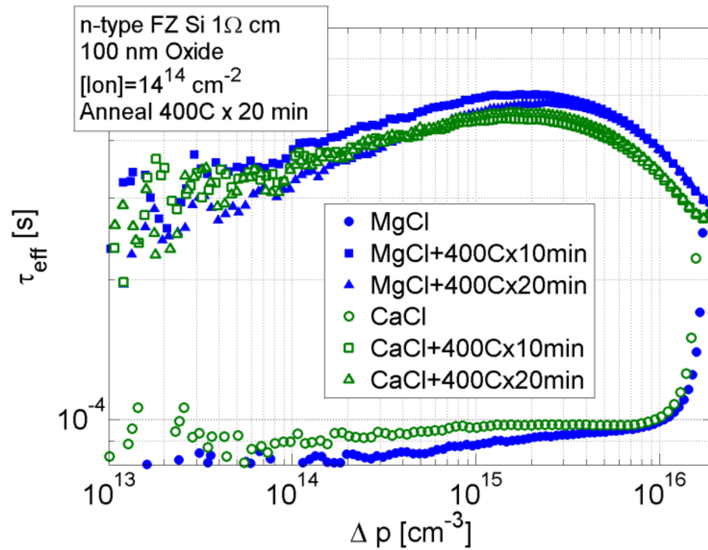

Figure 72. Effective lifetime for oxidised n-type FZ Si when MgCl and CaCl ionic charge is migrated using diffusion (Samples n5_1 and n5_2 respectively)

5.2.1.3 Caesium

Caesium hydroxide was also used here as a precursor for ionic charge FEP. Cs, in comparison with Na and K, is a large atom and it was thought possible that it might therefore diffuse/inject slowly into SiO_2. However, this was not the case as observed in Figure 73 where injection dependent effective lifetime (τ_{eff}) is plotted for a specimen deposited with 10^{14} cm^{-2} CsOH molecules, and annealed at 400 ^{o}C in 20 minute intervals. A maximum effective lifetime of 0.5 ms was obtained after 40 minutes, equivalent to a S_{eff} of 18 cm/s. Annealing for 60 minutes generated interface defect states as indicated by a decrease in effective lifetime, compared to that after 40 minutes.

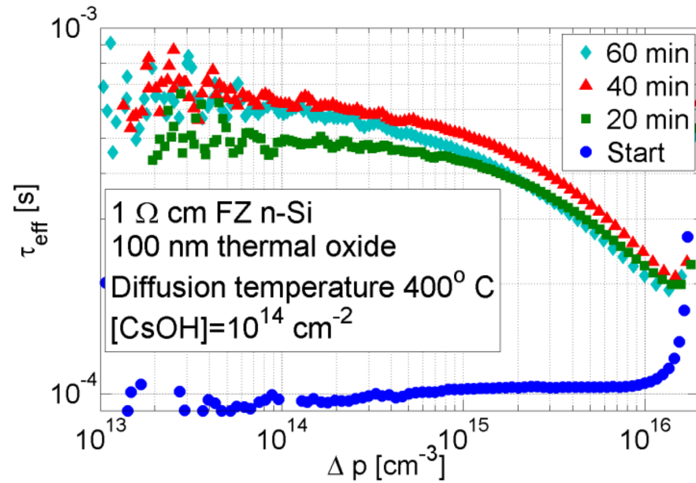

Figure 73. Effective lifetime for oxidised n-type FZ Si when CsOH ionic charge is migrated using diffusion at 400 ^{o}C (Sample n4_5)

5.2.2 Drift using corona charge induced electric field

Injection of Na and K species into oxide films has been observed to be a slow process in the temperature range 400-500 ^{o}C. To accelerate ionic injection the use of an additional drift component was proposed. This was provided by corona deposited charge on top of the dielectric, which created an electric field. The drift process was conducted in a single step at 400 ^{o}C after depositing ~10^{12} q/cm^2 corona charge on top of the dielectric, Figure 74. Section 5.1.3 showed the surface potential for this set of specimens after corona-anneal processing. Figure 74 illustrates the effective lifetime after the different processing steps for drift and diffusion of Na and K into SiO_2 in the same set. After corona charge deposition, an effective lifetime at $\Delta p=10^{15}$ cm^{-3} injection is 2.7 ms for Na, K and control samples. This is equivalent to a S_{eff}< 2.34 cm/s. After migration of charge at high temperature, the effective lifetime decreases to 1.3 ms for all samples, indicating that a small portion of the charge was neutralised or compensated, or that surface states have been generated at the oxide/silicon interface. If the lifetime lowering was only due to neutralised charge, this is estimated to be 2 x 10^{11} q/cm^2, according to the analysis presented in Section 3.3 of Chapter 3. Since the surface potential of these samples fell to near zero after the anneal (section 5.1.3), it is believed that all charge remaining in the film is located at or near the oxide/silicon interface. This correlates well with findings made when using only diffusion (Section 5.1.2). No major

differences in lifetime were observed between Na, K and control samples such that no conclusions can be drawn here with regards to the nature of the charge providing the FEP, corona charge or alkali cations.

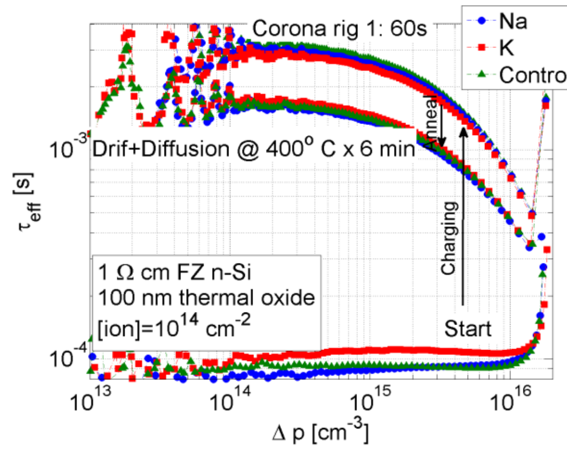

Figure 74. Effective lifetime for oxidised n-type FZ Si when Na and K ionic charge is migrated using drift and diffusion (samples n7_1 and n7_3 respectively, control sample n7_6)

When this processing is applied in shorter subsequent thermal anneals, Figure 75, the largest decrease in effective lifetime is shown over the first 2-6 minutes. Only a marginal change in lifetime is observed after annealing for 6 and 10 minutes, compared to that after 2 minutes. No substantial difference in effective lifetimes is noticed between Na, K, and control samples. Once again a disadvantage of this method is that part of the drift driving force given is eliminated as corona charge also migrates to the oxide/silicon interface. The experimental techniques used could not elucidate any further differences between the dynamics of different kinds of ions or that of corona charge.

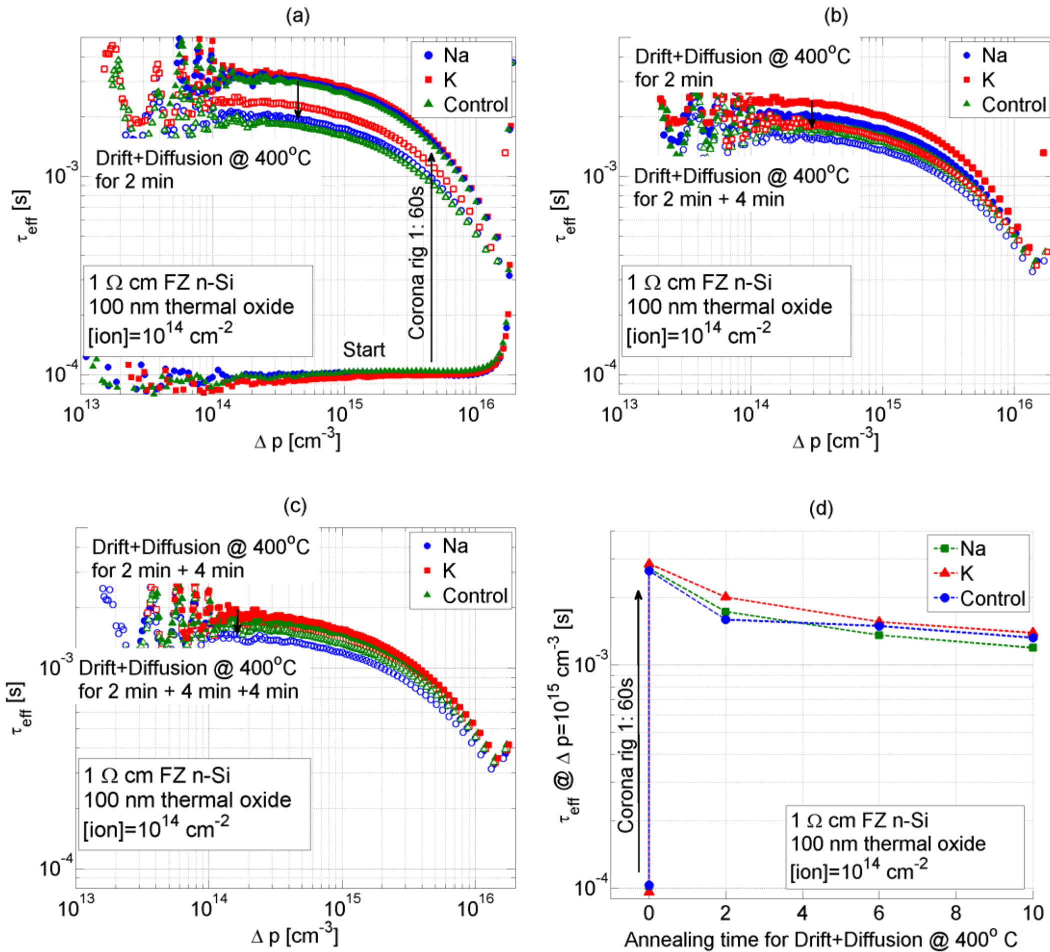

Figure 75. Effective lifetime for oxidised n-type FZ Si when Na and K ionic charge is migrated using drift and diffusion in three consecutive steps of a. 2, b. 4 and c. 4 minutes. (Samples n7_2 and n7_4 respectively, control sample n7_5). d. Effective lifetime as a function of time for the samples in a,b and c.

5.2.3 Discussion

It was found that ionic charge can produce high quality of surface passivation. SRV< 15 cm/s and 10 cm/s were achieved using sodium and potassium ions respectively. The rate of de-trapping of potassium was found to be slower than that of sodium, as is evident from the longer time needed for the effective lifetime to plateau. This is in agreement with the parameters for de-trapping dynamics previously reported, and with previously published results on alkali ions in MOS structures [200]. Although migration of alkali ions to the oxide/silicon interface provided FEP, it was found that ions present at the oxide/silicon interface also produced trap states hence reducing the chemical passivation. Once the number of migrated ions has sufficiently diminished the chemical component, FEP will no longer

compensate for the loss in chemical passivation and the lifetime is reduced. This was demonstrated by a plateau followed by a decrease in effective lifetime as more ions migrated into the oxide.

Other ionic species such as magnesium, calcium and caesium were investigated but did not produce such effective passivation as that obtained with sodium and potassium. Effective lifetimes saturated at ~ 0.5 ms after 20-40 minutes. Despite the larger size of these ionic species, the rate of injection (de-trapping from the air/oxide interface) seemed comparable to that for Na ions. It is possible that Mg and Ca ions migrate into the oxide as 2+ charged species, and this produces an apparent faster injection. This hypothesis was not confirmed here. Additionally no apparent difference between de-trapping of Mg and de-trapping of Ca is observed, as indicated in the similar lifetimes measured after 10 and 20 minute anneals. This suggests a similar concentration of ions have been injected into the oxide and are providing passivation. It should be noted that a possible scenario is that most of the improvement in FEP is due to unintentional contamination of Na and K and not the deposited alkaline species. This may occur due to lack of cleanliness as these experiments were not conducted in clean room conditions. However, a control specimen was reported in Figure 70 and unwanted contamination is seen to require longer time periods before similar passivation is achieved. Thus the results here are believed to be due to Mg, Ca and Cs ions. Effective lifetime after migration of Mg and Ca ions showed a clear peak and decrease for low carrier injections. These features are characteristic of the change in capture cross sections and the energy dependence of interface defects. This suggests that when Mg and Ca ions are injected into SiO_2 and re-trapped at the oxide/silicon interface, different states are produced.

The dynamic behaviour of ionic species was indirectly studied here when a drift component is added using corona charge. Effective lifetime decreased when submitting an oxide deposited with sodium and potassium ions, followed by corona charge, to a high

temperature anneal. This indicated that either a number of states had been generated at the oxide/silicon interface, or that a portion of charge was lost over the first 2-6 minutes. A key issue with this methodology is that the nature of the charged ion that provides FEP could not be distinguished. Control specimens showed identical behaviour. An analysis of the effect of sodium and potassium ions in FEP, or their dynamic behaviour, is not possible at this stage.

5.2.4 Summary

The present chapter has illustrated the potential of ionic charge to produce effective passivation of silicon surfaces. This significant finding was achieved by thermally evaporating ionic species on to the surface of an oxide, dissociating them at high temperature and, by a combination of diffusion and drift mechanisms, injecting and migrating cations through the oxide until they get re-trapped at the oxide/semiconductor interface. The ability of ionic species to field effect passivate has not been investigated before. This is the first time such ionic charge has been used to produce passivation of silicon surfaces and values of SRV< 10 cm/s have been reported.

5.3 Stability of ion induced passivation

Chapter 4 presented a new methodology by which corona charge could be stabilized on the surface of an oxide film for long periods of time. The stability observed, however, was not sufficient for practical solar cells as it only reached 3,000-4,000 days. This section presents an evaluation of the stability of extrinsic FEP achieved using alkali ion migration into oxide films. This is studied for both mechanisms of migration; diffusion and drift.

5.3.1 High Temperature diffused ions

5.3.1.1 Sodium and potassium

After high temperature diffusion, samples were kept in plastic bags and measured sporadically over a period of 600 days. Figure 76 illustrates the time evolution of τ_{eff} at

Δp=10^{15} cm^{-3} for specimens that had sodium and potassium in-diffused at different temperatures. Here, an initial lowering of effective lifetime is observed over the first 50 days, for all temperatures. Disregarding any chemical change of the silicon-oxide interface, this initial lifetime decrease likely indicates that some of the cations at the oxide/silicon interface are either compensated or de-trapped from the interface. After this initial period, the remaining ions are highly stable, as observed by the constant value of effective lifetime. This is a significant finding in particular considering that samples in Figure 76 did not undergo chemical HDMS treatment. The relative loss of FEP in the first 50-100 days is comparable for all temperatures and for both Na and K ions. This indicates that the mechanism of neutralisation is independent of the ion type and diffusion temperature. It is also observed that K ions diffused at 450 ^{o}C showed the most effective passivation with S_{eff} below 12 cm/s for the whole measurement period. For K ions migrated at this temperature, an average decay time constant for the period between 50 and 600 days was estimated to be ~7,500 $\pm$ 70% days.

In Chapter 4 water was found to be a major contributor to leakage and/or neutralisation of charge in corona charged oxides. The effect of water has also been tested for ionic extrinsic FEP. Figure 77 illustrates effective lifetime for specimens with Na and K diffused into SiO_2 at 400 ^{o}C. After diffusion, HMDS chemical treatment 1 was applied and samples were monitored over 700 days. The initial lowering of effective lifetime was not observed in HMDS treated samples. Instead, a long slow decay over the whole measurement period was observed. Decay time constants of ~4,000 days $\pm$20% and ~7,100 days $\pm$32% was estimated for the lifetime decay in HMDS treated samples diffused with Na and K.

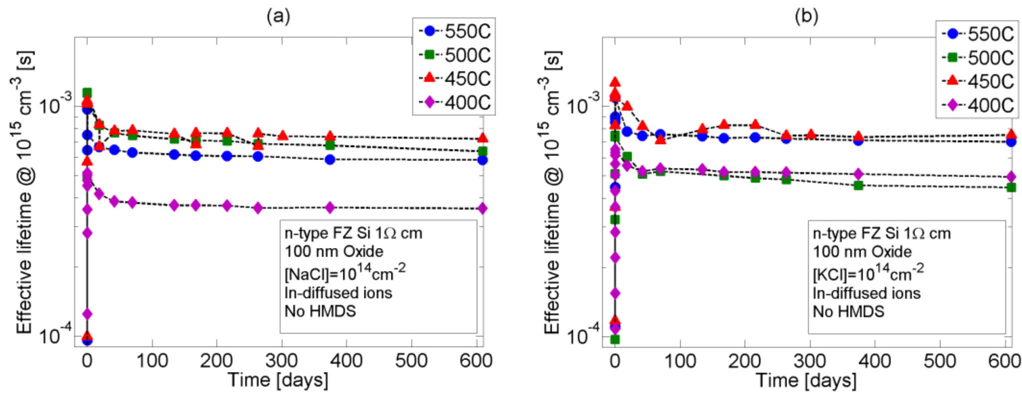

Figure 76. Effective lifetime for oxidised n-type FZ Si when ionic charge is diffused into the oxide using for a. NaCl (Samples n9_3,2,1,5 for diffusions at 400, 450, 500 and 550 ^{o}C) and b. KCl (Samples n10_3,2,1,7, for diffusions at 400, 450, 500 and 550 ^{o}C).

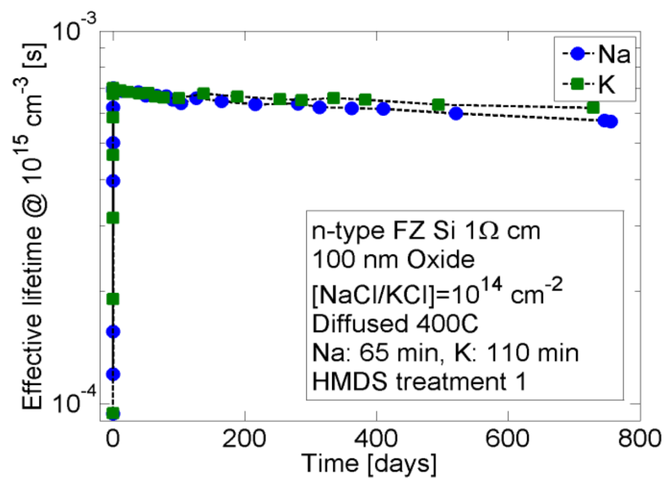

Figure 77. Effective lifetime for oxidised and HMDS treated n-type FZ Si when ionic charge is diffused at 400 ^{o}C into the oxide using NaCl and KCl (Samples n2_1 and n4_1).

5.3.1.2 Calcium and magnesium

Samples with Ca and Mg diffused into SiO_2 were also kept in plastic bags and measured over a period of 700 days. Figure 78 illustrates their τ_{eff} evolution. Similar to what was observed with Na and K, an initial fast lowering of effective lifetime is observed over the first 50 days. After this initial period, however, lifetime is seen to slowly decay with a time constant of ~1,200 $\pm$ 20% days. The relative loss of FEP throughout the measurement period is comparable for both Mg and Ca ions. HMDS treatment was not applied to these specimens. The lack of effective passivation indicates that these ions are not well suited for long term surface passivation of silicon surfaces when injected into a SiO_2 matrix.

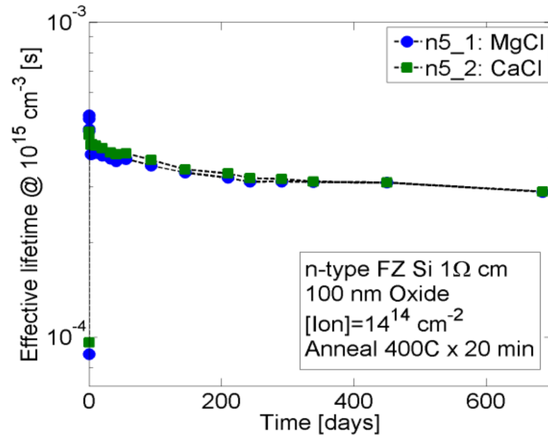

Figure 78. Effective lifetime for oxidised n-type FZ Si when ionic charge is diffused at 400 °C into the oxide using MgCl (Samples n5_1) and CaCl (Sample n5_2).

5.3.2 Corona charge drifted ions

5.3.2.1 Sodium and potassium

After high temperature diffusion and drift of Na and K ions into oxide films, samples were monitored over a period of 600 days. Once embedded in the dielectric, both Na and K ions have been seen to be stable for a period of up to 600 days, while samples lacking ionic species were seen to decay more quickly as illustrated in Figure 79. The effective lifetime for specimens with Na ions is observed to decay with a fast decay constant in the first 100 days, to about 70% of its original value. After this, a slow decay is observed for the remaining period of the measurement with an estimated decay time constant of ~ 3,300 ±28% days. The oxide with embedded K ions, on the other hand, only showed a decrease in effective lifetime of < 10% over the first 100 days, after which a decay time constant of ~6,200 ±30% days is estimated. By the end of the measurement period this specimen showed a S_{eff}< 7.2 cm/s.

The effective lifetime of control specimens without ionic species intentionally deposited is illustrated in Figure 79.c and f. They showed a fast decay period that extended for 200 days, reducing the effective lifetime to less than 50% of its original value. After this, charge in the dielectric was seen to decay with a time constant of ~2,000 ±45% days.

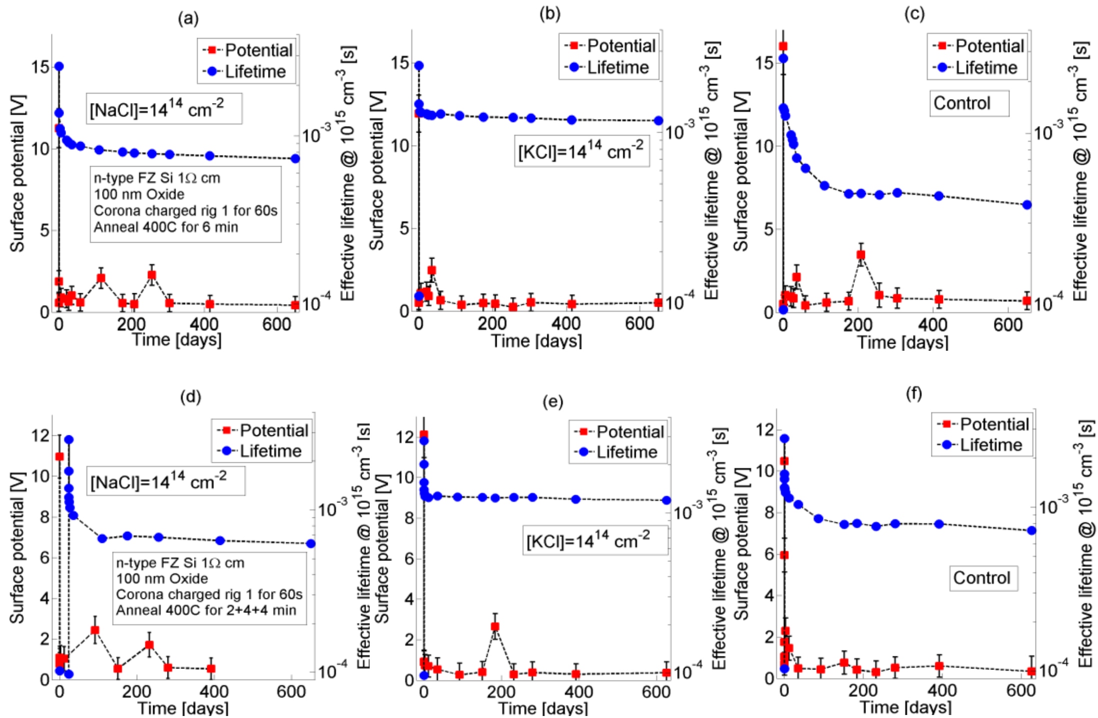

Figure 79. Surface potential and effective lifetime for oxidised n-type FZ Si when NaCl, a. Sample n7_1 and d. Sample n7_2, and KCl, b. Sample n7_3 and e. Sample n7_4, ionic charge is migrated into the oxide using corona drift and three diffusion steps. Control Samples c. n7_6 and f. n7_5 went through the same processing without ionic species. The top row samples were diffused in a single step for 6 minutes. Bottom row samples were diffused in three steps for 2, 4 and 4 minutes subsequently.

5.3.2.1.1 Surface chemical treatments

In Chapter 4 it was demonstrated that water absorption promoted lateral surface conductivity in oxide layers, and that this was detrimental to corona charge stability. Additionally, samples that underwent extrinsic chemical passivation using FGA were shown to have lower surface recombination when an extrinsic FEP component was added. This section describes how the stability of ionic extrinsic FEP is influenced by chemically treating the film with a hydrophobic HMDS coating and chemically passivating the oxide/silicon interface using a FGA. An oxidised silicon specimen was FGA treated, deposited with KOH ions, corona charged, annealed at 300 ^{o}C to drift and diffuse the charge into the oxide, and then HMDS treated using method 1. Figure 80 illustrates the effective lifetimes of this specimen and a control lacking ionic species at the surface. Similarly to results in Chapter 4, the effective lifetime after FGA and corona charge is higher than for samples without FGA processing, for example Figure 74. The anneal and HMDS treatment decreased the effective lifetime due to either charge leakage or chemical de-passivation. A lifetime measurement

after 15 days revealed that virtually no passivation loss occurred in the sample drifted with ionic species while a small reduction in lifetime was observed in the control sample.

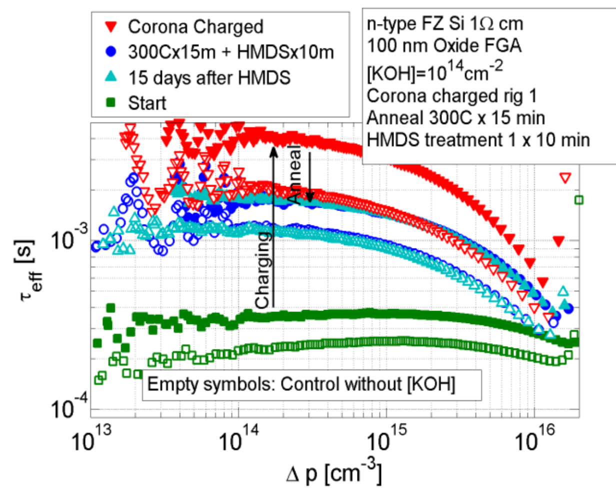

Figure 80. Effective lifetime for oxidised n-type FZ Si when K ionic charge is migrated using drift and diffusion on a specimen treated with FGA and HMDS (Sample n16_2, control sample n16_7)

The effective lifetime of these specimens was then recorded for a period of 700 days, and it was compared to specimens with and without HMDS and FGA treatments. These results are illustrated in Figure 81. A significant improvement in passivation stability was achieved for the film that had ionic species drifted into it with HMDS and FGA treatments, Figure 81.a. A decay time constant of ~9,400 ±40% days was calculated for this specimen. A time constant of ~1,200 days ± 72% was calculated for the control specimen in the same figure thus demonstrating that the presence of ionic species in the oxide strongly improved the stability and quality of extrinsic FEP. In the absence of the FGA treatment, Figure 81.b, the effectiveness of extrinsic FEP is reduced, as evidenced by the lower lifetime, yet it remains higly stable with a decay time constant of ~ 9,200 ± 32% days. In the absence of the HMDS treatment, Figure 81.c, the effectiveness of extrinsic FEP at the start of the measurement period is comparable to that in the sample HMDS treated, Figure 81.a. The stability, however, deteriorates and the decay time constant lowers to ~ 3,200 ± 15% days. In the absence of both surface treatments, FGA and HMDS, the quality of passivation and its stability degrade as illustrated by an effective lifetime below 1 ms and a decay time constant ~ 8300 ±50% days, Figure 81.d.

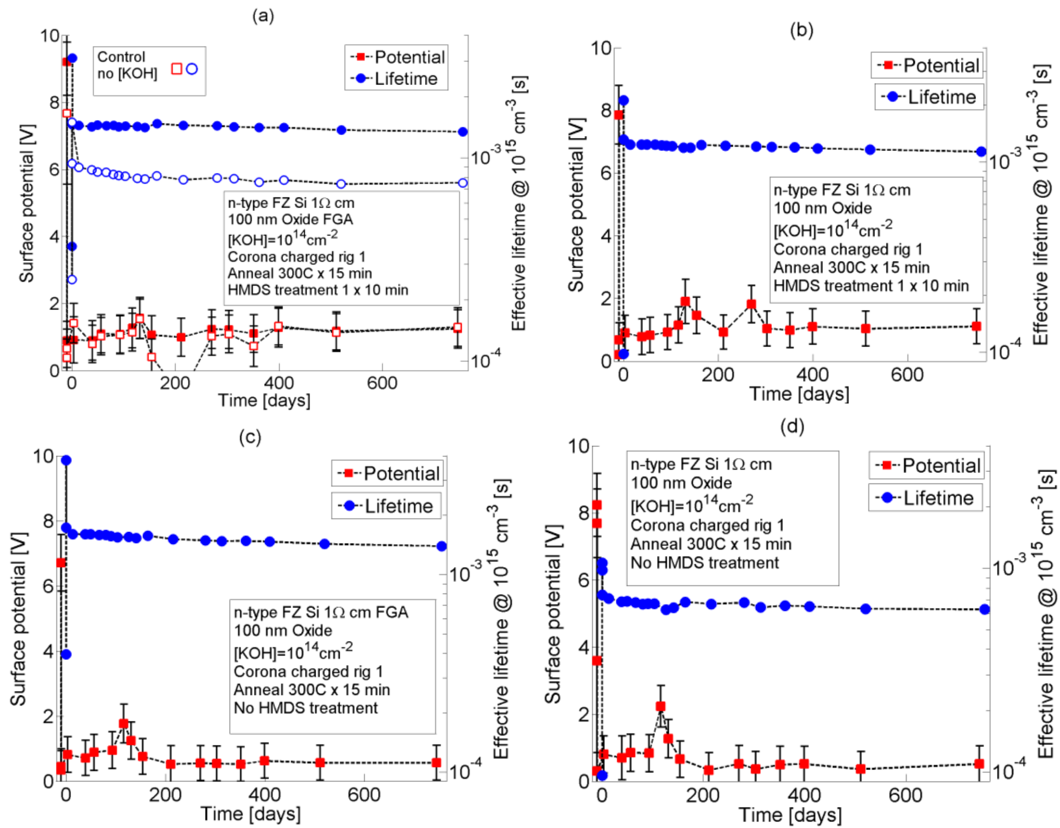

Figure 81. Surface potential and effective lifetime for oxidised n-type FZ Si when KCl ionic charge is migrated using drift and diffusion on a. FGA and HMDS treated oxide (Samples n16_2, control sample n16_7), b. Non-FGA treated, but HMDS treated (Sample n2_4), c. FGA treated but not HMDS treated (Sample n16_1) and d. Neither FGA or HMDS treated (Sample n2_3).

The in-diffusion of ionic species shown in Figure 80 and Figure 81 was conducted at 300 ^{o}C for a period of 15 minutes. This process is too slow if these methods are to be applied to the commercial manufacture of silicon solar cells. Migration of species can be sped up by increasing the temperature at which the process takes place to 500 ^{o}C, as illustrated in Figure 82. Figure 82.a illustrates effective lifetime and surface potential of specimens with and without a surface ionic concentration. Here it is shown again that the migration of K into the oxide provides effective and stable passivation with a decay time constant of ~12,600 ± 44% days. It is important to note that this stability exceeds that previously reported for samples that did not undergo HMDS processing. The control specimen, lacking surface KCl, showed a decay time constant of ~ 1,400 ± 37% days.

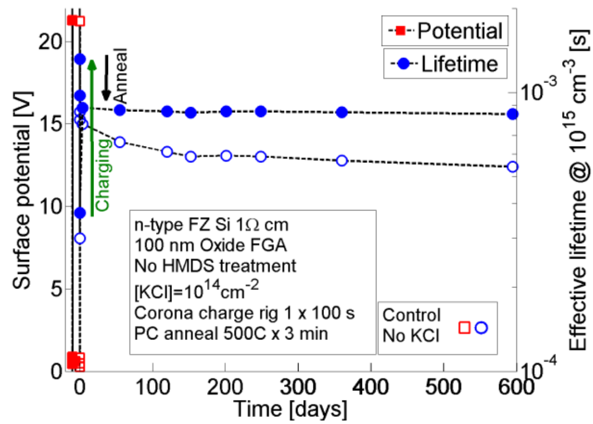

Figure 82. Surface potential and effective lifetime for oxidised n-type FZ Si when K ionic charge is migrated into the oxide using a. drift and diffusion (Sample n17_2, control sample n17_6). Arrows indicate the order of the process.

5.1.1.1. Calcium and magnesium

Specimens deposited with calcium and magnesium chloride at the surface were corona charged and annealed to migrate ions into the oxide via a combined diffusion and drift mechanism. Figure 83 illustrates surface potential and effective lifetime for a period of 600 days after charge is migrated into the oxide. Both of these alkaline ionic species have produced poor stability of passivation. This could be due to an insufficient concentration of alkaline species migrating into the oxide and/or the lack of HMDS treatment. It was observed that when the migration is performed only using diffusion, Section 5.2.1.2, only a small concentration of ions migrate into the oxide over a period of time ~ 20 min at 400 ^{o}C. It was believed that a higher concentration could be driven into the oxide by enhancing the movement of ions using electric field drift, yet that has not been observed here. When corona charge is deposited on the surface of the dielectric and subsequently annealed the total number of ions and their stability seems comparable to that observed in section 5.3.1.2. It is concluded here that Mg and Ca are not suitable ionic species to provide effective and stable extrinsic FEP using a base oxide layer.

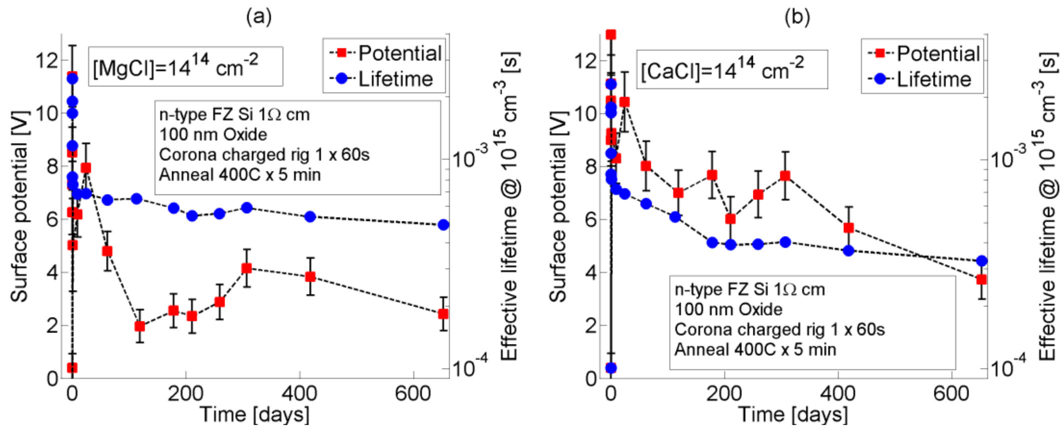

Figure 83. Surface potential and effective lifetime for oxidised n-type FZ Si when a. Mg (Sample n6_1) and b. Ca (Sample n6_2) ionic charge is migrated into the oxide using drift and diffusion.

5.3.3 Discussion

High stability of extrinsic FEP has been demonstrated in oxides containing both sodium and potassium ions. When only a diffusion mechanism is used to drive ions into the film, good stability of passivation is observed with decay time constants of lifetime reaching 8,000 days, Figure 84. This high stability is observed for oxides with Na and K ions diffused at 400-450 ^{o}C. Diffusion at higher temperatures seems to affect the long-term stability of passivation. The decay in effective lifetime observed over a period of 600 days can be due to a reduction in either component of passivation. First, a reduction in chemical passivation may be taking place. Section 5.2.1.1 reported that charged ions migrating to the oxide/silicon interface produced a number of interface states during the migration process. The loss in chemical passivation in such case is likely due to the bond straining or breakage caused by the presence of ionic species at the oxide/silicon interface. Once the ions are there it is unlikely that they continue to produce loss in chemical passivation. Chapter 4 reported that chemical de-passivation could take place due to hydrogen release or interface ‘bad spots’ with excessive electric field strength. If the long-term decay in ionic FEP was of chemical origin, it would likely be due to a similar mechanism.

The second component of passivation that could decay with time is field effect. In this case three scenarios are possible: First, a high concentration of charge (>4 x 10^{12} q/cm^{2}) is present at the interface and it decays at a high rate. For high charge concentrations

effective lifetime is weakly dependent on charge, as shown in Chapter 3, thus the decay in lifetime observed is very slow. Second, a moderate concentration of charge (~ 1-3 x 10^{12} q/cm^2) is present at the oxide/silicon interface, for which effective lifetime is highly dependent on charge, and thus a slow decay in lifetime relates to a slow decay in charge. Third, the concentration of charged ions is high and its decay rate is slow, in which case minimal lifetime decay would be observed.

The concentration of charge diffused into the film can be estimated using a combination of data in Figure 66 and Figure 71. This estimation is shown in Table 5. It is clear that the ion diffusion process in these specimens could have produced a very high concentration of charge at the oxide/silicon interface, in particular for specimens with Na ions. This suggests that if the long-term decay in ionic FEP was of field effect origin, it would likely be due to the first and third scenarios described above. In either case it can be concluded that leakage of ionic charge seems comparable for Na and K ions at the oxide/silicon interface.

Ion	**Temperature [C]**	**Diffusion time [s]**	**Estimated charged ion concentration [q cm^{-2}]**
Na	400	4200	4 x 10^{12}
Na	450	1200	8 x 10^{12}
Na	500	600	8 x 10^{12}
K	400	6000	3 x 10^{12}
K	450	1500	4.5 x 10^{12}
K	500	720	5 x 10^{12}

Table 5. Estimated concentration of charged ions diffused into oxide films at different temperatures. Obtained from a combination of data in Figure 66 and Figure 71.

Figure 84 also illustrates the quality of passivation achieved by the end of the measurement period. Oxides diffused with both types of ions are seen to provide similar levels of passivation, with effective lifetimes ~ 0.6-0.7 ms. This indicates that only a

moderate passivation of the surface has been achieved. Results in section 5.1.3 showed that the activation energy to inject K ions from the oxide surface is higher than for Na ions. Since the same diffusion time and temperature was applied to specimens with both Na and K, it is expected that oxides with Na species would have a larger concentration of charged ions. This was confirmed by the estimation in Table 5. Despite this larger concentration of charge, the passivation quality obtained with Na and K ions is similar, thus suggesting that a fair number of interface states have been generated by the Na ions and provoked chemical de-passivation during the ion migration process.

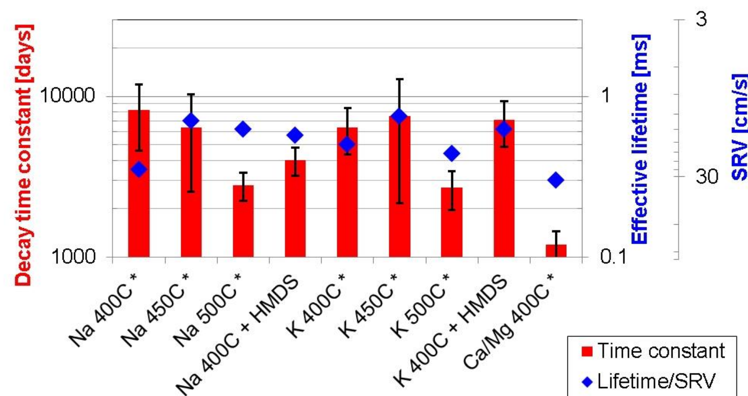

Figure 84. Summary of effectiveness and stability of passivation in oxides with diffused ionic charge. Effective lifetimes at the end of the measuring period are reported. The decay time constant is estimated between day 5 and the end of the period. * indicates that effective lifetime showed a rapid decay in the first 1-50 days followed by a slow decay.

In sections 5.1.3 and 5.2.2 it was proposed that injection and migration of ions in a dielectric film occurred faster thanks to the added drift component of electric field given by corona charge. However, during the migration process, no difference in surface potential and effective lifetime was observed between specimens with and without ionic species. In this section, for the first time, the dynamic behaviour of charge is seen to depend strongly on the presence and type of ion in the dielectric. When drift and diffusion are combined, highly stable extrinsic FEP is achieved, with decay time constants exceeding 10,000 days, Figure 85. A comparison of stability of passivation in Figure 84 versus that in Figure 85 shows that when the drift and diffusion mechanisms are combined, better levels of stability and effectiveness of passivation are achieved. Additionally, more effective and stable passivation

was also observed on oxides containing K ions than those with Na, as evidenced in higher lifetimes and decay time constants. Oxides that underwent FGA showed a better quality of passivation, as expected, but no improvement in stability. Given the discussion of decay mechanisms above, the better passivation achieved with K can be due to a smaller concentration of K trapped ions that have not caused as much interface damage as in the case of Na.

In the ion drift process, effective lifetime is first seen to increase with corona charge deposition, and subsequently fall due to the high temperature drift and diffusion. The decrease in lifetime after a high temperature charge migration has been previously related to loss in both chemical and field effect passivation. The concentration of charge in this case cannot be estimated since charge from both the corona and the alkali ions can be contributing to passivation, and the oxide/silicon interface properties change as the migration takes place. No definite mechanism for the longer stability of passivation in oxides with K ions is suggested here.

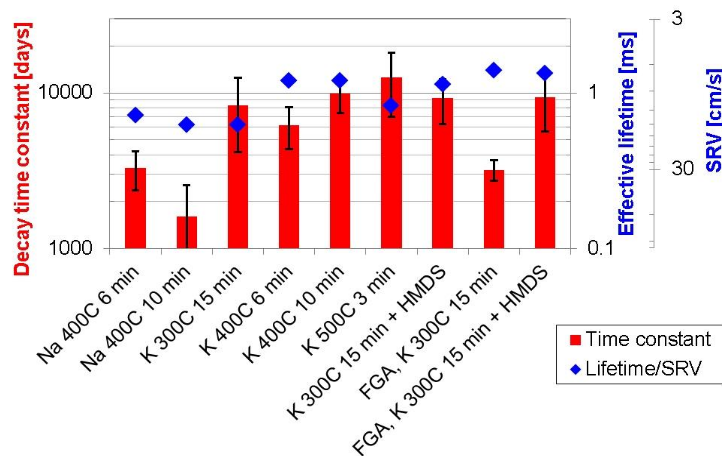

Figure 85. Summary of effectiveness and stability of passivation in oxides with drifted and diffused ionic charge. Effective lifetimes at the end of the measuring period are reported. The decay time constant estimated between day 50 and the end of the period. Time quoted for the total length of the drift and diffusion process.

In the previous chapter, corona extrinsic FEP was concluded to be unpractical when the surface conductivity of the films was not eliminated. It was demonstrated that improved stability could be achieved by sealing the oxide surface and preventing water absorption by

using an intermediate surface chemical treatment of hexamethyldisilazane (HMDS) vapour [123]. Figure 84 illustrates the stability of FEP in HMDS treated specimens diffused with Na and K ions. In these samples effective lifetime did not show the initial rapid (~50 day) decay observed for un-treated samples. The origin of this fast decay component is still uncertain. However, these results suggest that during the HMDS process, the moderate temperature provides energy to accelerate the fast decay such that it is not observed any longer. However, no definite conclusion can be drawn based on this data. It is noted, though, that samples that were not HMDS treated still retained a large part of their charge. When both diffusion and drift mechanisms were used, no significant difference was noticed in the effective lifetime decay of HMDS treated and un-treated specimens. Overall, these results indicate that the ionic FEP is less susceptible than corona FEP to lateral conduction due to water absorption at the films surface.

5.3.4 Summary

The present chapter has illustrated the potential of ionic charge to produce stable extrinsic FEP. Charge stable within the dielectric has been shown to provide effective passivation for periods exceeding 600 days. This is the first time that long term stability of ionic charge has been presented for a dielectric/semiconductor system with particular emphasis on its passivation properties. This remarkable finding proves that extrinsic FEP, in particular using ionic species, has great potential as a new and controlled method of passivation capable of lasting for years. The high stability achieved using alkali ions is of great importance for the passivation of silicon solar cells, since passivation methods are expected to last for the lifetime of the cells, i.e. 20-30 years. The best stability observed in this work was that of an oxide film with K ions diffused and drifted in a 3 minute process. The addition of a drift mechanism via corona charge proved beneficial. Although the migration process can cause a level of interface damage, the charge migrated into the oxide presents better stability than only using diffusion. A lifetime decay time constant of 11,000 days was inferred. This

implies a 37% reduction in in effective lifetime over a 30 year lifespan. Given the short length of this process (~3 min), it is likely that this processing technique can be optimised to obtain fast and effective migration of ionic charge by tailoring the corona charge concentration, ion type, ion concentration, and temperature and time of the drive-in step. Such a technique could produce effective and stable passivation for the lifetime of a solar cell.

The quality of passivation achieved using ionic FEP was not as high as that reported in Chapter 4. SRV values of ~ 6-12 cm/s were inferred thus indicating that either the chemical or the FEP components are not fully exploited. It appears that sufficient charge is present in the oxide yet this charge is mainly located at the oxide/silicon interface where it can damage the chemical properties of the interface. This level of passivation is acceptable for current commercial solar cells with efficiencies ~ 18%. However, for high efficiency (>20%) silicon cells this technique must be improved such that passivation is exploited to the maximum. The relative importance of field effect passivation in solar cells will be explored in Chapter 6.

5.4 Chapter summary

It has been shown that ionic charge can be migrated into a silicon dioxide film and is stable for over 700 days with lifetime decay time constants of over 11,000 days. This is a remarkable increase in the stability of any extrinsic field-effect passivation method ever reported, and it is hugely promising for passivation of silicon surfaces in solar cells. In order to achieve this stability, two distinct mechanisms were used. First, a pure diffusion mechanism in which ionic species are injected, diffused and trapped inside the film at high temperature due to concentration gradients only. Second, a drift mechanism established by an electric field that enhances the de-trapping of species at the oxide surface due to Columbic force. Positively charged alkali ions have been embedded into SiO_2 using these combined

mechanisms, and shown to produce effective and stable passivation of 1 Ωcm n-Si surfaces. S_{eff} values in the range 5-10 cm/s have been demonstrated for oxide passivated FZ n-Si for periods in excess of 600 days. This shows that ionic FEP is a potential technique to reduce surface recombination in a controlled and durable manner. In the best case, an oxide film can be FGA treated, ionically charged with K ions, and HMDS protected to provide effective passivation with SRV $<$ 6 cm/s. This passivation would degrade by less than 37% over a period of 30 years. This method is therefore a step towards controlled FEP that can improve the passivation properties of dielectric films whilst allowing their optical properties to be adjusted independently by modifying the deposition parameters.

Model parameters that describe alkali ion de-trapping in this system were deduced and are in qualitative agreement with previously reported data. Higher de-trapping activation energies are found for ions located at a free surface compared to those previously reported for ions located at an oxide/metal interface of a MOS capacitor. In addition, the results presented indicate that other ionic species, not only alkali but also alkaline and perhaps some other metals, should have the potential to be fixed into a dielectric matrix and provide effective and durable FEP. This passivation technique provides an alternative method of passivation whereby chemical, field effect, and optical properties in a dielectric film can be exploited separately to produce improvements in the conversion efficiency of silicon solar cells.

CHAPTER 6
INFLUENCE OF FIELD EFFECT PASSIVATION ON SILICON SOLAR CELLS

Silicon solar cells exceeding 25% efficiency are now possible thanks to innovative geometries and very precise fabrication processes [209]. The highest efficiency is normally demonstrated in cells with sophisticated and optimised processing steps, which are often only carried out by research institutions rather than industrial companies. The challenge remains to develop industrially compatible processes in such a way that they are implemented and improve the production cost and/or performance of commercial solar cells.

Minimising surface recombination losses is a key requirement in the fabrication of high efficiency (>20%) silicon solar cells. Previous chapters have shown how outstanding passivation can be achieved. The present chapter explores the benefits that reduced surface recombination have on solar cell performance. The relevant cell geometries are discussed and simulated to quantify the improvements resulting from improved FEP. Research scale silicon cells are then characterised under enhanced extrinsic FEP and the measured improvements are reported.

6.1 Solar cell geometries

Chapter 1 set out the basic concepts underlying the operation of a silicon solar cell. Figure 3 illustrated the most practical cell implementation where the antireflective coating provides surface passivation and the rear contact covers the entire cell surface. However, such a geometry is not optimum due to shadowing of the cell by the front metallic contacts, surface

recombination, and carrier transport [210]. Today, the two most common and efficient geometries are the passivated emitter rear locally-diffused (PERL) and the back-junction back-contact (BJBC) cells.

PERL silicon solar cells were first proposed in the late 1980's by M.A. Green's group at the University of New South Wales [211], [212]. Many improvements have since been made and 25% efficiency cells have been achieved [213]. PERL cells include front pyramidal texturing and surface passivation, a locally diffused rear contact, and a rear surface passivation film [214]. These features are illustrated in Figure 86.

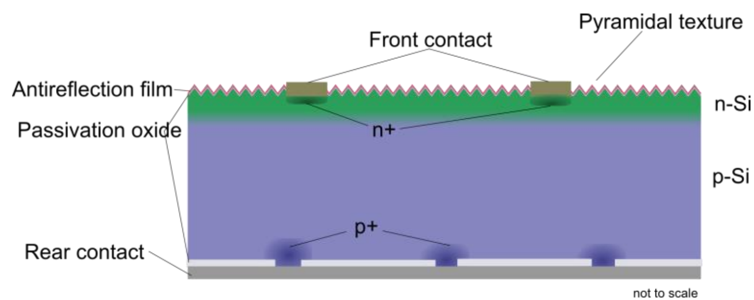

Figure 86. Passivated emitter, rear locally-diffused (PERL) cell geometry, including a double layer of oxide and antireflection coating, and front diffused contacts.

A key improvement in this cell is the superior surface passivation achieved using front and rear thermal silicon dioxide. Recombination losses have been reduced by eliminating the entire rear contact so that most of the rear surface is passivated and carriers are collected at local ohmic contacts. The front surface passivation and antireflection coatings are separate in order to achieve the best properties for both; the excellent chemical passivation of SiO_2 combined with the appropriate refractive index and fixed charge density of SiN. All these finely tuned processes demonstrate how important surface passivation is to cell efficiency [214].

BJBC cells were introduced by Schwartz in 1975 with the main objective of reducing shadowing and resistive losses from front contacts [215]. Interdigitated rear-contact metallization was soon suggested as the technology to connect the cell to the module more

easily [216], and thereafter this cell has been better known as the Interdigitated Back Contact (IBC) cell. A schematic of a state-of-the-art IBC cell is shown in Figure 87.

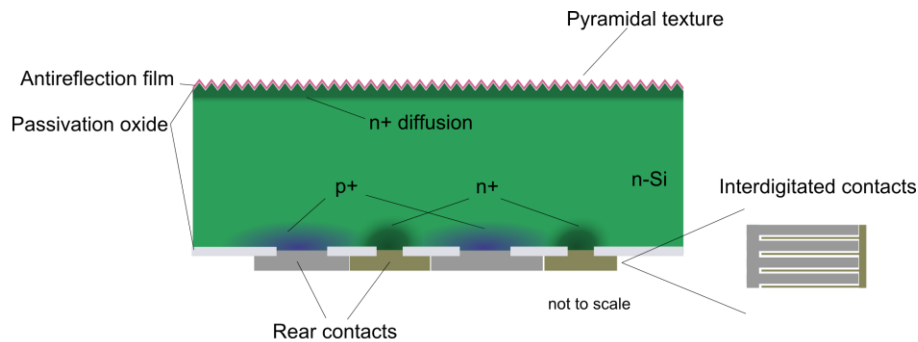

Figure 87. Back-junction back-contact (BJBC) cell geometry and its interdigitated contacts.

Today's highest efficiency *commercial* solar cell is an IBC geometry produced by Sun Power (24% Maxeon cell) [217]. It includes both n and p type local diffusions on the rear side, so that passivation is maximised and resistive losses minimised. A front surface antireflective coating enhances light absorption, while an oxide and an n+ front surface field (FSF) are used to reduce surface recombination to a minimum as explained in Chapter 1 [55], [218]. Photo generation in IBC solar cells occurs very near the front surface, thus increasing the importance of minimizing front surface recombination. The rear surface, although oxide passivated, mainly minimises resistance losses and maximises collection efficiency in both the ohmic and the emitter junctions.

Several methods to improve the cell n and p diffusions, contacts and metallisation, light management, and carrier recombination have been proposed. These aim to improve efficiency and reduce cost in both PERL and IBC solar cells [56], [219], [220]. The next section explores the quantitative improvement enhanced FEP makes in solar cell performance, as calculated via simulations. The final section in this chapter illustrates improvements in real IBC solar cells.

6.2 Modelling cell efficiency and surface recombination

Improvements in solar cell efficiency (η) are often described in terms of cell electrical parameters such as the open circuit voltage (V_{oc}), the closed circuit current density (J_{sc}) or the emitter saturation current (J_0). Higher V_{oc} and J_{sc}, and lower J_0, indicate better performance of the cell. However, improvements in these metrics may not always be related to surface recombination, therefore care must be taken when assessing improvements due to improved surface recombination velocity.

Rohatgi et al [221] published a comprehensive study showing how different surface passivation schemes provide improvements to cell efficiency. They separated different factors by passivating both diffused and undiffused surfaces and they simulated cell efficiency using the measured parameters on the cell simulator PC1D [145]. They found that up to 0.5% (absolute) gain in efficiency could be obtained from improving front surface passivation in screen-printed front contact solar cells, and over 2% gain from improving the rear surface. Hofmann et al [222] simulated cell efficiency as a function of rear surface recombination velocity. They plotted open-circuit voltage V_{oc} and energy conversion efficiency η for cell thicknesses ranging from 50 to 300 μm, and rear surface recombination velocities between 100 cm/s and 10^6 cm/s. They found a strong interdependence between surface passivation and cell efficiency. The thinner the solar cells the stronger this dependence is. Improvements of over 2% absolute could be achieved by changing an aluminium back surface field (BSF) scheme (SRV ~10^6 cm/s) to a locally contacted oxide passivated one (SRV ~10 cm/s). In similar work, Doshi and Rohatgi [223] reported 1% absolute increase in 18% efficient screen-printed solar cells by providing a better front surface passivation. A rapid thermal oxide used in the front passivation scheme caused V_{oc} and J_{sc} to increase by 20 mV and 1 mA/cm^2 respectively, while J_0 reduced by a factor of ten.

These indicate the benefits of enhanced surface passivation in both the front and rear of the cell for front contact cell geometries. These studies, however, did not assess the field effect component of passivation alone, nor did they study the more efficient back-contact solar cell geometry.

The efficiency increase achieved using improved surface passivation –e.g. when reducing S_{eff} from 10^{3-4} cm/s to <10 cm/s, depends on different cell parameters including base and emitter doping concentrations, contact areas, texturing, and cell type. However, most studies coincidently report absolute increments between 0.5 and 1% from enhanced front side passivation, and 1 to 3% from rear side passivation in solar cells with efficiencies of about 18% [176], [189], [221], [223], [224]. Such increases are very worthwhile, especially if a fast, cheap and reliable surface passivation technology is developed that can be easily incorporated into in-line silicon solar cell production. Such technology is the objective of this thesis. This section describes a modelling analysis of the effect of extrinsic FEP on the performance of silicon solar cells, furthering those findings currently reported. This is conducted first in a standard front contacted commercial cell using the simulation tool PC1D. The analysis is is then extended to the more efficient IBC cells.

6.2.1 FEP in a front contacted cell (PC1D simulations)

6.2.1.1 Simulation setup

A standard front contacted cell was simulated for this work using PC1D [145]. The cell schematic is illustrated in Figure 88. The cell area was 100 cm^2 and its parameters were taken as those typical of commercial cells. These are listed in Table 6. They include a base series resistance, emitter shunt conductance, a shallow diffused emitter, front pyramidal texture, a limited front reflectance across the solar spectrum, a back surface field (BSF), and surface recombination for front and back surfaces which ignores the field effect component and carrier type. The simulation methodology involved setting a concentration of surface charge at the front/back surface and then finding the maximum power point of the cell, and

the V_{oc} and J_{sc} parameters. This procedure was carried out on a p-type cell: p base and an n+ emitter.

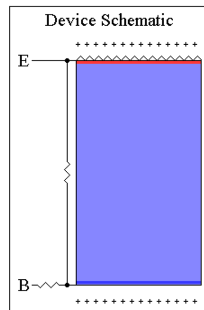

Figure 88. PC1D device schematic for a front contacted p-type Si solar cell with surface charge, shunt and series resistance and a textured surface.

Parameter	Value	Units
Thickness	160	μm
Analysis area	100	cm^2
Doping concentration	5×10^{15}	cm^{-3}
Front diffusion, Emitter (Erfc 0.2 μm)	10^{20}	cm^{-3}
Rear diffusion, BSF (Erfc 0.1 μm)	10^{20}	cm^{-3}
Circuit series resistance	0.015	Ω
Shunt conductance	0.05	S
Illumination AM1.5G	0.1	W/cm^2
Temperature	25	^oC
Bulk lifetime	10	ms
Front S_n=S_p	10^4	cm/s
Rear S_n=S_p	10^4	cm/s
Exterior Frn reflectance	10	%

Table 6. Cell parameters for PC1D simulation

6.2.1.2 Results

Figure 89 illustrates the simulated η, V_{oc} and J_{sc} of this cell when positive and negative charge is present on its front surface. Figure 90 illustrates these same parameters when the charge is on its back surface. It is important to note that this simulator assumes all charge is compensated by charges in the silicon rather than in the metal contacts, top or bottom. When positive charge is deposited on top of the n+ emitter, Figure 89, η improves by 0.25% absolute, while V_{oc} improves by 8 mV and J_{sc} by 0.1 mA/cm^2. These improvements in device operation are related to better surface passivation, achieved by field effect repulsion of charged carriers, and to the improved collection efficiency caused by a larger surface field at

the metal semiconductor contact. It is noted that surface recombination is very fast for this heavy doping concentration, yet FEP can produce a worthwhile improvement in performance. When negative charge is deposited, the concentration of holes increases in the electron-abundant front surface region. This produces a rapid increase in recombination and thus reduction in the efficiency of the cell and its V_{oc} and J_{sc}. As negative charge increases the surface carrier concentration is depleted and then inverted. This prevents carrier collection at the metal contact thus worsening cell performance and limiting the accuracy of the solution algorithm. The lack of convergence observed for high negative charge concentrations is due to band pinning when the band edges reach the Fermi energy.

When charge is present on the cell's back surface, Figure 90, improvements in all performance parameters are smaller than for when charge is on the front surface. η, V_{oc} and J_{sc} improved by 0.15%, 5 mV and 0.04 mA/cm^2, respectively, when negative charge was present on the heavily doped p-type back surface. These improvements are achieved due to the increased field effect passivation and collection efficiency when negative dielectric charge creates an accumulation region in the cell p-type back surface. The cell performance depends less on the FEP characteristics of the back surface charge yet the improvements obtained are still worthwhile. At the rear of the cell, generation of carriers is minimal. Collection happens immediately after a minority carrier has been swept across the PN junction. This makes recombination at the front surface more important for overall cell performance. Additionally, the presence of the back surface field for the model cell proposed reduces the extent to which FEP can reduce back surface recombination. Similarly to the case at the front surface, charge with the same polarity as the material doping (positive) will induce a depletion and then an inversion region that augments recombination strongly and thus worsens the performance of the cell.

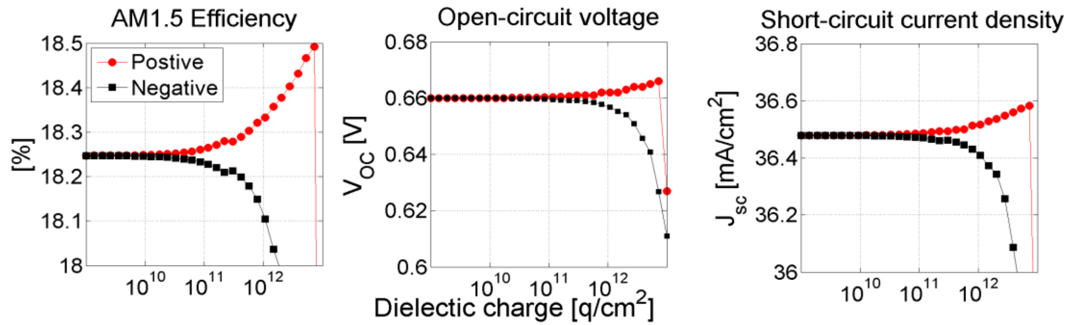

Figure 89. Cell performance when FEP is altered in the front surface by changing dielectric charge in a p-type front contacted cell.

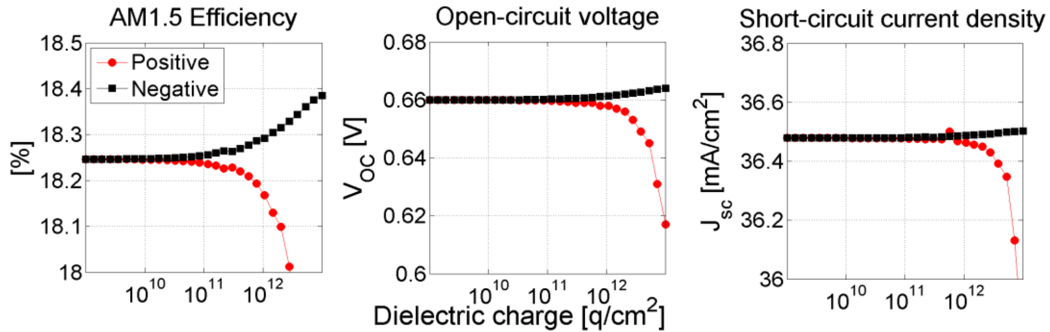

Figure 90. Cell performance when FEP is altered in the rear surface by changing dielectric charge in a p-type front contacted cell.

The effect of base doping, emitter doping, back surface field and cell thickness is also explored for this standard front contacted cell. Figure 91 illustrates the AM1.5 efficiency of a cell as a function of these parameters. Figure 91.a illustrates the dependence of efficiency with base dopant concentration. An improvement in efficiency with extrinsic FEP is observed for all doping levels, and for both front and rear surface charge. Higher dopant densities can improve the material's conductance and provide a better V_{oc}, but they can also reduce the cell J_{sc} by increasing the amount of intrinsic recombination. It therefore follows that efficiency has a curvilinear dependency with base dopant density. An intermediate dopant concentration, near 5 x 10^{15} cm^{-3}, is optimal for this cell geometry. Figure 91.b illustrates the dependence of efficiency with emitter dopant concentration. Improvements in efficiency due to front positive surface charge vary widely depending on the emitter doping. Improvements due to back negative charge are negligible for all cases. Similar to the case of base doping, a higher emitter dopant density will reduce the sheet resistivity, thus allowing better lateral conduction and V_{oc} but reducing carrier lifetime and J_{sc}. An intermediate doping density thus provides the best efficiency given no external FEP. The best performance,

however, is observed for the lightly doped emitter when sufficient front surface FEP is provided. This reduces surface recombination and improves collection probability while limiting intrinsic recombination in the lightly doped emitter. A 2.1% absolute improvement in efficiency is achieved from extrinsic FEP. Figure 91.c illustrates the effect of the BSF on the cell performance. A higher dopant density directly improves the passivation and collection efficiency at the back contacts. Depositing negative charge on the back surface improves efficiency regardless of the dopant concentration. When lighter doping concentrations are selected the relative improvement in efficiency is higher. Lighter doping also allows a direct reduction in intrinsic recombination such that higher overall efficiencies are achieved with external FEP. When no FEP is used, the BSF with high dopant density performs best. In this case the intrinsic bulk recombination plays a minor role since negligible carrier generation takes places near the back of the cell. Similarly, the lateral conductivity has little effect since carriers are readily available throughout the base region. Positive charge on the front surface increases efficiency equally for all BSF dopant densities, by ~ 0.1% absolute. Figure 91.d shows the effect of wafer thickness. The thinner the cell the fewer carriers get absorbed and thus the lower its efficiency. FEP influences similarly the front and back surface regardless of the cell thickness. The lack of absorption for thin cells is one of the drawbacks of this standard geometry. This is normally solved using sophisticated light management designs [225].

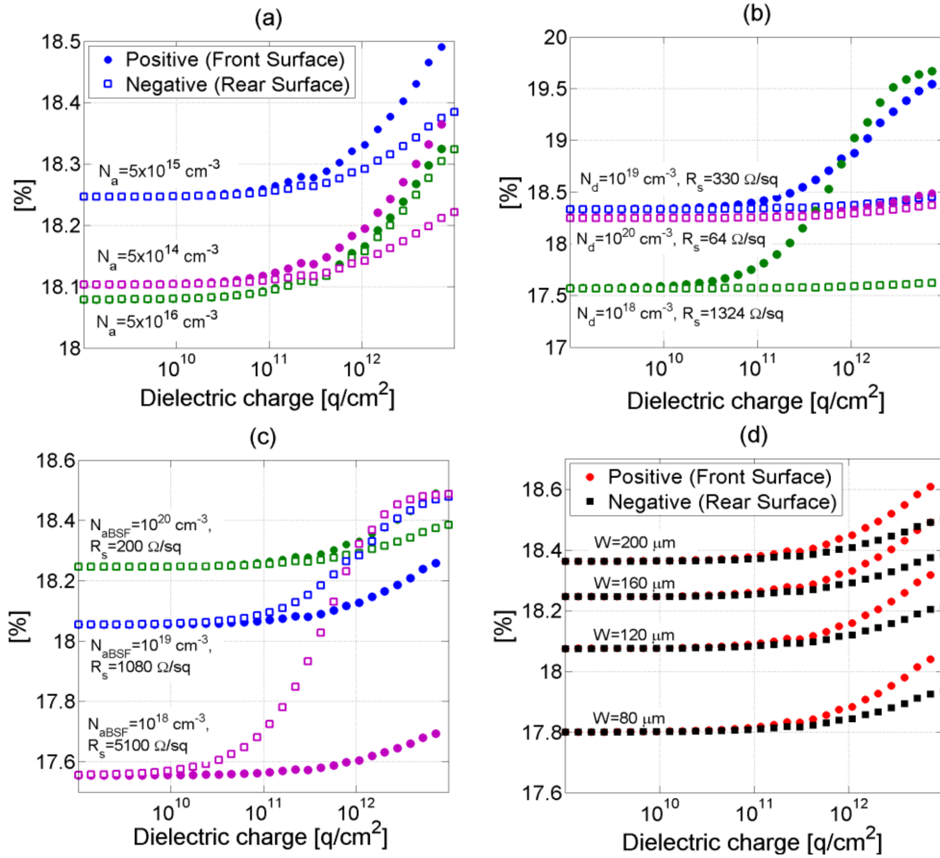

Figure 91. AM1.5 cell efficiency when FEP is applied to the front and rear surface in a p-type front contacted cell for different a. base doping concentration, b. emitter doping concentration, c. BSF doping concentration, and d. cell thickness. Simulation parameters are those given in Table 6 unless specified in the figure labels.

6.2.1.3 Discussion

One-dimensional simulations have shown that extrinsic FEP applied as surface charge on the front and back of a cell can improve performance significantly. Surface charge of the same polarity as that of the majority carrier produces an accumulation region that repels minority carriers from the surface and thus reduces defect mediated SRH recombination at the surface. In addition, the collection efficiency of the base and collector contacts also improves with the presence of charge when the accumulation region arises near the top and bottom contact nodes in PC1D. A limitation of the one-dimensional simulations is that charge is present directly above the contact node. In reality, charge would be located only where there is a lack of a metal contact. The metal contact requires a heavily doped region and an ohmic contact to the metal thus making surface charge irrelevant. Separating the effects of carrier recombination and metal contact collection is not possible here. Despite this, it is feasible

that a large part of the improvement relates to reduced surface recombination. The cell with 10^{13} q/cm^2 charge concentration performed 0.1-1.4% relatively better. The more significant effect was observed when the front surface had FEP rather than the back surface, and with η and V_{oc} presenting the most substantial gains.

The equivalent SRV for this standard front contact cell can be inferred using the modelling formalism in Chapter 3. When the positive charge concentration at the surface of a heavily doped (~10^{20}cm^{-3}) emitter is increased to 10^{13} q/cm^2, the SRV is reduced from its flat-band value, 10^5 cm/s (an order of magnitude higher than the $S_{n,p}$ values reported in Table 6 due to the high dopant density (Chapter 3) to 2 x 10^4 cm/s. This is almost an order of magnitude reduction in SRV purely due to extrinsic FEP. An equal improvement in SRV is observed for negative charge at the surface of the heavily doped BSF. For comparison, this is equivalent to reducing SRV in 1 Ωcm (N_{dop}=5 x 10^{15} cm^{-3}) Si from 7 x 10^3 cm/s down to <10 cm/s. This is over two orders of magnitude reduction in SRV. The improvements in SRV reported in Chapters 3 and 4 are about two orders of magnitude, yet there the highest lifetime is produced with a dielectric charge concentration of ~ 3-6 x 10^{12} q/cm^2. Although minimal improvement in lifetime was observed by exceeding these charge concentrations, it is noted that a charge as high as 10^{13} q/cm^2 is possible in oxide films, or other high permittivity dielectrics [226]

Simulation results for different base doping, emitter doping, back surface field and cell thicknesses were also reported here. The relative improvement in performance was seen irrespective of the wafer thickness and base doping. Lightly doped emitter and back field layers caused a more pronounced improvement in performance with charge density, and overall a better performance for high concentrations of charge. This indicates that when independently optimising passivation for a dielectric is possible, other cell characteristics can be jointly tailored to produce an overall better efficiency. Once again, the limitation of this argument lies in the fact that in PC1D the improvement in efficiency due to passivation

cannot be separated from that due to better collection efficiency. This is better described when using two-dimensional simulations in PC2D.

6.2.1.4 Summary

This section showed that up to 1.4% relative higher efficiency can be achieved for front contact solar cells by using extrinsic passivation. Moreover, by using extrinsic passivation, other parameters of the cell can be independently tailored and optimised. These improvements in efficiency are worthwhile, in particular considering the simplicity and low-cost of the extrinsic passivation techniques reported in this work. It is hence concluded that the passivation obtained from extrinsic FEP methods has the potential of improving cell efficiency without significant added cost.

6.2.2 FEP in a back contacted cell (PC2D simulations)

6.2.2.1 Simulation setup

Back contacted solar cells have been shown to perform substantially better than front contacted ones thanks to the reduction in shadowing and resistive losses. A commercial IBC solar cell was simulated in PC2D [227] to quantify the improvements available when extrinsic FEP is applied. The cell schematic is illustrated in Figure 92 where the simulation domain has been defined using 20 x 20 elements. The cell area was 1 cm^2 and its parameters were taken as those typical of a high efficiency (> 20%) IBC cell fabricated by Fraunhofer ISE (for example cells of Type A and C in reference [220]), as listed in Table 7. All remaining parameters are left at the default values used in the IBC cell simulation example provided by Paul Basore on the PC2D software website [228]. These include a base series resistance, no emitter shunt conductance, a diffused emitter defined by its sheet resistance in the top row of the simulation domain, front pyramidal texture, and limited front reflectance across the solar spectrum.

The surface recombination in PC2D is characterized by the dark saturation current density J_0. The J_0 metric includes recombination occurring in the doped (bent band) region near the surface, for example in front and back surface fields, or at ohmic contacts. J_0 is preferred to S_{eff} since the former is independent of base doping density, thus in the context of different highly doped surface layers the J_0 metric becomes more convenient. However, the surface recombination velocity can be analytically related to J_0 according to the approximations drawn by Mäckel and Varner [229] but additional assumptions would be required. J_0 is normally expressed as the sum of a component with an ideality factor of one (J_{01}) and a component with an ideality factor of two (J_{02}). The latter has been disregarded since Chapter 3 demonstrated that SCR recombination that produces a dark saturation current with ideality factor of two is negligible in oxide passivated Si. Here, J_{01} was found using a simulation method recommended by Cabanas-Holmen and Basore [230]. This involved simulating a diode comprising a moderately doped base and the highly doped surface layer such as that proposed for the IBC cell, Table 7. This simulation was executed for a varying concentration of surface charge and for a front surface both diffused and un-diffused with an n++ front surface field.

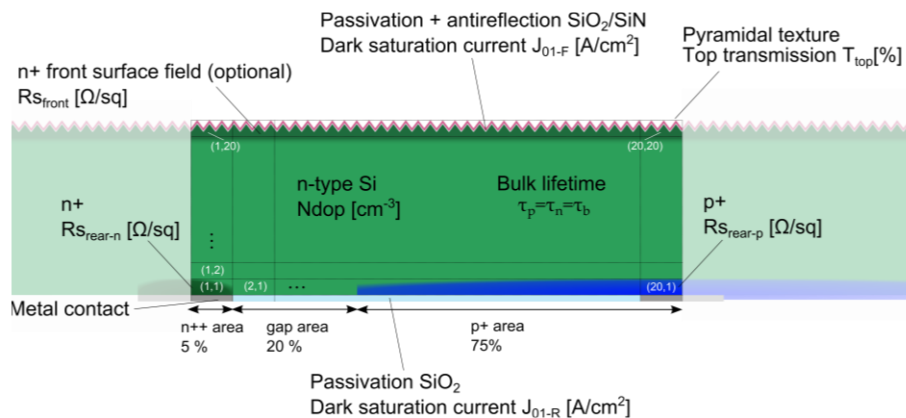

Figure 92. Simulation domain and definition of regions for the IBC cell modelled in PC2D.

Parameter	Value	Units
Thickness	160	μm
Unit cell width	500	μm
Analysis area	1	cm^2
Doping concentration	5×10^{15}	cm^{-3}
Hole diffusion coefficient	11.6	cm^2/s
Electron diffusion coefficient	32.3	cm^2/s
Circuit series resistance	0.4	Ω
Illumination AM1.5G	0.1	W/cm^2
Temperature	25	C
Mid-gap bulk recombination lifetime (τ_b)	10	ms
FSF, Erfc $n_{peak}=5 \times 10^{18}$, 0.4 μm (R_s)	253	Ω/sq
Front Sn=Sp	2000	cm/s
Rear recombination J_{o1} at n+ region	4×10^{-13}	A/cm^2
Rear recombination J_{o1} at n region	2×10^{-14}	A/cm^2
Rear recombination J_{o1} at p+ region	1.5×10^{-13}	A/cm^2

Table 7. Simulation parameters for back contact cell modelled in PC2D.

6.2.2.2 Results

Figure 93 illustrates the performance of a model IBC solar cell including an n+ FSF of R_s =253 Ω/sq. Figure 93.a shows the dark saturation current calculated in PC1D for the model diode. Positive charge deposited on the top surface improved η, J_{sc} and V_{oc} by 0.51%, 0.6 mA/cm^2 and 5 mV, respectively. This is illustrated in Figure 93.b, c and d. Negative charge, on the other hand, produced a reduction in the performance of the cell. When charge of the same polarity as the material's majority carriers is present (negative) a depletion region is generated. This increases the concentration of opposite polarity carriers, the minority carriers. Since recombination is dependent on the presence of both carriers, such depletion and eventual inversion of the surface carrier increases recombination strongly, thus reducing the performance of the cell. Excessive negative charge on the model diode in PC1D results in lack of convergence due to insufficient carrier collection at the emitter contact. This explains why only values for charge > -2×10^{12} q/cm^2 are reported in Figure 93.

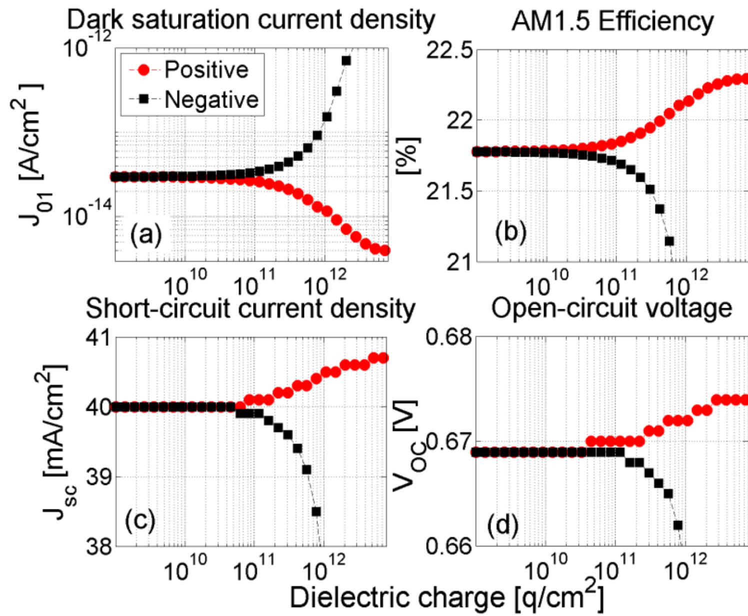

Figure 93. a. Dark saturation current in a model diode simulated in PC1D when surface charge is changed, b-d. Cell performance simulated in PC2D when FEP is altered in the front surface by changing J_{01} in a n-type IBC cell that includes a 253 **Ω**/sq FSF for passivation.

Figure 94 illustrates the resulting performance of the same IBC cell when the FSF is not present. In absence of an FSF, recombination at the front surface reduces by over 3 orders of magnitude when FEP is applied. This is observed in the decrease in dark saturation current in Figure 94.a. The effect of such large reduction in recombination is plotted in Figure 94b-d. η, J_{sc} and V_{oc} are seen to improve by 12%, 20 mA/cm^2 and 60 mV, respectively, when front surface charge increases from 10^9 to 10^{13} q/cm^2. This is an astounding improvement in cell efficiency.

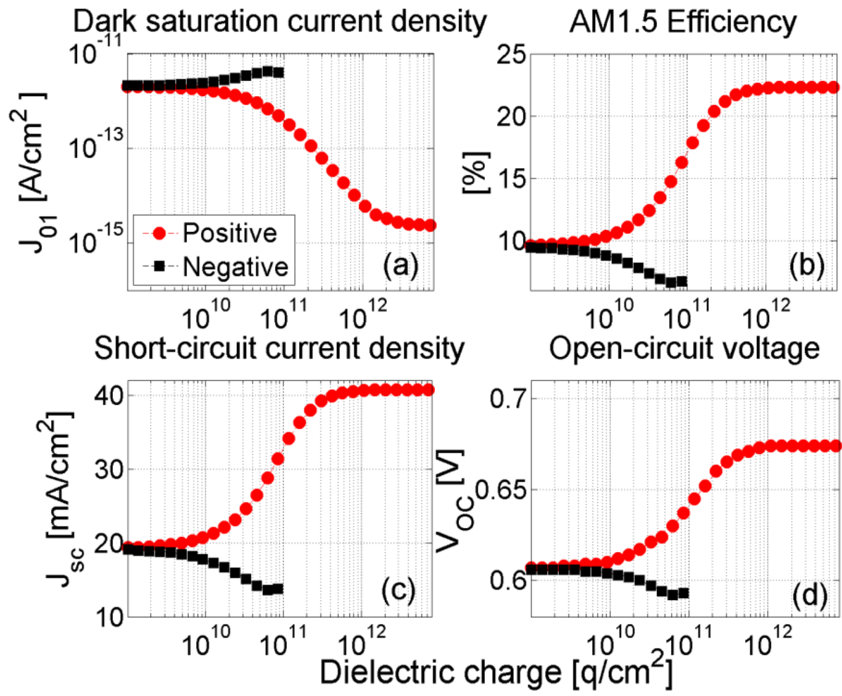

Figure 94. a. Dark saturation current in a model diode simulated in PC1D when surface charge is changed, b-d. Cell performance simulated in PC2D when FEP is altered in the front surface by changing J_{01} in a n-type IBC cell that does not include a FSF.

6.2.2.3 Discussion

Passivation of the front surface in an IBC cell was controlled using the dark saturation current density, which was modelled via a 1D ideal PN junction for a varying concentration of surface charge. The dark saturation current density was in turn used as an input parameter to model the performance of an IBC cell in PC2D. The simulation results indicate that a direct reduction in surface recombination is possible when applying charge to the front surface of IBC cells, and such improvement transfers directly to better cell operation with improvements in efficiency of 0.5% absolute when the cell presents a FSF, and over 12% when it lacks a FSF. It is important to note that, at its highest point, the efficiency obtained for a cell *without* the expensive FSF exceeds that obtained in a cell with a FSF and no dielectric charge. When charge is present in both the FSF and no-FSF cells the efficiency of the no-FSF cell exceeds that of a FSF cell by 0.03% absolute. This is due to a reduction in intrinsic Auger and radiative recombination in the heavily doped surface region which is required to produce a FSF, while the extrinsically deposited charge still maintains the positive effect of FEP, and is a low cost method. Passivation dielectrics in solar cells already

present an intrinsic charge, but such charge is rarely optimal. For instance, for a SiN_x film with 10^{12} q/cm^2, an improvement of 0.15% and 0.1% in absolute cell efficiency is still possible when increasing surface charge to 10^{13} q/cm^2, for a cell with and without a FSF respectively. This indicates that regardless of the presence of a FSF, the cell efficiency is largely governed by the passivation quality of the front surface, and that extrinsic FEP alone can provide extraordinary passivation and thus cell performance.

Improvements in J_{sc} were substantial as well, in particular that of the J_{sc} when the cell lacked a FSF. V_{oc} improved as well, but to a much lesser extent. Overall, IBC cells with a FSF and a surface charge of 10^{13} q/cm^2 performed 1-2.5% relatively better. The equivalent SRV for this IBC cell with a FSF is inferred to be 8 x 10^3 cm/s when the dielectric charge is 10^9 q/cm^2, and 10^3 cm/s when dielectric charge is increased to 10^{13} q/cm^2. This is almost an order of magnitude reduction in SRV purely due to extrinsic FEP, and is consistent with the experimental results presented in Chapter 4. IBC cells without a FSF and a surface charge of 10^{13} q/cm^2 performed 100-200% relatively better. The equivalent SRV for this IBC cell with a FSF is inferred to be 10^3 cm/s when the dielectric charge is 10^9 q/cm^2, and <2 cm/s when dielectric charge is increased to 10^{13} q/cm^2. This is nearly three orders of magnitude reduction in SRV and, as demonstrated in Chapters 4 and 5, could be achieved in a straightforward manner using the new extrinsic FEP techniques proposed in this work.

In comparison to the front contacted cell geometry, it is seen that the relative importance of the front surface is higher for the back contacted cell geometry. Charge carriers are generated very near the front surface and they must diffuse to the back of the cell before being collected at the junction and generating electricity. Front surface passivation is therefore a key requirement for this geometry. Furthermore, for the IBC cell modelled in PC2D, the improvements obtained with positive charge only relate to the increased field effect passivation at the front surface. These improvements are worthwhile, particularly when the passivating film lacks intrinsic charge. This is rarely the case since most dielectrics

present both chemical and FEP components. Although an optimal (according to [220]) FSF has been applied to this cell, the performance is still seen to improve when FEP is increased.

6.2.2.4 Summary

This section showed that up to 200% relatively better performance of IBC solar cells is achieved by using extrinsic passivation. Moreover, a cell which presents a passivating FSF also benefits from extrinsic FEP, yet the need for such FSF is eliminated since for the same dielectric charge IBC cells lacking the FSF are seen to perform slightly better. This important finding translates into cost-reduction in the production line of IBC cells, since no lengthy high temperature diffusions are required on the front surface to produce the FSF. It is therefore concluded that low-cost extrinsic FEP methods of passivation are extremely promising when used in IBC cells.

6.3 Influence of FEP on research scale IBC cells

The simulation results reported in this chapter demonstrate that extrinsic FEP can produce significant improvements to cell performance. Quantifying such improvements in real solar cells requires custom-made cells, where the front surface dielectric only provides moderate chemical passivation and no FEP. In this way the field effect component of passivation can be studied independently when applying extrinsic FEP, for example using corona charge. To accomplish this, a collaboration was established with Fraunhofer ISE, Germany. They provided research scale 2 x 2 cm^2 IBC solar cells with an oxide/nitride passivation film. This front passivation scheme was not ideal since it already included a level of FEP, yet it provided a good basis to evaluate extrinsic FEP at device level. IBC solar cells were tested at laboratories in Oxford and Fraunhofer ISE. The following two sections present the results of this evaluation. Firstly cells were brought to Oxford and tested under non-standard conditions. After a positive effect was found, the same extrinsic FEP technique was used in Germany and the results recorded under standard testing conditions.

6.3.1 In-house non-standard solar simulator

Two identical back-contact n-type silicon solar cells with a SiO_2/SiN_x passivated front side and no FSF (Structure A in reference [220]) were tested for enhanced and controlled FEP after applying corona charge. Corona rig 1 was used to charge the cell front surface in 5 seconds steps. Changes in V_{oc}, J_{sc}, and output power (P_{out}) were evaluated by plotting IV characteristics while the cells were illuminated with a controlled 50 Watt Xenon light source as described in Chapter 2. Figure 95 illustrates normalized changes in V_{oc}, J_{sc} and P_{out} of the cells tested. Absolute values here are not important since the testing conditions were not standard. External deposition of charge was observed to enhance front surface passivation of both cells as seen by an improvement in J_{sc}. This directly relates to a better collection probability [231]. Average P_{out} and J_{sc} values increased by 2.5% and 1.8% relative. Figure 95 also illustrates that excessive charge deposition can degrade the quality of the passivation since steps 5 and 6 presented a moderate lowering in P_{out} and J_{sc}. If a passivation enhancement step were to be applied to the fabrication of cells, the corona charge density would have to be optimised so as not to degrade the film passivation. After this improvement in passivation was recorded at the laboratories in Oxford, a new batch of cells was supplied by Fraunhofer ISE and standard testing was conducted. This is covered in the next section.

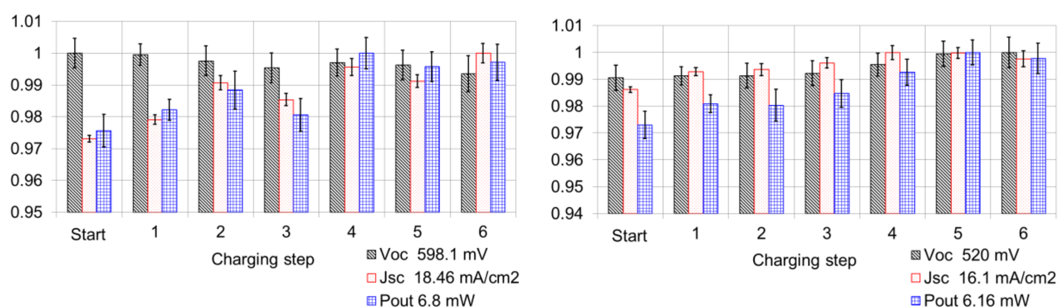

Figure 95. Normalised V_{oc}, J_{sc} and P_{out} for two identical back-junction back-contact n-type silicon solar cells. The cells were submitted to 6 corona charging steps using a single point at 9 kV potential, 8 cm from the cell, each lasting 5 seconds. Normalisation values of V_{oc}, J_{sc} and P_{out} are included for each cell.

6.3.2 FEP cells evaluated using standard testing conditions

Fourteen IBC cells provided by Fraunhofer ISE have been evaluated in this project. They included a variety of cells with and without a FSF. These were tested by the author to determine the effect of extrinsic FEP using an ISO calibrated solar simulator at Fraunhofer ISE. Solar cell testing was conducted using a similar methodology to that used at Oxford. The cells were charged for a period of time and then directly taken to the solar simulator for characterisation. The details of the solar simulator are given in Chapter 2. The corona discharge rig at Fraunhofer ISE was a point to plane configuration with a distance of 8 cm, and 8kV applied to the point electrode. Kelvin Probe measurements were not available at Fraunhofer ISE hence the corona charge is reported as a function of deposition time rather than surface potential or charge concentration. However, as an indication, the charge deposition rate was estimated using the improvement in effective lifetime in oxide passivated specimens, as described in Chapter 4. This produced a value around ~ 3 x 10^{11} q/cm^2 per second. Table 1 describes the cell characteristics and illustrates the cell parameters (V_{oc}, J_{sc} and P_{out}) under illumination as corona charge is deposited on the front surface. In some cases the IV characteristics were acquired several times to account for experimental error in the handling and measuring procedures. When this was the case the graphs in Table 1 show error bars indicating the standard deviation of the measurements. Previous cell testing performed in-house had shown that excessive concentration of charge resulted in a degradation of the cell performance. This was confirmed here. To visualise the performance improvement better, the optimal time has been extracted from the graphs and the cell parameters have been quoted at before and after a corona discharge for the optimal period of time. This is shown in the left column of Table 1. These results show that regardless of the presence of a FSF a substantial improvement in cell performance is available when positive charge is added to the front surface of IBC cells. Only in two instances did extrinsic FEP not improve cell performance. Twelve different cells showed a level of improvement in efficiency, ranging from 0.01 to 0.7% absolute, with an average improvement of 0.18% absolute. J_{sc} improved

by 0.3 mA/cm^2 on average, while V_{oc} improved by 0.5 mV. This demonstrates that extrinsic FEP can be used controllably to enhance the passivation properties of IBC cells and therefore improve their performance.

Cell Reference Name Front surface passivation	Plot of efficiency, V_{oc} and J_{sc} as a funciton of corona charge

t_{cor} [s]	η [%]	J_{sc} [mA/cm₂]	V_{oc} [mV]

t = Optimal corona charge time

BC47-22G
SiO_2/SiN_x
No front surface field

t_{cor} [s]	η [%]	J_{sc} [mA/cm₂]	V_{oc} [mV]
0	15.92	34.30	642.56
6	16.07	34.72	641.75

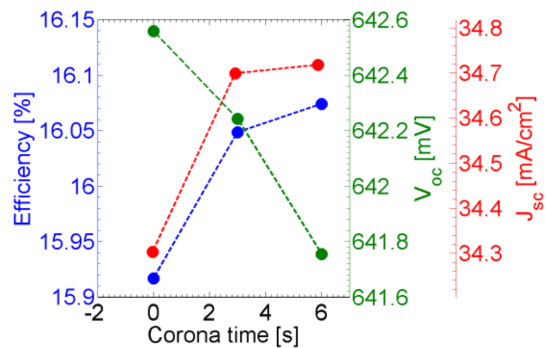

BC47-23A
SiO_2/SiN_x
No front surface field

t_{cor} [s]	η [%]	J_{sc} [mA/cm₂]	V_{oc} [mV]
0	15.24	29.79	638.14
21	15.99	31.23	637.72

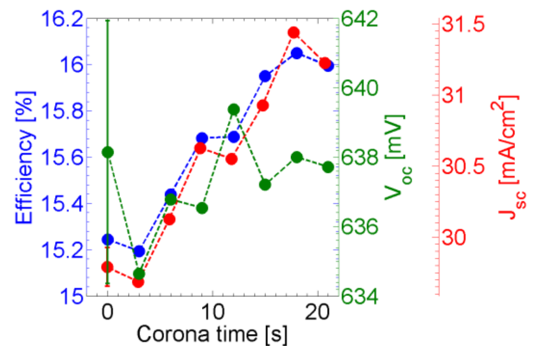

BC47-24A
SiO_2/SiN_x
No front surface field

t_{cor} [s]	η [%]	J_{sc} [mA/cm₂]	V_{oc} [mV]
0	16.72	36.33	635.59
12	16.79	36.46	635.31

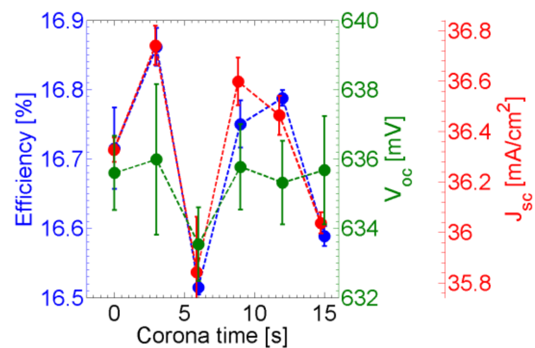

BC47-24D
SiO_2/SiN_x
No front surface field

t_{cor} [s]	η [%]	J_{sc} [mA/cm2]	V_{oc} [mV]
0	16.04	34.31	634.07
6	15.88	33.84	628.32

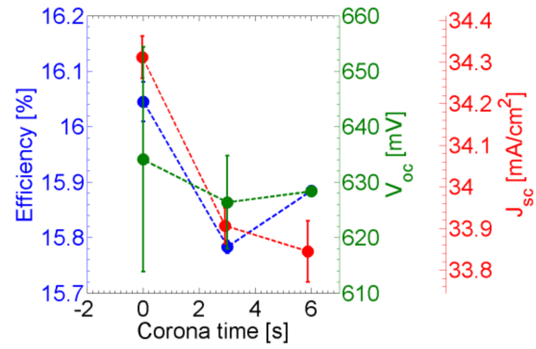

BC47_24G
SiO_2/SiN_x
No front surface field

t_{cor} [s]	η [%]	J_{sc} [mA/cm2]	V_{oc} [mV]
0	13.87	34.87	633.67
6	13.79	34.87	633.36

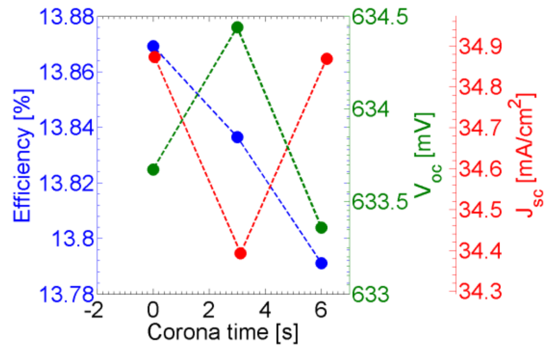

BC47-25C
SiO_2/SiN_x
No front surface field

t_{cor} [s]	η [%]	J_{sc} [mA/cm2]	V_{oc} [mV]
0	14.15	36.34	624.97
15	14.47	36.36	627.40

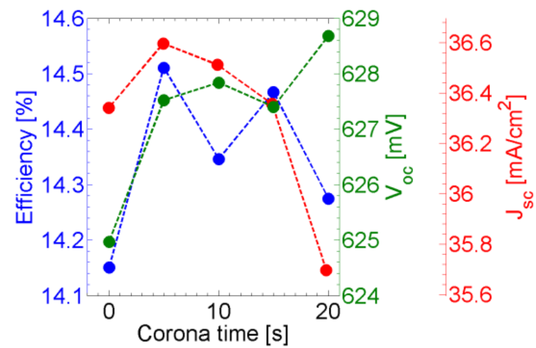

BC47-18A
SiO_2/SiN_x
Front surface field (148 Ω/sq)

t_{cor} [s]	η [%]	J_{sc} [mA/cm2]	V_{oc} [mV]
0	20.36	38.15	661.59
30	20.50	38.28	663.25

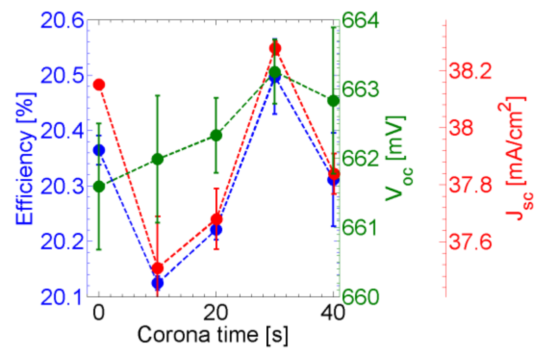

BC47-17G

SiO_2/SiN_x

Front surface field (148 Ω/sq)

t_{cor} [s]	η [%]	J_{sc} [mA/cm$_2$]	V_{oc} [mV]
0	20.24	38.63	660.77
30	20.29	38.80	660.88

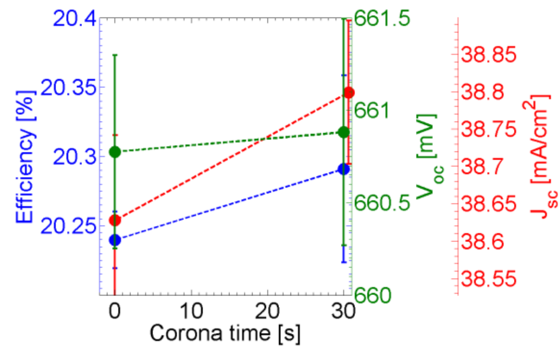

Theta07_17E

SiO_2/SiN_x

Front surface field (148 Ω/sq)

t_{cor} [s]	η [%]	J_{sc} [mA/cm$_2$]	V_{oc} [mV]
0	17.85	38.43	628.03
5	17.92	38.36	642.43

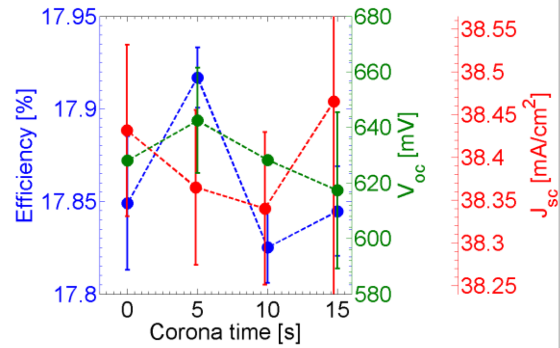

Theta07_17F

SiO_2/SiN_x

Front surface field (148 Ω/sq)

t_{cor} [s]	η [%]	J_{sc} [mA/cm$_2$]	V_{oc} [mV]
0	17.64	37.67	625.00
9	17.98	38.22	627.01

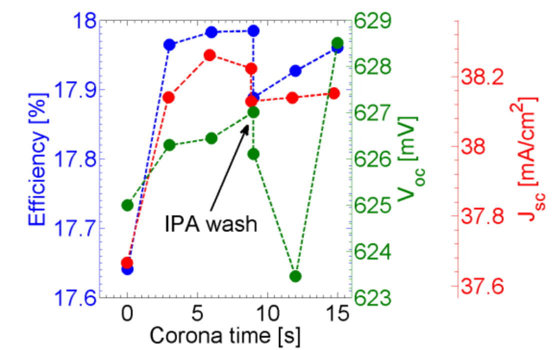

Theta07-17G

SiO_2/SiN_x

Front surface field (148 Ω/sq)

t_{cor} [s]	η [%]	J_{sc} [mA/cm$_2$]	V_{oc} [mV]
0	18.02	38.28	646.78
40	18.11	38.30	628.90

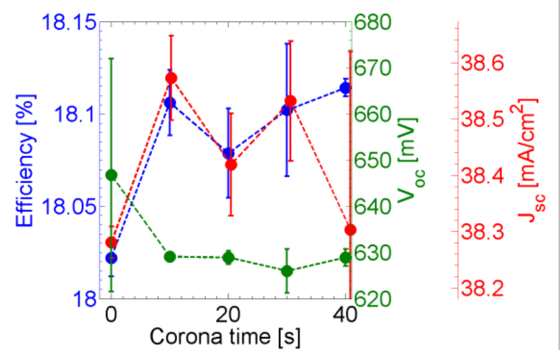

Theta07_18G
SiO_2/SiN_x
Front surface field (148 Ω/sq)

t_{cor} [s]	η [%]	J_{sc} [mA/cm_2]	V_{oc} [mV]
0	17.74	38.28	624.29
10	17.84	38.47	625.56

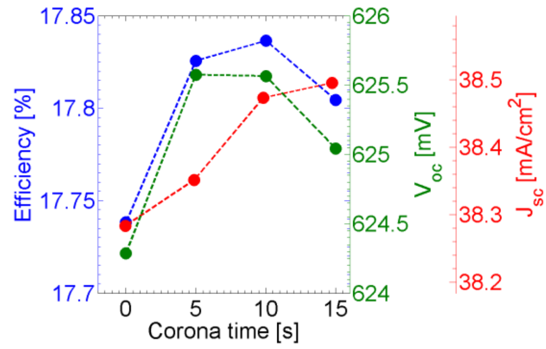

Theta07-18E
SiO_2/SiN_x
Front surface field (148 Ω/sq)

t_{cor} [s]	η [%]	J_{sc} [mA/cm_2]	V_{oc} [mV]
0	17.73	38.33	628.41
21	17.80	38.40	628.65

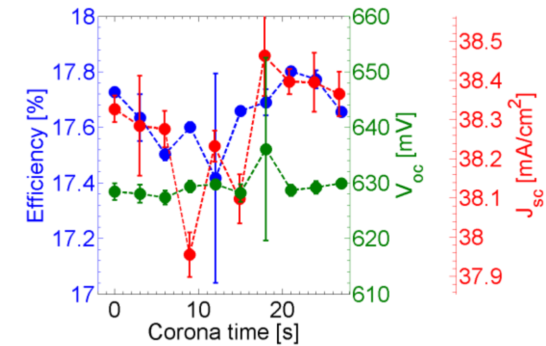

Theta07-18F
SiO_2/SiN_x
Front surface field (148 Ω/sq)

t_{cor} [s]	η [%]	J_{sc} [mA/cm_2]	V_{oc} [mV]
0	17.96	38.24	631.57
10	17.98	38.37	630.43

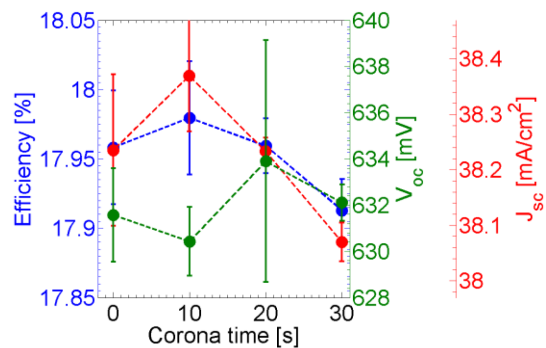

Table 8. Summary of performance improvements in IBC cells deposited with positive corona charge.

6.3.3 Discussion and summary

Research scale IBC cells have been characterised as a function of improved FEP produced using corona charge. On average, four IBC solar cells lacking a FSF were seen to have an absolute improvement in efficiency of 0.3% $\pm$0.3, while eight IBC cells with a FSF improved by 0.13% $\pm$0.12. This indicates that the improvements achieved varied widely, yet extrinsic FEP produces a higher improvement in efficiency for cells that do not have a FSF, as predicted from simulations. It is therefore clear that improvements in cell performance are still to be achieved by further optimising surface passivation, even in state-of-the-art high efficiency IBC solar cells as those produced at Fraunhofer ISE. A small improvement in J_{sc}

was also recorded while V_{oc} remained largely independent of the deposited charge. This agreed qualitatively with the simulation results.

Current commercial solar cells include an antireflection/passivation film with a trade-off of chemical, field effect and optical properties. The idea of independently optimising each of these properties was introduced in this project. This experimental assessment of cell performance as a function of front FEP indicates the potential advantage provided by extrinsically and independently improving front surface passivation via dielectric charge. This provides a small but worthwhile increase in solar power generation by improving a single feature of the cell production process. However, the main benefit of replacing the FSF used in present IBC cells with extrinsic FEP may well not be the increase in efficiency but rather the significant reduction in price that would ensue. The process of applying charge during in-line processing to an oxide dielectric (including its introduction by drift of charged ions) is much simpler and cheaper than the processes required to produce a FSF. Presently IBC cells are the market leader in terms of efficiency but their commercial deployment has been limited due to their price. It is hoped that if similar efficiency IBC cells can be produced using the cheap extrinsic FEP process that their deployment will become much more common. This would represent a significant improvement in average PV cell efficiency since the present day dominant technology of front contact cells with typical efficiencies of order 18% would be replaced by IBC cells with typical efficiencies of 24%. This ~30% relative improvement in efficiency would be highly significant.

6.4 Chapter summary

Commercial solar cells at present are nearly all a front contact variation of the PERL geometry. However, it is widely known that rear contact cells, which do not suffer from the shadowing of the electrical contacts and associated resistive losses when such contacts are necessarily made very narrow, can perform more efficiently than their counter parts [70]. In

these cells charge carriers are photo-generated near the front and must diffuse to the rear contact without recombining. Surface recombination thus remains a critical factor and it is increasingly stressed throughout photovoltaics research and the industry. Back-contacted research-level solar cells with efficiencies of 25.6% have now been reported, with surface passivation being a major factor in this improvement [209]. Optimal passivation in such cells, however, has been achieved using sophisticated and expensive passivation methods difficult to scale to mass production, including ALD AlO_x and FSF. In this project it is proposed that cost effective passivation techniques can be implemented by extrinsically treating dielectric films to independently enhance the chemical and field effect components of passivation. In previous chapters, extrinsic FEP has been shown to be effective and, to a large extent, stable. The effect of FEP in device operation has been directly quantified by the simulation of one and two dimensional solar cells. Front and back contact geometries were tested and in both cases substantial improvements in performance were evident.

The potential increase in cell V_{oc}, J_{sc} and η has been assessed here by means of simulation and experimental tests of n-type IBC cells. A relative increase in η and J_{sc} was simulated and observed when charging the cell front surface. This demonstrates that cell performance is highly dependent on front surface passivation. The latter must be effectively optimised to achieve maximum cell performance and this is rarely the case in finished state-of-the-art solar cells. Extrinsic passivation of silicon solar cells has never been thought to be practical due to its lack of stability. However, the work presented here has demonstrated a leap in improving charge stability on surface dielectrics such that external optimisation of passivation characteristics is now a possibility. This chapter has elucidated how important such improvement may be and it is concluded here that the performance obtained when extrinsically improving FEP is extremely promising.

CHAPTER 7
SUMMARY AND FURTHER WORK

7.1 The importance of field effect passivation in solar cells

Photovoltaic conversion of solar to electrical energy is a key technology to provide the world with renewable, inexpensive and reliable electricity. Efficiency in silicon solar cells is limited by the unwanted recombination of photo-excited electron-hole pairs at crystallographic defects, including surfaces and interfaces. The reduction of such recombination at surfaces and interfaces is a key factor in achieving high efficiency cells. Current silicon solar cells are nearly all "front contact" cells in which metallic contacts are formed on the solar facing surface. However, it is widely believed that next generation cells will be rear contact cells which do not suffer from the shadowing of the electrical contacts and the associated resistive losses when such contacts are necessarily made narrow. Rear contact cells can perform 4% absolute (20% relative) more efficiently [70] but charge carriers photo-generated near the front must diffuse to the rear contact without recombining. Consequently, the recombination rates at the front surface and in the bulk are factors especially critical to their efficiency. Recombination in the bulk is mainly caused by impurities and defects in the crystal. New processing technologies and the trend for thinner cells has reduced the importance of bulk recombination. Surface recombination on the other hand remains a critical factor in rear contact solar cells –good surface passivation is much more important for next generation back contact cells compared to conventional cells.

Currently, industrial solar cells are passivated with a single or double layered dielectric coating that provides both chemical and field-effect passivation simultaneously. In addition, when used on the cell's front surface, the film thickness and chemistry is adjusted to tune its optical properties, but industrially deposited films cannot optimise all three. This work demonstrated that extrinsic passivation, obtained *after* film deposition, allows more flexibility in the combined optimisation of the optical properties and the chemical and field effect passivation properties of dielectric films on semiconductors. Moreover, an increase in cell V_{oc}, J_{sc} and η has been observed in simulations and experimental cell testing when extrinsic FEP, using corona charge, is added to the front surface of IBC solar cells. Although extrinsic passivation of silicon solar cells has been regarded impractical, due to its lack of stability, the work presented here demonstrated that a significant increase in performance can be obtained when extrinsically improving FEP. Enhanced, stable and extrinsic FEP is therefore an extremely promising method to passivate solar cells.

7.2 Modelling SRV as a function of dielectric charge and minority carrier injection

The Shockley-Read-Hall extended formalism has been used with a new parametrisation of interface charge, and electron and hole recombination velocities. This approach allowed the most accurate description to date of surface recombination for a range of dielectric charge and minority carrier concentrations. It also showed that recombination at the silicon surface can be modelled without the need for a term accounting for SCR or SDR recombination. The use of such a term has been demonstrated to be unrealistic unless a high defect density is present near the surface, for which there are neither physical grounds nor experimental evidence, at least in the case of an oxide/silicon interface.

An experimental methodology has been proposed in order to characterise surface recombination as a function of dielectric charge and minority carrier concentration. This

allowed studying SRV for a wide range of both variables and without the effects of dielectric charge non-uniformities. The combination of the experimental and modelling methodologies provided values for interface trap density, and surface recombination for holes and electrons at the FZ-Si/SiO_2 interface. For this system it was concluded that the electron recombination velocity, and hence the capture cross section, is higher than for holes, but to a lesser extent compared to that previously suggested in the literature [138]. Additionally, it was concluded that the density of interface states increases significantly towards the band edges. This increase is higher than that reported before. Such 'tail' states result in a substantial concentration of charge trapped at interface states, rather than in the silicon near surface region, as would be desired.

7.3 Extrinsic Field effect passivation using corona charge

In this work it was demonstrated that deposition of charge onto the surface of a dielectric using corona discharge produced excellent extrinsic FEP, which greatly improved the overall passivation quality of the film. Extremely low surface recombination was obtained by independently combining the best chemical and field effect passivation components of dielectric films, both of intrinsic and extrinsic nature. An outstanding SRV of 0.15 cm/s has been demonstrated on 1Ωcm n-Si using an oxide/nitride passivation layer, with extrinsic FEP providing a significant part of the passivation ability of this film. Additionally, the lowest SRV for a single oxide layer on ~1 Ωcm n-type silicon has also been reported here, SRV < 1.5 cm/s. In brief, world record passivation quality was demonstrated on double layer dielectric and single layer films. This highlights the strong potential of extrinsic enhancement of FEP to significantly improve solar cell efficiency [221]. Extrinsic field-effect passivation by additional deposition of charge, however, has never been used at a practical level. The

lack of stability of corona charge deposited on dielectric films has been the overriding issue preventing the adoption of this concept in real device manufacturing [123].

Here, it was further shown that the passivation obtained from corona charge could be effectively stabilised on singe SiO_2 and double SiO_2/SiN_x dielectric layers. When the charge resided at the dielectric surface, good stability was achieved by dehydrating and chemical protecting the surface of the dielectrics to eliminate lateral conduction produced by water absorption. A decay time constant of effective lifetime of 3,000 days was estimated in a corona charge oxide film, grown on 1 Ωcm n-type silicon, FGA, and HMDS chemically treated. Similarly a decay time constant of 1,200 days was inferred for an oxide/nitride film similarly processed. In addition, a post-charge deposition heat treatment at 400 ^{o}C was shown to rapidly drive charge into the dielectric layers. An astounding decay time constant of 10,000 days was inferred for the passivation quality of an oxide film grown on textured 1 Ωcm n-type silicon that was submitted to a 400 ^{o}C anneal after corona charging, and no HMDS protection. Despite the fact that this decrease in passivation still exceeds that required for a practical solar cell, these results show substantial progress towards an effective and *stable* method to provide extrinsic FEP.

7.4 Extrinsic Field effect passivation using ionic charge

Corona deposited charge has been seen highly stable on the surface and bulk of dielectric films for periods of over 2 years. However, although this is worth further study, it seems likely that it is not a sufficiently long term or robust solution to be of practical use for solar cells. Instead, new ways have been developed to drive ionic charge into the bulk of a dielectric film at elevated temperature, which is then quenched in on cooling. Ionic charge has been migrated into a silicon dioxide film and observed to be stable for over 700 days with minimal loss in passivation efficiency. The longest effective lifetime decay time

constant obtained in this work was when using extrinsic ionic FEP. An oxide film was deposited with K ionic species, which were then migrated into the film at 500 ^{o}C for 3 minutes. The decay time constant of passivation was ~11,000 days. The passivation quality of a cell using a dielectric film extrinsically passivated with this method would degrade by less than 37% in a period of 30 years. This method is therefore hugely promising for passivation of silicon surfaces in solar cells. SRV in the range 5-10 cm/s have been demonstrated for extrinsic ionic FEP oxides on FZ n-Si. This is a moderately good quality of passivation but it can still be improved further. Overall, this new method represents a major advancement in controlled and stable FEP, and it presents huge potential for passivation of silicon surfaces in solar cells.

7.5 Further work

This thesis has reported a new parametrisation that allows an accurate description of SRV as a function of dielectric charge and injection level. In conducting this work it was noted that additional effects and systems could be studied in more detail as follows:

- The specimens used in this thesis were 3 x 3 cm^2 cleaved pieces. The sensor coil in the lifetime instrument is 2 cm wide, yet it appears that the photo-conductance signal detects a region 3 cm in diameter. Effective lifetimes as high as those reported in this thesis result in diffusion lengths of several millimetres. This indicates that a significant concentration of carriers is flowing towards the sample edges (SRV ~10^3 cm/s) and this may be affecting the measurement when lifetimes over 5 ms are observed.
- The saturation of effective lifetime (SRV) for sufficiently high dielectric charge concentrations has not been studied in detail. When excessive charge is deposited on the dielectric films, the compensating charge in the semiconductor is expected to saturate as the intrinsic energy approaches one of the bands, and these are hence

pinned. In this regime Fermi-Dirac statistics must be used and the SRH formalism modified.

- The experimental and modelling methodologies developed have been mainly applied to the oxide/silicon system, and have provided meaningful and accurate fits. However, other dielectric/silicon systems must be studied as well to confirm the versatility of the proposed parametrisation. This includes dielectrics relevant to solar cells such as silicon nitride, aluminium oxide, and amorphous silicon.

It has also been shown that corona charge can be stabilized over a time-scale of years using a method to chemically seal the dielectric surface against water absorption, or using a migration process at high temperature to embed the charge inside the dielectric. These methods have shown promise yet a number of points remain unclear and should be explored further:

- When corona charge is deposited, it was shown that the charge lies at the surface of the dielectric. However, the exact nature, trapping energy and interaction dynamics of the deposited corona charge are still not fully understood.
- If the corona charge decay mechanism is purely related to lateral conductivity of the dielectric, a thin HMDS barrier at the edge of the specimens could fully prevent charge from reaching the edge of the dielectric, and annihilating with charge carriers in silicon.
- In such case it is also important to evaluate the stability and robustness of a HMDS film, or even a different hydrophobic sealant that is compatible with semiconductor processing technology.
- When corona charged specimens are annealed, or the corona charge deposition is conducted at high temperatures to migrate charge into the film, the nature of the moving charge, its dynamic behaviour, and its effect in the different components of passivation are unknown.

- When charge is migrated into the film, it has been observed to move rapidly to the dielectric/silicon interface, and cause damage to the passivation. Can such chemical damage be prevented or recovered? Perhaps by avoiding the corona charge reaching the interface.
- A long-term decay in passivation was observed and it did not correspond to a loss in dielectric charge. This appears to be a loss in the chemical passivation but a definite mechanism is still not clear.
- When the surface of silicon has been textured, notable stability of corona extrinsic FEP was observed despite the lack of HMDS. The influence of texturing in the passivation stability has not been studied in detail here, yet this is of great importance since all solar cells present this surface texturing.

Effective and stable passivation was also shown here using ionic species. Initial results seem to indicate that this trapped charge will last indefinitely, but this has yet to be proved. The science underpinning this process should be examined in more detail, including the relevance to manufacture of solar cells. The following aspects should be considered:

- The mechanism by which the charge is captured at the film surface is not fully understood and as yet only a fraction of the charge deposited on the surface of the dielectric is subsequently quenched into the bulk of the film.
- The mechanism of separation of anions and cations at the dielectric surface is not clear, and can be affected by the presence of other gas species, for example oxygen.
- Initial results indicate that, with the application of an electric field using corona, sufficient ionic charge can be drifted into the dielectric at 400 ^{o}C in just a few minutes. This process is still lengthy compared to time for industrial passivation of cells (< 1min).
- This work indicates that other ionic species, not only alkali but also alkaline and perhaps some other metals, have the potential to be fixed into a dielectric matrix and

provide effective and durable FEP. Potential ionic metals include but are not limited to Mg, Ca, Sr, Ba, Rb, Cs, Al, Cu, Au.

- During ionic migration a concentration of charge is created in the semiconductor to compensate the field effect of the ions. The influence that such compensation charge has in the transport dynamics of ionic species is uncertain.
- Ionic charge is seen to create defect states when it reaches the dielectric/silicon interface. New methods by which the location and magnitude of charge can be tailored to produce optimum passivation should be investigated.
- It appears that ionic charge migrates preferentially to interfaces. It is hence proposed that a bi- or tri-layer can provide the intermediate interface required for ions, such that they do not reach the silicon surface. An oxide/nitride film was not explored for this purpose since nitride films are well known to prevent diffusion of alkali contamination. However, in presence of a third layer, ions can sit at the interface between the outer two dielectrics. This possibility is worth further study.
- These methods have also showed possible the use of lower cost dielectric films with relatively poor chemical passivation, in combination with a strong extrinsic FEP component. An additional topic of further work is the passivation characteristics of different cheaper dielectrics that could be deployed into solar cells. A study of a broader set of metal ionic species on a dielectric/silicon system is also possible, including other dielectrics like Si_3N_4 and Al_2O_3.

These methods should be brought into practice in real solar cells. For this, it is important to investigate further the effects of passivation in cell performance. This includes, for example:

- A more rigorous assessment of the effect of surface recombination via computer modelling and cell design.

- Custom designed research-scale cells including tailored passivation schemes in which FEP can be exploited.
- Direct use of extrinsic FEP in the manufacture of solar cells.
- Evaluation of performance over time and under aging conditions.

Finally, it is important to note that the presented methods are susceptible to environmental factors, such as elevated temperature, and UV radiation. Preliminary research shows that the level of ultraviolet radiation is a key limitation to most passivation solutions and it should therefore be considered when attempting to apply methods to the commercial use of devices [190]. Successfully developed extrinsic FEP methods must be tested under severe conditions. This will allow an assessment of the influence of the device working conditions on the proposed solutions.

References

[1] *Climate Change Indicators in the United States*. Washington: United States Environmental Protection Agency, 2012.

[2] *Climate Change 2013 The Physical Science Basis*. New York: Intergovernmental Panel on Climate Change - Cambridge University Press, 2013.

[3] A. J. McMichael, R. E. Woodruff, and S. Hales, "Climate change and human health: present and future risks.," *Lancet*, vol. 367, no. 9513, pp. 859–69, Mar. 2006.

[4] Department for Environment Food and Rural Affairs, "Adapting to climate change, UK Climate Projections," London, 2009.

[5] *Key World Energy Statistics*. Paris: International Energy Agency (IEA), 2013.

[6] *International Energy Outlook*. Washington: U.S. Energy Information Administration, 2013.

[7] *World Energy Outlook*. London: International Energy Agency, 2013.

[8] C. Kaminker, O. Kawanishi, F. Stewart, B. Caldecott, and N. Howarth, "Institutional Investors and Green Infrastructure Investments," *Work. Pap. Financ. Insur. Priv. Pensions - OECD Publ.*, no. 35, 2013.

[9] *Set for 2020*. Brussels: European Photovoltaic Industry Association, 2012.

[10] *Renewables 2013 Global Status Report*. Paris: REN21, 2013.

[11] *RE-Think 2050 - A 100% Renewable energy vision for the European Union*. European Renewable Energy council, 2010.

[12] International Energy Agency, "Technology Roadmap: Solar Photovoltaic Energy - 2014 edition," Paris, France, 2014.

[13] G. Masson, M. Latour, M. Rekinger, I.-T. Theologitis, and M. Papoutsi, *Global Market Outlook for Photovoltaics 2013-2017*. European Photovoltaic Industry Association, 2013.

[14] SunPower, "SunPower Solar Panels," *E20 Series*, 2012. [Online]. Available: http://global.sunpowercorp.com/products/solar-panels/.

[15] A. Luque and S. Hegedus, Eds., *Handbook of Photovoltaic Science and Engineering*. Wiley, 2003.

[16] D. M. Chapin, C. S. Fuller, and G. L. Pearson, “A New Silicon P-N Junction Photocell for Converting Solar Radiation into Electrical Power,” *J. Appl. Phys.*, vol. 25, no. 5, pp. 676–677, 1954.

[17] W. Shockley, “The Theory of P-N Junctions in Semiconductors and P-N Junction Transistors,” *Bell Syst. Tech. J.*, vol. 28, no. 3, pp. 435–489, 1949.

[18] J. L. Moll, “The Evolution of the Theory for the Voltage-Current Characteristic of P-N Junctions,” *Proc. Inst. Radio Eng.*, vol. 46, no. 6, pp. 1076–1082, 1958.

[19] C. T. Sah, R. N. Noyce, and W. Shockley, “Carrier Generation and Recombination in P-N Junctions and P-N Junction Characteristics,” *Proc. Inst. Radio Eng.*, vol. 45, no. 9, pp. 1228–1243, 1957.

[20] S. Sze and N. Kwok Kwok, *Physics of Semiconductor Devices*, Third Edit. John Wiley and Sons, Inc, 2007.

[21] S. Rein, *Lifetime Spectroscopy: A Method of Defect Characterization in Silicon for Photovoltaic Applications*. Springer, 2005.

[22] W. Shockley and W. T. Read, “Statistics of the Recombinations of Holes and Electrons,” *Phys. Rev.*, vol. 87, no. 5, pp. 835–842, 1952.

[23] W. Gerlach, H. Schlangenotto, and H. Maeder, “On the radiative recombination rate in silicon,” *Phys. Status Solidi*, vol. 13, no. 1, pp. 277–283, Sep. 1972.

[24] J. Dziewior and W. Schmid, “Auger coefficients for highly doped and highly excited silicon,” *Appl. Phys. Lett.*, vol. 31, no. 5, p. 346, Sep. 1977.

[25] A. Hangleiter and R. Häcker, “Enhancement of band-to-band Auger recombination by electron-hole correlations,” *Phys. Rev. Lett.*, vol. 65, no. 2, pp. 215–218, Jul. 1990.

[26] S. W. Glunz, D. Biro, S. Rein, and W. Warta, “Field-effect passivation of the SiO2 Si interface,” *J. Appl. Phys.*, vol. 86, no. 1, pp. 683–691, 1999.

[27] P. P. Altermatt, J. Schmidt, G. Heiser, and A. G. Aberle, “Assessment and parameterisation of Coulomb-enhanced Auger recombination coefficients in lowly injected crystalline silicon,” *J. Appl. Phys.*, vol. 82, no. 10, p. 4938, Nov. 1997.

[28] A. Richter, S. W. Glunz, F. Werner, J. Schmidt, and A. Cuevas, “Improved quantitative description of Auger recombination in crystalline silicon,” *Phys. Rev. B*, vol. 86, no. 16, p. 165202, Oct. 2012.

[29] R. N. Hall, “Electron-Hole Recombination in Germanium,” *Phys. Rev.*, vol. 87, no. 2, p. 387, 1952.

[30] A. G. Aberle, “Surface passivation of crystalline silicon solar cells: A review,” *Prog. Photovoltaics*, vol. 8, no. 5, pp. 473–487, 2000.

[31] King, R. R., Sinton, R. A., Swanson, R. M., and Ciszek, T. F., “Low surface recombination velocities on doped silicon and their implications for point contact solar cells,” *IEEE Photovolt. Spec. Conf.*, pp. 1168–1173, 1987.

[32] J. Schmidt and A. G. Aberle, “Carrier recombination at silicon-silicon nitride interfaces fabricated by plasma-enhanced chemical vapor deposition,” *J. Appl. Phys.*, vol. 85, no. 7, pp. 3626–3633, 1999.

[33] A. G. Aberle, “Overview on SiN surface passivation of crystalline silicon solar cells,” *Sol. Energy Mater. Sol. Cells*, vol. 65, no. 1–4, pp. 239–248, 2001.

[34] W. Soppe, H. Rieffe, and A. Weeber, “Bulk and surface passivation of silicon solar cells accomplished by silicon nitride deposited on industrial scale by microwave PECVD,” *Prog. Photovoltaics*, vol. 13, no. 7, pp. 551–569, 2005.

[35] M. J. Kerr and A. Cuevas, “Very low bulk and surface recombination in oxidized silicon wafers,” *Semicond. Sci. Technol.*, vol. 17, no. 1, pp. 35–38, Jan. 2002.

[36] M. J. Kerr, J. Schmidt, A. Cuevas, and J. H. Bultman, “Surface recombination velocity of phosphorus-diffused silicon solar cell emitters passivated with plasma enhanced chemical vapor deposited silicon nitride and thermal silicon oxide,” *J. Appl. Phys.*, vol. 89, no. 7, pp. 3821–3826, 2001.

[37] A. Das, R. Kyungsun, and A. Rohatgi, “20% Efficient Screen-Printed n-Type Solar Cells Using a Spin-On Source and Thermal Oxide/Silicon Nitride Passivation,” *IEEE J. Photovoltaics*, vol. 1, no. 2, 2011.

[38] S. Mack, A. Wolf, C. Brosinsky, S. Schmeisser, A. Kimmerle, P. Saint-Cast, M. Hofmann, and D. Biro, “Silicon surface passivation by thin thermal Oxide/PECVD layer stack systems,” *IEEE J. Photovoltaics*, vol. 1, no. 2, 2011.

[39] Y. Larionova, V. Mertens, N.-P. Harder, and R. Brendel, “Surface passivation of n-type Czochralski silicon substrates by thermal-SiO2/plasma-enhanced chemical vapor deposition SiN stacks,” *Appl. Phys. Lett.*, vol. 96, no. 3, p. 032105, Jan. 2010.

[40] B. Hoex, S. B. S. Heil, E. Langereis, M. C. M. van de Sanden, and W. M. M. Kessels, “Ultralow surface recombination of c-Si substrates passivated by plasma-assisted atomic layer deposited Al2O3,” *Appl. Phys. Lett.*, vol. 89, no. 4, 2006.

[41] G. Agostinelli, A. Delabie, P. Vitanov, Z. Alexieva, H. F. W. Dekkers, S. De Wolf, and G. Beaucarne, “Very low surface recombination velocities on p-type silicon wafers passivated with a dielectric with fixed negative charge,” *Sol. Energy Mater. Sol. Cells*, vol. 90, no. 18–19, pp. 3438–3443, 2006.

[42] G. Dingemans, N. M. Terlinden, M. A. Verheijen, M. C. M. van de Sanden, and W. M. M. Kessels, “Controlling the fixed charge and passivation properties of Si(100)/Al(2)O(3) interfaces using ultrathin SiO(2) interlayers synthesized by atomic layer deposition,” *J. Appl. Phys.*, vol. 110, no. 9, 2011.

[43] E. Cornagliotti, A. Sharma, L. Tous, L. Black, A. Uruena De Castro, M. Aleman, F. Duerinckx, R. Russell, P. Choulat, J. John, B. Dielissen, R. Gortzen, and J. Szlufcik,

"Large area n-type c-Si solar cells featuring rear emitter and efficiency beyond 21%," in *6th World Conference on Photovoltaic Energy Conversion*, 2014, p. na.

[44] H. Heezen, R. Görtzen, F. Souren, X. Gay, I. Melnyk, S. Yang, X. Qu, X. Mao, H. Kühnlein, H. Nussbaumer, A. Heeren, S. Queisser, A. Pediaditakis, S. Patzig-Klein, B.-U. Sander, O. Voigt, R. Sastrawan, J. Horzel, B. Latzel, C. Schmitt, and D. Pysch, "Implementation of an ALD-Al2O3 PERC-Technology into a Multi- and Monocrystalline Industrial Pilot Production," *29th Eur. Photovolt. Sol. Energy Conf. Exhib.*, pp. 612–616, Nov. 2014.

[45] S. Olibet, E. Vallat-Sauvain, C. Ballif, L. Korte, and L. Fesquet, "Silicon Solar Cell Passivation using Heterostructures," 2007.

[46] M. Hofmann, C. Schmidt, N. Kohn, J. Rentsch, S. W. Glunz, and R. Preu, "Stack system of PECVD amorphous silicon and PECVD silicon oxide for silicon solar cell rear side passivation," *Prog. Photovoltaics*, vol. 16, no. 6, pp. 509–518, 2008.

[47] M. Hofmann, S. Janz, C. Schmidt, S. Kambor, D. Suwito, N. Kohn, J. Rentsch, R. Preu, and S. W. Glunz, "Recent developments in rear-surface passivation at Fraunhofer ISE," *Sol. Energy Mater. Sol. Cells*, vol. 93, no. 6–7, pp. 1074–1078, 2009.

[48] J.-W. A. Schuttauf, K. H. M. van der Werf, I. M. Kielen, W. G. J. H. M. van Sark, J. K. Rath, and R. E. I. Schropp, "High quality crystalline silicon surface passivation by combined intrinsic and n-type hydrogenated amorphous silicon," *Appl. Phys. Lett.*, vol. 99, no. 20, 2011.

[49] M. J. Kerr and A. Cuevas, "General parameterization of Auger recombination in crystalline silicon," *J. Appl. Phys.*, vol. 91, no. 4, p. 2473, Feb. 2002.

[50] R. Ferre, A. Orpella, D. Munoz, I. Martín, F. Recart, C. Voz, J. Puigdollers, P. R. i Cabarrocas, and R. Alcubilla, "Very low surface recombination velocity of crystalline silicon passivated by phosphorus-dopeda-SicxNy:H(n) alloys," *Prog. Photovoltaics Res. Appl.*, vol. 16, no. 2, pp. 123–127, Mar. 2008.

[51] M. J. Kerr and A. Cuevas, "Recombination at the interface between silicon and stoichiometric plasma silicon nitride," *Semicond. Sci. Technol.*, vol. 17, no. 2, pp. 166–172, Feb. 2002.

[52] F. Werner, B. Veith, V. Tiba, P. Poodt, F. Roozeboom, R. Brendel, and J. Schmidt, "Very low surface recombination velocities on p- and n-type c-Si by ultrafast spatial atomic layer deposition of aluminum oxide," *Appl. Phys. Lett.*, vol. 97, no. 16, p. 162103, Oct. 2010.

[53] J. Mandelkorn and J. H. Lamneck, "Simplified fabrication of back surface electric field silicon cells and novel characteristics of such cells," *9th Photovolt. Spec. Conf. Palo Alto, CA*, 1972.

[54] J. Mandelkorn, J. H. Lamneck, and L. R. Scudder, "Design, fabrication and characteristics of new types of back surface field cells," *10th Photovolt. Spec. Conf. Palo Alto, CA*, 1973.

[55] S. Kluska, F. Granek, M. Rüdiger, M. Hermle, and S. W. Glunz, "Modeling and optimization study of industrial n-type high-efficiency back-contact back-junction silicon solar cells," *Sol. Energy Mater. Sol. Cells*, vol. 94, no. 3, pp. 568–577, Mar. 2010.

[56] F. Granek, M. Hermle, D. M. Huljić, O. Schultz-Wittmann, and S. W. Glunz, "Enhanced lateral current transport via the front N + diffused layer of n-type high-efficiency back-junction back-contact silicon solar cells," *Prog. Photovoltaics Res. Appl.*, vol. 17, no. 1, pp. 47–56, Jan. 2009.

[57] J. E. Cotter, J. H. Guo, P. J. Cousins, M. D. Abbott, F. W. Chen, and K. C. Fisher, "P-Type Versus n-Type Silicon Wafers: Prospects for High-Efficiency Commercial Silicon Solar Cells," *Electron Devices, IEEE Trans.*, vol. 53, no. 8, pp. 1893–1901, 2006.

[58] J. Schmidt and A. G. Aberle, "Easy-to-use surface passivation technique for bulk carrier lifetime measurements on silicon wafers," *Prog. Photovoltaics*, vol. 6, no. 4, pp. 259–263, 1998.

[59] W. Olthuis and P. Bergveld, "On the charge storage and decay mechanism in silicon dioxide electrets," *IEEE Trans. Electr. Insul.*, vol. 27, no. 4, pp. 691–697, 1992.

[60] L. B. Loeb, *Electrical Coronas, Their Basic Physical Mechanisms*. University of California Press, 1965.

[61] D. K. Schroder, M. S. Fung, R. L. Verkuil, S. Pandey, W. H. Howland, and M. Kleefstra, "CORONA-OXIDE-SEMICONDUCTOR device CHARACTERIZATION," *Solid. State. Electron.*, vol. 42, no. 4, pp. 505–512, Apr. 1998.

[62] T. C. Kho, S. C. Baker-Finch, and K. R. McIntosh, "The study of thermal silicon dioxide electrets formed by corona discharge and rapid-thermal annealing," *J. Appl. Phys.*, vol. 109, no. 5, p. 6, 2011.

[63] H. Amjadi, "Investigations on charge storage and transport in plasma-deposited inorganic electrets," *Dielectr. Electr. Insul. IEEE Trans.*, vol. 6, no. 2, pp. 236–241, Apr. 1999.

[64] H. Amjadi, "The mechanism of voltage decay in corona-charged layers of silicon dioxide during UV irradiation," *Dielectr. Electr. Insul. IEEE Trans.*, vol. 7, no. 2, pp. 222–228, Apr. 2000.

[65] U. Mescheder, B. Müller, S. Baborie, and P. Urbanovic, "Properties of SiO 2 electret films charged by ion implantation for MEMS-based energy harvesting systems," *J. Micromechanics Microengineering*, vol. 19, no. 9, p. 94003, 2009.

[66] P. Molinie, "Measuring and modeling transient insulator response to charging: the contribution of surface potential studies," *Dielectr. Electr. Insul. IEEE Trans.*, vol. 12, no. 5, pp. 939–950, 2005.

[67] J. A. Malecki, "Linear decay of charge in electrets," *Phys. Rev. B*, vol. 59, no. 15, pp. 9954–9960, Apr. 1999.

[68] M. A. Green, “Quo Vadis Silicon Photovoltaics?,” in *26th European Photovoltaic Solar Energy Conference and Exhibition*, 2011.

[69] C. A. Wolden, J. Kurtin, J. B. Baxter, I. Repins, S. E. Shaheen, J. T. Torvik, A. A. Rockett, V. M. Fthenakis, and E. S. Aydil, “Photovoltaic manufacturing: Present status, future prospects, and research needs,” *J. Vac. Sci. Technol. A Vacuum, Surfaces, Film.*, vol. 29, no. 3, pp. 30801–308016, May 2011.

[70] M. Rudiger, H. Steinkemper, M. Hermle, and S. W. Glunz, “Numerical Current Density Loss Analysis of Industrially Relevant Crystalline Silicon Solar Cell Concepts,” *IEEE J. Photovoltaics*, vol. 4, no. 2, pp. 533–539, Mar. 2014.

[71] G. M. Sessler, *Electrets*, Second Enl. Berlin, Germany: Springer, 1987.

[72] L. Kasprzak and A. Hornung, “Polarization and Depolarization in PSG Films,” *IBM J. Res. Dev.*, vol. 19, no. 2, pp. 127–132, Mar. 1975.

[73] B. P. Rai and R. S. Srivastava, “Mobile ion instability in SiO 2 films on silicon,” *Int. J. Electron.*, vol. 46, no. 4, pp. 381–392, Apr. 1979.

[74] Y. T. Yeow, J. W. Clancy, and D. R. Lamb, “The influence of phosphosilicate glass deposition conditions on the surface state charge at the silicon-silicon dioxide interface!,” *Int. J. Electron.*, vol. 34, no. 1, pp. 115–119, Jan. 1973.

[75] M. Goldman, A. Goldman, and R. S. Sigmond, “The corona discharge, its properties and specific uses,” *Pure Appl. Chem.*, vol. 57, no. 9, pp. 1353–1362, 1985.

[76] M. Abdel-Salam, L. Fouad, S. Elhazek, and M. K. Gohar, “Positive corona discharge in a three-electrode system,” *J. Electrostat.*, vol. 24, no. 1, pp. 33–44, 1989.

[77] L. Dascalescu, A. Samuila, D. Rafiroiu, A. Iuga, and R. Morar, “Multiple-needle corona electrodes for electrostatic processes application,” *Ind. Appl. IEEE Trans.*, vol. 35, no. 3, pp. 543–548, 1999.

[78] R. B. Comizzoli, “Uses of Corona Discharges in the Semiconductor Industry,” *J. Electrochem. Soc.*, vol. 134, no. 2, p. 424, Feb. 1987.

[79] J. Hong, J. Chen, X. Li, and A. Ye, “Effects of the Bias-Controlled Grid on Performances of the Corona Poling System for Electro-Optic Polymers,” *Int. J. Mod. Phys. B*, vol. 19, pp. 2205–2211, 2005.

[80] M. M. Shahin, “Mass-Spectrometric Studies of Corona Discharges in Air at Atmospheric Pressures,” *J. Chem. Phys.*, vol. 45, no. 7, p. 2600, Oct. 1966.

[81] *Diffusion in Solids*, vol. 155. Berlin, Heidelberg: Springer Berlin Heidelberg, 2007.

[82] P. Padma Kumar and S. Yashonath, “Ionic conduction in the solid state.” Indian Academy Sciences, 28-Jan-2006.

[83] A. J. Moulson and J. M. Herbert, *Electroceramics: Materials, Properties, Applications*, Second Edi. John Wiley & Sons, Ltd, 2003.

[84] G M Taylor, “Electrostatic bonding - applications and principles,” *Weld. Inst. Res. Bull.*, pp. 55–58, 1983.

[85] G. White, A. Newsam, and G. Taylor, “Electrostatic bonding for electronic applications,” *Weld. Inst. Res. Bull.*, pp. 129–133, 1985.

[86] P. Nitzsche, “Ion Drift Processes in Pyrex-Type Alkali-Borosilicate Glass during Anodic Bonding,” *J. Electrochem. Soc.*, vol. 145, no. 5, p. 1755, May 1998.

[87] C. D. Tudryn, “Characterization of anodic bonding,” Massachusetts Institute of Technology, 2004.

[88] G. Wallis, “Field Assisted Glass-Metal Sealing,” *J. Appl. Phys.*, vol. 40, no. 10, p. 3946, Sep. 1969.

[89] K. B. Albaugh, P. E. Cade, and D. H. Rasmussen, “Mechanisms of anodic bonding of silicon to pyrex glass,” in *IEEE Technical Digest on Solid-State Sensor and Actuator Workshop*, pp. 109–110.

[90] T. M. . Lee, D. H. . Lee, C. Y. . Liaw, A. I. . Lao, and I.-M. Hsing, “Detailed characterization of anodic bonding process between glass and thin-film coated silicon substrates,” *Sensors Actuators A Phys.*, vol. 86, no. 1–2, pp. 103–107, Oct. 2000.

[91] E. Cattaruzza, F. Gonella, S. Ali, C. Sada, and A. Quaranta, “Silver and gold doping of SiO2 glass by solid-state field-assisted diffusion,” *J. Non. Cryst. Solids*, vol. 355, no. 18–21, pp. 1136–1139, Jul. 2009.

[92] M. Yamin, “Charge-storage effects in silicon dioxide films,” *IEEE Trans. Electron Devices*, vol. 11, no. 11, pp. 531–532, Nov. 1964.

[93] M. Yamin, “Charge storage effects in silicon dioxide films,” *IEEE Trans. Electron Devices*, vol. 12, no. 3, pp. 88–96, Mar. 1965.

[94] M. Yamin, “Observations on phosphorus stabilized SiO2 films,” *IEEE Trans. Electron Devices*, vol. 13, no. 2, pp. 256–259, Feb. 1966.

[95] D. R. Kerr, J. S. Logan, P. J. Burkhardt, and W. A. Pliskin, “Stabilization of SiO2 Passivation Layers with P2O5,” *IBM J. Res. Dev.*, vol. 8, no. 4, pp. 376–384, Sep. 1964.

[96] D. R. Kerr, “Effect of Temperature and Bias on Glass-Silicon Interfaces,” *IBM J. Res. Dev.*, vol. 8, no. 4, pp. 385–393, Sep. 1964.

[97] P. Balk and J. M. Eldridge, “Phosphosilicate glass stabilization of FET devices,” *Proc. IEEE*, vol. 57, no. 9, pp. 1558–1563, 1969.

[98] E. H. Snow, A. S. Grove, B. E. Deal, and C. T. Sah, “Ion Transport Phenomena in Insulating Films,” *J. Appl. Phys.*, vol. 36, no. 5, pp. 1664–1673, 1965.

[99] E. H. Snow and B. E. Deal, “Polarization Phenomena and Other Properties of Phosphosilicate Glass Films on Silicon,” *J. Electrochem. Soc.*, vol. 113, no. 3, p. 263, Mar. 1966.

[100] E. Yon, W. H. Ko, and A. B. Kuper, "Sodium distribution in thermal oxide on silicon by radiochemical and MOS analysis," *IEEE Trans. Electron Devices*, vol. 13, no. 2, pp. 276–280, Feb. 1966.

[101] S. Krivec, M. Buchmayr, T. Detzel, T. Froemling, J. Fleig, and H. Hutter, "The effect of bias-temperature stress on Na+ incorporation into thin insulating films.," *Anal. Bioanal. Chem.*, vol. 400, no. 3, pp. 649–57, May 2011.

[102] H. Amjadi and C. Thielemann, "Silicon-based inorganic electrets for application in micromachined devices," *IEEE Trans. Dielectr. Electr. Insul.*, vol. 3, no. 4, pp. 494–498, 1996.

[103] A. E. Guile, "Stored charges in relatively thin oxide films," *J. Phys. D. Appl. Phys.*, vol. 5, no. 6, pp. 1153–1156, Jun. 1972.

[104] S. Fujita, K. Shinyama, and M. Baba, "Dielectric properties of electron beam irradiated PEEK," in *10th International Symposium on Electrets (ISE 10). Proceedings (Cat. No.99 CH36256)*, pp. 115–118.

[105] D. Hohm, "Silicon-dioxide electret transducer," *J. Acoust. Soc. Am.*, vol. 75, no. 4, p. 1297, Apr. 1984.

[106] J. Zhang, X. Zou, and Y. Zhang, "Improvement of the performance of the PECVD SiO_2/Si_3N_4 double-layer electrets," *IEEE Trans. Dielectr. Electr. Insul.*, vol. 18, no. 2, pp. 456–462, Apr. 2011.

[107] P. Gunther, "Charging, long-term stability, and TSD measurements of SiO/sub 2/ electrets," *IEEE Trans. Electr. Insul.*, vol. 24, no. 3, pp. 439–442, Jun. 1989.

[108] P. Gunther and Z. Xia, "Transport of detrapped charges in thermally wet grown SiO2 electrets," *J. Appl. Phys.*, vol. 74, no. 12, pp. 7269–7274, 1993.

[109] Y. Fei, Z. Xu, and C. Chen, "Charge storage stability of SiO/sub 2/ film electret," in *Proceedings. IEEE SoutheastCon 2001 (Cat. No.01CH37208)*, pp. 1–7.

[110] L. Huamao, X. Zhongfu, S. Shaoqun, Z. Hongyan, C. Yang, and Z. Jianwei, "The charge dynamics of thermally wet grown SiO/sub 2/ electret by corona charging method with constant grid current," in *9th International Symposium on Electrets (ISE 9) Proceedings*, pp. 133–138.

[111] Nung-Pyo Hong,Jin-Woong Hong, "Charge storage characteristics of SiO/sub 2//Si/sub 3/N/sub 4/ double layer electret," in *Proceedings of the 2004 IEEE International Conference on Solid Dielectrics, 2004. ICSD 2004.*, 2004, pp. 170–173.

[112] H. Amjadi, "Charge storage in double layers of thermally grown silicon dioxide and APCVD silicon nitride," *IEEE Trans. Dielectr. Electr. Insul.*, vol. 6, no. 6, pp. 852–857, 1999.

[113] V. Leonov, P. Fiorini, and C. Van Hoof, "Stabilization of positive charge in SiO/sub 2//Si/sub 3/N/sub 4/ electrets," *Dielectr. Electr. Insul. IEEE Trans.*, vol. 13, no. 5, pp. 1049–1056, 2006.

[114] Z. Chen, Z. Lv, and J. Zhang, "PECVD SiO_2/Si_3N_4 double layers electrets on glass substrate," *IEEE Trans. Dielectr. Electr. Insul.*, vol. 15, no. 4, pp. 915–919, Aug. 2008.

[115] X. Zou and J. Zhang, "Study on PECVD SiO2/Si3N4 double-layer electrets with different thicknesses," *Sci. China Technol. Sci.*, vol. 54, no. 8, pp. 2123–2129, May 2011.

[116] J. Seiffe, L. Gautero, M. Hofmann, J. Rentsch, R. Preu, S. Weber, and R. A. Eichel, "Surface passivation of crystalline silicon by plasma-enhanced chemical vapor deposition double layers of silicon-rich silicon oxynitride and silicon nitride," *J. Appl. Phys.*, vol. 109, no. 3, p. 034105, Feb. 2011.

[117] J. Y. Lee and S. W. Glunz, "Investigation of various surface passivation schemes for silicon solar cells," *Sol. Energy Mater. Sol. Cells*, vol. 90, no. 1, pp. 82–92, Jan. 2006.

[118] E. Warburg, *Handbuch der physik, Vol 14*. Berlin: Springer, 1927.

[119] B. L. Henson, "A derivation of Warburg's law for point to plane coronas," *J. Appl. Phys.*, vol. 52, no. 6, p. 3921, Jun. 1981.

[120] F. Woodcock, "Passivation of Semiconductor Surfaces for High-Efficiency Solar Cells," Oxford, 2014.

[121] R. S. Bonilla, F. Woodcock, and P. R. Wilshaw, "Very low surface recombination velocity in n-type c-Si using extrinsic field effect passivation," *J. Appl. Phys.*, vol. 116, no. 5, p. 054102, 2014.

[122] R. S. Bonilla, C. Reichel, M. Hermle, and P. R. Wilshaw, "Electric Field Effect Surface Passivation for Silicon Solar Cells," *Solid State Phenom.*, vol. 205–206, pp. 346–351, Jan. 2013.

[123] R. S. Bonilla and P. R. Wilshaw, "Stable field effect surface passivation of n-type Cz silicon," in *Energy Procedia - Proceedings of the 3rd Silicon PV Conference*, 2013, vol. 38, no. null, pp. 816–822.

[124] T. W. Hickmott, "Thermally stimulated ionic conductivity of sodium in thermal SiO2," *J. Appl. Phys.*, vol. 46, no. 6, pp. 2583 – 2598, 1975.

[125] www.sintoninstruments.com, "Sinton Instruments." 2012.

[126] R. A. Sinton, A. Cuevas, and M. Stuckings, "Quasi-steady-state photoconductance, a new method for solar cell material and device characterization," in *Photovoltaic Specialists Conference, 1996., Conference Record of the Twenty Fifth IEEE*, 1996, pp. 457–460.

[127] R. A. Sinton and A. Cuevas, "Contactless determination of current–voltage characteristics and minority-carrier lifetimes in semiconductors from quasi-steady-state photoconductance data," *Appl. Phys. Lett.*, vol. 69, no. 17, p. 2510, Oct. 1996.

[128] K. L. Luke and L.-J. Cheng, "Analysis of the interaction of a laser pulse with a silicon wafer: Determination of bulk lifetime and surface recombination velocity," *J. Appl. Phys.*, vol. 61, no. 6, p. 2282, Mar. 1987.

[129] A. B. Sproul, "Dimensionless solution of the equation describing the effect of surface recombination on carrier decay in semiconductors," *J. Appl. Phys.*, vol. 76, no. 5, p. 2851, Sep. 1994.

[130] MATLAB, "Parametric Fitting - MATLAB & Simulink." [Online]. Available: http://uk.mathworks.com/help/curvefit/parametric-fitting.html. [Accessed: 24-May-2015].

[131] E. H. Nicollian and A. Goetzberger, "MOS Conductance Technique for Measuring Surface State Parameters," *Appl. Phys. Lett.*, vol. 7, no. 8, p. 216, Nov. 1965.

[132] S. M. Sze, *Semiconductor Devices: Physics and Technology*. John Wiley and Sons, Inc.

[133] KP Technology, "Single Point Kelvin Probe," 2012. [Online]. Available: www.kelvinprobe.com.

[134] I. D. Baikie, S. Mackenzie, P. J. Z. Estrup, and J. A. Meyer, "Noise and the Kelvin method," *Rev. Sci. Instrum.*, vol. 62, no. 5, pp. 1326–1332, May 1991.

[135] W. T. Kelvin, *Contact electricity of metals*. London: W. Clowes and sons, 1897.

[136] J. C. Rivière, "Contact Potential Difference Measurements by the Kelvin Method," *Proc. Phys. Soc. Sect. B*, vol. 70, no. 7, pp. 676–686, Jul. 1957.

[137] D. K. Schroder, *Semiconductor material and device characterization*. John Wiley & Sons, Inc., 2006.

[138] R. B. M. Girisch, R. P. Mertens, and R. F. Dekeersmaecker, "Determination of Si-SiO2 Interface Recombination Parameters using a Gate-Controlled Point-Junction Diode under Illumination," *IEEE Trans. Electron Devices*, vol. 35, no. 2, pp. 203–222, 1988.

[139] R. A. Abbott and T. I. Kamins, "Sodium migration through electron-gun evaporated Al2O3 and double layer Al2O3SiO2 structures," *Solid. State. Electron.*, vol. 13, no. 5, pp. 565–576, May 1970.

[140] S. Baker-Finch and K. R. McIntosh, "Characterisation of Corona-Charged Oxide-Passivated Silicon," in *3 rd International Solar Energy Society Conference – Asia Pacific Region*.

[141] L. E. Black and K. R. McIntosh, "Defect Generation at Charge-Passivated Si/SiO2 Interfaces by Ultraviolet Light," *IEEE Trans. Electron Devices*, vol. 57, no. 8, pp. 1996–2004, Aug. 2010.

[142] ASTM International, "ASTM G173-03(2012) Standard Tables for Reference Solar Spectral Irradiances: Direct Normal and Hemispherical on 37° Tilted Surface." West Conshohocken, 2012.

[143] A. G. Aberle, S. Glunz, and W. Warta, "Impact of illumination level and oxide parameters on Shockley-Read-Hall recombination at the Si-SiO2 interface," *J. Appl. Phys.*, vol. 71, no. 9, pp. 4422–4431, 1992.

[144] Synopsys Inc, "Device Simulation Tools - Sentaurus." [Online]. Available: http://www.synopsys.com/TOOLS/TCAD/DEVICESIMULATION/Pages/default.aspx. [Accessed: 20-Aug-2012].

[145] U. of N. S. Wales, "PC1D." [Online]. Available: http://www.pv.unsw.edu.au/info-about/our-school/products-services/pc1d. [Accessed: 20-Aug-2012].

[146] S. Dauwe, "Low-temperature Surface Passivation of Crystalline Silicon and its Application to the Rear Side of Solar Cells," Univeristy of Hannover, 2004.

[147] S. W. Glunz, A. B. Sproul, W. Warta, and W. Wettling, "Injection-level-dependent recombination velocities at the Si-SiO2 interface for various dopant concentrations," *J. Appl. Phys.*, vol. 75, no. 3, p. 1611, Feb. 1994.

[148] W. Mönch, *Semiconductor Surfaces and Interfaces*, Third Edit. Springer, 2001.

[149] L. F. Shampine, M. W. Reichelt, and J. Kierzenka, "Solving Boundary Value Problems for Ordinary Differential Equations in MATLAB with bvp4c," *http://www.mathworks.com/bvp_tutorial.*, 2000.

[150] D. Neamen, *Semiconductor Physics and Devices*, Fourth. McGraw-Hill Higher Education, 2012.

[151] S. Steingrube, P. P. Altermatt, D. S. Steingrube, J. Schmidt, and R. Brendel, "Interpretation of recombination at c-Si/SiN[sub x] interfaces by surface damage," *J. Appl. Phys.*, vol. 108, no. 1, p. 014506, Jul. 2010.

[152] I. Martin, B. Hoex, M. C. M. van de Sanden, R. Alcubilla, and W. M. M. Kessels, "The origin of emitter-like recombination for inverted c-Si surfaces," in *23rd European Photovoltaic Solar Energy Conference*.

[153] Z. Hameiri, F.-J. Ma, and K. R. McIntosh, "Investigation of low injection effects using the local ideality factor obtained from effective lifetime measurements," in *2014 IEEE 40th Photovoltaic Specialist Conference (PVSC)*, 2014, pp. 1842–1847.

[154] A. Aberle, S. Glunz, and W. Warta, "Field effect passivation of high efficiency silicon solar cells," *Sol. Energy Mater. Sol. Cells*, vol. 29, no. 2, pp. 175–182, Mar. 1993.

[155] S. Dauwe, J. Schmidt, A. Metz, and R. Hezel, "Fixed charge density in silicon nitride films on crystalline silicon surfaces under illumination," in *Conference Record of the Twenty-Ninth IEEE Photovoltaic Specialists Conference, 2002.*, pp. 162–165.

[156] K. J. Weber, H. Jin, C. Zhang, N. Nursam, W. E. Jellett, and K. R. McIntosh, "Surface Passivation using Dielectric Films: How Much Charge is Enough?," in *24th European Photovoltaic Solar Energy Conference*, 2009.

[157] V. Leonov, P. Fiorini, and C. Van Hoof, "Stabilization of positive charge in SiO2/Si3N4 electrets," *IEEE Trans. Dielectr. Electr. Insul.*, vol. 13, no. 5, pp. 1049–1056, Oct. 2006.

[158] F.-J. Ma, G. G. Samudra, M. Peters, A. G. Aberle, F. Werner, J. Schmidt, and B. Hoex, "Advanced modeling of the effective minority carrier lifetime of passivated crystalline silicon wafers," *J. Appl. Phys.*, vol. 112, no. 5, p. 054508, Sep. 2012.

[159] B. Veith, T. Ohrdes, F. Werner, R. Brendel, P. Altermatt, N.-P. Harder, and J. Schmidt, "Injection dependence of the effective lifetime of n-type Si passivated by Al2O3 : an edge effect?," in *Proceedings of SiliconPV 2013 - Solomat*, pp. Hamelin, Germany.

[160] F.-J. Ma, Z. Hameiri, G. S. Samudra, M. Peters, and B. Hoex, "Numerical analysis of injection level dependent effective lifetime on 125 mm undiffused lifetime samples," in *2014 IEEE 40th Photovoltaic Specialist Conference (PVSC)*, 2014, pp. 3313–3316.

[161] D. Vuillaume and J. C. Bourgoin, "Characterization of Si-SiO2 interface states: Comparison between transient capacitance and conductance techniques," *J. Appl. Phys.*, vol. 58, no. 5, p. 2077, Sep. 1985.

[162] O. Engström, *The MOS System*. Cambridge University Press, 2014.

[163] J. T. Ryan, A. Matsuda, J. P. Campbell, and K. P. Cheung, "Interface-state capture cross section—Why does it vary so much?," *Appl. Phys. Lett.*, vol. 106, no. 16, p. 163503, Apr. 2015.

[164] T. J. Tredwell and C. R. Viswanathan, "Determination of interface-state parameters in a MOS capacitor by DLTS," *Solid. State. Electron.*, vol. 23, no. 11, pp. 1171–1178, Nov. 1980.

[165] A. Ricksand and O. Engström, "Deep-level transient spectroscopy: Increased accuracy of interpretation of silicon/silicon dioxide interface state data by the assistance of computer simulations," *J. Appl. Phys.*, vol. 70, no. 11, p. 6915, Jan. 1991.

[166] K. R. McIntosh and L. E. Black, "On effective surface recombination parameters," *J. Appl. Phys.*, vol. 116, no. 1, p. 014503, Jul. 2014.

[167] W. D. Eades and R. M. Swanson, "Calculation of surface generation and recombination velocities at the Si-SiO2 interface," *J. Appl. Phys.*, vol. 58, no. 11, p. 4267, Dec. 1985.

[168] L.M. and Terman, "An investigation of surface states at a silicon/silicon oxide interface employing metal-oxide-silicon diodes," *Solid. State. Electron.*, vol. 5, no. 5, pp. 285–299, 1962.

[169] C. N. Berglund, "Surface states at steam-grown silicon-silicon dioxide interfaces," *Electron Devices, IEEE Trans.*, vol. 13, no. 10, pp. 701–705, Oct. 1966.

[170] R. Castagne and A. Vapaille, "Description of the SiO2?Si interface properties by means of very low frequency MOS capacitance measurements," *Surf. Sci.*, vol. 28, no. 1, pp. 157–193, 1971.

[171] K. R. McIntosh, S. C. Baker-Finch, N. E. Grant, A. F. Thomson, S. Singh, and I. D. Baikie, "Charge Density in Atmospheric Pressure Chemical Vapor Deposition TiO[sub 2] on SiO[sub 2]-Passivated Silicon," *J. Electrochem. Soc.*, vol. 156, no. 11, p. G190, Nov. 2009.

[172] E. H. Nicollian and J. R. Brews, *MOS (Metal Oxide Semiconductor) — Physics and Technology*. Wiley, New York, 1982.

[173] A. S. Grove, E. H. Snow, B. E. Deal, and C. T. Sah, "Simple Physical Model for the Space-Charge Capacitance of Metal-Oxide-Semiconductor Structures," *J. Appl. Phys.*, vol. 35, no. 8, pp. 2458–2460, 1964.

[174] T. Ohmi, S. Sudoh, and H. Mishima, "Static charge removal with IPA solution," *IEEE Trans. Semicond. Manuf.*, vol. 7, no. 4, pp. 440–446, 1994.

[175] D. Macdonald, R. A. Sinton, and A. Cuevas, "On the use of a bias-light correction for trapping effects in photoconductance-based lifetime measurements of silicon," *J. Appl. Phys.*, vol. 89, no. 5, p. 2772, Mar. 2001.

[176] O. Schultz, M. Hofmann, S. W. Glunz, and G. P. Willeke, "Silicon oxide/silicon nitride stack system for 20% efficient silicon solar cells," in *Conference Record of the Thirty-first IEEE Photovoltaic Specialists Conference*, 2005, pp. 872–876.

[177] R. S. Bonilla, G. Martins, and P. R. Wilshaw, "Investigation of parasitic edge recombination in high-lifetime oxidized n-Si," *Solid State Phenom.*, vol. 242, 2016.

[178] A. G. M. Goldman, R. S. Sigmond, M. Goldman, A. Goldman, and R. S. Sigmond, "The corona discharge, its properties and specific uses," *Pure Appi. Chem., ,* vol. 57, no. 9, pp. 1353–1362, 1985.

[179] I. Faulkner, "Corona Enhanced Oxidation of Materials," University of Oxford, 2013.

[180] C. M. Osburn and D. W. Ormond, "Dielectric Breakdown in Silicon Dioxide Films on Silicon," *J. Electrochem. Soc.*, vol. 119, no. 5, p. 591, May 1972.

[181] K. Nakamura, T. Takahashi, T. Hikichi, and I. Takata, "An observation of breakdown characteristics on thick silicon oxide," in *Proceedings of International Symposium on Power Semiconductor Devices and IC's: ISPSD '95*, 1995, pp. 374–379.

[182] K. F. Schuegraf, "Effects of temperature and defects on breakdown lifetime of thin SiO/sub 2/ at very low voltages," *IEEE Trans. Electron Devices*, vol. 41, no. 7, pp. 1227–1232, Jul. 1994.

[183] K. F. Schuegraf and C. Hu, "Metal-oxide-semiconductor field-effect-transistor substrate current during Fowler–Nordheim tunneling stress and silicon dioxide reliability," *J. Appl. Phys.*, vol. 76, no. 6, p. 3695, Sep. 1994.

[184] J. F. Verweij and J. H. Klootwijk, "Dielectric breakdown I: A review of oxide breakdown," *Microelectronics J.*, vol. 27, no. 7, pp. 611–622, Oct. 1996.

[185] D. M. Brown and P. V. Gray, "Si-SiO[sub 2] Fast Interface State Measurements," *J. Electrochem. Soc.*, vol. 115, no. 7, p. 760, Jul. 1968.

[186] J. A. Voorthuyzen, W. Olthuis, P. Bergveld, and A. J. Sprenkels, "Research and development of miniaturized electrets," *IEEE Transactions on Electrical Insulation*. IEEE, 01-Mar-1989.

[187] R. Kressmann, G. M. Sessler, and P. Gunther, "Space-charge electrets," *IEEE Trans. Dielectr. Electr. Insul.*, vol. 3, no. 5, pp. 607–623, 1996.

[188] P. Gunther, "Mechanism of charge storage in electron-beam or corona-charged silicon-dioxide electrets," *IEEE Trans. Electr. Insul.*, vol. 26, no. 1, pp. 42–48, 1991.

[189] A. Das, K. Ryu, and A. Rohatgi, "20% Efficient Screen-Printed n-Type Solar Cells Using a Spin-On Source and Thermal Oxide/Silicon Nitride Passivation," *IEEE J. Photovoltaics*, vol. 1, no. 2, pp. 146–152, Oct. 2011.

[190] R. S. Bonilla, C. Reichel, M. Hermle, and P. R. Wilshaw, "On the location and stability of charge in SiO2/SiNx dielectric double layers used for silicon surface passivation," *J. Appl. Phys.*, vol. 115, no. 14, p. 144105, Apr. 2014.

[191] J. Robertson, "Defects and hydrogen in amorphous silicon nitride," *Philos. Mag. Part B*, vol. 69, no. 2, pp. 307–326, Feb. 1994.

[192] J. Schmidt, F. Werner, B. Veith, D. Zielke, S. Steingrube, P. P. Altermatt, S. Gatz, T. Dullweber, and R. Brendel, "Advances in the Surface Passivation of Silicon Solar Cells," *Energy Procedia*, vol. 15, no. null, pp. 30–39, Jan. 2012.

[193] M. H. Kang, K. Ryu, A. Upadhyaya, and A. Rohatgi, "Optimization of SiN AR coating for Si solar cells and modules through quantitative assessment of optical and efficiency loss mechanism," *Prog. Photovoltaics Res. Appl.*, vol. 19, no. 8, pp. 983–990, Dec. 2011.

[194] S. Y. Herasimenka, C. J. Tracy, V. Sharma, N. Vulic, W. J. Dauksher, and S. G. Bowden, "Surface passivation of n-type c-Si wafers by a-Si/SiO2/SiNx stack with <1 cm/s effective surface recombination velocity," *Appl. Phys. Lett.*, vol. 103, no. 18, p. 183903, Oct. 2013.

[195] J. Schmidt, M. Kerr, and A. Cuevas, "Surface passivation of silicon solar cells using plasma-enhanced chemical-vapour-deposited SiN films and thin thermal SiO 2 /plasma SiN stacks," *Semicond. Sci. Technol.*, vol. 16, no. 3, pp. 164–170, Mar. 2001.

[196] V. Sharma, C. Tracy, D. Schroder, S. Herasimenka, W. Dauksher, and S. Bowden, "Manipulation of K center charge states in silicon nitride films to achieve excellent surface passivation for silicon solar cells," *Appl. Phys. Lett.*, vol. 104, no. 5, p. 053503, Feb. 2014.

[197] F. Granek and C. Reichel, “Back-contact back-junction silicon solar cells under UV illumination,” *Sol. Energy Mater. Sol. Cells*, vol. 94, no. 10, pp. 1734–1740, Oct. 2010.

[198] K. Jager and R. Hezel, “Optical stability of silicon nitride MIS inversion layer solar cells,” *IEEE Trans. Electron Devices*, vol. 32, no. 9, pp. 1824–1829, Sep. 1985.

[199] L. Guo and R. Hezel, “Studies on evaporated cesium incorporation in MIS inversion layer solar cells,” *Solid. State. Electron.*, vol. 37, no. 9, pp. 1659–1662, Sep. 1994.

[200] M. R. Boudry and J. P. Stagg, “The kinetic behavior of mobile ions in the Al-SiO2-Si system,” *J. Appl. Phys.*, vol. 50, no. 2, p. 942, Feb. 1979.

[201] D. R. Kerr, “A Review of Instability Mechanisms in Passivation Films,” in *8th Reliability Physics Symposium*, 1970, pp. 1–8.

[202] J. Piprek, “Numerical Analysis of TVS Ionic Current Applied to the Na+ Motion in Implanted MOS Oxide Layers,” *Phys. Status Solidi*, vol. 112, no. 2, pp. 551–560, Apr. 1989.

[203] S. R. Hofstein, “An investigation of instability and charge motion in metal-silicon oxide-silicon structures,” *IEEE Trans. Electron Devices*, vol. 13, no. 2, pp. 222–237, Feb. 1966.

[204] J. J. Moré, “The Levenberg-Marquardt algorithm: Implementation and theory,” in *Numerical Analysis*, Springer Berlin Heidelberg, 1978, pp. 105–116.

[205] P. K. Nauta and M. W. Hillen, “Investigation of mobile ions in MOS structures using the TSIC method,” *J. Appl. Phys.*, vol. 49, no. 5, p. 2862, May 1978.

[206] G. F. Derbenwick, “Mobile ions in SiO2: Potassium,” *J. Appl. Phys.*, vol. 48, no. 3, p. 1127, Mar. 1977.

[207] J. P. Stagg, “Drift mobilities of Na+ and K+ ions in SiO2 films,” *Appl. Phys. Lett.*, vol. 31, no. 8, p. 532, Oct. 1977.

[208] G. Greeuw and J. F. Verwey, “The mobility of Na+, Li+, and K+ ions in thermally grown SiO2 films,” *J. Appl. Phys.*, vol. 56, no. 8, p. 2218, 1984.

[209] Panasonic Corporation, *Panasonic HIT Solar Cell Achieves World’s Highest Energy Conversion Efficiency of 25.6% at Research Level*. URL: panasonic.co.jp/corp/news/, 2014.

[210] A. Goodrich, P. Hacke, Q. Wang, B. Sopori, R. Margolis, T. L. James, and M. Woodhouse, “A wafer-based monocrystalline silicon photovoltaics road map: Utilizing known technology improvement opportunities for further reductions in manufacturing costs,” *Sol. Energy Mater. Sol. Cells*, vol. 114, pp. 110–135, Jul. 2013.

[211] A. Wang, J. Zhao, and M. A. Green, “24% efficient silicon solar cells,” *Appl. Phys. Lett.*, vol. 57, no. 6, p. 602, Aug. 1990.

[212] A. W. Blakers, A. Wang, A. M. Milne, J. Zhao, and M. A. Green, “22.8% efficient silicon solar cell,” *Appl. Phys. Lett.*, vol. 55, no. 13, p. 1363, Sep. 1989.

[213] M. A. Green, “The path to 25% silicon solar cell efficiency: History of silicon cell evolution,” *Prog. Photovoltaics Res. Appl.*, vol. 17, no. 3, pp. 183–189, May 2009.

[214] J. Zhao, A. Wang, P. Alatermatt, S. Wenham, and M. Green, “24% efficient perl silicon solar cell: Recent improvements in high efficiency silicon cell research,” *Sol. Energy Mater. Sol. Cells*, vol. 41–42, no. null, pp. 87–99, Jun. 1996.

[215] R. J. Schwartz and M. D. Lammert, “The interdigitated back contact solar cell: A silicon solar cell for use in concentrated sunlight,” *IEEE Trans. Electron Devices*, vol. 24, no. 4, pp. 337–342, Apr. 1977.

[216] J. Dicker, J. O. Schumacher, W. Warta, and S. W. Glunz, “Analysis of one-sun monocrystalline rear-contacted silicon solar cells with efficiencies of 22.1%,” *J. Appl. Phys.*, vol. 91, no. 7, p. 4335, Apr. 2002.

[217] D. D. Smith, P. J. Cousins, A. Masad, S. Westerberg, M. Defensor, R. Ilaw, T. Dennis, R. Daquin, N. Bergstrom, A. Leygo, X. Zhu, B. Meyers, B. Bourne, M. Shields, and D. Rose, “SunPower’s Maxeon Gen III solar cell: High efficiency and energy yield,” in *2013 IEEE 39th Photovoltaic Specialists Conference (PVSC)*, 2013, pp. 0908–0913.

[218] D. De Ceuster, P. Cousins, D. Rose, M. Cudzinovic, and W. Mulligan, “Low Cost, High Volume Production of >22% Efficiency Silicon Solar Cells,” in *22nd European Photovoltaic Specialist Conference*, 2007.

[219] C. Reichel, M. Bivour, F. Granek, M. Hermle, and S. W. Glunz, “Improved diffusion profiles in back-contacted back-junction Si solar cells with an overcompensated boron-doped emitter,” *Phys. status solidi*, vol. 208, no. 12, pp. 2871–2883, Dec. 2011.

[220] F. Granek, M. Hermle, and S. W. Glunz, “Analysis of the current linearity at low illumination of high-efficiency back-junction back-contact silicon solar cells,” *Phys. status solidi - Rapid Res. Lett.*, pp. 151–153, Jul. 2008.

[221] A. Rohatgi, P. Doshi, J. Moschner, T. Lauinger, A. G. Aberle, and D. S. Ruby, “Comprehensive study of rapid, low-cost silicon surface passivation technologies,” *IEEE Trans. Electron Devices*, vol. 47, no. 5, pp. 987–993, May 2000.

[222] M. Hofmann, S. Kambor, C. Schmidt, D. Grambole, J. Rentsch, S. W. Glunz, and R. Preu, “PECVD-ONO: A New Deposited Firing Stable Rear Surface Passivation Layer System for Crystalline Silicon Solar Cells,” *Adv. Optoelectron.*, vol. 2008, pp. 1–10, 2008.

[223] P. Doshi and A. Rohatgi, “18% efficient silicon photovoltaic devices by rapid thermal diffusion and oxidation,” *IEEE Trans. Electron Devices*, vol. 45, no. 8, pp. 1710–1716, 1998.

[224] J. Dupuis, E. Fourmond, V. M.-T. Yen, O. Nichiporuk, M. Greffioz, N. Le Quang, and M. Lemiti, “Study of Rear PECVD Dielectric Stacks for Industrial Silicon Solar

Cells," in *24th European Photovoltaic Solar Energy Conference*, 2009, pp. 1623–1627.

[225] J. Eisenlohr, N. Tucher, A. J. Bett, H. Hauser, M. Graf, J. Benick, J. C. Goldschmidt, B. Bläsi, and M. Hermle, "Novel light trapping concepts for crystalline silicon solar cells using diffractive rear side structures," in *SPIE Photonics Europe*, 2014, p. 91400C.

[226] G. D. Wilk, R. M. Wallace, and J. M. Anthony, "High-κ gate dielectrics: Current status and materials properties considerations," *J. Appl. Phys.*, vol. 89, no. 10, p. 5243, May 2001.

[227] P. A. Basore and K. Cabanas-Holmen, "PC2D: A Circular-Reference Spreadsheet Solar Cell Device Simulator," *IEEE J. Photovoltaics*, vol. 1, no. 1, pp. 72–77, Jul. 2011.

[228] P. A. Basore, "PC2D," *Visited 2015*. [Online]. Available: http://www.pc2d.info/.

[229] H. Mäckel and K. Varner, "On the determination of the emitter saturation current density from lifetime measurements of silicon devices," *Prog. Photovoltaics Res. Appl.*, p. n/a–n/a, Feb. 2012.

[230] P. A. Basore and K. Cabanas-Holmen, "Comparison of 1D and 2D Model Results for Selective Emitter and Interdigitated Back Contact Cells," *27th Eur. Photovolt. Sol. Energy Conf. Exhib.*, pp. 1462–1464, Oct. 2012.

[231] M. Hermle, F. Granek, O. Schultz, and S. W. Glunz, "Analyzing the effects of front-surface fields on back-junction silicon solar cells using the charge-collection probability and the reciprocity theorem," *J. Appl. Phys.*, vol. 103, no. 5, p. 054507, Mar. 2008.

[232] J. D. Jackson, *Classical Electrodynamics*, 3rd ed. Wiley, 1999.

[233] W. M. Gosney, "Surface Properties in the System: Silicon-Silicon Dioxide-Aluminum Oxide," University of California at Berkeley, 1970.

[234] A. S. Grove and D. J. Fitzgerald, "Surface effects on p-n junctions: Characteristics of surface space-charge regions under non-equilibrium conditions," *Solid. State. Electron.*, vol. 9, no. 8, pp. 783–806, Aug. 1966.

[235] S. R. Hofstein, "Proton and sodium transport in SiO2 films," *IEEE Trans. Electron Devices*, vol. 14, no. 11, pp. 749–759, Nov. 1967.

[236] T. W. Hickmott, "Dipole layers at the metal-SiO2 interface," *J. Appl. Phys.*, vol. 51, no. 8, p. 4269, Aug. 1980.

[237] J. Li-Jiu, W. Yang-yuan, Z. Li-chun, and N. Xuie-win, "The kinetic behaviour of mobile ions in SiO2 studied with TSIC and TVS measruements," in *The Physics of MOS Insulators. Proceedings of the International Topical Conference*, 1980, pp. 34–38.

[238] C. Choquet and B. Balland, “New accurate exploitation of thermally stimulated ionic current curves for alkali contaminated metal-oxide-silicon structures,” *Appl. Phys. Lett.*, vol. 52, no. 21, p. 1791, May 1988.

APPENDIX A

Insulator charge calculation

The concentration of charge in the insulator and at the Si surface states can be calculated from the CV characteristics of the MIS capacitor in flat-band conditions. Figure 17.c illustrates the flat-band condition –i.e. when charge in the metal contact compensates the metal-to-semiconductor work function difference, the insulator charge, and the surface states charge. The gate potential that takes the semiconductor into the flat-band condition ($\phi_s =$ 0 V) is:

$$V_{g-fb} = \frac{\Phi_{ms}}{\mathrm{q}} + V_i \tag{A. 1}$$

Where the subscript *fb* indicates the flat-band condition. It therefore follows that finding V_{g-fb} would allow the calculation of the insulator voltage V_i, and therefore the insulator charge concentration. For flat-band conditions, the semiconductor high frequency capacitance is defined as [172]:

$$C_{fb} = \frac{\varepsilon_S}{L_d} = \frac{\varepsilon_S}{\sqrt{\frac{\varepsilon_S V_t}{q|N_{dop}|}}} \tag{A. 2}$$

Where $V_t = kT/q$ is the thermal energy, ε_S is the silicon permittivity, and N_{dop} is the semiconductor dopant density which has been defined here as negative for n-type silicon and positive for p-type such that $N_{dop} = N_{acceptors} - N_{donors}$, and L_d is the Debye length: a characteristic length in semiconductors that indicates the distance over which free charges can be screened. The insulator capacitance is determined by the maximum capacitance

measured on a CV curve where the semiconductor is in a heavy accumulation regime (large positive V_g for n-Si). When the semiconductor is in heavy accumulation the depletion region capacitor becomes infinite and the equivalent capacitance is that of the insulator. This is indicated in the bottom graph in Figure 17.b. The capacitor area (thickness) can be calculated if the thickness (area) is known assuming a parallel plate capacitor:

$$C_i = K_i \varepsilon_0 \frac{A}{t_i} \tag{A. 3}$$

Where A is the capacitor area, t_i its thickness, and K_i its relative permittivity. Finding V_{g-fb} from a CV measurement is therefore possible by calculating:

$$C_{fb}(V_{g-fb}) = \left. \frac{C_{meas} C_i}{C_{meas} - C_i} \right|_{V_g = V_{g-fb}} \tag{A. 4}$$

Where C_{meas} is the experimentally measured capacitance. This allows one to find the potential across the insulator V_i, which is in turn used to calculate its charge concentration.

Green's reciprocity theorem can be used to prove that, given a charge Q between two conducting (or semiconducting) planes, the total induced charge in one of the planes is equal to -Q times the fractional perpendicular distance to the opposite plane [98], [232]. Integrating the charge contribution from $x = 0$ to $x = t_i$, the total charge induced potential in the semiconductor, that is thus compensated in the metal, is given by:

$$V_i = -\frac{1}{K_i \varepsilon_0} \int_0^{t_i} x \rho_i(x) dx \tag{A. 5}$$

Where $\rho_i(x)$ is the volumetric charge distribution in the insulator, including its interface to the semiconductor. In practice, it has been observed that most charge in insulators lies near their interfaces [190]. It is hence useful to approximate the volumetric charge distribution as $\rho_i(x) = \sigma_i \delta(x - t_i)$, where $\delta(x)$ is the Dirac-Delta function. This

describes a sheet of charge σ_i located at t_i distance from the metal. The insulator potential becomes:

$$V_i = -\frac{\sigma_i t_i / K_i}{\varepsilon_0} = -\frac{\sigma_i}{\varepsilon_0 K_i / t_i} = -\frac{\sigma_i}{C_i / A} \quad \text{(A. 6)}$$

This calculation results in a surface charge concentration σ_i, located (presumably) at the insulator/semiconductor interface. It is noted that CV measurements do not provide the location of the charge in the insulator. A clear example of this is the charge calculation on a double layered insulator system, where the potential drop is affected by two different permittivities. The relation between insulator induced potential and insulator charge for this case was drawn by Gosney [233] and reproduced by Abbot and Kamins [139]:

$$V_i = -\frac{1}{K_1 \varepsilon_0} \int_0^{t_1} x \rho_i(x) dx - \frac{1}{K_2 \varepsilon_0} \int_{t_1}^{t_1 + t_2} \left(\frac{K_2 t_i}{K_1} + (x - t_i) \right) \rho_2(x) dx \quad \text{(A. 7)}$$

As an example a silicon nitride/silicon dioxide/silicon system is considered. The nitride is the first dielectric, adjacent to the metal gate, having a thickness t_1 and a relative permittivity K_1, and the oxide is the second dielectric with thickness t_2 and permittivity K_2. Solutions to equation (A. 7) for different charge distributions can be drawn as:

$$\rho(x) = \sigma_i \delta(x - t_1) \rightarrow \qquad V_i = \frac{\sigma_i}{\varepsilon_0 K_1 / t_1} \quad \text{(A. 8)}$$

$$\rho(x) = \sigma_i \delta(x - (t_1 + t_2)) \rightarrow \qquad V_i = \frac{\sigma_i}{\left(\frac{t_1}{\varepsilon_0 K_1} + \frac{t_2}{\varepsilon_0 K_2} \right)^{-1}} \quad \text{(A. 9)}$$

$$\rho(x) = \frac{\sigma_i}{t_1 + t_2} \rightarrow \qquad V_i = \frac{1}{2\varepsilon_0} \frac{\sigma_i}{t_1 + t_2} \left(\frac{t_1^2}{K_1} + \frac{2 t_1 t_2}{K_1} + \frac{t_2^2}{K_2} \right) \quad \text{(A. 10)}$$

The capacitance-voltage technique was used in the present work to find the charge concentration based on the observed insulator potential. Therefore, it is of interest to calculate the charge concentration using the different assumed charge distributions above and have a qualitative description of its differences. Figure 96.a illustrates the resulting charge density in a 100/60 nm oxide/nitride double layer on 1 Ωcm Si when the insulator potential

found from CV measurements is V_i = -5 V. Here, it is clear that depending on the charge location, different values of charge can be calculated. This confirms that charge calculations using CV measurements are only meaningful if the location of the charge is correctly assumed. This issue is addressed using a separate method to profile the location of charge in the bulk of the insulator system, Section 2.5.2.1.

Notice that the quantities $\varepsilon_0 K_1/t_1$ in equation (A. 8) and $\left(\frac{t_1}{\varepsilon_0 K_1} + \frac{t_2}{\varepsilon_0 K_2}\right)^{-1}$ in equation (A. 9) are experimentally measured as the insulator capacitance per unit area, and are therefore less susceptible to errors arising from assumed values for dielectric constants used in equation (A. 10). In this same example is it also useful to calculate the insulator voltage as a function of the position of a fixed plane charge distribution. Figure 96.b shows the change in the CV flat-band voltage of as a function of the position of a plane with charge density σ_i. In this two layer system it is evident that the closer the charge lies to the silicon, the more influence it has on the flat-band gate voltage inferred from a CV measurement. The dependence is linear with a slope given by the insulator characteristics. Higher permittivity produces a smaller change in the flat-band gate potential.

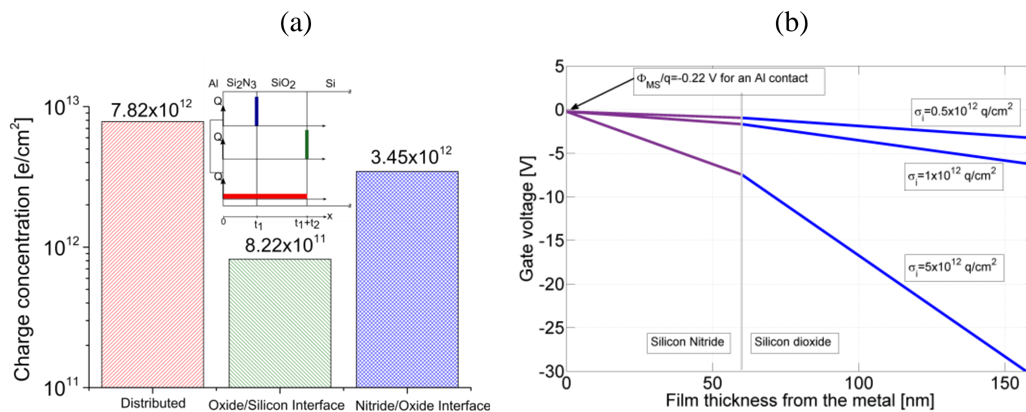

Figure 96: a. Example of surface charge concentration calculated for three different assumed charge distributions in a 100/60 nm oxide/nitride double layer dielectric film, giving a -5 V insulator voltage. b. Change of gate potential as a function of a planar charge distribution situated at different positions in an Al/Si_3N_4/SiO_2/Si system.

Characterisation of surface state density using high frequency CV measurements

The density of interface trap states D_{it} is a metric of the level of chemical passivation a dielectric provides. Figure 17.b illustrates the stretch-out effect that interface trap states have on the transition from low to high capacitance observed during CV measurements together with the equivalent circuit that accounts for them. This section describes how CV measurements can be used to estimate the distribution of interface trap sates as a function of energy in the bandgap $D_{it}(E)$.

The semiconductor capacitance includes the depletion region capacitance C_D plus the interface state capacitance C_{it}. For an interface defect density D_{it}(E), the change in charge at the interface is $dQ_{it} = qD_{it}dE$, and $dE = qd\phi_s$ such that:

$$C_{it} = \frac{dQ_{it}}{d\phi_s} = q^2 D_{it} \tag{A. 11}$$

The voltage divider given by the insulator and semiconductor capacitances in series produces a semiconductor to gate potential ratio:

$$\frac{d\phi_s}{dV_g} = \frac{C_i}{C_i + (C_D + C_{it})} \tag{A. 12}$$

Such that the density of states can be found as [132]:

$$D_{it} = \left| \frac{C_i}{q^2} \left[\left(\frac{d\phi_s}{dV_g} \right)^{-1} - 1 \right] - \frac{C_d}{q^2} \right| \tag{A. 13}$$

where the $\frac{d\phi_s}{dV_g}$ relation is theoretically found for the MIS capacitor measured. This technique was first proposed by Terman [168]. A semiconductor in not-flat-band condition presents a charge concentration Q_{Si} such that the insulator potential V_i, and hence the gate potential, is increased in $\Delta V = Q/C$. The gate potential is therefore given by:

$$V_g = V_{g-fb} + \phi_s + \frac{Q_{Si}}{\varepsilon_i / t_i} \quad \text{(A. 14)}$$

And the space charge density in silicon is given by [234]:

$$Q_{Si} = -\frac{|\phi_s|}{\phi_s}(2kTn_i\varepsilon_s)^{1/2}\sqrt{\mathrm{e}^{\frac{\phi_p-\phi_s}{V_t}} - \mathrm{e}^{\frac{\phi_p}{V_t}} + \mathrm{e}^{\frac{\phi_s-\phi_n}{V_t}} - \mathrm{e}^{-\frac{\phi_n}{V_t}} + \phi_s\left(\frac{N_{dop}}{V_t n_i}\right)} \quad \text{(A. 15)}$$

Where ϕ_p and ϕ_n are the quasi Fermi levels when carriers are photo-generated in the semiconductor, and n_i is the intrinsic carrier concentration in the semiconductor. Quasi Fermi levels are included here for completeness since they will be used in Chapter 3. In the absence of carrier photo-generation they become the semiconductor Fermi level:

$$\phi_F = -\frac{N_{dop}}{|N_{dop}|} V_t \ln\left(\frac{|N_{dop}|}{n_i}\right) \quad \text{(A. 16)}$$

A MATLAB script was written to find the SCR potential, ϕ_{scr} that corresponded to the measured gate potential according to equations (A. 14) and (A. 15). This was achieved by minimising the function *F* using a Levenberg-Marquardt algorithm:

$$F = \left[V_{g-fb} + \phi_{scr} + \frac{Q_{si}}{\frac{\varepsilon_i}{t_i}}\right]_{theory} - \ V_{g-measured} \quad \text{(A. 17)}$$

As an example, Figure 20 illustrates a CV curve of an Al/SiO_2/Si MIS capacitor fabricated from wafer n14_6 (see Section 2.2.3). This algorithm has been applied and $D_{it}(E)$ found by directly replacing the $\frac{d\phi_s}{dV_g}$ relation into equation (A. 13). The ideal theoretical high frequency capacitance has been included in Figure 20.a for comparison. In the presence of light, some photo-generation of carriers occurs. This reduces the depletion region for negative gate voltages, thus inducing a higher measured capacitance than that predicted theoretically. Further details on the theory of MIS capacitors can be found in Sze's book [132].

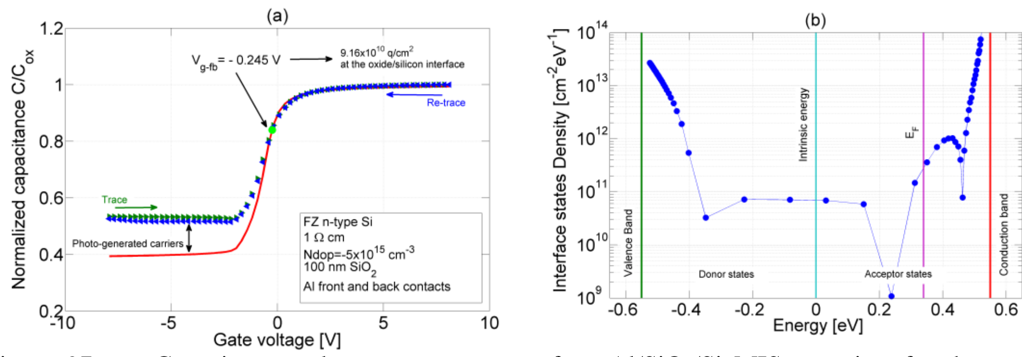

Figure 97: a. Capacitance-voltage measurement of an Al/SiO_2/Si MIS capacitor for the upsweep (trace) and the down-sweep (re-trace). The red trace is the theoretically calculated capacitance for this MIS capacitor including the insulator charge, b. Oxide/silicon interface state density calculated using Terman's high frequency method.

APPENDIX B

Modelling ionic injection with first order kinetics

The TSIC experiments conducted in this project helped investigate the injection and migration of ions inside dielectric films. This section provides a framework to analyse the results of these experiments and study the transport of ions in dielectrics. The first studies of ionic transport of charge were carried out by Hofstein in a metal/oxide/semiconductor (MOS) structure, using bias-temperature stress and capacitance-voltage [203], [235]. Hofstein found evidence that the charge transport was limited by ions' release from traps at interfaces, rather than by the diffusion behaviour of the species in the bulk SiO_2. This differs from the physical model proposed by Snow et al. [98] in which it is assumed that the drift activation energy is directly related to the diffusion coefficient for ion motion in a 'bulk' oxide. Hofstein concluded that charge transport in SiO_2 is caused by a fixed number of ions, that lay at the interface and that are confined in a trap of activation energy E_a. Thorough studies of trap-mediated transport dynamics of ions in the Si/SiO_2 systems followed by Hickmott [124], [236], and Boudry and Stagg [200], [207]. They used TSIC to conclude that the ionic species would concentrate at interfaces in a range of different energy traps rather than at a single energy. The accumulation of sodium at interfacial traps has also been recently confirmed by Krivec et al [101] using TSIC and time-of-flight-secondary ion mass spectrometry (ToF-SIMS).

It has been shown that first order kinetics accurately predicts the ion dynamics, once the initial distribution of trapping energy of ions at an interface is known [203]:

$$\frac{dn(E,t)}{dt} + n(E,t)s(E)\exp\left(-\frac{E}{kT}\right) = 0 \tag{A. 18}$$

where $n(E,t)$ is the number of ions in a trap of energy E at time t, $s(E)$ is a pre-exponential factor that represents the number of attempts ions make to surmount a trap of energy E, and is defined as $s(E) = \beta\sqrt{E}$. And $T(t)$ is the temperature as a function of time.

The solution to this equation is given by:

$$n(E,t) = n(E,0)\exp\left[-\int_0^t \beta\sqrt{E}\exp\left(-\frac{E}{kT(t')}\right)dt'\right] \tag{A. 19}$$

Boudry and Stagg [200] have reported a complete mathematical description of this problem. However, they did not report the method used to calculate the initial distribution of ions $n(E,0)$. Approximations to this distribution have been used by assuming a single activation energy [124], a Gaussian distribution of traps as a function energy [201], [202], or even a convolution of Dirac functions and the measured current density [237]. In 1988, Choquet and Balland [238] published the first accurate attempt to calculate the initial ion distribution, yet some discrepancies were found in their calculation. Thus there still exists uncertainty in determining the initial energy distribution of trapped ions. In the present work a Gaussian function has been used to approximate $n(E,0)$ finding the best fit empirically. This has been found to be a reasonable approximation as will be shown in Chapter 4.

APPENDIX C

Summary of samples and processing

Processing abbreviations:

- Corona discharge: CD
- Anneal at X temperature – Y time: AnnX-Y
- Kelvin probe surface potential map: KPmap
- Long term τ_{eff} and KP monitoring: LT
- Surface treatments: (T) textured, (F) FGA, (H) HMDS.
- Alkali ion deposited: K, Na, Cs, etc.

Sample	Silicon	Res [Ωcm]	Dielectric	Thickness [nm]	Processing
n6b_3	FZ	1	SiO_2	100	+CD, -CD
nCb3	Cz	5	SiO_2	87.5	H, +CD, KPmap, LT
n6b_4	FZ	1	SiO_2	100	+CD, KPmap
nT1_9	FZ (T)	1	SiO_2	100	+CD, Ann400C-1m, LT
n1_2	FZ	1	SiO_2	100	+CD
n7_8	FZ	1	SiO_2	100	+CD
n17b_1	FZ	1	SiO_2	100	F, +CD x2,
n10_5a	FZ	1	SiO_2	100	+CD
n17_8	FZ	1	SiO_2	100	F,+CD

nE1	Cz	5	SiO_2	21.5	+CD
nC8	Cz	5	SiO_2	87.5	+CD
n9_x1	FZ	1	SiO_2	100	+CD
nC1	Cz	5	SiO_2	87.5	+CD
n9_x1	FZ	1	SiO_2	100	+CD, LT
n1_6	FZ	1	SiO_2	100	H,+CD, LT
n17_5	FZ	1	SiO_2	100	F, H,+CD, LT
n17_7	FZ	1	SiO_2	100	F,+CD, LT
nCb4	Cz	5	SiO_2	87.5	H, +CD, Ann400C-10m, LT
nCb7	Cz	5	SiO_2	87.5	H, +CD, LT
nBb1	Cz	5	SiO_2	21.5	H, +CD, Ann400C-10m, LT
nBb2	Cz	5	SiO_2	21.5	H, +CD, LT
n1_1	FZ	1	SiO_2	100	H,+CD, Ann400C-5m, LT
n7_6	FZ	1	SiO_2	100	+CD, Ann400C-5m, LT
Ox1-1_5	FZ	1	SiO_2/SiN_x	10/60	F,+CD, LT
Ox1-5_6	FZ (T)	1	SiO_2/SiN_x	10/60	F,+CD, LT
n17_8	FZ	1	SiO_2	100	F,+CD, LT
n19_3	FZ	1	SiO_2/SiN	100/80	F+CD, LT
n21b_5	FZ	1	SiO_2/SiN	100/80	F,+CD
n6_5	FZ	1	SiO_2/SiN	100/80	+CD, LT
n6_8	FZ	1	SiO_2/SiN	100/80	H,+CD, LT
Ox1-1_1	FZ	1	SiO_2/SiN_x	10/60	F,+CD, LT
Ox1-1_4	FZ	1	SiO_2/SiN_x	10/60	F, H, +CD, LT
Ox1-5_1	FZ (T)	1	SiO_2/SiN_x	10/60	F,+CD, LT

Ox1-5_5	FZ (T)	1	SiO_2/SiN_x	10/60	H, F,+CD, LT
n5_x2	FZ	1	SiO_2	100	Na
n14_6	FZ	1	SiO_2	100	Na, Ann450C-18m
n7_1	FZ	1	SiO_2	100	Na, Ann400C-10m
n7_2	FZ	1	SiO_2	100	Na, +CD, Ann400C-10m
n7_3	FZ	1	SiO_2	100	K, +CD, Ann400C-10m
n7_4	FZ	1	SiO_2	100	K, +CD, Ann400C-10m
n7_5	FZ	1	SiO_2	100	+CD, Ann400C-10m
n7_6	FZ	1	SiO_2	100	+CD, Ann400C-10m
n2_1	FZ	1	SiO_2	100	Na, Ann400C-60m, H, LT
n2_5	FZ	1	SiO_2	100	K, Ann400C-90m
n2_8	FZ	1	SiO_2	100	Ann400C-90m
n5_3	FZ	1	SiO_2	100	Ann400C-130m
n9_1	FZ	1	SiO_2	100	Na, Ann500C-10m, LT
n9_2	FZ	1	SiO_2	100	Na, Ann450C-20m, LT
n9_3	FZ	1	SiO_2	100	Na, Ann400C-70m, LT
n9_5	FZ	1	SiO_2	100	Na, Ann550C-5m, LT
n10_1	FZ	1	SiO_2	100	K, Ann500C-10m, LT
n10_2	FZ	1	SiO_2	100	K, Ann450C-20m, LT
n10_3	FZ	1	SiO_2	100	K, Ann400C-100m, LT
n10_7	FZ	1	SiO_2	100	K, Ann550C-5m, LT
n5_1	FZ	1	SiO_2	100	Mg, Ann400C-20m, LT
n5_2	FZ	1	SiO_2	100	Ca, Ann400C-20m, LT
n4_5	FZ	1	SiO_2	100	Cs, Ann400C-60m

n7_1	FZ	1	SiO_2	100	Na, +CD, Ann400C-6m, LT
n7_3	FZ	1	SiO_2	100	K, +CD, Ann400C-6m, LT
n7_6	FZ	1	SiO_2	100	+CD, Ann400C-6m, LT
n7_2	FZ	1	SiO_2	100	Na, +CD, Ann400C-10m, LT
n7_4	FZ	1	SiO_2	100	K, +CD, Ann400C-10m, LT
n7_5	FZ	1	SiO_2	100	+CD, Ann400C-10m, LT
n2_3	FZ	1	SiO_2	100	K, +CD, Ann300C-15m, LT
n2_4	FZ	1	SiO_2	100	K, +CD, Ann300C-15m, H, LT
n4_1	FZ	1	SiO_2	100	K, +CD, Ann400C-110m H, LT
n16_1	FZ	1	SiO_2	100	F, K, +CD, Ann300C-15m, LT
n16_2	FZ	1	SiO_2	100	F, K, +CD, Ann300C-15m, H, LT
n16_7	FZ	1	SiO_2	100	F, +CD, Ann300C-15m, H, LT
n17_2	FZ	1	SiO_2	100	F, K, +CD, Ann500C-3m, LT
n17_6	FZ	1	SiO_2	100	F, +CD, Ann500C-3m, LT
n6_1	FZ	1	SiO_2	100	Mg, +CD, Ann400C-5m, LT
n6_2	FZ	1	SiO_2	100	Ca, +CD, Ann400C-5m, LT